

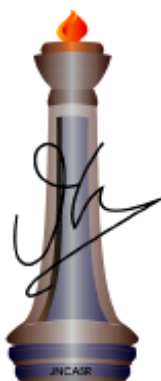
Temporal Control over Growth of Dynamic Charge-Transfer Stacks

A Thesis Submitted for the Degree of

Doctor of Philosophy

By

Ankit Jain



New Chemistry Unit

Jawaharlal Nehru Centre for Advanced Scientific Research

(A Deemed University)

Bangalore - 560064 (INDIA)

June 2016

Temporal Control over Growth of Dynamic Charge-Transfer Stacks

A Thesis Submitted for the Degree of

Doctor of Philosophy

By

Ankit Jain

UNDER THE SUPERVISION OF

Prof. Subi J. George

New Chemistry Unit

Jawaharlal Nehru Centre for Advanced Scientific Research

(A Deemed University)

Bangalore-560064 (INDIA)

June 2016

“I dream my painting and I paint my dream.”

- Vincent van Gogh

Dedicated to Supramolecular Chemistry

Laboratory at JNCASR

DECLARATION

I hereby declare that the thesis entitled “*Temporal Control over Growth of Dynamic Charge-Transfer Stacks*” is an authentic record of research work carried out by me at the New Chemistry Unit, Jawaharlal Nehru Centre for Advanced Scientific Research, Bangalore, India under the supervision of **Prof. Subi J. George** and that it has not been submitted elsewhere for the award of any degree or diploma.

In keeping with the general practice in reporting scientific observations, due acknowledgment has been made whenever the work described is based on the findings of other investigators. Any omission that might have occurred due to oversight or error in judgment is regretted.

Ankit Jain



**Jawaharlal Nehru Centre for
Advanced Scientific Research**

Prof. Subi J. George
New Chemistry Unit
Jawaharlal Nehru Centre for Advanced
Scientific Research (JNCASR)
Bangalore-560064,India
Phone : +91 80 2208 2964
Fax: + 91 80 22082627
E-mail: george@jncasr.ac.in

Date

June 6, 2016

CERTIFICATE

I hereby certify that the work described in this thesis titled “*Temporal Control over Growth of Dynamic Charge-Transfer Stacks*” has been carried out by **Ankit Jain** at the New Chemistry Unit, Jawaharlal Nehru Centre for Advanced Scientific Research, Bangalore, India under my supervision and it has not been submitted elsewhere for the award of any degree or diploma.

Subi J. George

(Research Supervisor)

ACKNOWLEDGEMENTS

*During the course of my Ph.D., I have been helped by a large number of people, to whom I will always be grateful. Firstly, I would like to offer my most sincere thanks to one person who has stayed with me from the beginning to the end of Ph.D., my research supervisor, **Prof. Subi Jacob George**. I am thankful to him for introducing me to the field of supramolecular chemistry and for giving me the freedom to work on various problems. His ever-enthusiastic nature, constant encouragement and support has helped me in successful completion of this work.*

*I would like to express my gratitude to **Prof. C. N. R. Rao, FRS** for being a constant source of inspiration. His lectures on history of science have been an experience of a lifetime. I am also grateful to him for creating such a vibrant research atmosphere to carry out this work.*

My special thanks to my labmates, the Suprachem group members: Dr. Venkat, Dr. Mohit, Dr. Chidambar, Dr. Bhawani, Krishnendu, Ananya, Suman, Aritra, Shikha, Pooja, Sergio and Beatrice for their cooperation, useful discussions and for creating a friendly atmosphere in the lab. Working with them was a real pleasure.

I am thankful to all the faculty members of NCU and CPMU for their guidance and support.

It is a great pleasure to thank my collaborators: Prof. M. Eswaramoorthy (JNCASR), Amritroop Achari (JNCASR), Prof. P. Vemula (NCBS) and Ashish Dhyani (NCBS) for fruitful collaborations.

I am thankful to Prof. Subi J. George, Prof. H. Ila, Prof. S. Rajaram, Prof. R. Viswanatha, Prof. T. K. Maji, Prof. P. Sebastian, Prof. U. K. Gautam from JNCASR and Prof. P. Balaram and Prof. S. P. Sharma from IISc for their coursework.

I am thankful to Prof. S. Rajaram, Prof. M. Eswaramoorthy, Prof. Hemalatha Balaram, Prof. P. Vemula (NCBS), Prof. E. W. Meijer, Prof. A. P. H. J. Schenning, Prof. O. A. Scherman and Prof. L. De Cola for useful discussions.

I express my sincere thanks to all my teachers, especially from SASTRA University, for their encouragement at various stages of my academic career.

I am thankful to the following people for various technical assistance: Prof. Ranjani V. and G. K. M. Grandhi (TCSPC), Mrs. Usha (TEM); Ashish (cryo-TEM, NCBS); Mr. Anil (Rheometer, Anton Paar); Mrs. Selvi (FESEM); Mr. Vasu (UV, PL, IR); Mr. Mahesh (SEM and NMR); Mr. Sandeep (DLS, Malvern); Sonu and Amrit (pH, DLS and Zeta Potential) and Shivakumar (HRMS).

I am grateful to summer students: Charu, Nivin, Archismita, Nithya and Pooja for working with me on various projects.

I am thankful to academic and administrative staff of JNCASR for their assistance.

I am thankful to my friends Mohit, Pavan, Amrit, Chidambar, Satya, Nishit, Ravi, Abhishek, Prasanna, Nitesh, Urmi, Piyush, Sonu, Arjun, Ramana, Umesh, Diwakar, Zia ul, Chandradhish, Krishna, Shivaprasad, Vijay, Anand, Yugandar, Dheeraj, Chandan, Pandu and Avinash for useful discussions.

Besides the research life, I am thankful to Prof. Subi J. George and his family members for their hospitality and affection.

Financial assistance from Jawaharlal Nehru Center for Advanced Scientific Research (JNCASR), is gratefully acknowledged.

A deep sense of gratitude to my family for their support, love and affection throughout my life. A special thank you to my wife Kalpita for her constant encouragement and faith.

Ankit

Preface

This thesis presents the design strategies to achieve temporal control over the growth of supramolecular assemblies. In the present work dynamic charge-transfer stacks have been taken as a model supramolecular system to prove the concepts.

The thesis is majorly divided into Six Chapters.

Chapter 1 presents the introduction, which aims to summarize the challenges and state of the art in achieving complete structural and functional control over supramolecular assemblies. The highlight would be on the requirement of a temporal control on the growth to achieve the next level of complexity and functional control on these stacks. The discussion starts with conventional self-assembly and moves on to more exotic properties such as living supramolecular polymerization. While discussing various existing strategies we attempt to arrive at a common strategy for the same. We then digress into biological self-assembly and discuss about the chemical reaction driven characteristic as their main tool to assemble aggregates in a living supramolecular fashion. Finally, a platform is set for the need of chemical reaction driven self-assembly in synthetic systems.

Chapter 2 describes a novel design strategy of using an external chemical reaction to control the one dimensional growth of charge-transfer stacks. Dynamic imine bond formation is used as an external chemical reaction in this work. Co-dependence of the reaction and aggregation has been uniquely established. Detailed morphological studies prove a narrow polydispersity of aggregates. Exploring the concept further the possibility of supramolecular hetero-structures has been delved into.

In **Chapter 3**, the advantage of stimuli responsiveness of imine bond formation has been explored. Additional strategies such as ligand dilution and an enzymatic pH control were introduced in combination with the external reaction to achieve delayed growth of assemblies. We thus show that the rate of aggregate formation can be either controlled by competitive inhibition or even bio-catalytically. A delayed deactivator approach was employed to design transient supramolecular structures. Varying concentration of

deactivator gave varying lifetimes of the transient aggregate. We have also shown that these aggregates can be re-fueled multiple times.

Chapter 4 presents a unique design to have reconfigurational control over the composition of donor acceptor molecules in an ensemble of various charge-transfer assemblies. Aggregation driven covalent synthesis has been taken as an inspiration and strategies to develop its non-covalent analogue has been explored. Systematic studies have been performed on ensembles up to four components and aggregation driven supramolecular ensemble reconfiguration has been established.

In **Chapter 5**, strategies have been explored to develop synthetic systems using ATP as a fuel for dissipative growth. Taking inspiration from the plethora of operations that ATP carries out in biological systems, we have shown dissipative conformational and aggregation control. Concepts developed in Chapter 4 have been utilized here and the effect of a dissipative aggregation has been studied on an ensemble and a possibility of dissipative reconfiguration has been explored. This design was successfully shown in one to three component ensembles.

Chapter 6 deals with the acceleration of a ring closure photo-oxidation reaction due to the specific structural constraints provided by layered materials. A stilbene derivative has been used as a prototype reactant and the dihydrophenanthrene intermediate has been isolated and characterized *en route* to the complete photo-oxidation. Combining the gathered evidence, a possible mechanism for the chemical transformation has been proposed. Thus, the structural microenvironment induced by layered materials could be a unique platform to probe and stabilize a plethora of photo-oxidative reactions and intermediates. We have also shown the utility of this transformation in achieving a photo control over the CIE co-ordinates of white light emission in these hybrids. Using such a control various white light standards have been achieved.

TABLE OF CONTENTS

Declaration	i
Certificate	iii
Acknowledgments	v
Preface	vii
Table of contents	ix

CHAPTER-1

Introduction

Towards Chemical Reaction Driven Living Supramolecular Polymerization

Abstract	3
1.1 Introduction	4
1.2 Conventional Supramolecular Polymerization	5
1.3 Seeded Supramolecular Polymerization	9
1.4 Living Supramolecular Polymerization	10
1.5 Self-assembly of Biological Systems	21
1.6 Chemical-Fuel Driven Self-assembly	23
1.7 Conclusion and Outlook	26
1.8 References and Notes	27

CHAPTER-2

Kinetically Controlled Living Supramolecular Polymerization

Abstract	33
2.1 Introduction	34
2.2 Results and Discussion	39
2.2.1 Living Supramolecular Polymerization	39
2.2.2 Hetero-Nucleation	59
2.3 Conclusion and Outlook	62
2.4 Experimental Section	63
2.5 References and Notes	65

CHAPTER-3

Programmable Growth and Decay of Dynamic Charge-Transfer Stacks

Abstract		69
3.1	Introduction	70
3.2	Results and Discussion	76
3.2.1	Controlled Growth by Ligand Dilution	76
3.2.2	Control of Growth by Delayed pH Activation	78
3.2.3	Controlled Decay of Supramolecular Fibers	83
3.3	Conclusion and Outlook	90
3.4	Experimental Section	91
3.5	References and Notes	92

CHAPTER-4

Aggregation Controlled Rearrangement of an Ensemble Containing Non-covalent Charge Transfer Stacks

Abstract		97
4.1	Introduction	98
4.2	Results and Discussion	99
4.3	Conclusion and Outlook	111
4.4	Experimental Section	111
4.5	References and Notes	112

CHAPTER-5

Strategies for Dissipative Conformational and Ensemble Control

Abstract		117
5.1	Introduction	118
5.2	Results and Discussion	122
5.2.1	Conformational Control Under Non-Equilibrium	124
5.2.2	Ensemble Control Under Non-Equilibrium	127

5.3	Conclusion and Outlook	131
5.4	Experimental Section	131
5.5	References and Notes	132

CHAPTER-6

Photo-Chemistry on Clay-Chromophore Hybrids

Chapter-6a	<i>Shining the Light on Clay-Chromophore Hybrids: Layered Templates for Accelerated Ring Closure Photo-Oxidation</i>	
Abstract		137
6a.1	Introduction	138
6a.2	Results and Discussion	139
6a.2.1	Design Strategy	139
6a.2.2	Clay-Dye conjugation	142
6a.2.3	Photo-Chemical Studies	143
6a.3	Conclusion and Outlook	153
6a.4	Experimental Section	157
6a.5	Appendix	159
6a.6	References and Notes	174
Chapter-6b	<i>Light Induced in-situ Post-Modification of Clay-Chromophore Hybrids for Multiple White Light Emissions</i>	
Abstract		177
6b.1	Introduction	178
6b.2	Results and Discussion	180
6b.3	Conclusion and Outlook	188
6b.4	Experimental Section	189
6b.5	References and Notes	189
Curriculum Vitae		193
List of Publications		195

Chapter-1

Introduction

*Towards Chemical Reaction Driven Living Supramolecular
Polymerization*

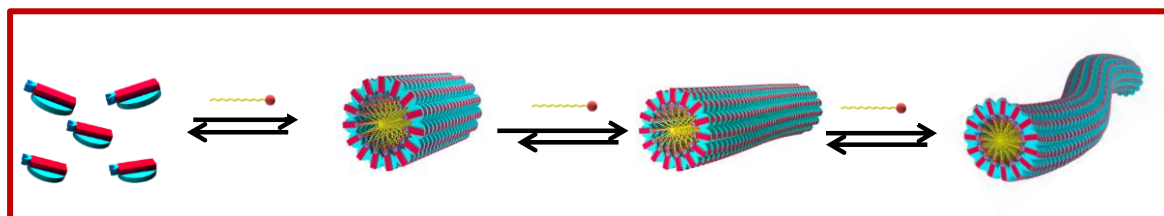
Chapter-1 (Introduction)

Towards Chemical Reaction Driven Living Supramolecular Polymerization

Abstract

Self-assembly has always been a promising route to achieve novel materials. This has been possible by decades of research and laying down of principles governing the phenomenon. Almost all of this assembly is under thermodynamic parameters and provide minimal help in exploring a temporally driven dimension of self-assembly. On the other hand in biological systems, which have always served as an omnipresent inspiration for self-assembly, control their aggregates and function temporally with unparalleled deft. Considering the conventional self-assembly one wonders if the complexity and dexterity of biological systems is ever to be matched and perhaps one might tread on diverse scientific routes for kinetically controlled self-assembly.

We in this Chapter explore the existing literature and delve of such a possibility. We start from a brief outlook about conventional methods to assemble chromophores and then proceed to a discussion about existing methods for achieving living supramolecular polymerization. Towards the end we also discuss about strategies for obtaining assemblies under non-equilibrium. In discussing these topic we wish to lay the ground work for upcoming discussion in subsequent chapters where we explore novel strategies for the same.



1.1. Introduction

Supramolecular chemistry has developed into many facets since its inception.¹⁻⁴ Each of these facets caters to several novel ideas towards a plethora of applications.⁵ However the true goal and inspiration of self-assembly i.e. mimicking the naturally occurring biological systems still remain an insurmountable challenge.⁶ This needs to be scaled not just for the sake of the intellectual challenge it possess but also because while doing so we might stumble into the key concepts one might need to build a complex system with the desired control and precision that truly brings down the curtain on the true potential of supramolecular assemblies towards potential applications.⁷⁻⁹

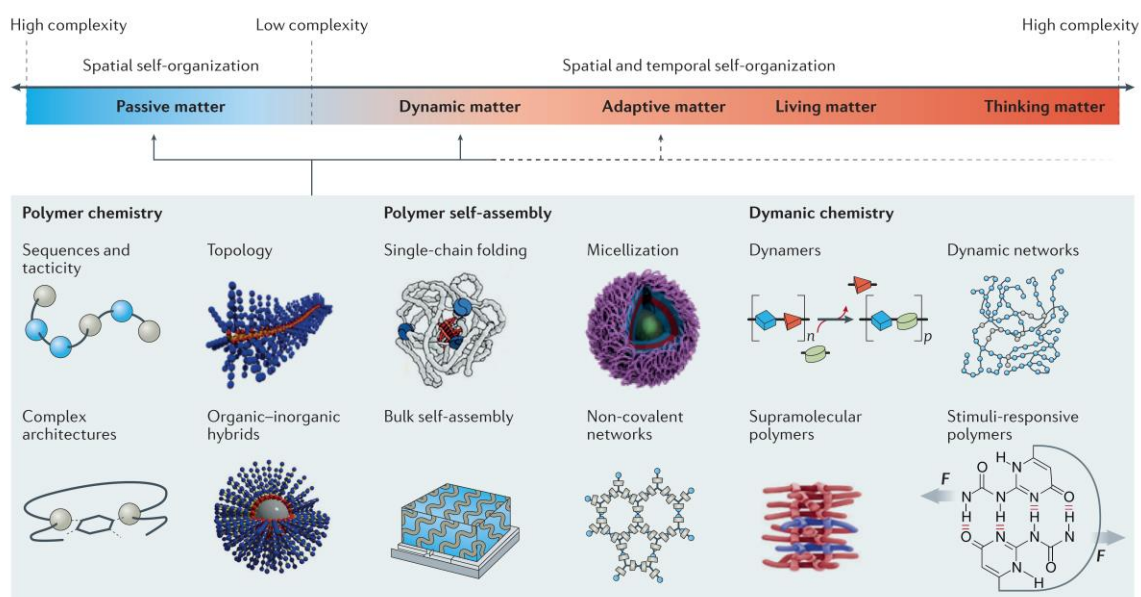


Figure 1.1. Schematic showing the shift from conventional materials to complex soft matter. The Figure shows the current state of the art polymer synthesis categorised against the class of soft matter differentiated by their spatial and temporal degrees of freedom (Figure reprinted with permission from Ref. 11).

Apart from the applications that ensue from a complex system one must understand that for a biological system an aggregate is more than a structure, it is in fact the basis of its function.¹⁰ Therefore to understand or replicate these systems truly we must delve into not just equilibrium systems but rather non-equilibrium systems as it is these which are truly employed in either

biological self-organisation or to the keys of origin of life via its self-replicating trait (Figure 1.1).¹¹⁻¹⁷

This thesis aims at understanding a very key concept of biological self-assembly which is temporal control over aggregates *via* a chemical fuel as we think this approach can singlehandedly cater to various existing challenges of supramolecular chemistry such as a living supramolecular polymerization, control over nucleation rate, transient materials and formation of supramolecular hetero-structures.

1.2. Conventional Supramolecular Polymerization

However before we delve into the key concepts that comprise the thesis a discussion is warranted towards classical or conventional self-assembly, the concepts of which might not directly answer the questions on afore mentioned challenges but form an important intellectual evolutionary step towards it. Conventional self-assembly occurs under thermodynamic control.¹⁸ They have been described on the basis of the thermodynamic equilibrium that governs their growth. Two major classes of supramolecular polymerization are namely Isodesmic growth and Co-operative growth.¹⁹ As mentioned above these mechanisms are differentiated by the equilibrium constraints imposed by the specific molecular design. Isodesmic growth is defined by a supramolecular polymerization process that occurs via energetically identical steps. This refers to a situation where the association constant with the i^{th} monomer is same as the one with $(i+1)^{\text{th}}$. In free energy terms, as the Isodesmic supramolecular polymerization precedes the successive addition of monomer to the growing chain leads to a constant decrease in the free energy, which in turn is indicative of the fact that affinity of a subunit for a polymer end is independent of the length of the polymer (Figure 1.2a,b). The amounts of monomers included in the supramolecular stack increases with increase in monomer concentration and the number average degree of polymerization is given as $C_t^{0.5}$, where C_t is the monomer concentration (Figure 1.2c). There is however a drawback associated with this kind of growth and that is the requirement of high association constants ($> 10^6 \text{ M}^{-1}$) for supramolecular polymer with high number average degree of

polymerization. A further analysis of these growth parameters suggest that as the polymerization proceeds, the poly-dispersity index grows steadily to the value of 2, a value at a higher end considering the use of supramolecular materials for precise applications. Recent reports suggest that the molecular design motif behind isodesmic growth could be the lack of either molecular rigidity, a macro dipole along the axis of growth or both.²⁰ A representative molecule for the isodesmic growth is hexa-*peri*-hexabenzocoronene (HBC) (**1-5**). Mullen and Aida *et al.* have individually carried out extensive research on derivatives of this particular molecule and various spectroscopic data suggests that the molecule favours an isodesmic mechanism in various solvents. The molecules based on this moiety generally shows enthalpically favoured and entropically disfavoured supramolecular polymerization and thus increasing the alkyl chains on these derivatives decreases their propensity to assemble as the steric interaction effects the enthalpy of polymerization (Figure 1.2d).²¹

Another common mechanism for supramolecular polymerization is the co-operative growth. In this particular mechanism growth occurs via two distinct stages. The first stage is isodesmic approach to the degree of polymerization towards a critical nuclei size. The association constant for this stage is generally denoted as K_n . Following the nuclei formation the incoming monomers associate with a linear isodesmic trend having an association constant of K_e , with K_e being greater than K_n (Figure 1.3a). This phase is referred to as the growth phase. In terms of the free energy during the nucleation phase there is an increase in free energy and is thus energetically unfavourable (Figure 1.3b). In a co-operative supramolecular polymerization, the nucleus is thus the least stable specie and hence the least prevalent in the reaction. After formation of the nuclei however the supramolecular polymerization becomes energetically favourable and thus proceeds energetically downhill. Considering the nuclei being energetically unfavourable there is a finite time towards the formation of elongated aggregates.²² This time gap can be removed by the addition of seeds to the polymerizing solution this process is called seeding and will be discussed later in this chapter. There is however a critical concentration and critical temperature towards the stability of the nuclei (Figure 1.3c). Considering the nuclei is a dimer,

the association constant for dimerization is generally denoted as K_2 and the equilibrium constants for all the subsequent steps is denoted as K .

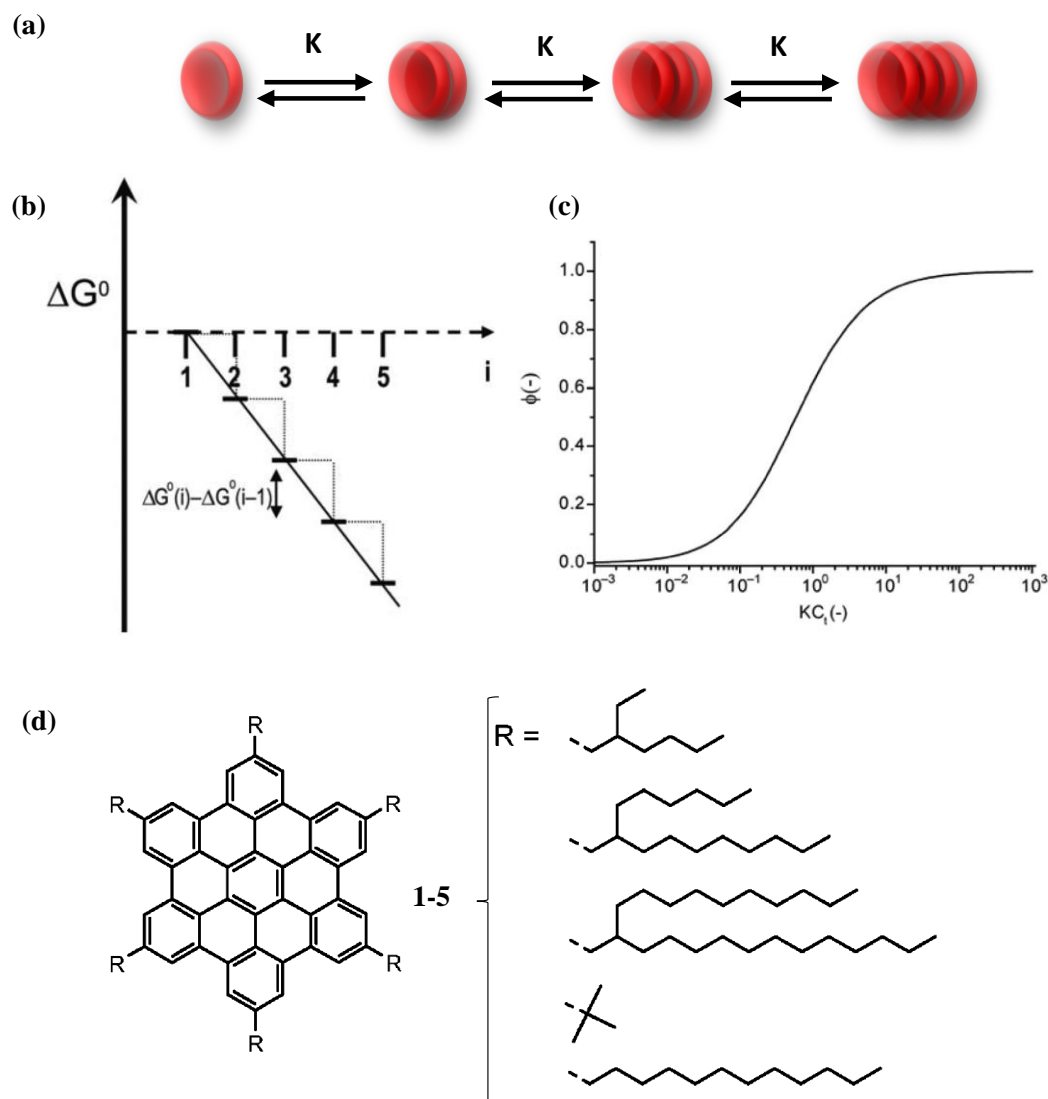


Figure 1.2. (a) Schematic representing the isodesmic growth, (b) and (c) Graphical representation of Gibbs free energy on increase of aggregate size and the increase in fraction of monomers in aggregated state upon the increase of concentration in an isodesmic growth respectively. (d) Molecular structures of various HBC derivatives which show isodesmic growth. (Figure 1.2b and 1.2c reprinted with permission from Ref. 18, Figure 1.2d with permission from Ref. 21).

The ratio of K_2/K is defined as the co-operativity factor (σ) and is generally less than 1. Lower the value of σ more co-operative is the system. The key difference between isodesmic and co-operative supramolecular polymerization is that in isodesmic system there is a gradual increase

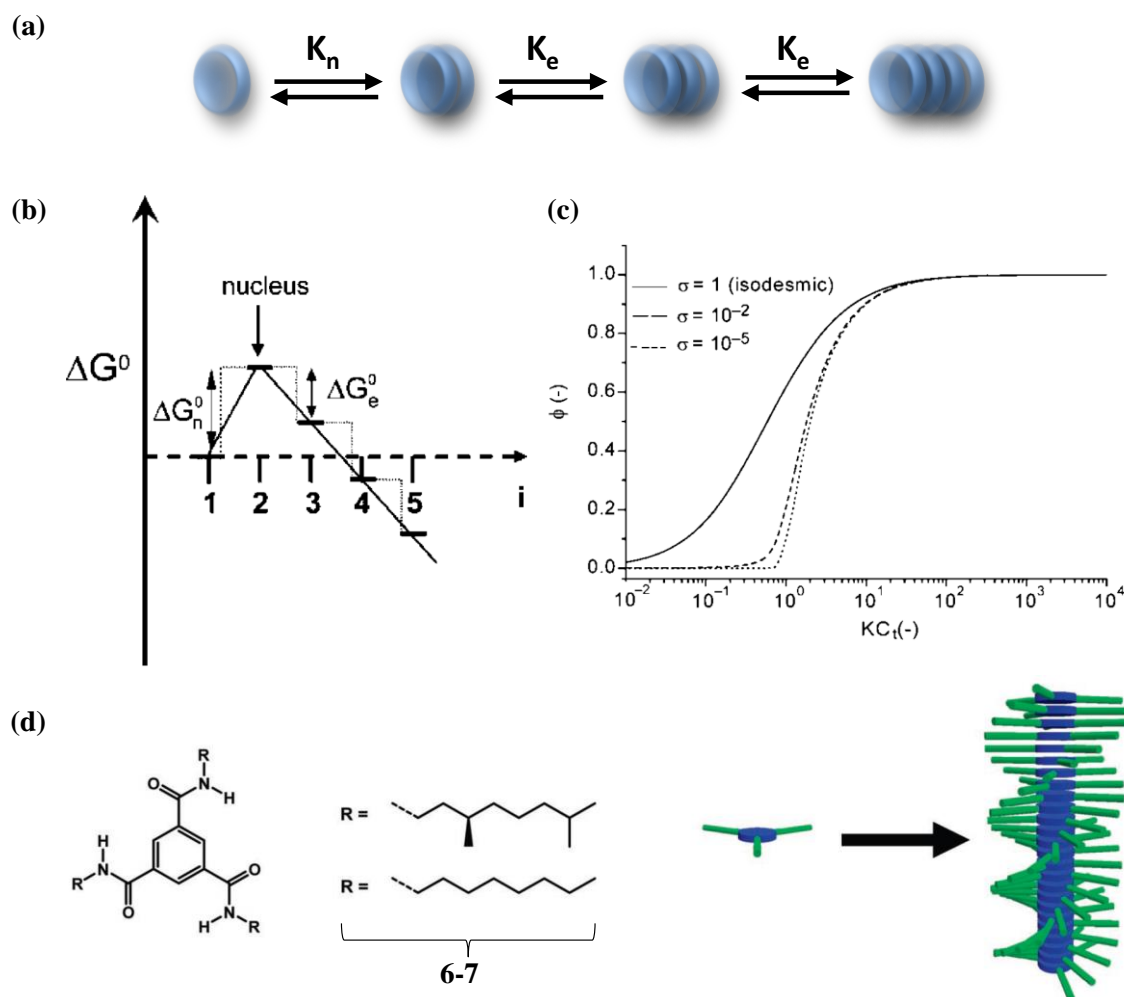


Figure 1.3. (a) Schematic representing the co-operative growth, (b) and (c) Graphical representation of Gibbs free energy on increase of aggregate size and the increase in fraction of monomers in aggregated state upon the increase of concentration in an co-operative growth respectively. (d) Molecular structures of various BTA derivatives which show co-operative growth. (Figure 1.3b and 1.3c reprinted with permission from Ref. 18, Figure 1.3d with permission from Ref. 23).

in the degree of polymerization as concentration increases whereas in a co-operative system there is a critical concentration and only beyond which aggregation occurs. Furthermore a higher degree of polymerization can also be achieved by lower σ value and not just by higher association constants. A cooperative supramolecular polymerization is thus characterized by a bimodal distribution that is due to the presence of monomers and supramolecular polymers that have elongated. Nucleation-elongation has been a trait in various biological and synthetic systems and if a molecule that is representative of this mechanism it is C_3 -symmetrical trialkylbenzene-1,3,5-

tricarboxamides (BTA) (**6-7**) (Figure 1.3d).²³ These molecules assemble in co-operative fashion with σ value of 2.3×10^{-2} . As mentioned earlier, in recent studies the presence of a macro-dipole (created by the H-bonds) is considered to be a reason behind the co-operativity of these molecules.²⁴

These basic mechanisms do define the thermodynamics and kinetics of supramolecular polymerization however the conventional approaches of assembly based on increasing concentration and decreased temperature does not give any insights into stabilization of nuclei. The approach to get kinetic stability of the nuclei is also not defined by conventional methods.

1.3. Seeded Supramolecular Polymerization

Conventionally addition of small crystallites to the supersaturated salt solution accelerates the rate of crystallization, this process is called seeding. Seeding effects are ubiquitous in biological systems as well.²⁵ Protein aggregates of actin and flagellin have been shown to undergo seeding.²⁶ They have tremendous biological relevance as they govern processes ranging from cell motility to cellular traffic.²⁷ A detailed discussion of their self-assembly would follow later in the Chapter. In an ideal scenario for seeded supramolecular polymerization the rate of nuclei formation should be slow and the rate of aggregate elongation should be fast and favoured. Moreover as the “seeds” or preformed supramolecular polymer is added to the solution, the addition of monomers to the nuclei seed dominates the kinetic process.²⁸

The reaction thus can be characterized as living supramolecular polymerization where the ends of the aggregate are always active for further growth. Conventionally, the equilibrium size distribution of a nucleation–elongation polymerization is expected to be a broad, exponential one. A valid assumption in this scenario would be that all the nuclei have equal propensity to associate with monomers and grow, the growth rates thus for all nuclei are nearly equal and hence the polydispersity of a seeded supramolecular polymerization is expected to be less (Figure 1.4). This

therefore sets the platform for mono-disperse ($PDI < 1.4$) aggregates that can be generated with controlled length.

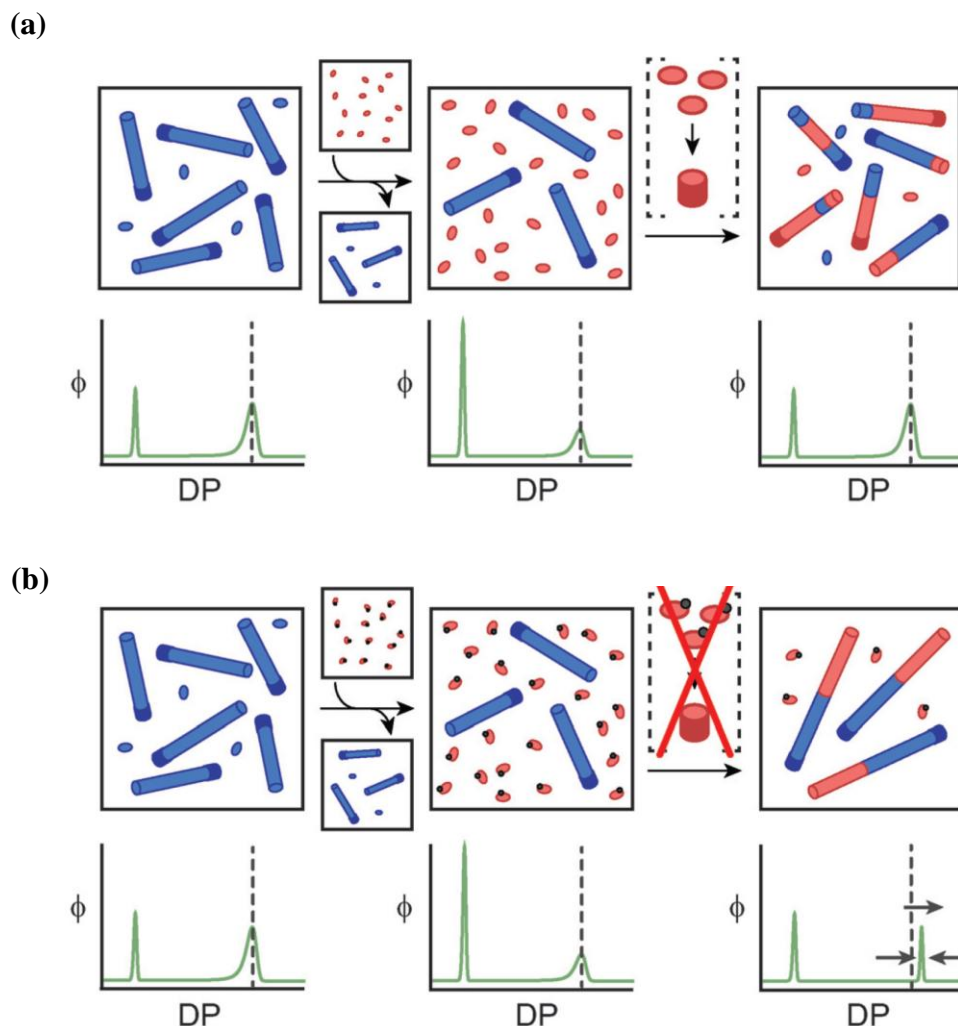


Figure 1.4. (a) and (b) Show the schematic of conventional and living or seeded polymerization along with distribution of Degree of polymerization (DP), respectively. In Figure 4a, incoming monomers (red) undergo independent nucleation even in the presence of existing nuclei (blue), moreover their DP distribution is broad. In Figure 4b incoming monomers (red) undergo addition on existing nuclei (blue) rather than independent nucleation. Their DP distribution is also narrow. (Reproduced with permission from Ref. 13).

1.4. Living Supramolecular Polymerization

As mentioned earlier a seeded supramolecular polymerization with always activated ends is classified as a living supramolecular polymerization. It is characterized by its strict control of

polydispersity and hence the aggregate structure. Achieving such a control has been challenging for chemists in synthetic systems and only few systems have evolved to show this exclusive genre of supramolecular polymerization.^{29,30} In this particular section we would discuss some of these outstanding works and try to decipher a commonality among them.

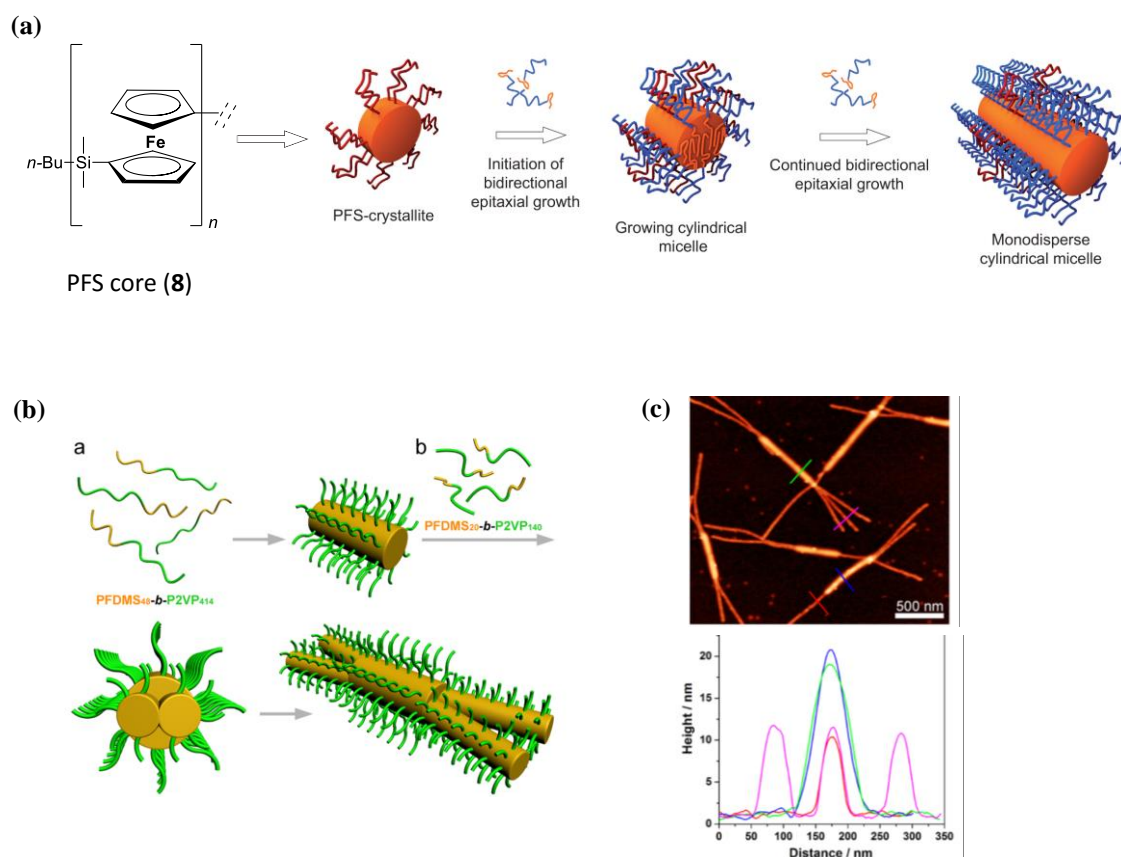


Figure 1.5. (a) Schematic representation of crystallization induced supramolecular living polymerization, (b) Schematic of the process to obtain branched nano-structures and (c) AFM images of the nanostructures with height profile below. (Fig. 1.5a reproduced with permission from Ref. 35, Fig. 1.5b and c reproduced with permission from Ref. 40).

As mentioned before living supramolecular polymerization is a bright prospect towards mono-disperse self-assembly. Mono-dispersity of structures is a major requisite that can bring about a sea change in supramolecular electronics and related applications. Monodispersity in non-spherical objects is a requisite that supramolecular chemistry has never been famed for, until the work of Manners *et al.* involving crystallization driven self-assembly.³¹ For all the promise that

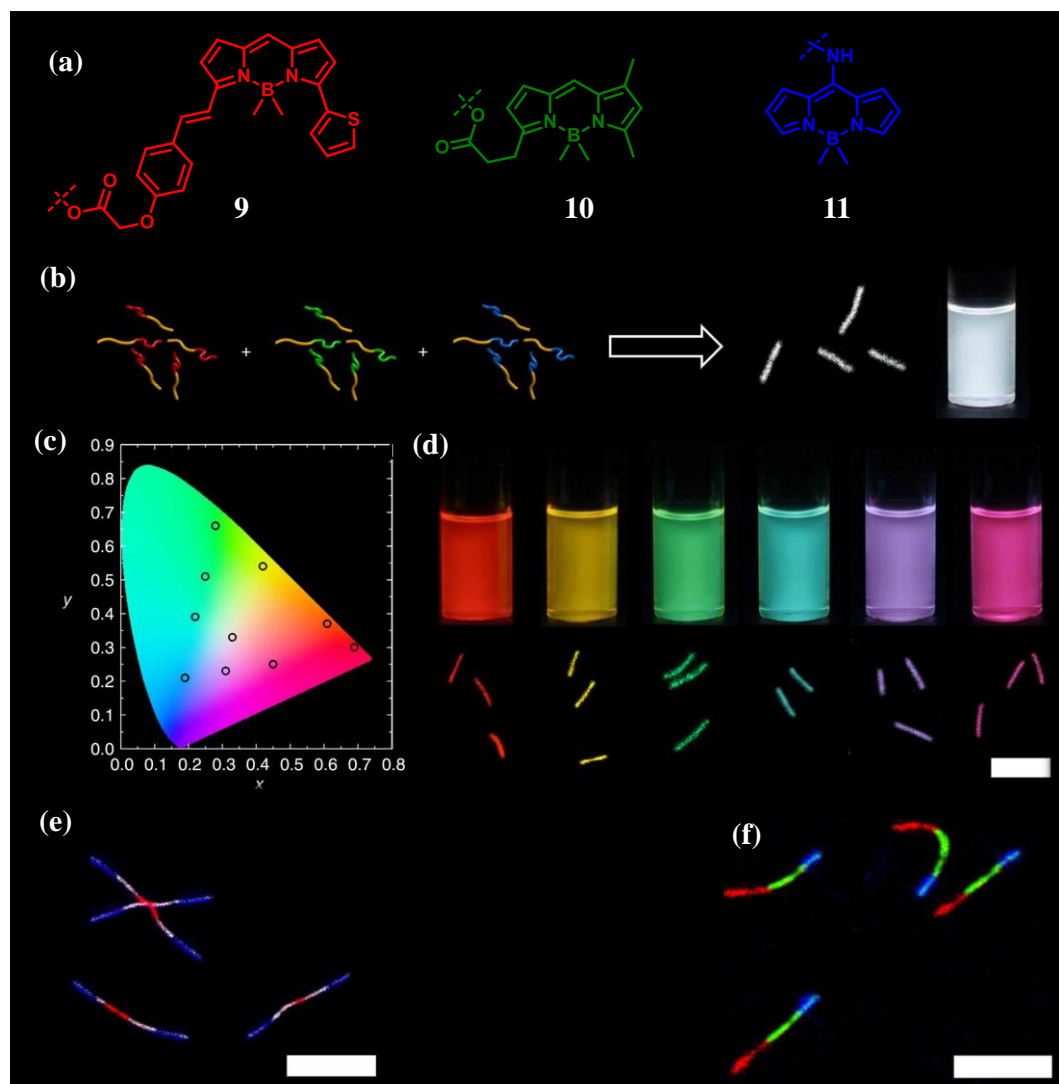


Figure 1.6. (a) Molecular structure of BODIPY dyes (9-11) (b) Schematic representation of the process of mixing independent micelles to get structures of various colors, (c) CIE 1931 chromaticity diagram for the solutions, (d) Photographs of the solutions under UV illuminations, below are their confocal images, scale $3\ \mu\text{m}$, (e) Confocal images of the centro-symmetric, multi-colour, multi-block, supramolecular polymer, scale $5\ \mu\text{m}$ and (f) Confocal images of the non-centro-symmetric, multi-colour, multi-block, supramolecular polymer, scale $5\ \mu\text{m}$. (Reproduced with permission from Ref. 41).

supramolecular chemistry holds, it was held back by its characteristic of producing aggregates with uncontrolled dimensions. This ensemble of sizes act as diluents of the functionality and precise control over these is rudimentary.

Although biomolecule templated self-assembly of π -conjugated systems has been investigated to control the dimensions, hydrophobic interaction upon concentration/drying on

surfaces results in their agglomeration and thus derails the purpose. Manners *et al.* employed a unique crystallization driven self-assembly which was used to assemble their polymers in a way analogous to living polymerization in conventional literature (Figure 1.5a).³² They used a diblock copolymer for their experiments. Apart from the several combinations tried, the common block remains polyferrocenylsilane (PFS) (**8**), which is responsible for the crystalline core.³³ Other blocks have been selected such that there exists a selective solubility as compared to the PFS block, for example polyisoprene (PI) or poly(dimethylsiloxane) (PDMS). Selective solubility enables the PFS blocks to self-assemble as the PI or PDMS blocks wrap around making the whole structure a cylindrical micelle, with a living end capable of further propagation on monomer availability.³⁴ For the experiment, seeds of pre-assembled micelles were added to the solution containing the free polymer and further growth has been investigated. The authors have pointed out that even though the “living” capability exists in these polymers when seeds of a size more than 100 nm and length dispersity of 1.4, these conditions were not sufficient to yield mono disperse lengths.³⁵ To attain their goal they needed to decrease both the length and the dispersity which was a significant challenge by itself. They finally standardized the conditions so as to yield nuclei of a size of around 20 nm and length dispersity of 1.03. These technological leaps finally allowed them to attain mono disperse structures. This opened an avenue with enormous possibilities.³⁶ One of the first issues this approach could cater to was the formation of designer aggregates, i.e. aggregates which possess a variety of shapes and could be attained by simple chemical modification to the core.³⁷⁻³⁹ Demonstrating the above in one such study, Manners *et al.* ended up creating branched micelles (Figure 1.5b).⁴⁰ The supramolecular copolymer used blocks of poly(ferrocenyldimethylsilane) (PFDMS) and poly(2-vinylpyridine) (P2VP). The study uses the concept of using a seed twice the diameter as incoming polymers destined to form the supramolecular branches. This allows nucleation of more than one polymer at the seed end, hence giving the branching. Since the ferrocenyl part is the self-assembling back bone, the higher its composition, the higher the micellar diameter goes - therefore the seed contains twice as much as PFDMS as compared to the polymers for branches. Following the addition pattern of seeds to a solution of “to be branches” polymer, they could attain a branched micellar structure previously

unattainable in such a controlled manner. This approach makes attaining supramolecular block co-polymers a mundane task, and the complexity that can be further generated has been best exemplified by the formation of multi colored fluorescent micelles in their recent report (Figure 1.6).⁴¹ Keeping the block of ferrocenyl silane constant, the other block contained fluorescent BODIPY (boron-dipyrromethene) dyes (**9-11**). Since the block addition can be controlled, one can envisage a whole variety of colours that can be attained by mixing blocks of basic colours in various proportions. The above has been demonstrated by scaling most of the area of the CIE (International Commission on Illumination) co-ordinate space just by changing the block proportions. Furthermore, complex unsymmetrical optical architectures have also been achieved using unidirectionally growing nuclei.⁴² Though the method of crystallization driven self-assembly have only recently been shown in small molecules, the above still remains the only example of such unprecedented control over the self-assembly.^{43,44}

Living or seeded supramolecular assembly has also been to possess large scale alignment of mono-disperse aggregates of small π -conjugated molecules by Giuseppone *et al.* in a fascinating light induced living polymerization.^{45,46} This study features triarylamine based molecules (**12**). They discovered that this class of molecules in chloroform solution and exposure to light readily changed color and gave rise to the triaryl ammonium radical. Evolution of the radical can be seen over time if one follows the reaction by EPR. Further analysis showed that a small quantity of these radicals formed CT pairs with neutral species upon generation and this triggers an aggregation of neutral molecules further (Figure 1.7a). The whole process is triggered by light. The uniqueness of this approach was demonstrated a couple of years later by the same group. They employed the same concept of light induced aggregation, only this time across a channel with an applied voltage.⁴⁷ Aggregate alignment has previously been performed by using a multitude of external physical interaction or by crosslinking the aggregates by a pincer approach. As the light is shined the free radicals are created, further forming CT pairs with neutral molecules. Being charged, the pair aligns itself due to the applied voltage and hence results in further growth across the channels (Figure 1.7 b-d). This observation is ground breaking in terms

of the fact that misaligned nanostructures across an electrode channel was a major disadvantage, and the fact that they can now be grown between the gap is a unique example of soft lithography.

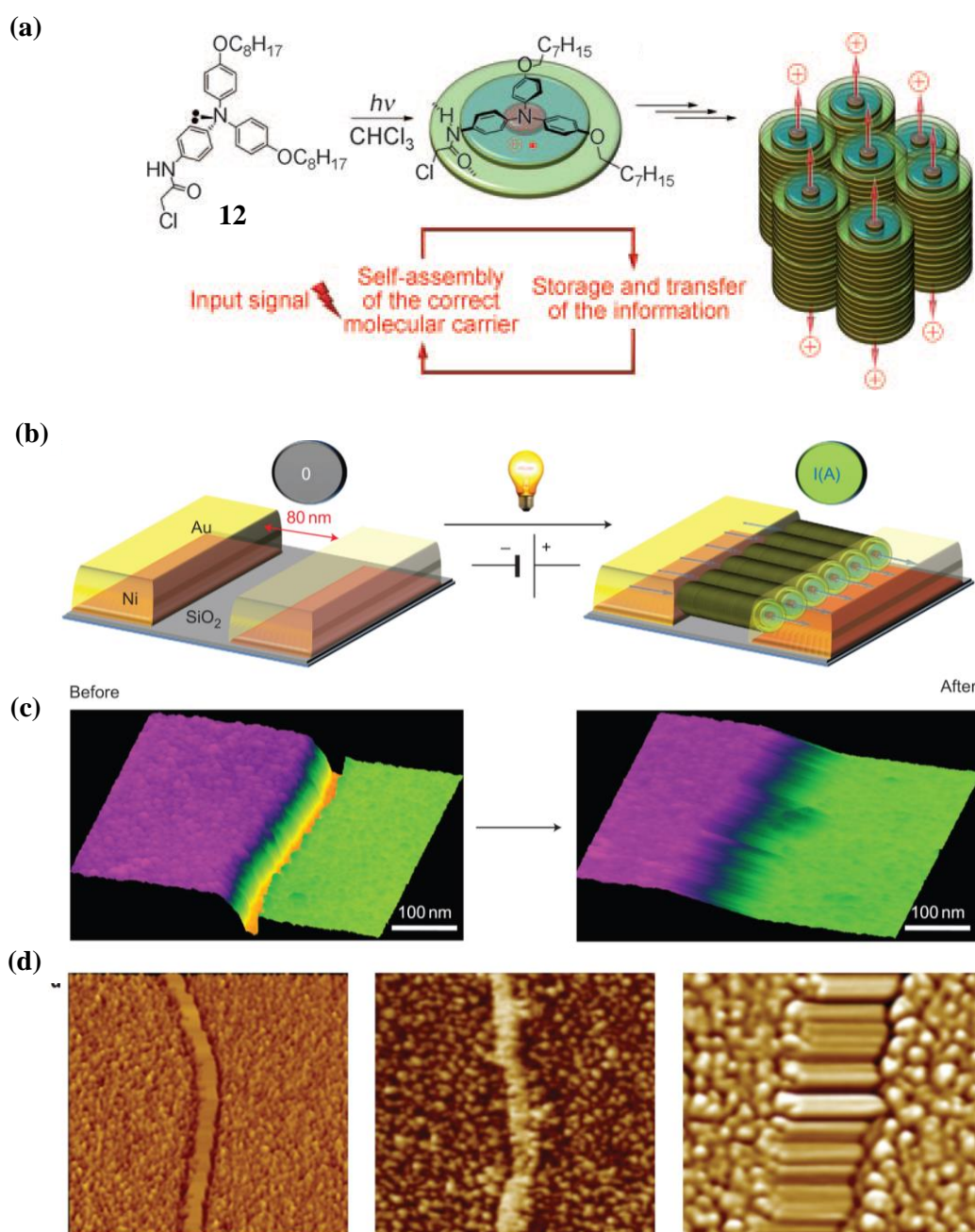


Figure 1.7. (a) Schematic representation of the light induced self-assembly of **12**, (b) Schematic representation of alignment of **12** across gold electrodes upon application of light and potential, (c) AFM image of the electrode gap before (left) and after (right) of light irradiation, (d) AFM phase images of electrode gap before [1500 X 1500 nm²](left), after [1500 X 1500 nm²](middle) and after [250 X 250 nm²](right) irradiation. (Fig. 1.7a reproduced with permission from Ref. 45, Fig. 1.7b-d reproduced with permission from Ref. 47).

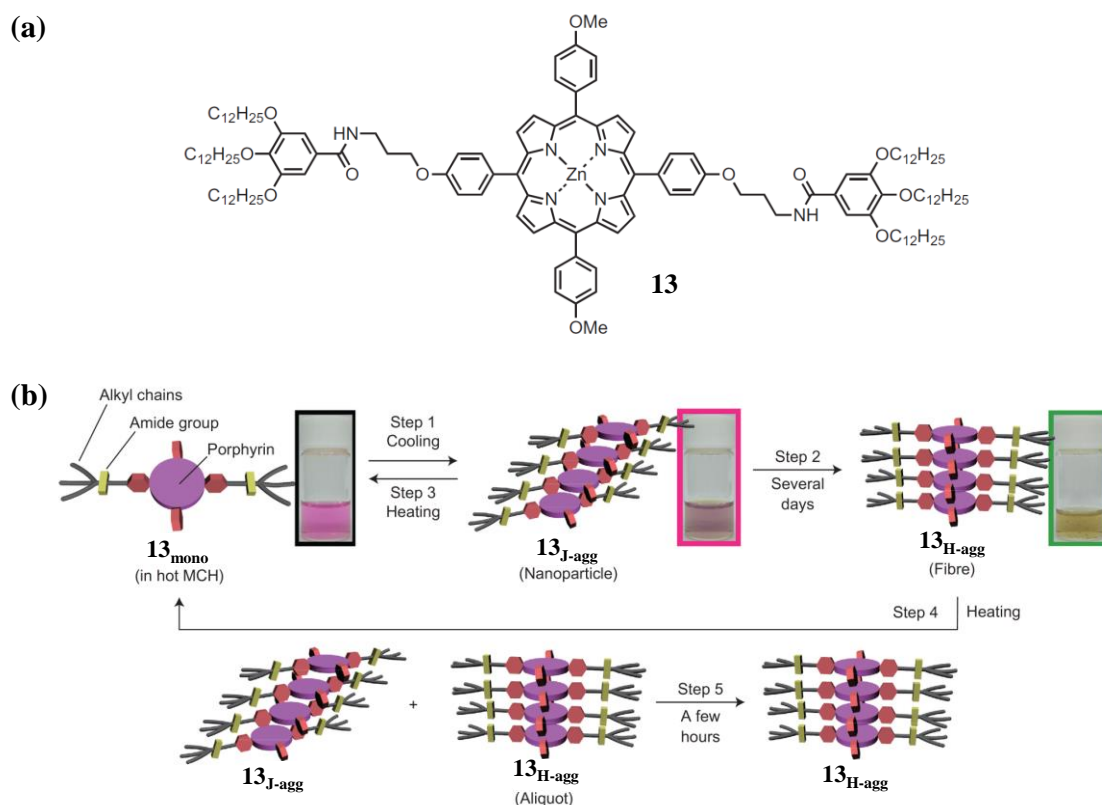


Figure 1.8. (a) Molecular structure of zinc porphyrin diamide moieties (**13**) and (b) Schematic representation showing the seeding behavior of **13** (Reproduced with permission from Ref. 48).

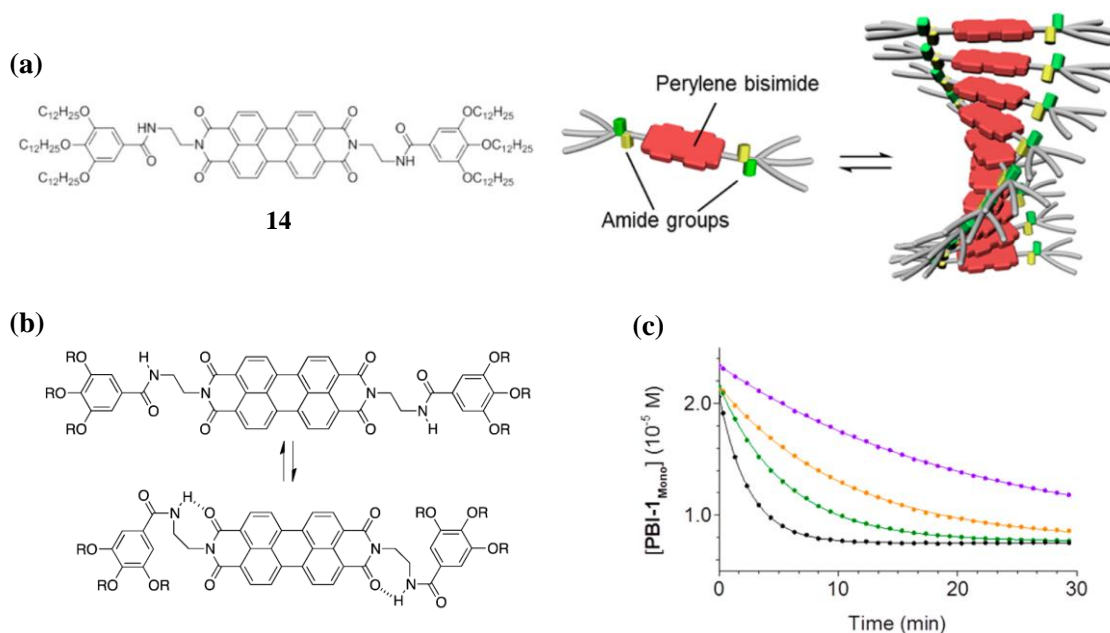


Figure 1.9. (a) and (b) Molecular structure of perylene bisimide moiety (**14**) and H-bonded closed and open structure, respectively. (c) Graph showing the increasing rate of growth with increased concentrations of seed (purple to black) (Reproduced with permission from Ref. 49).

Recently Takeuchi and Würthner *et al.* have shown the existence of living supramolecular polymerization in porphyrin and perylene bisimide based dyes, respectively. Takeuchi *et al.* show with the use of zinc porphyrin diamide moieties (**13**) that these molecules initially form J-type aggregates and manifest themselves as nano-particles.⁴⁸ However after few days of aging these can be converted to H-type aggregates which are long nano-fibers. The H-type aggregate can be converted to free solution by providing a critical amount of heat. Interestingly, the free monomers can be directly converted to nano fibrous H-aggregates if an aliquot of H-aggregated seed are introduced into the solution (Figure 1.8). The kinetic interplay between J and H-type of aggregated polymorphs gives this system the required temporal delay in nucleation. Würthner *et al.* on the other hand show that instead of a supramolecular conformation, a molecular conformation can be used as a buffer between active and inactive supramolecular species.^{49,50} Würthner *et al.* have shown in perylene bisimide moieties (**14**) that active and inactive conformation can be switched with respect to the absence and presence of intra-molecular H-bonds respectively. In this particular case the intra-molecular H-bonded state has a conformation that cannot assemble further. However as these H-bonds break the molecule switches its conformation to active and can now assemble via inter-molecular interactions. The process of growth can be accelerated depending on the seed concentration of the active conformation aggregates (Figure 1.9).

In a seminal paper by Aida *et al.* a general strategy for such chain growth supramolecular polymerization has been exemplified. They have employed a corannulene core with five amide appended thioalkyl side chains (**15-20**). These corannulene derivatives are chiral because of their C₅-symmetric nonplanar bowl shape.⁵¹⁻⁵³ A thermal racemization process is possible due to bowl-to-bowl inversion even at room temperature. These molecules adopt a closed bowl shaped conformation in non-polar solvents as the amides orient themselves to allow intra-molecular H-bonding interaction.⁵⁴ In an intelligent strategy they also synthesized the methylated derivative of the penta amide precursor which would then be incapable of forming the closed conformation. Finally in an experiment the methylated specie, when added to the pristine precursor solution acts

as an initiator to open up the closed H-bonded conformation and thus results in elongated aggregates. The growth further shows stereo selective seeding effects in turn confirming the living nature of the moieties (Figure 1.10).

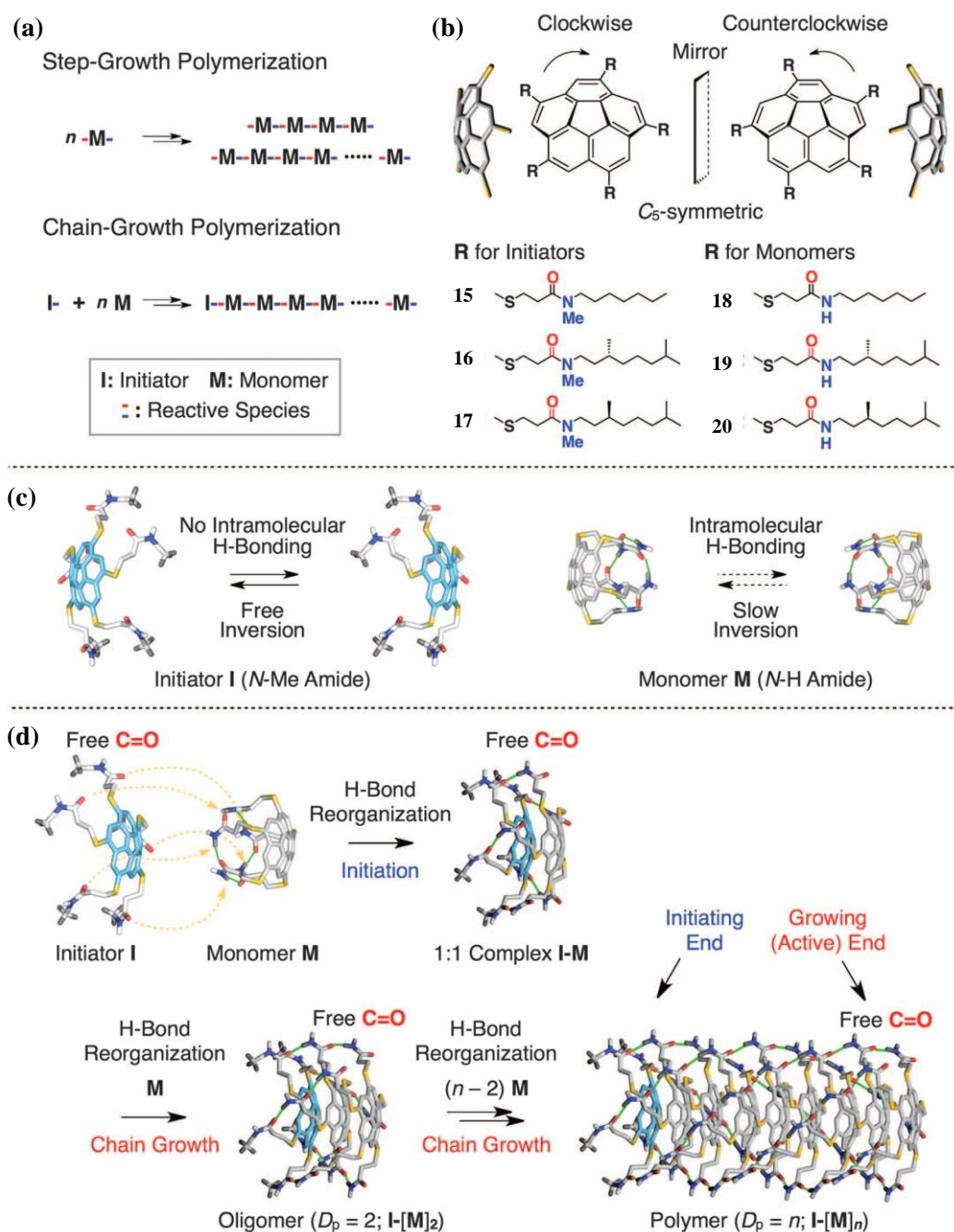


Figure 1.10. (a) and (b) Schematic for step growth and chain growth polymerization and molecular structures of corannulene moieties (15-20) respectively. (c) and (d) Schematic for thermal racemization and H-bonded closed states and schematic for supramolecular living growth of 18-20 initiated by 15-17 respectively. (Reproduced with permission from Ref. 54).

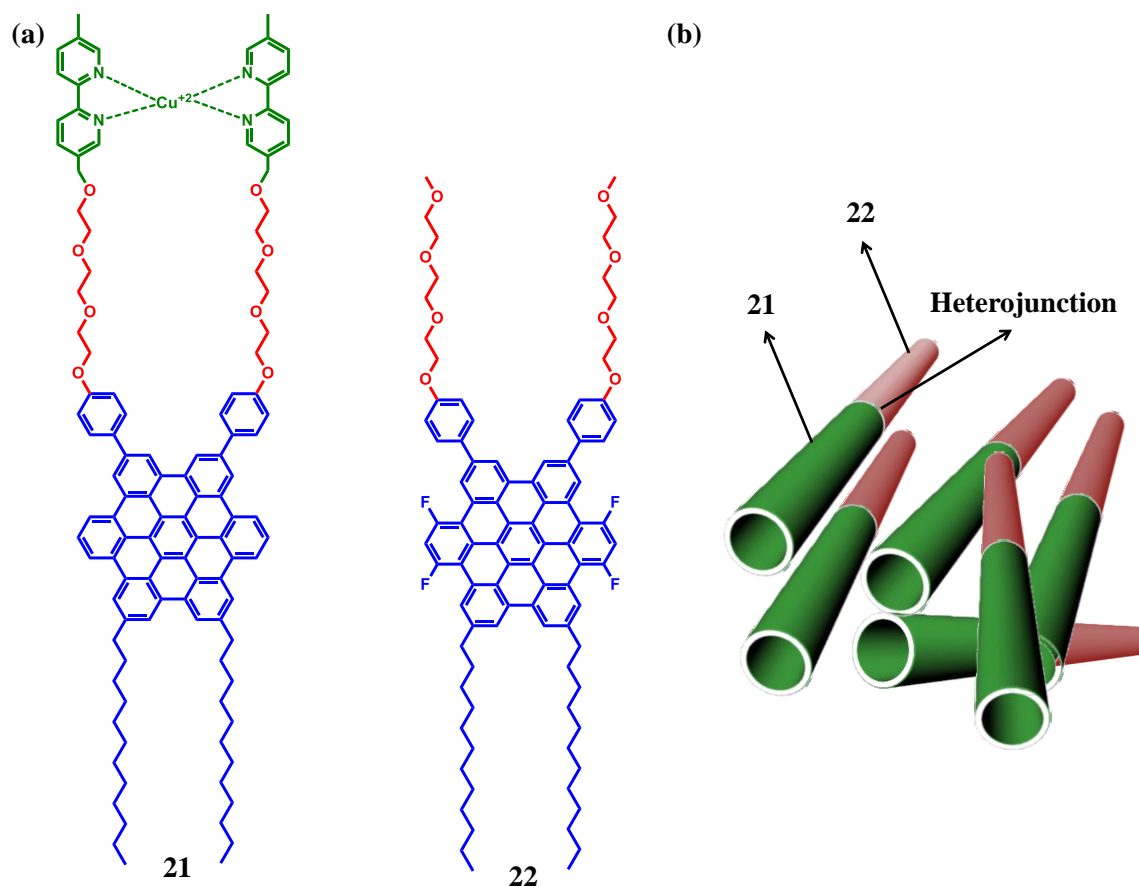


Figure 1.11. (a) Molecular structure of HBC derivatives used for supramolecular p-n junction and (b) Schematic representation of supramolecular hetero junction

Unrelated to the current strategy, from another set of molecules Aida *et al.* achieved supramolecular p-n junction as a supramolecular block co-polymer.⁵⁵ The formation of a supramolecular p-n junction has been a challenge because of multitude of challenges. Firstly, controlling the dynamics so as to hold nanometer domains of p-type and n-type together by a non-covalent force next to each other requires exceptional control of dynamicity. Secondly, Molecular design has to be such that narcissistic self-sorting of one of the electro-active component occurs but nucleates on the counterpart and not independently. These represent formidable challenges to overcome and Aida *et al.* take advantage of the amphiphilicity for crossing the hurdles. Their molecular design involves using an amphiphilic p-type HBC appended with 2,2' bipyridine moieties on the hydrophilic end (**21**). The bipyridines have two important functions. First, as the nanotubes form they spontaneously bundle together which can be detrimental to the final aim as it

would not result in single fibers with p-n junctions due to ineffective “seed” action. Thus, copper triflate is added at this point which binds to the bipyridine causing nanotubes to disperse into single nanotube due to the charge repulsion. Now, these single tubular nuclei are primed for further growth of an n-type molecule on them. Hence, it elucidates the second more important function of the copper bipyridine complex that is to keep the donor nucleus intact from further solution dynamics. n-type molecule that needs to be chosen has to be structurally very similar so as to not trigger homo-nucleation. Keeping the above in mind molecule chosen is the tetra fluoro derivative which is in size and shape comparable but has an inverse electronic nature (22). Thus, as all the prerequisites are intelligently met when the p-type nuclei are mixed with monomers of n type they grow together to yield a supramolecular p-n junction (Figure 1.11). Their existence can be visualized by TEM-EDX mapping and FP-TRMC measurement further confirm their presence as elucidated by long living charge carriers ($\tau_{1/e}(\text{Block}) = 3 \text{ to } 6 \text{ times } \tau_{1/e}(\text{individual components})$). The same strategy was later used to achieve homo-chiral supramolecular block copolymers.⁵⁶

All the strategies and the molecules discussed above though do not have a common chemical strategy; however a general theme is to be noted. As discussed in the previous section a successful seeded polymerization emanates from slower nuclei formation and faster growth. All the above examples have used varied chemical strategies to buffer the concentration of active self-assembling to inactive self-assembling molecules. This equilibrium between these two species makes sure that nucleation rate is slower than aggregate elongation. Considering the application of living supramolecular aggregates there is therefore an urgent need to discover general strategies for creation of this equilibrated buffer between inactive and active species. Infact, if one considers the biological realm such a strategy already exists which is chemical reaction mediated activation of self-assembling monomers. To further understand this concept one must delve into biological self-assembly of proteins.

1.5. Self-assembly of Biological Systems

Seeded or living supramolecular polymerization is a ubiquitous trait in various filamentous structures found in the cellular realm. We shall discuss a few examples in this discussion.

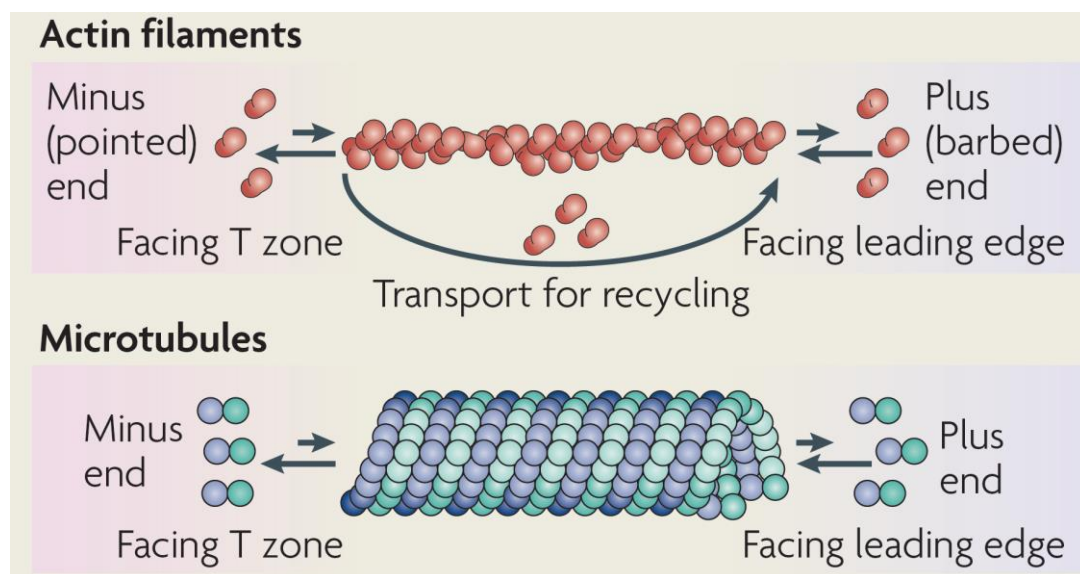


Figure 1.12. Schematic representation of dynamic instability in actin filaments and microtubules (Reproduced with permission from Ref.58).

One of the microfilaments whose seeding characteristics have been extensively studied is actin (Figure 1.12).^{57,58} Actin is a globular protein which is found in eukaryotic cells. It exists in two basic forms G-actin (globular) and F-actin (filamentous). G-actin exists as free monomer and F-actin forms a linear polymer microfilament. These two forms are important in cellular functions such as mobility and cell division. ATP is used as a chemical motif that binds to G-actin and turns those into activated monomers which further assemble to give oligomers and then to subsequent nuclei. These activated monomers then assemble catalytically over the nuclei. There have been *in vitro* experiments also suggesting that G to F conversion in actin is further catalysed when pre-existing nuclei of F-form are added to the solution, suggesting an auto-catalytic seeded growth.⁵⁹ In this case we see how a chemical reaction (with ATP) buffers the concentration between inactive G-forms and active F-forms. This binding kinetics gives the additional time delay in formation of nuclei as opposed to fast growth that follows after. This however is just one half of

the actin assembly. F-actin is formed when bound to ATP, but also acts as an ATPase thus also slowly hydrolysing it. This hydrolysis results in depolymerisation of the fibers and hence results in dynamic instability. This dynamic instability though has immense biological relevance, but can also be a viable route to attain transient self-assembling materials which dis-assemble in a pre-programmed manner.⁶⁰ These materials are obviously advantageous in areas where the material needs to be discarded after the function such as a drug carrying matrix.

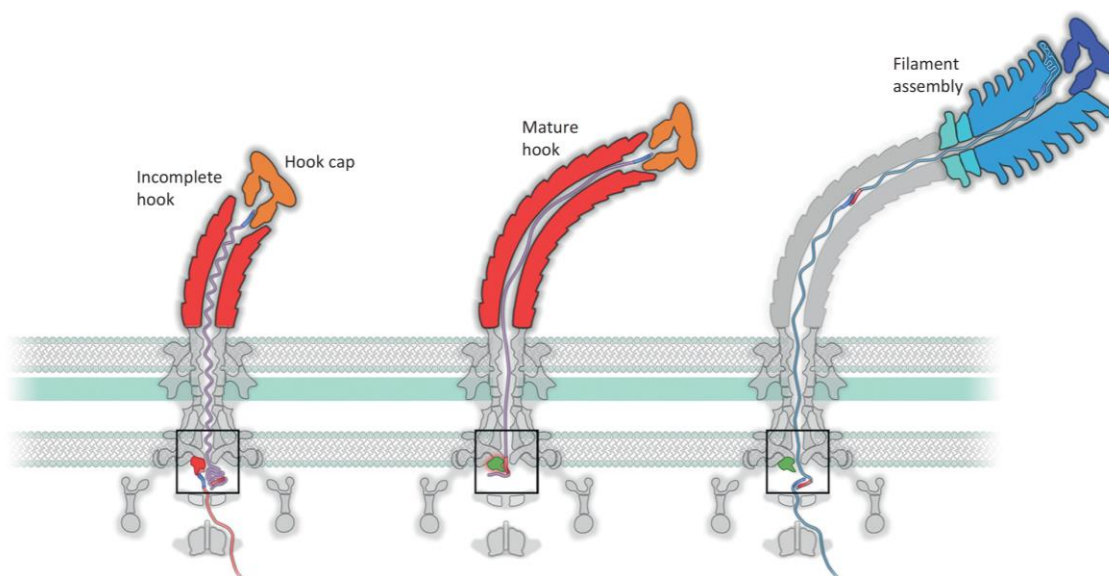


Figure 1.13. Schematic representation of flagellin showing growth from the tip (Reproduced with permission from Ref.62).

Another example of seeded living supramolecular polymerization is flagellin (Figure 1.13).^{61,62} Flagellin is a globular protein that is a prime component in filaments of bacterial flagellum which give bacteria their mobility.⁶³ These flagellin molecules have been assembled in vitro and shown that their assembly elongates much faster in presence of pre formed flagellum nuclei.⁶⁴ Inside a cellular environment as well, these structures show a remarkable tendency of growing from the ends when they are broken.^{65,66} Addition on the nuclei end is obviously thermodynamically favoured, but the intermediate concentration of flagellin monomers is maintained by a series of genetic switches or in other words, chemical stimuli. These stimuli keep a tab on the flagellin concentration such that free monomer adds only at the active end.^{67,68}

In both of the above examples we saw that nature follows a chemical reaction mediated nucleation-propagation assembly. This strategy, apart from providing the necessary kinetic delay, provides an excellent strategy for temporal modulation of self-assembly as chemical reaction in turn can be subjected to external stimuli which can affect their rates and hence in directly affect the self-assembly process. This crucial step in evolution works out then to act as a cellular sensor for external environments as external environments can perturb these reactions which affect the assembly process and finally alter the cellular function.

1.6. Chemical-Fuel Driven Self-Assembly

There are various examples known self-assembly processes governed by templates and bond formation,⁶⁹⁻⁷² however the reports of a self-assembling system showing the characteristics of biological self-assembly as shown above are extremely rare.

Van Esch *et al.* have used dibenzoyl-(1)-cystine moiety (**23**) for demonstration of their chemical fuel driven transient assembly.⁷³ These molecules are water soluble carboxylates in nascent form, however as soon as methyl iodide (Fuel) is added to the system the carboxylates start to get methylated and are finally converted to esters. These esters being insoluble in the aqueous media start to aggregate. However the ester formation is a reversible reaction in aqueous conditions and as the feed of methyl iodide is exhausted the reverse reaction starts to take effect and hence result in final hydrolysis (Figure 1.14). The whole temporal map starts with free monomers and moves to aggregate formation with finally shedding methanol as a bi-product to give the free monomers back again. The complete cycle resembles the transient formation of aggregates in biological systems and thus is therefore ground breaking in synthetic systems.⁷⁴ In an another extension of this work with other carboxylate derivatives (**23-25**) Van Esch *et al.* showed that similar transient assemblies can be achieved with Dimethyl sulphate as the methylation agent.⁷⁵ For this particular system the pH of the solution was kept to be 11 (Figure 1.15). This pH was necessary to hydrolyse the esters that are formed due to the consequent

methylation. Interestingly in this work the authors also show that the growth and decay of the aggregates occur at the opposite end.

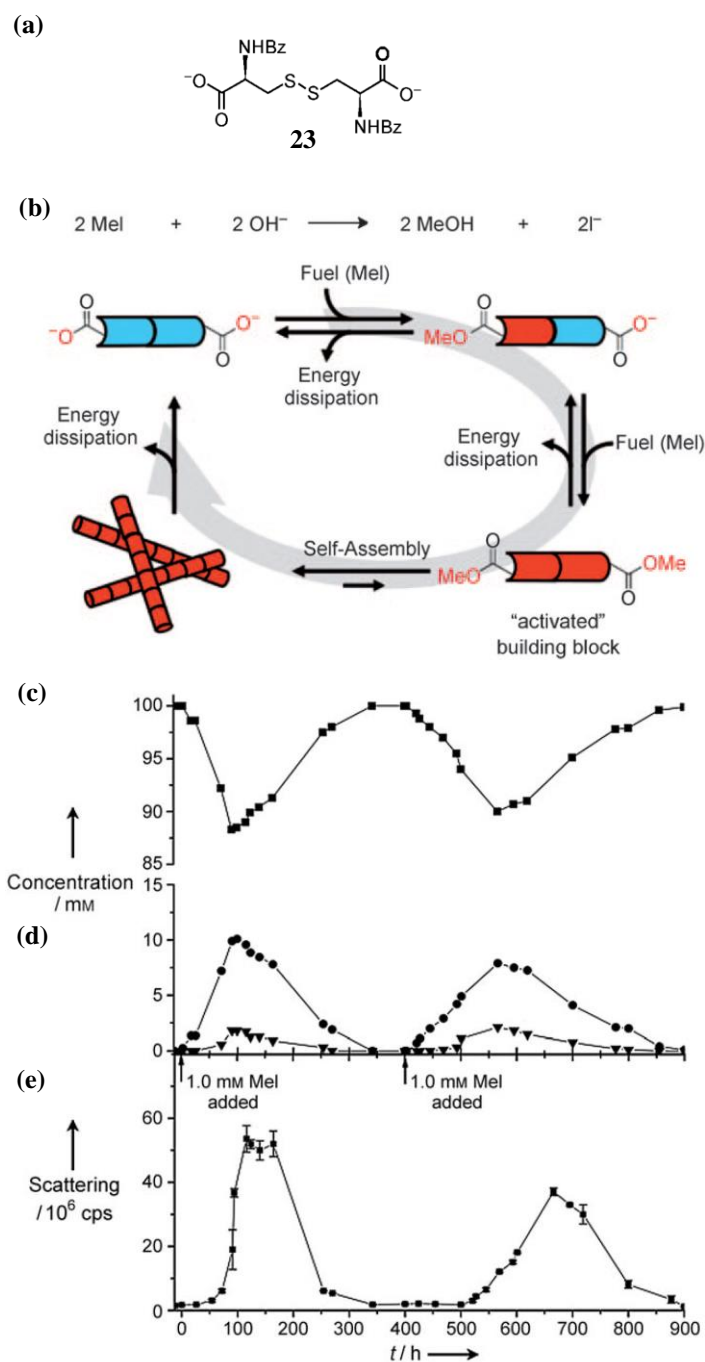


Figure 1.14. (a) and (b) Molecular structure of dibenzoyl-L-cystine (**23**) derivative and graphical representation of the MeI driven transient assembly respectively. (c)-(d) Concentration profiles of **23**(square), **23-OMe** (Circle), **23-OMe₂** (Triangle) respectively. (e) Transient assembly followed with Dynamic light scattering (DLS). (Reproduced with permission from Ref.73).

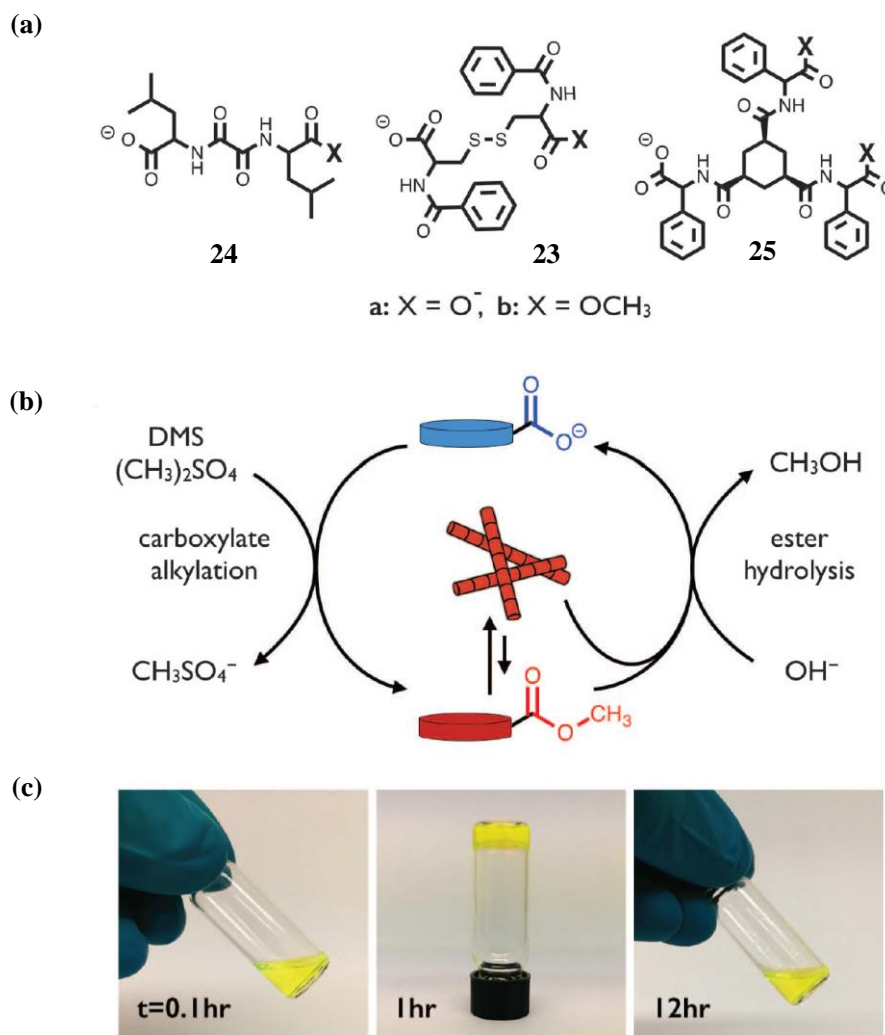


Figure 1.15. (a) and (b) Molecular structure of various dicarboxylate (23-25) derivatives and graphical representation of the DMS driven transient assembly respectively. (c) Photograph showing the sol (0.1 hr) to gel (1hr) to sol (12 hr) behaviour, establishing the transient assembly (Reproduced with permission from Ref.75).

After frame by frame analysis of the sample's microscopy they deduced that various fibers are growing and decaying at the same time bringing the whole system a step closer to biological systems.

Though these systems show a fuel driven assembly they do not show any evidence for a seeded or a living assembly.

1.7. Conclusion and Outlook

We in this Chapter presented a discussion based on recent scientific reports that living supramolecular assemblies and transient materials form the future of supramolecular systems in order to make controlled aggregates. We also took a close look at the strategies that have been adopted for attaining them and apart from a few exceptions a common theme emerges towards buffering of active to inactive concentration via a slow equilibrium. In every system however a different chemical strategy has been used to achieve this goal. More over there have been no attempts or modification of these systems which can modulate the rate of nucleation and hence the growth. Also these approaches give no insights into making materials that not only have controlled growth but also have programmable decay (dynamic instability).

We also looked at some of the examples form nature that show dynamic instability as well as seeded polymerization and they seemed to be governed by chemical reaction equilibrium. Furthermore we discussed some of the synthetic attempts made towards making chemical reaction dependent self-assembly. Though these systems are transient we do not have a system that shows living or a seeded nature.

The problem in hand is therefore cut out for us. On one hand, there are living supramolecular systems known but work with different strategies to slow the nuclei formation and on another is a chemical reaction driven system that is transient but not living. In the biological realm however these situation co-exist and are driven by a chemical reaction. The work of this thesis intends to shed light on this very chasm between these two properties and to see if we can achieve them via a common approach. We also wish to go ahead and show the true flexibility of a fuel driven system and that is to change the rates of polymerisation and depolymerisations depending on external stimuli that affect the chemical reaction and in turn affect the self-assembly characteristic.

1.8. References and Notes

1. Brunsveld L.; Folmer B. J. B.; Meijer E. W.; Sijbesma R. P. *Chem. Rev.* 2001, **101**, 4071.
2. Hoeben F. J. M.; Jonkheijm P.; Meijer E. W.; Schenning A. P. H. J. *Chem. Rev.* 2005, **105**, 1491.
3. Schenning A. P. H. J.; Meijer E. W. *Chem. Commun.* 2005, 3245.
4. Schenning A. P. H. J.; Jonkheijm P.; Hoeben F. J. M.; van Herrikhuyzen J.; Meskers S. C. J.; Meijer E. W.; Herz L. M.; Daniel C.; Silva C.; Phillips R. T.; Friend R. H.; Beljonne D.; Miura A.; Feyter S. De; Zdanowska M.; Uji-I H.; De Schryver F. C.; Chen Z.; Würthner F.; Mastorrent M.; den Boer D.; Durkut M.; Hadley P. *Synt. Met.* 2004, **147**, 43.
5. Aida T.; Meijer E. W.; Stupp S. I. *Science* 2012, **335**, 813.
6. Service R. F. *Science* 2005, **309**, 95.
7. Praveen V. K.; Ranjith C.; Bandini E.; Ajayaghosh A.; Armaroli N. *Chem. Soc. Rev.* 2014, **43**, 4222.
8. Rodriguez D. G.; Schenning A. P. H. J. *Chem. Mater.* 2011, **23**, 310.
9. Babu S. S.; Praveen V. K.; Ajayaghosh A. *Chem. Rev.* 2014, **114**, 1973.
10. Lehn J.-M. *Proc. Natl. Acad. Sci. U.S.A.* 2002, **99**, 4763.
11. Lutz J.-F.; Lehn J.-M.; Meijer E. W.; Matyjaszewski K. *Nature Review Materials* 2016, doi:10.1038/natrevmats.2016.24.
12. Roduner E.; Radhakrishnan S. G. *Chem. Soc. Rev.* 2016, doi: 10.1039/c6cs00115g.
13. van der Zwaag D.; de Greef T. F. A.; Meijer E. W. *Angew. Chem. Int. Ed.* 2015, **54**, 8334.
14. Epstein I. R.; Xu B. *Nat. Nano.* 2016, **11**, 312.
15. Clixby G.; Twyman L. *Org. Biomol. Chem.* 2016, doi: 10.1039/C6OB00280C.
16. Mann S. *Nat. Mater.* 2009, **8**, 781.
17. Pross A. *J. theor. Biol.* 2003, **220**, 393.
18. de Greef T. F. A.; Smulders M. M. J.; Wolffs M.; Schenning A. P. H. J.; Sijbesma R. P.; Meijer E. W. *Chem. Rev.* 2009, **109**, 5687.
19. Zhao D.; Moore J. S. *Org. Biomol. Chem.* 2003, **1**, 3471.

20. Kulkarni C.; Bejagam K. K.; Senanayak S.; Narayan K. S.; Balasubramanian S.; George S. J. *J. Am. Chem. Soc.* 2015, **137**, 3924.
21. Kastler, M.; Pisula, W.; Wasserfallen, D.; Pakula, T.; Mullen, K. *J. Am. Chem. Soc.* 2005, **127**, 4286.
22. Markvoort A. J.; ten Eikelder H. M. M.; Hilbers P. A. J.; de Greef T. F. A. *ACS Cent. Sci.* 2016, **2**, 232.
23. Smulders, M. M. J.; Schenning, A. P. H. J.; Meijer, E. W. *J. Am. Chem. Soc.* 2008, **130**, 606.
24. Kulkarni C.; Balasubramanian S.; George S. J. *ChemPhysChem* 2013, **14**, 661.
25. Morris A. M.; Watzky M. A.; Finke R. G. *Biochimica et Biophysica Acta* 2009, **1794**, 375.
26. Huck J.; Philp D. *Supramolecular Chemistry: From Molecules to Nanomaterials*, 2012, doi: 10.1002/9780470661345.smc158.
27. Lodish H.; Berk A.; Kaiser C. A.; Krieger M.; Scott M. P.; Bretscher A.; Ploegh H.; Matsudaira P.; *Molecular Cell Biology* 2007, 780-851, 6th Ed., W. H. Freeman publishers.
28. Scheibel T.; Parthasarathy R.; Sawicki G.; Lin X-M.; Jaeger H.; Lindquist S. L. *Proc. Natl. Acad. Sci. U.S.A.* 2003, **100**, 4527.
29. Mukhopadhyay R. D.; Ajayaghosh A. *Science* 2015, **349**, 241.
30. Schmelz J.; Schacher F. H.; Schmalz H. *Soft Matter* 2013, **9**, 2101.
31. Wang X.; Guerin G.; Wang H.; Wang Y.; Manners I.; Winnik M. A. *Science* 2007, **317**, 644.
32. Gädt T.; Jeong N. S.; Cambridge G.; Winnik M. A.; Manners I. *Nat. Mat.* 2009, **8**, 144.
33. Rider, D. A.; Manners, I. *Polymer Reviews* 2007, **47**, 165.
34. Soto A. P.; Gilroy J. B.; Winnik M. A.; Manners I. *Angew. Chem. Int. Ed.* 2010, **49**, 8220.
35. Gilroy J. B.; Gadt T.; Whittell G. R.; Chabanne L.; Mitchels J. M.; Richardson R. M.; Winnik M. A.; Manners I. *Nat. Chem.* 2010, **2**, 566.
36. McGrath, N.; Patil, A. J.; Watson, S. M. D.; Horrocks, B. R.; Faul, C. F. J.; Houlton, A.; Mann, S.; Manners, I. *Chem. Eur. J.* 2013, **19**, 13030.
37. Qiu H.; Cambridge G.; Winnik M. A.; Manners I. *J. Am. Chem. Soc.* 2013, **135**, 12180.
38. Jia L.; Zhao G.; Shi W.; Coombs N.; Gourevich I.; Walker G. C.; Guerin G.; Manners I.; Winnik M. A. *Nat. Commun.* 2014, **5**, 1.

39. Li X.; Gao Y.; Boott C. E.; Winnik M. A.; Manners I. *Nat. Commun.* 2015, **6**, 1.
40. Qiu H.; Du V. A.; Winnik M. A.; Manners I. *J. Am. Chem. Soc.* 2013, **135**, 17739.
41. Hudson Z. M.; Lunn D. J.; Winnik M. A.; Manners I. *Nat. Commun.* 2014, **5**, 1.
42. Rupar P. A.; Chabanne L.; Winnik M. A.; Manners I. *Science* 2012, **337**, 559.
43. Robinson M. E.; Lunn D. J.; Nazemi A.; Whittell G. R.; Cola L. D.; Manners I. *Chem. Commun.* 2015, **51**, 15921.
44. Aliprandi A.; Mauro M.; Cola L. D. *Nat. Chem.* 2016, **8**, 10.
45. Moulin E.; Niess F.; Maaloum M.; Buhler E.; Nyrkova I.; Giuseppone N. *Angew. Chem. Int. Ed.* 2010, **49**, 6974.
46. Nyrkova I.; Moulin E.; Armaoiv J. J.; Maaloum M.; Heinrich B.; Rawiso M.; Niess F.; Cid J. J.; Jouault N.; Buhler E.; Semenov A. N.; Giuseppone N. *ACS Nano*, 2014, **8**, 10111.
47. Faramarzi V.; Niess F.; Moulin E.; Maaloum M.; Dayen J.-F.; Beaufrand J.-B.; Zanettini S.; Doudin B.; Giuseppone N. *Nat. Chem.* 2012, **4**, 485.
48. Ogi S.; Sugiyasu K.; Manna S.; Samitsu S.; Takeuchi M. *Nat. Chem.* 2014, **6**, 188.
49. Ogi S.; Stepanenko V.; Sugiyasu K.; Takeuchi M.; Würthner F. *J. Am. Chem. Soc.* 2015, **137**, 3300.
50. Ogi S.; Stepanenko V.; Thein J.; Würthner F. *J. Am. Chem. Soc.* 2016, **138**, 670.
51. Kang J.; Miyajima D.; Itoh Y.; Mori T.; Tanaka H.; Yamauchi M.; Inoue Y.; Harada S.; Aida T. *J. Am. Chem. Soc.* 2014, **136**, 10640.
52. Deng R.; Liu X. *Nat. Chem.* 2015, **7**, 472.
53. Wu Y.-T.; Siegel J. S. *Chem. Rev.* 2006, **106**, 4843.
54. Kang J.; Miyajima D.; Mori T.; Inoue Y.; Itoh Y.; Aida T. *Science* 2015, **347**, 646.
55. Zhang W.; Jin W.; Fukushima T.; Saeki A.; Seki S.; Aida T. *Science* 2011, **334**, 340.
56. Zhang W.; Jin W.; Fukushima T.; Mori T.; Aida T. *J. Am. Chem. Soc.* 2015, **137**, 13792.
57. Shikinaka K.; Takaoka S.; Kakugo A.; Osada Y.; Gong J. P. *J. App. Pol. Sci.* 2009, **114**, 2087.
58. Lowery L. A.; Vactor D. V. *Nat. Rev. Molecular cell Biology* 2009, **10**, 332.
59. Kasai M.; Asakura S.; Oosawa F. *Biochim. Biophys. Acta.* 1962, **57**, 22.
60. Mitchison T.; Kirschner M. *Nature* 1984, **312**, 237.

61. Evans L. D. B.; Poulter S.; Terentjev E. M.; Hughes C.; Fraser G. M. *Nature*, 2013, **504**, 287.
62. Evans L. D. B.; Hughes C.; Fraser G. M. *Trends in Microbiology* 2014, **22**, 566.
63. Lam A. T.; Curschellas C.; Krovvidi D.; Hess H. *Soft Matter*, 2014, **10**, 8731.
64. Asakura S.; Eguchi G. *J. Mol. Biol.* 1964, **10**, 42.
65. Drechsel D. N.; Hyman A. A.; Cobb M. H.; Kirschner M. W. *Molecular Biology of the Cell* 1992, **3**, 1141.
66. Gadelha H.; Gaffney E. A.; Smith D. J.; Kirkman-Brown J. C. *J. R. Soc. Interface* 2010, **7**, 1689.
67. Homma M.; Fujita H.; Yamaguchi S.; Iino T. *J. Bacteriol.* 1984, **159**, 1056.
68. Auvray F.; Thomas J.; Fraser G. M.; Hughes C. *J. Mol. Biol.* 2001, **308**, 221.
69. Boekhoven J.; Poolman J. M.; Maity C.; Li F.; van der Mee L.; Minkenberg C. B.; Mendes E.; van Esch J. H.; Eelkema R. *Nat. Chem.* 2013, **5**, 433.
70. Wu X.; Chen X.-X.; Zhang M.; Li Z.; Gale P. A.; Jiang Y.-B. *Chem. Commun.* 2016, doi:10.1039/x0xx00000x.
71. Nguyen R.; Allouche L.; Buhler E.; Giuseppone N. *Angew. Chem. Int. Ed.* 2009, **48**, 1093.
72. Minkenberg C. B.; Homan B.; Boekhoven J.; Norder B.; Koper G. J. K.; Eelkema R.; van Esch J. H. *Langmuir* 2012, **28**, 13570.
73. Boekhoven J.; Brizard A. M.; Kowlgi K. N. K.; Koper G. J. K.; Eelkema R.; van Esch J. H. *Angew. Chem. Int. Ed.* 2010, **49**, 4825.
74. Koper G. J. K.; Boekhoven J.; Hendriksen W. E.; van Esch J. H.; Eelkema R.; Pagonabarraga I.; Rubí J. M.; Bedeaux D. *Int. J. Thermophys.* 2013, **34**, 1229.
75. Boekhoven J.; Hendriksen W. E.; Koper G. J. K.; Eelkema R.; van Esch J. H. *Science* 2015, **349**, 1075.

Chapter-2

Kinetically Controlled Living Supramolecular Polymerization

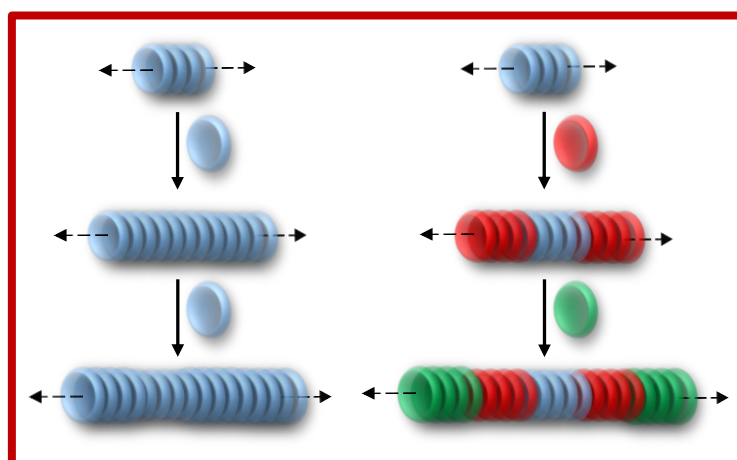
Chapter-2

Kinetically Controlled Living Supramolecular Polymerization

Abstract

Living supramolecular polymerization is one of the most exotic areas in supramolecular chemistry. It promises controlled synthesis of aggregates which would prove to be an important asset if one considers the applicability of such materials. Biological systems also undergo aggregation via a kinetically controlled living manner. However they do so by buffering the inactive and active aggregate state with a chemical reaction. This strategy allows further coupling of environmental stimuli with the reaction and hence tuning the temporal profile of aggregation and hence the related function. Among the strategies that have been employed in reported literature most of them use a buffering mechanism between active and inactive aggregation however that is dependent on conformation variability of the molecule and not governed by a chemical reaction.

In this work we explore the possibility of attaining a chemical reaction driven living supramolecular polymerization. We have used imine bond formation as the dynamic reaction and Charge transfer interaction as the guiding force behind a linear assembly. Later in the chapter we also explore the possibility of formation of supramolecular hetero structures.



2.1. Introduction

Importance and various strategies to achieve living supramolecular polymerization have been detailed in Chapter 1. In introducing this Chapter we would like to begin with the system characteristics in hand along with the rationale for choosing one.

To achieve a living supramolecular polymerization, as detailed in Chapter 1, we have devised a strategy so as to temporally control the growth of a stack via a reversible chemical reaction. There are however a plethora of reactions known that have been employed in dynamic combinatorial chemistry.¹ Out of these reactions we particularly choose imine formation as our reversible reaction to drive our aggregation. A simple reason behind this choice lies in the fact that this reaction has been used extensively for aggregating dynamic surfactants.

Dynamic surfactants is a term given to an amphiphile formed by two components, usually one is hydrophobic while the other is hydrophilic, joined by a dynamic bond. These surfactants find their application in stimuli responsive supramolecular structure generation. van Esch and Zhang *et al.* have independently advanced the knowledge in this area to a great extent.²⁻⁶ They have come up with hydrophobic and hydrophilic parts of different shapes so as to allow formation of amphiphiles of various structures. Most of these cases however end up being spherical micelles, which are advantageous for a surfactant application but are of no utility considering their use in formation of linear aggregates. Though using this strategy van Esch *et al.* show the formation of small cylindrical micelles (Figure 2.1),⁷ their definitive success in achieving long unidirectional growth is brought about by using directional aggregating enforcers such as the H-bond in this case.⁸

Another property that has been explored in these imine based dynamic amphiphiles is the tendency to generate auto catalytic growth (which is perhaps a requisite considering a linear living supramolecular system). This phenomenon was demonstrated by Giuseponne *et al.* albeit in spherical micellar system.⁹ In this study it was shown that these spherical micelles accommodate

the incoming free dynamers (segments capable of forming dynamic bonds) and increase in size, only to divide into shorter micelles on achieving a critical micellar size (Figure 2.2).

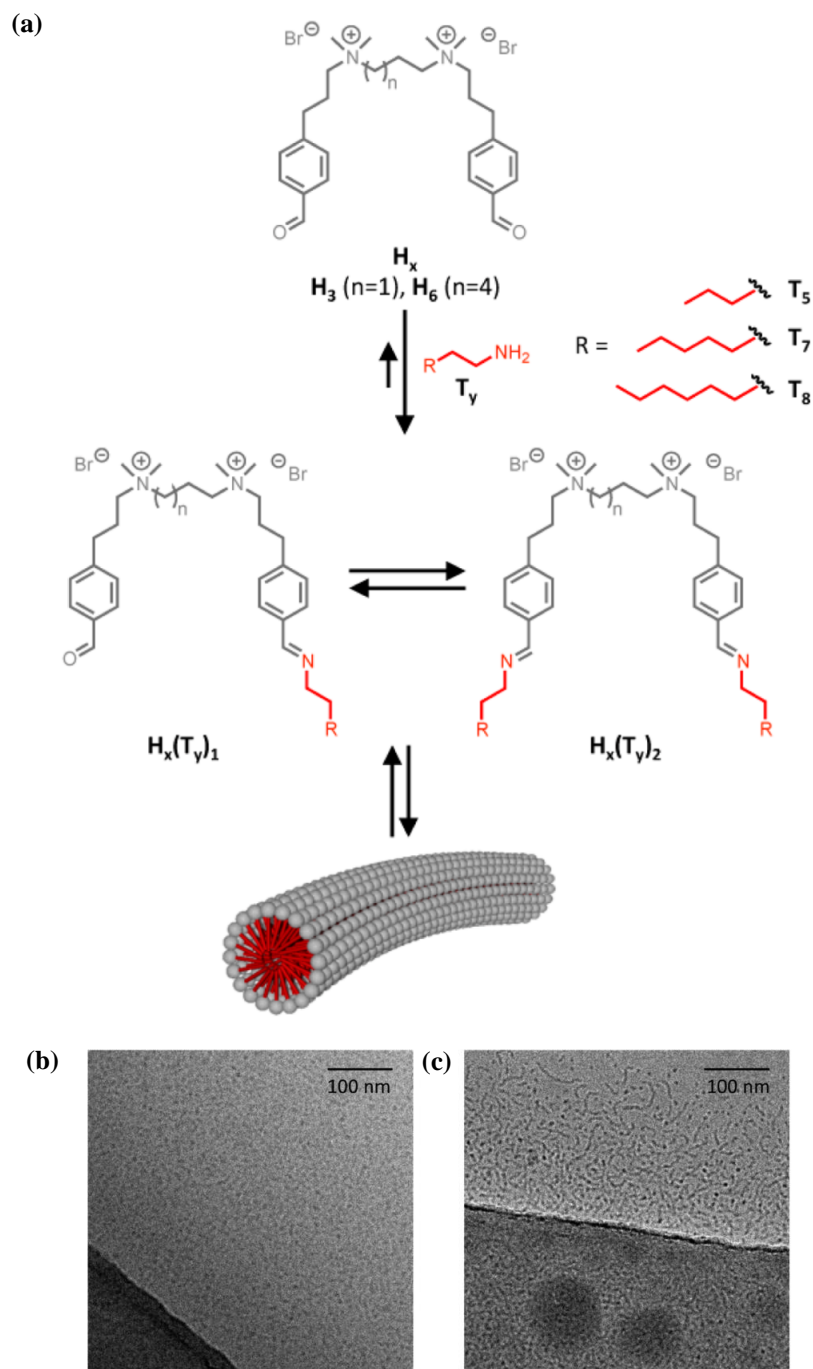


Figure 2.1. (a) Schematic representation of the molecular structure of dynamic surfactants formed with various alkyl chains. (b) and (c) cryo-TEM of the thus formed cylindrical micelles. (Reproduced with permission from Ref. 7).

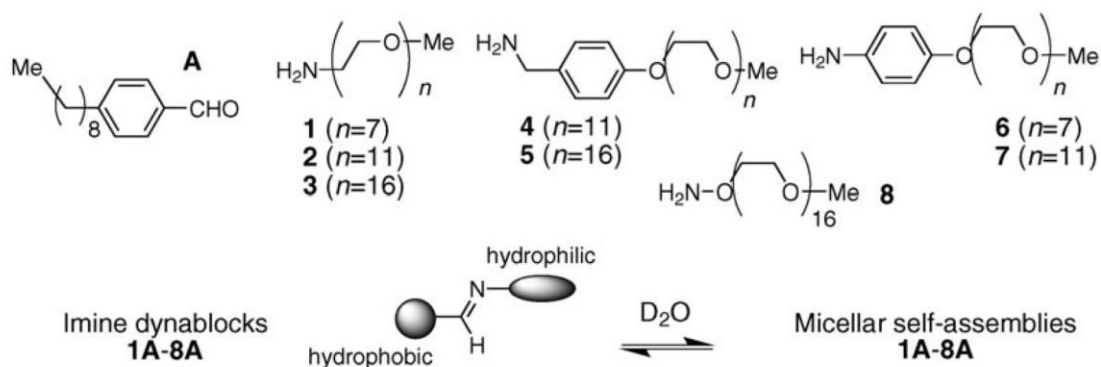


Figure 2.2. Schematic representation of the molecular structure of dynamers used in autocatalytic growth of spherical micelles. (Reproduced with permission from Ref. 9).

This action is auto catalytic as one micelle generates more micelles of the same kind. Though this autocatalysis is required for a living growth but the aspect of recruiting free molecules to the stack is the most important. This is because when the nuclei is introduced one would wish that the interface of the nucleus recruits free monomers to increase its length in order to satiate the interfacial energy. The aspect of dynamic imine aggregates have been exemplified by Lehn *et al.* in their recent work where the spacing between dynamic structures formed on liquid/graphite interface, as seen by STM (scanning tunnelling microscopy), can be altered by using a homologous series of di amines (Figure 2.3).¹⁰

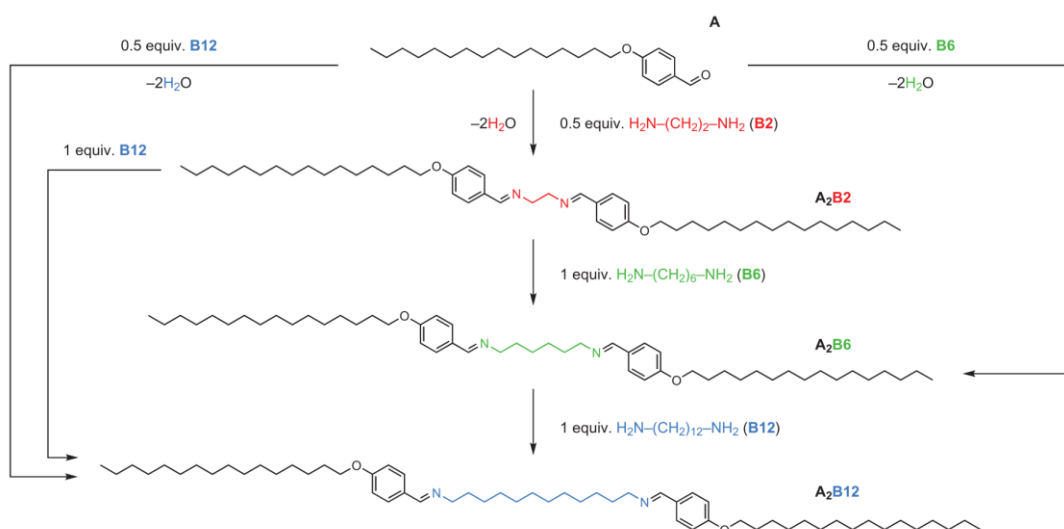


Figure 2.3. Schematic representation of the molecular structure showing dynamic bisimine exchange on liquid/graphite surface. (Reproduced with permission from Ref. 10).

Considering all the examples of imine based aggregates, to the best of our knowledge, living supramolecular polymerization of an imine based system has not been reported before. This premise drives our investigation further in search of such a phenomenon in living systems.

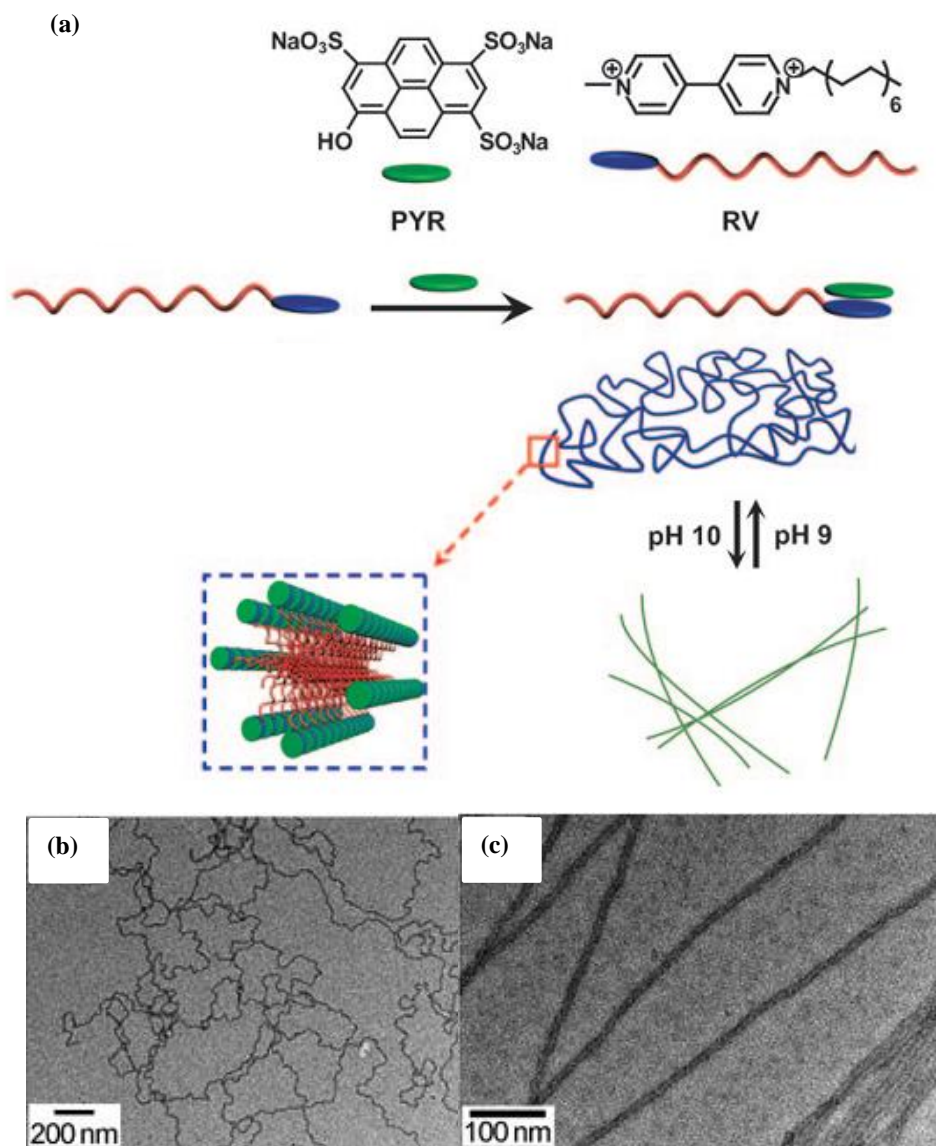


Figure 2.4. (a) Molecular structures of anionic donor (PYR) and cationic acceptor (RV) and schematic representation of the preparation of the pH-responsive nanofibers through self-assembly of PYR-RV supramolecular amphiphile. TEM images of the amphiphile in (b) pH 9 buffer and in (c) pH 10 buffer solution. (Reproduced with permission from Ref. 13).

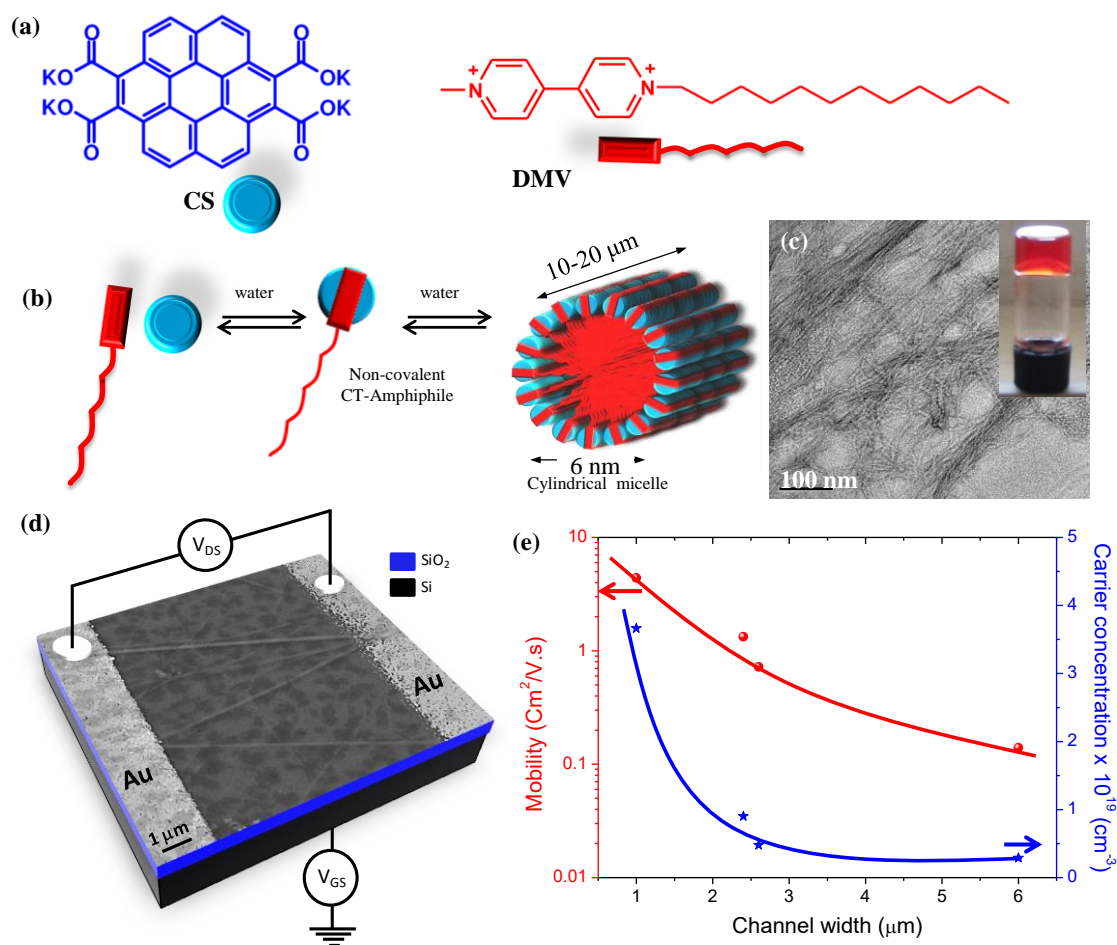


Figure 2.5. (a) Molecular structures of polycyclic aromatic donor (CS) and viologen acceptor (DMV). (b) Schematic representation of the non-covalent amphiphile and its self-assembly into high aspect ratio cylindrical micelles. (c) A SEM image of CT-nanofibers between gold electrodes adapted in the schematic of the FET. (d) Variation in the field effect mobility and the carrier concentration with the channel width. (Reproduced with permission from Ref. 17 and 20b).

As mentioned earlier linear aggregate systems based on imine bonds alone are rare and they require a directional self-assembling motif. In our case we wish to employ a charge transfer (CT) interaction as a directional motif. Zhang *et al.* first reported the supramolecular amphiphiles based on charge transfer (CT) systems (Figure 2.4).¹¹⁻¹⁵ In typical CT based supramolecular amphiphile system donor and acceptor molecules combine to yield species which has a polar head (the CT dimer) and a non-polar tail (hydrophobic chain connected to one of either donor or acceptor). This amphiphilic dimer can thus aggregate further. In a CT based system it is rather convenient to get a linear aggregate.

In our group we have investigated the possibility of novel supramolecular amphiphiles for exploiting their electronic prowess on a device structure.¹⁶⁻²⁰ One system that stands out of the many is the tetra potassium coronene salt (**CS**) and methyl viologen motif (**DMV**). **CS** and **DMV** on mixing spontaneously form linear supramolecular aggregates that can even gel at higher concentrations. **CS** and **MV** dimer forms the polar head which aggregates in a cylindrical micelle with alkyl chains in the interior (Figure 2.5). As mentioned earlier these aggregates at higher concentration form a gel with high aspect ratio fibers. These fibers are of great utility as they have an excellent performance on an electronic device and are stimuli response to the extent of detecting water content in exhaled breath.²¹

2.2. Results and Discussion

2.2.1. Living Supramolecular Polymerization

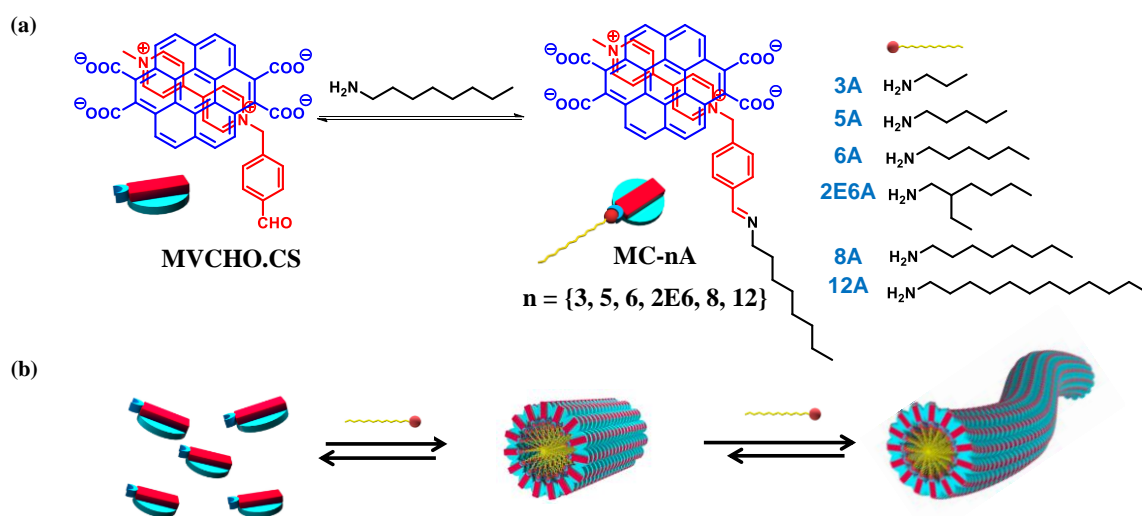


Figure 2.6. (a) Molecular structures of a complex between aromatic donor (**CS**) and benzaldehyde substituted viologen acceptor (**MVCHO**) along with various alkyl amines used in this study. (b) Schematic representation of the imine driven non-covalent amphiphile and its self-assembly into high aspect ratio cylindrical micelles.

Considering the combination of dynamic amphiphiles and a CT based supramolecular amphiphile we came up with the design of the molecules as shown in Figure 2.6. The basic CT pair is **MV**

and **CS** (blue), in which **MV** has been substituted with a benzaldehyde motif to give **MVCHO** (red). **CS** and **MVCHO** would form a CT pair that would only be capable of aggregating when a source of amine converts the CT pair to an amphiphile by an imine linkage. Various amines have been tried in this study and their utility would be pointed as and when necessary (Figure 2.6). We have tried only alkyl amines as we were interested in comparing the rate of reaction resulting due to aggregation alone and not the electronic effects.

We hypothesize that now, since the aggregation is governed by a slow chemical reaction, the resulting temporal control would be a two way street. By dual control we refer to the fact that the extent of aggregation would depend on the amount of amine present and on the other hand the equilibrium constant of the imine formation would be driven by the aggregating species (which refer to the fact that alkyl chains incapable of forming aggregates would consume less **MV-CHO** and *vice versa*). This interdependency is important as aggregation driven equilibrium changes could thus be exploited in hetero-nucleation (*vide infra*)

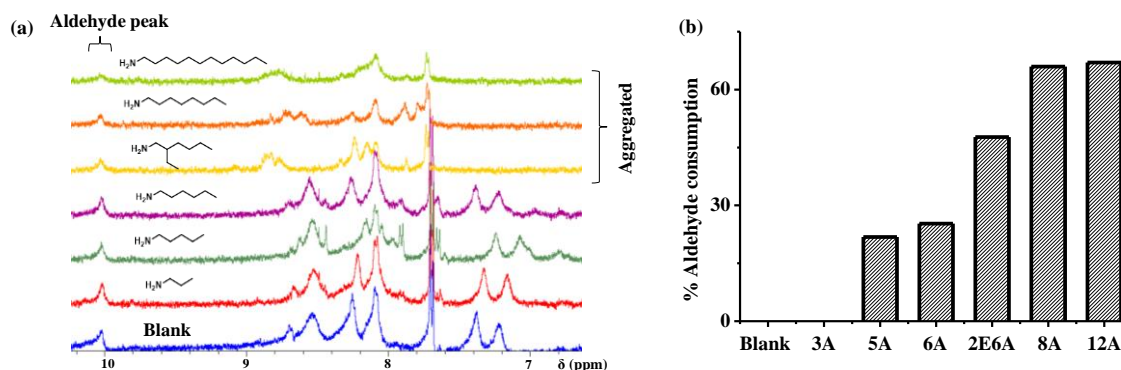


Figure 2.7. (a) ¹H-NMR of **MVCHO.CS** with various amines, (b) Graph showing the extent of aldehyde consumption with respect to each amine. ($[MVCHO] = [CS] = 1 \text{ mM}$, $[alkyl \text{ amine}] = 1 \text{ eq.}$, $\text{pH} = 11.0$, D_2O)

Before going ahead with the study we fixed the pH of the buffer to 11.0. This was due to combination of factors as pH 11.0 gave maximum imine formation and minimal side reactions in the time period of investigation.

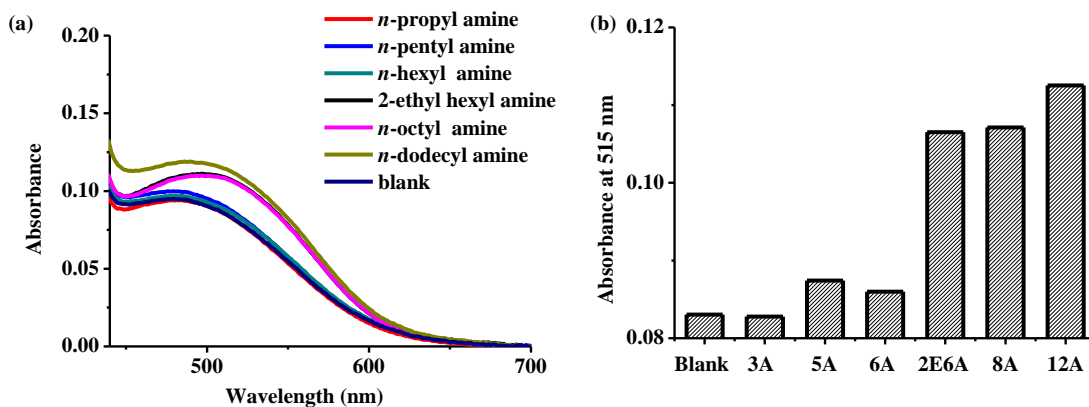


Figure 2.8. (a) UV-vis absorption spectra of **MVCHO-CS** with various amines and (b) Graph showing the extent of aggregation with respect to each amine. ($[MVCHO] = [CS] = 1 \text{ mM}$, $[alkyl \text{ amine}] = 1 \text{ eq.}$, $\text{pH} = 11.0$, H_2O)

To probe this interdependence of reactivity and growth, we performed sequential ^1H -NMR and UV-vis studies (Figures 2.7 and 2.8). In a typical NMR experiment the required amount on **MV-CHO** and **CS** were mixed and 1.0 eq. of alkyl amine was added to it. The resulting solution was incubated for 1 hour at 25°C . Blank solution in which no amine was added was also incubated under same conditions and duration before measurement. 1 mM of sodium acetate was added in each sample as an internal standard as acetate peaks come in an exclusive region (2.5 ppm). Considering the NMR spectra of each of these samples the consumption of aldehyde was measured against the internal standard. A brief look at even the blank sample shows merged, broad peaks and thus aldehyde consumption became necessary to be recorded by an internal standard as imine protons were indistinguishable from the merged peaks. Considering the NMR spectra the peaks more or less remained similar from blank to hexyl amine (**6A**). Beyond this the addition of 2-ethyl hexyl amine (**2E6A**), *n*-octyl amine (**8A**) and *n*-dodecyl amine (**12A**) showed marked changes in the pattern of spectra thus signifying aggregation. Moreover for each of these samples the extent of aldehyde consumption was tabulated versus the alkyl amine used. And as expected higher alkyl amine (**2E6A**, **8A**, **12A**) showed much higher aldehyde consumption than smaller alkyl amines (**3A**, **5A**, **6A**). This result hinted towards an aggregate driven equilibrium.

We also recorded UV-vis spectra of these samples. Aggregation features of the CT band in UV-vis spectroscopy warrants a mention. As has been reported earlier intensities of these CT bands depend heavily on the closeness of donor and acceptor molecules and are inversely proportional i.e. smaller the distance higher the CT band. Therefore a signature of aggregation in this system is the increased absorbance of the CT band. Considering this scenario the UV-vis spectra of each of the samples were recorded and their absorbance at 515 nm (to signify increase in absorbance) was tabulated against the alkyl amine used. The results obtained were in coherence with the $^1\text{H-NMR}$ data. Longer alkyl chains (**2E6A**, **8A**, **12A**) showed much higher tendency to aggregate than smaller alkyl amines (**3A**, **5A**, **6A**).

These two experiments unequivocally prove the existence of an aggregation driven equilibrium. Longer alkyl chains since are able to aggregate and push their equilibrium further. On the other hand smaller alkyl chains form imine only by their reactive capacity and are not driven to higher consumption due to lack of aggregation. This particular fact will be exploited later in the Chapter when we discuss hetero-nucleation (Section 2.2.2).

Moving ahead we wanted to analyse the temporal control that this system manifests and for doing the same we selected **8A** as the representative amine (case of **8A** is similar to other amines except **12A** which has been discussed later in this Chapter). Use of other amines has been duly mentioned separately in experiments. The kinetics of aggregation has been primarily analysed from UV-vis spectroscopy and has been monitored at 515 nm. This wavelength remains a default for all the systems unless otherwise noted.

8A stock solution was made in DMSO and was introduced by a pipette in an aqueous solution of pH = 11.0 containing **MVCHO** and **CS**. The dilution was maximum 0.1%. The kinetics of growth was then followed at 515 nm and an exponential trend was obtained (Figure 2.9a).

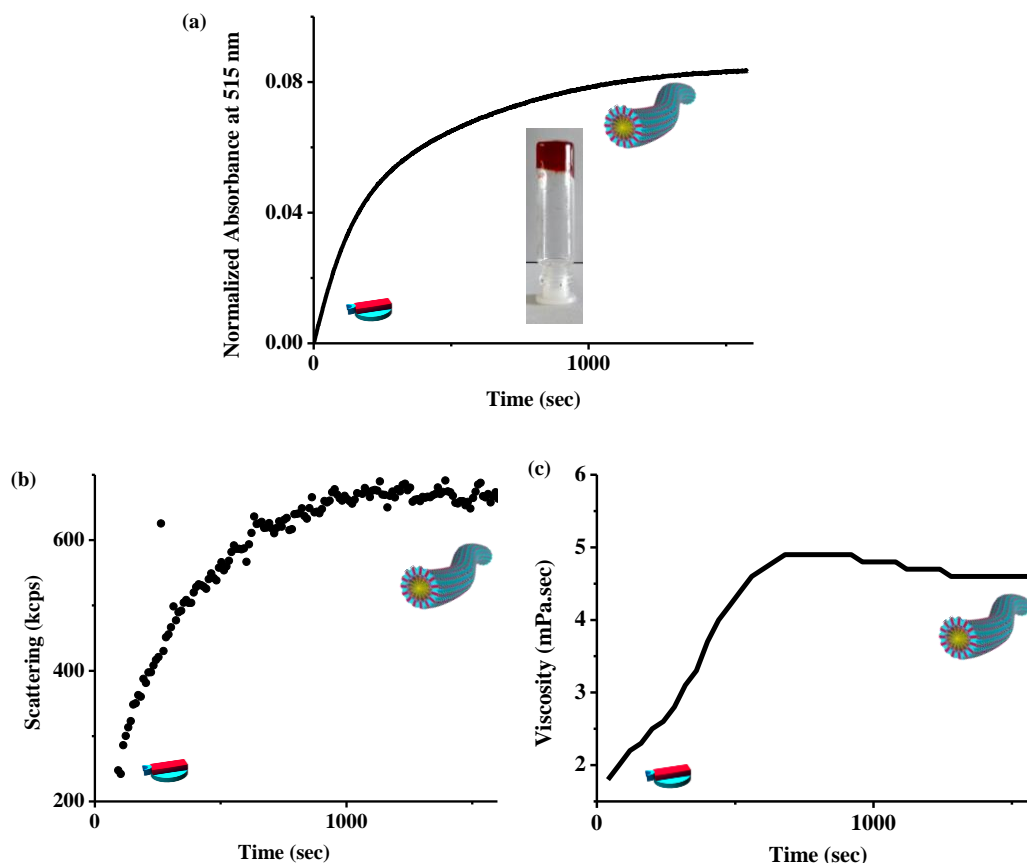


Figure 2.9. (a) UV-vis trend of *MVCHO.CS* with **8A** followed at 515 nm, (b) Scattering trend of *MVCHO.CS* with **8A** followed by DLS and (c) Viscosity trend of *MVCHO.CS* with **8A** ($[MVCHO] = [CS] = 1 \text{ mM}$, $[8A] = 1 \text{ eq.}$, $\text{pH} = 11.0$, H_2O).

At higher concentrations (10 mM) a gel was formed suggesting the existence of linear fibers. To confirm that this kinetics is due to aggregation we followed the same process through DLS (kcps measurement) and viscosity measurement over time (Figure 2.9 b,c). DLS measurement showed a gradual increase in scattering intensity after **8A** addition and in the viscosity measurement similar increase in viscosity over time was observed. These two measurements corroborate with the UV-vis trend, which was thus concluded to be representative of temporal aggregation.

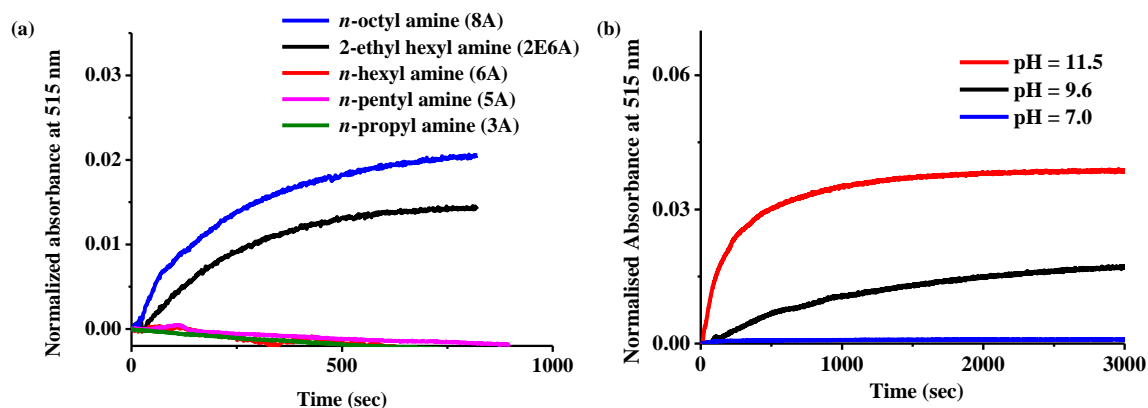


Figure 2.10. (a) UV-vis trend of *MVCHO.CS* with various amines followed at 515 nm, ($[MVCHO] = [CS] = 1 \text{ mM}$, $[\text{various amine}] = 0.33 \text{ eq.}$, $\text{pH} = 11.0$, H_2O) (b) UV-vis trend of *MVCHO.CS* with **8A** followed at 515 nm at different pHs ($[MVCHO] = [CS] = 1 \text{ mM}$, $[8A] = 1 \text{ eq.}$, H_2O).

To further cement the fact that aggregation is due to imine bond formation we recorded the UV-vis kinetics with various alkyl amines and as was suggested previously smaller alkyl chains showed no growth compared to **8A** and **2E6A**. Among **8A** and **2E6A** the former had a faster kinetics and more extent of aggregation suggestive of a stronger aggregation tendency (Figure 2.10a). Moreover since these imine bonds are pH sensitive (i.e. they form at basic pH and deform on decreasing pH to neutral) we studied the kinetics of growth with **8A** under variable pH (Figure 2.10b). The trend obtained showed faster and more extent of growth at a basic pH compared to lower pH. This coupled with the previous experiment suggested clearly that the kinetic trend is due to aggregation governed by imine bonds.

We thus moved ahead in our quest for a living supramolecular system and tested the kinetics of growth with varying equivalents of **8A** (Figure 2.11). This experiment is important as signatures of a sigmoidal growth should be visible here which would form the basis of further experiments. Figure 2.11a shows the trend of aggregation with various equivalents of **8A** (inset of Figure 2.11a zooms in on the early time points of aggregation). The primary observation was that the extent of aggregation increased with increasing equivalents of **8A**. This is however expected as the amount of alkyl amine controls the extent of aggregation possible. A more startling revelation however awaits if one looks at the early time points of aggregation. From 0.5

equivalents and below a sigmoidal growth is clearly visible. Sigmoidal growth clearly signifies a nucleation driven growth and is visible in equivalents less than 0.5.

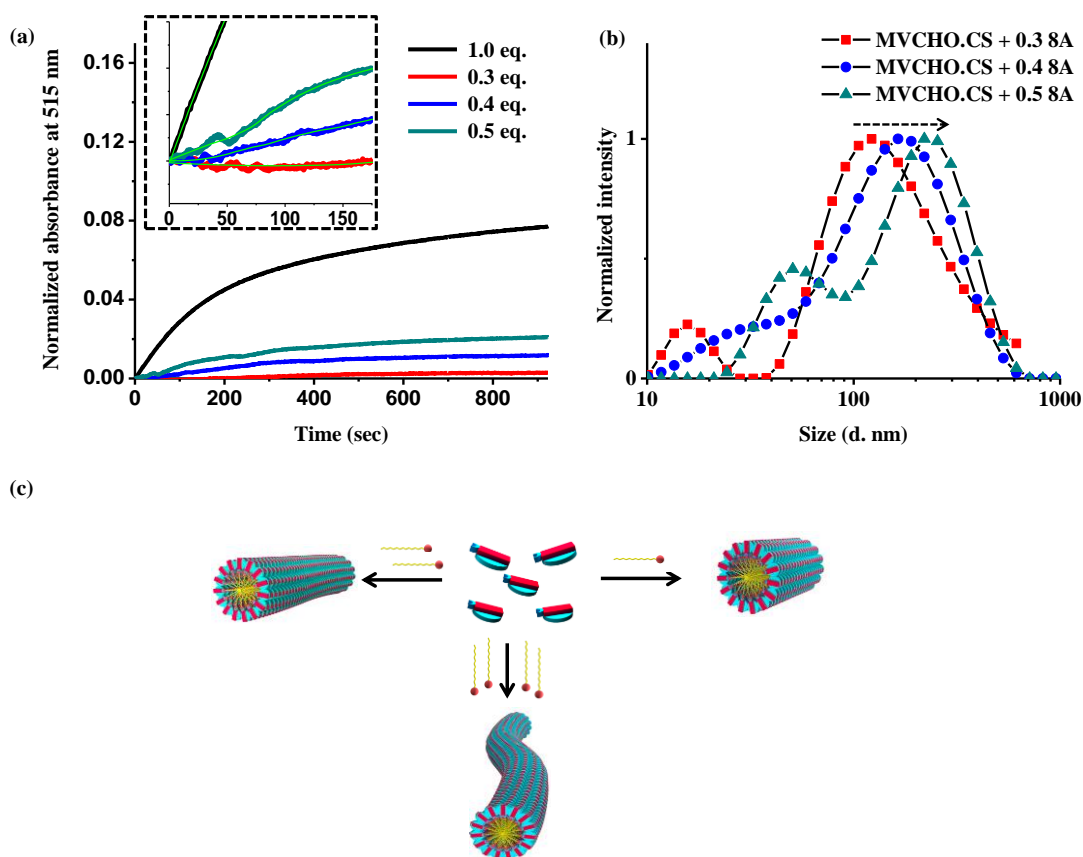


Figure 2.11. (a) and (b) UV-vis and DLS trend of *MVCHO.CS* with various equivalents of **8A** followed at 515 nm, ($[MVCHO] = [CS] = 1 \text{ mM}$, $\text{pH} = 11.0$, H_2O). (c) Schematic representation of extent of aggregation dependent on concentration of **8A**.

This could be due to the fact that at lower equivalents reaction is slow enough so that an independent nucleation phase is visible. At higher equivalents such as 1.0 perhaps the reaction/aggregation drive is too fast and thus a nucleation growth is not visible albeit present. We also measured the aggregate size by DLS with varying equivalents of **8A**. We observed that as **8A** equivalents increase, so does the size (Figure 2.11). This observation is in line with the UV trends and also rules out a templated autocatalytic growth as the size is clearly increasing.⁹

Buoyed by the presence of a nucleation growth mechanism we went ahead to test the living supramolecular polymerization hypothesis in our system. This refers to observing the

growth in a solution with pre-existing nuclei. In our case however the process to addition of nuclei is different as we can form the nuclei *in-situ* by addition of **8A** in batches instead of adding it in one go as has been done in previous experiments.

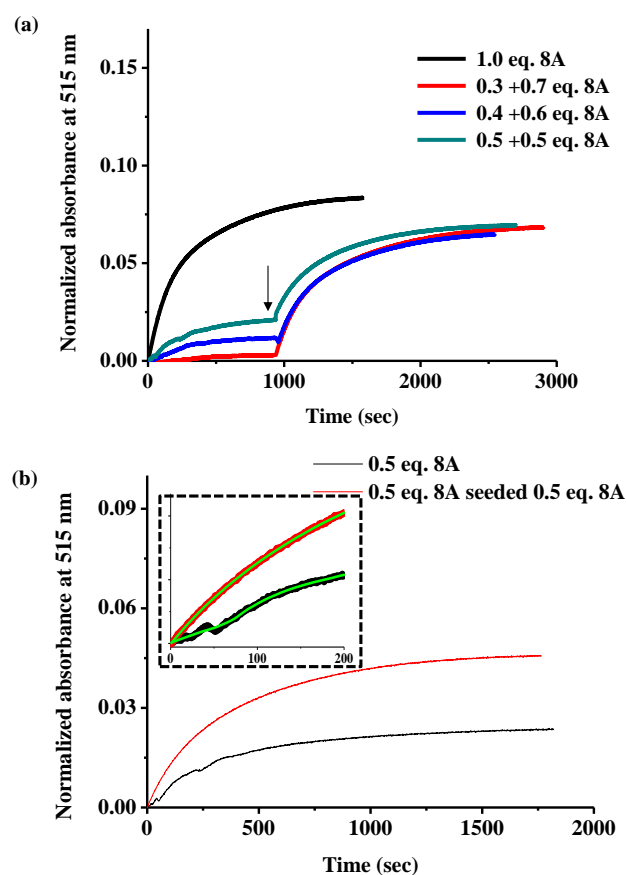


Figure 2.12. (a) UV-vis trend of **MVCHO.CS** with 1.0 eq of **8A** in batches followed at 515 nm, black arrow signifies addition of second batch ($[\text{MVCHO}] = [\text{CS}] = 1 \text{ mM}$, $\text{pH} = 11.0$, H_2O). (b) Overlay of the trend of 0.5+0.5 batch showing difference between seeded and un-seeded growth. Inset is a close up of earlier time points with green line as the smoothed overlay.

To a solution of **MVCHO** and **CS**, for each experiment net 1.0 eq. of **8A** was added in two batches with the batch proportion variable in each experiment. This refers to the experiments in which first batch of amine equivalents were varied from (0.3 to 0.5) and the next batch in each of these solutions was variable from (0.7 to 0.5) (Figure 2.12). This makes the net concentration of **8A** constant and variable the nuclei concentration. A clear change was observed in the growth profile after the second addition. This growth did not proceed via sigmoidal growth clearly

signifying that the consecutive growth is upon existing nuclei. The above study is strong evidence that secondary growth occurs via a living supramolecular polymerization.

To further strengthen our argument we performed the batch growth study also through DLS. We observed a clear size increase following the second addition as compared to the first addition. Moreover the changes in DLS sizes were proportional to the difference between equivalents in subsequent batches (shown in double sided arrows) (Figure 2.13).

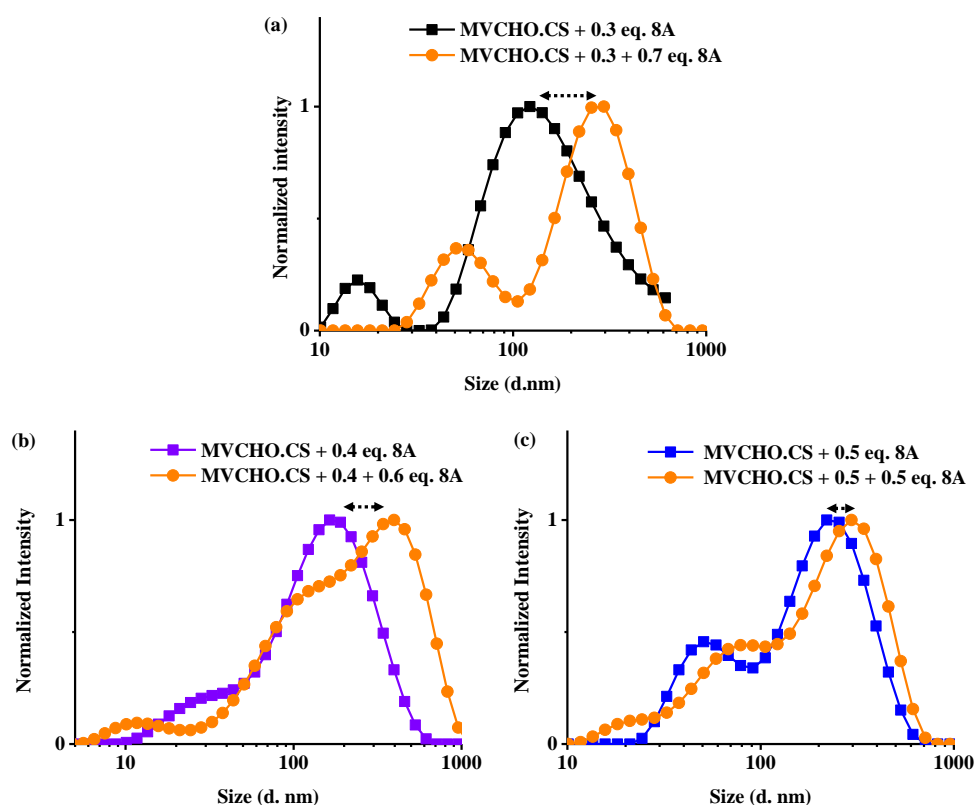


Figure 2.13. (a)-(c) DLS trend of *MVCHO.CS* with 1.0 eq of *8A* in batches followed by DLS, black double arrow points at the decreasing difference between maximum size ($[MVCHO] = [CS] = 1 \text{ mM}$, $\text{pH} = 11.0$, H_2O).

This change in size as well as non-sigmoidal growth signifies that as nuclei are formed subsequent monomers are recruited at the interface to stabilize the interfacial energy. This growth goes on until the alkyl amine is exhausted. This represents the first example ever reported of a chemical reaction driven living supramolecular assembly which is significant considering that biological systems buffer their function using a similar process. Another unique trait of our

system is *in-situ* generation of nuclei. This concept can be extended to further complexity as sequential addition can be made to the aggregates in multiple batches.

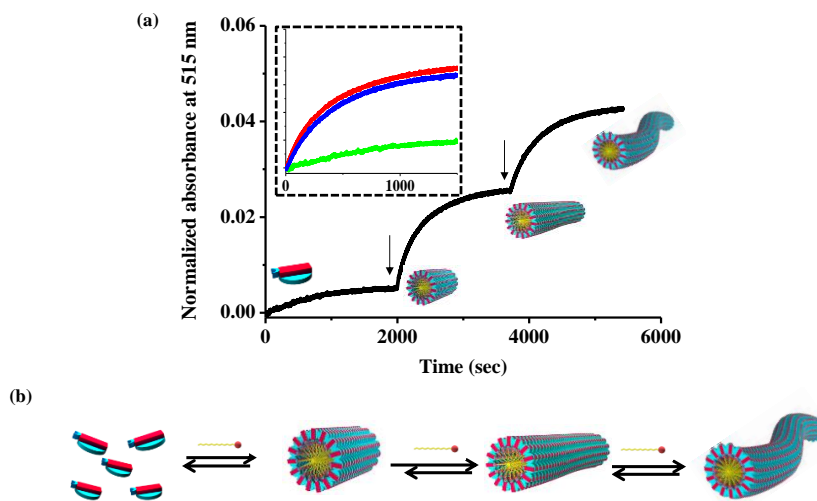


Figure 2.14. (a) UV-vis trend of *MVCHO:CS* with 0.99 eq of **8A** in 3 batches followed at 515 nm, black arrow signifies addition of a new batch ($[MVCHO] = [CS] = 1 \text{ mM}$, $\text{pH} = 11.0$, H_2O). Inset shows the overlay of the trend of 0.33 (green)+0.33 (red)+0.33 (blue) batch showing difference between seeded and un-seeded growth. (b) Schematic representation of the sequential growth experiment.

Going beyond two batches we went further to add **8A** in three batches of 0.33 eq. each (Figure 2.14). First batch growth was slower and did not attain a higher aggregation extent. However the second and third additions were considerably faster than the first addition and also had a considerably high extent of aggregation. This along with previous batch addition experiments suggest that initially when no nuclei is present the kinetics is slower and the equilibrium constant towards aggregation was less as well. However in subsequent additions since the nuclei is already present reaction proceeds at a much faster rate and ends up having a higher equilibrium towards aggregation.

To further consolidate the living supramolecular growth mechanism we did two series of experiments. In first series nuclei concentration was variable and monomer addition was constant ($x[n] + [m]$, $[n]$ is the nuclei concentration, $[m]$ monomer concentration, x is the variable ratio)

and in the second series nuclei concentration was kept constant and monomer concentration was variable ($[n]+x[m]$) (Figure 2.15).

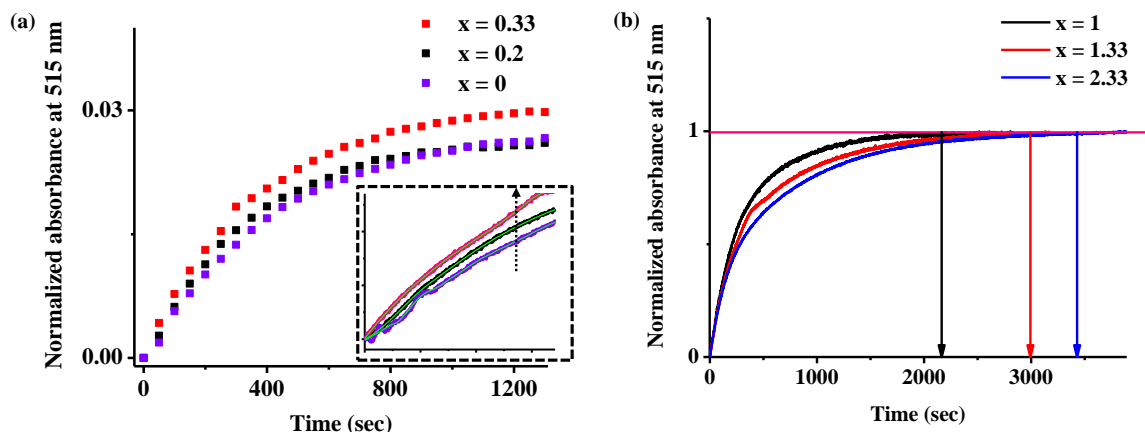


Figure 2.15. (a) and (b) UV-vis trend of *MVCHO.CS* with $x[n]+[m]$ and $[n]+x[m]$ experiments respectively followed at 515 nm, ($[MVCHO] = [CS] = 1$ mM, $pH = 11.0$, H_2O). Inset (a) shows the growth region at lesser time points with arrow signifying the increase in rate with increased value of x . Arrow drop lines in (b) show the time of saturation.

For a conventional living supramolecular polymerization it is expected that with the increase in nuclei concentration brings about an increase in rate of polymerization. Though few experiments showing a rate enhancement as nuclei are present have been presented before, to demonstrate the flexibility of the system we went ahead with $x[n] + [m]$ experiment. Clear rate enhancements were seen on variable concentration of nuclei. We should however point out that in this case the rate enhancement is not huge as in previous experiments where $x = 1$ and therefore a higher growth factor is expected. Another point that is perhaps worth conceding is that even though our system is a unique reaction driven nucleation assembly it does not seem to have a high catalytic efficiency as a very high percentage of nuclei are required to have a considerable rate change.

In the second experiment series of $[n] + x[m]$, nuclei concentration was kept constant and the monomer concentration was variable. Theoretically in such an experiment since monomer concentration is variable and nuclei concentration is constant higher amount of monomer should

require larger time to reach saturation. To our delight, as expected the time taken to saturate for a polymerization process with $x = 2.33$ (3430 secs) was much larger than compared to $x = 1$ (2165 sec). Thus, suggesting the previously hypothesized point that in a living supramolecular system if the nuclei concentration is constant, more number of monomers would take large amount of time to saturate the growth. The successful demonstration of these two experiments suggests that the growth pattern under study is indeed a living supramolecular polymerization.

Having established the growth mechanism spectroscopically we went ahead to seek further proof through accessing the morphology. Field emission scanning electron microscopy (FE-SEM) and Transmission electron microscopy (TEM) of the dried samples of **MC-8** showed the presence of fibrillar structures as was suspected as the solution at higher concentrations also formed a gel (Figure 2.16 a,b). These fibers however were the bundles of molecular aggregates as suggested by their width which ranges from (30-100 nm). Therefore to analyse the molecular aggregates we analysed the samples via cryo-TEM. From this analysis we could clearly see fibers of almost constant width (average around 6.6 nm) (Figure 2.16 c-e). This distance corroborated with the cylindrical micellar packing that has been observed in covalent homologues. Cryo-TEM experiment also clearly proved that the assembly is indeed linear and thus justifying our molecular design parameters.

Furthermore building on the cryo-TEM analysis we went ahead to calculate the polydispersity index (PDI) of our fibers. We understand that previous size approximations were from intensity percentage data of DLS (Figure 2.13). However this data can only be used to represent a trend and not the exact polydispersity as it is weighted heavily towards the higher aggregate lengths. Therefore we carried out cryo-TEM studies on an **MV-CHO:CS** sample in which **8A** has been added in two batches (0.5 + 0.5). Aliquots were taken from 15 min and 75 min (45 min after second addition) and were analysed by cryo-TEM. A frequency statistics was done on the obtained lengths and their number (L_n) and weighted average (L_w) was calculated. PDI was calculated as L_w/L_n (Figure 2.17).²²

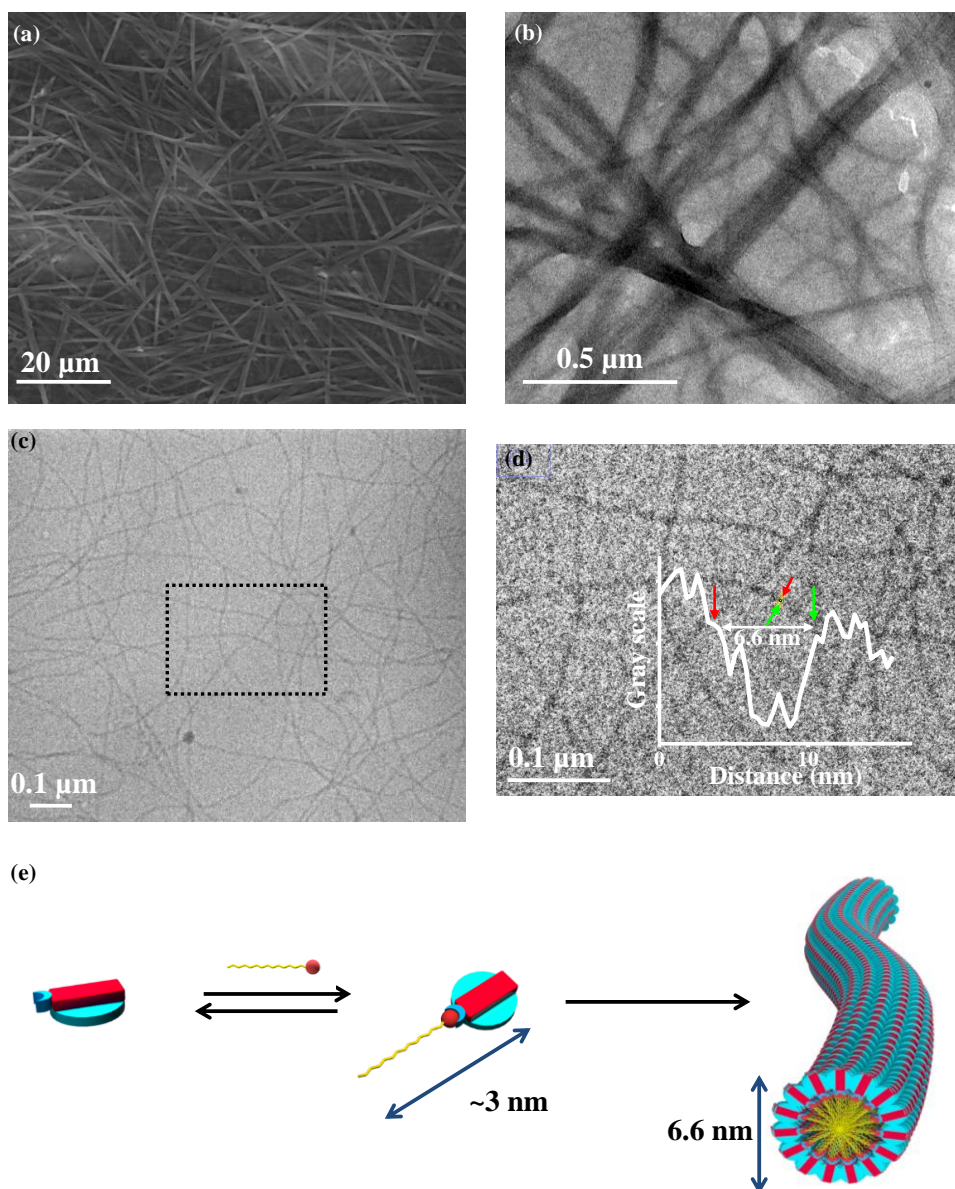


Figure 2.16. (a),(b) and (c) FE-SEM, TEM and cryo-TEM respectively of *MVCHO.CS* with 1,0 eq. of *8A*, ($[MVCHO] = [CS] = 1 \text{ mM}$, $\text{pH} = 11.0$, H_2O). (d) Zoomed region shown of black box marked in image c. Inset (c) Gray scale analysis to probe the width of the fiber. (e) Schematic representation of the cylindrical micelle packing with molecular dimensions.

For the 15 min aliquot 254 fibers were included in the statistics. Very small fibers (<10 nm) could not be measured with confidence and hence were not included. Among these 254 fibers the mean size was 186 nm and the PDI index was 1.3. For 75 min aliquot 234 fibers were included in the statistics. Among these fibers the mean size was 435 nm and the PDI was 1.12. These statistics suggest that both these aliquots are fairly mono disperse hence highlighting the advantages of living supramolecular polymerization and thus reiterating our previous conclusions

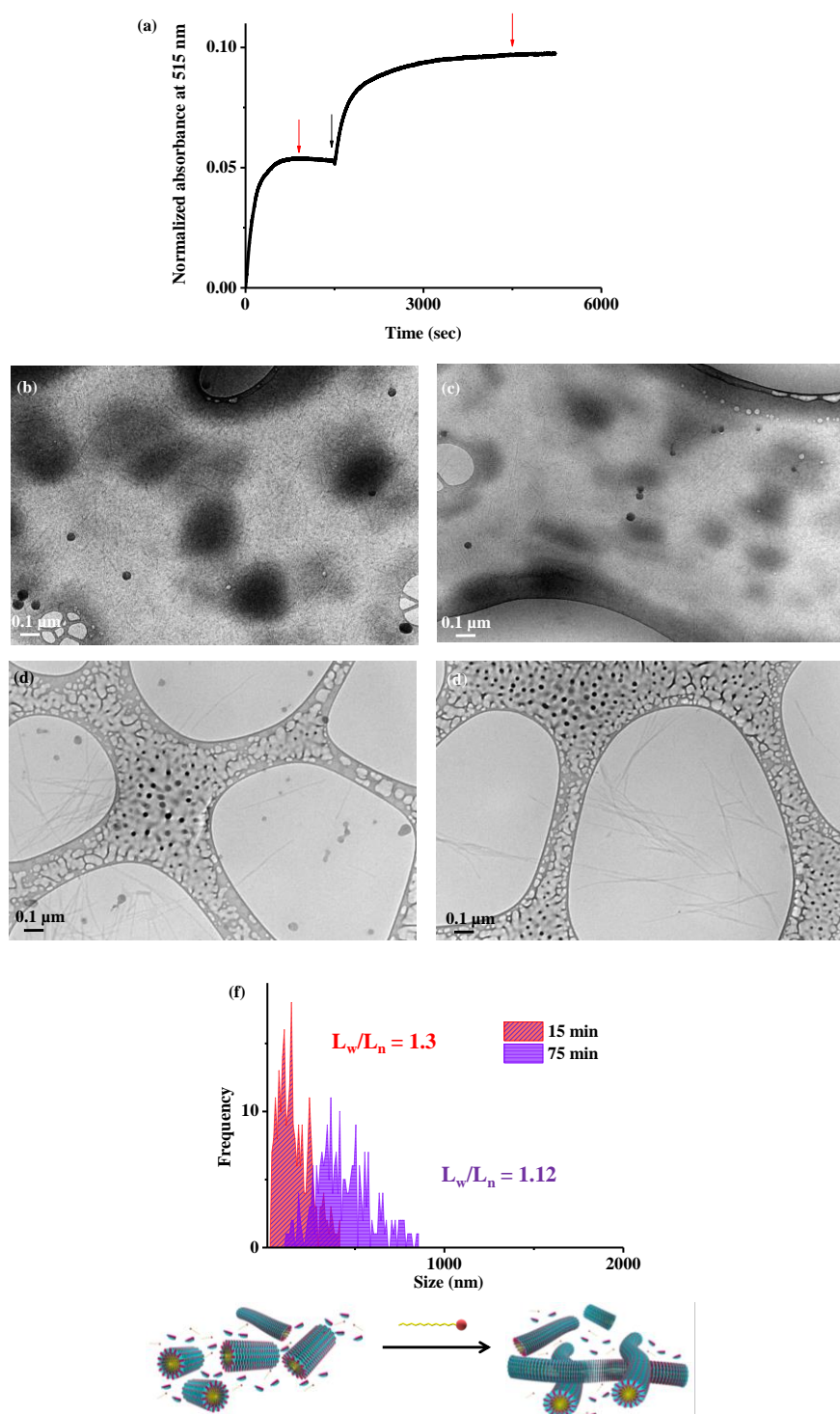


Figure 2.17. (a) UV-vis trend of *MVCHO.CS* with *8A* in two batches followed at 515 nm, black arrow signifies addition of second batch, red arrows signify the time points from which cryo-TEM aliquots were taken. ($[MVCHO] = [CS] = 2 \text{ mM}$, $[8A] = 0.5 + 0.5 \text{ eq.}$, $\text{pH} = 11.0$, H_2O) (b-c) and (d-e) cryo-TEM images at 15 min and 75 min respectively with their prospective schematic below. (f) Frequency distribution of lengths at 15 and 75 mins with their respective PDI indices.

Previous most of the studies in this Chapter were done on **8A** or its lower homologue. These amines do not have a considerable formation of independent micelles of their own and therefore are a good homogenous source in aqueous solution. However one must consider the question that what would be the scenario if alkyl amines formed their own micelles as well.

To study such a scenario we analysed the same **MVCHO.CS** aggregates with *n*-dodecyl amine (**12A**) instead of *n*-octyl amine (**8A**). We observed that as soon as **12A** is added to the solution containing **MVCHO** and **CS** an opaque suspension is formed (due to the micelle formation in water) (Figure 2.19). This suspension clears over time resulting in imine bound aggregate (Figure 2.18).

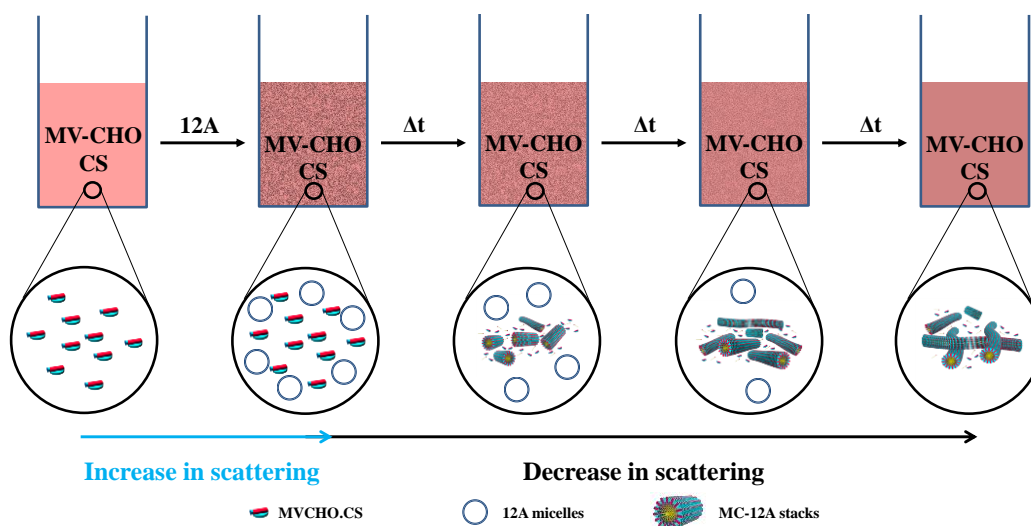


Figure 2.18. (a) Schematic showing the evolution of scattering over time in **MC-12A** formation

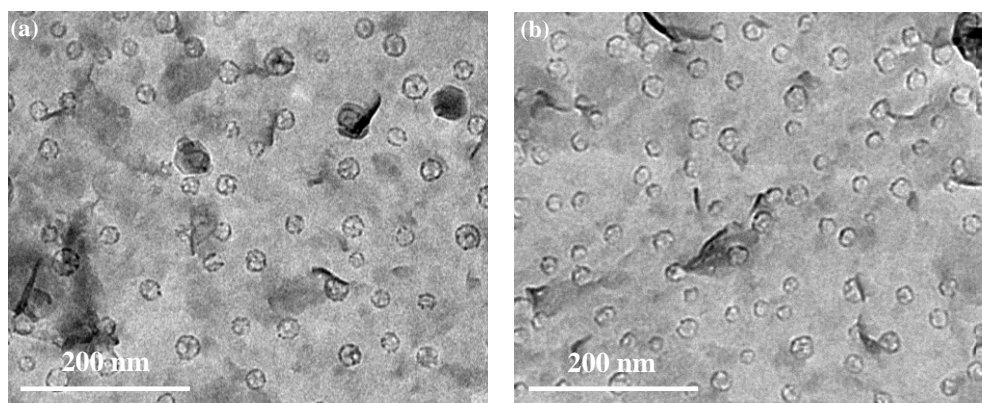


Figure 2.19. (a) and (b) TEM images of **12A** micelles.

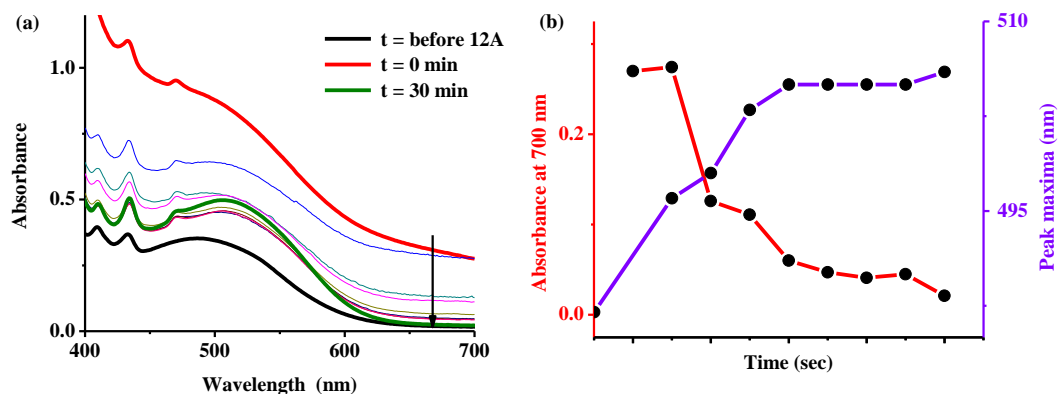


Figure 2.20. (a) UV-vis spectra of **MVCHO.CS** with 1.0 eq of **12A**, black arrow signifies decrease in scattering ($[MVCHO] = [CS] = 1 \text{ mM}$, $\text{pH} = 11.0$, H_2O). (b) Overlay of the trends of change in wavelength maxima and scattering over time from spectra in (a).

We followed the process with UV-vis spectra which confirmed the instantaneous increase of scattering on **12A** addition and then subsequent gradual decrease. It should be noted that the final spectra has very less scattering and has absorption features resembling that of an imine based aggregate (increased intensity of CT band). We plotted the shift in maxima wavelength with time (signifies imine based aggregation) and compared it to the scattering changes (Figure 2.20). To our surprise both these kinetics are very similar with shift in peak maxima wavelength signifying imine based aggregation and hence increases with time. On the other hand decrease in scattering suggests decrease in population of independent micelles of **12A** and hence represent consumption of **12A** into an imine based aggregate. Both kinetics hence represent the same process.

To confirm our hypothesis we performed the same study with Viologen moiety devoid of an aldehyde group (**MV**). We followed the scattering trace of **12A** at 750 nm. On addition of **12A** in a solution containing **MV.CS** no decrease in scattering was observed. However in case of **MVCHO.CS** a decrease was observed but was accompanied with initial lag phase (Figure 2.21). To this subsequent solution further aliquot of **12A** was added and immediate decay of scattering was observed without a lag phase.

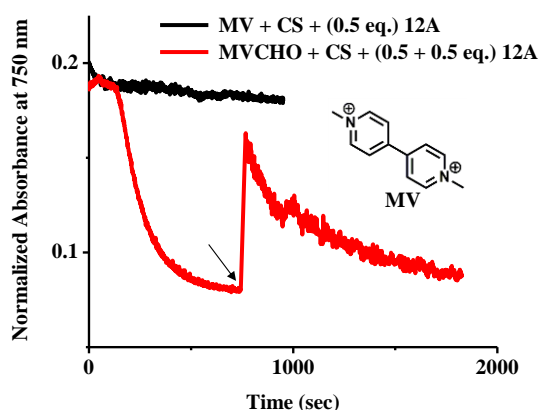


Figure 2.21. UV-vis trend of *MVCHO.CS* and *MV:CS* with 0.5 eq of **12A**, black arrow signifies addition of another batch of **12A** ($[MVCHO] = [CS] = [MV] = 1 \text{ mM}$, $\text{pH} = 11.0$, H_2O). Inset shows the molecular structure of *MV*.

This study is representative of various important points. First being the decrease in scattering is indeed due to **12A** consumption to form **MC-12A**. The fact that first aliquot addition has a lag phase however the second aliquot does not; is reminiscent of the seeded growth observed in case of **8A**. We hypothesize that when **12A** is added into the solution it forms its own micelles (Figure 2.19). However overtime **12A** begins to get consumed into **MC-12A** aggregates. The lag phase is perhaps a representation of another kinetic barrier that gets introduced due to mass transfer from **12A** micelles to **MC-12A** via dissolution. However when the second aliquot is added the activated nuclei that already exist consume **12A** at a much faster rate hence the disappearance of the lag phase. Additional lag phase makes sure that rate of formation of **MC-12A** nuclei is slow. A slower growth due to additional kinetic barrier thus forms for a good system to study living supramolecular polymerization as changes in kinetics are more evident. Further query arises in regards to what method should one follow to measure the growth trend of **MC-12A**. Direct increase in CT band is not an option in this case due to the significant amount of scattering produced by **12A** micelles. Since as shown in previous discussion the decrease in **12A** scattering is representative of **MC-12A** aggregation the growth has been monitored indirectly by **12A** consumption for further experiments.

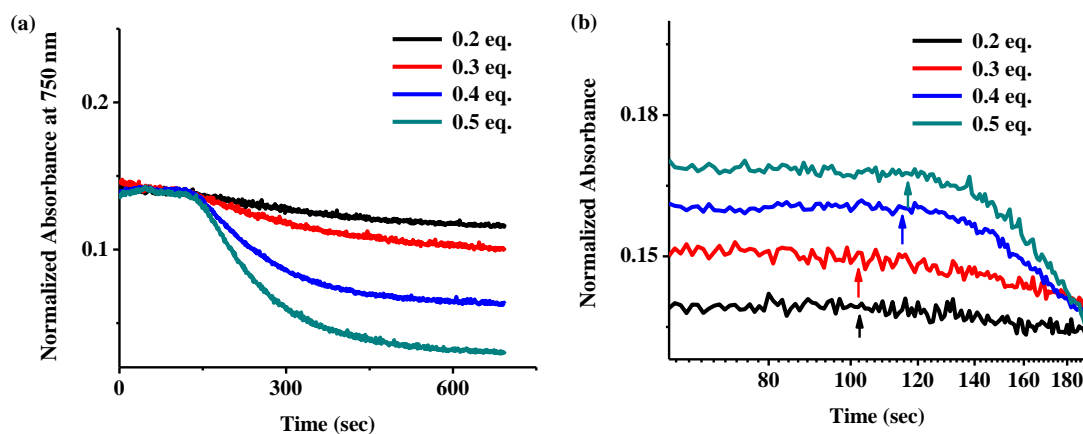


Figure 2.22. (a) UV-vis trend of *MVCHO.CS* with various equivalents of **12A**, ($[MVCHO] = [CS] = 1 \text{ mM}$, $\text{pH} = 11.0$, H_2O). (b) Manually displaced lag phases with arrows pointing towards the end of a lag phase at a particular equivalent of **12A**.

We performed sequential study of growth with various equivalents of **12A**. Similar to studies with **8A** this also showed increased rate and extent of aggregation with increase in the amount of **12A**. Also a closer look at the lag phase suggested the lag phase increased with increase in **12A** concentration, which is again suggestive of the fact that lag phase in this case is due to additional barrier of **12A** caused by its micelles (Figure 2.22).

We further went ahead to carry on living supramolecular polymerization experiments on this system and similar to the case in **8A** we added the amines in batches. First batch clearly showed the presence of a lag phase which was absent in the second addition. Moreover one can notice that at higher percentages of seed (high first aliquot proportion) absolutely no trace of sigmoidal growth was noticed however slight sigmoidal nature appears at lower seed ratios (0.2). This signifies perhaps the limit of nuclei concentration that can give rise to a catalytic growth (Figure 2.23). Again comparing to reported examples of seeded growth in supramolecular systems that have been discussed before we believe that for our system the catalytic efficiency of the nuclei is a limiting factor and perhaps an area that requires additional research.

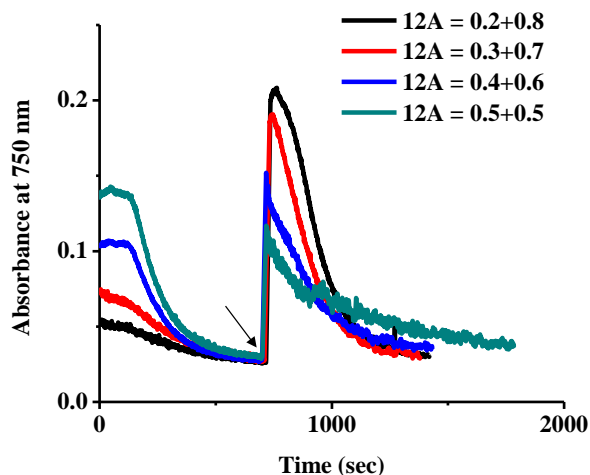


Figure 2.23. (a) UV-vis trend of *MVCHO.CS* with 1.0 eq of *12A* in various batches, black arrow signifies addition of another batch of *12A* ($[MVCHO] = [CS] = 1 \text{ mM}$, $\text{pH} = 11.0$, H_2O).

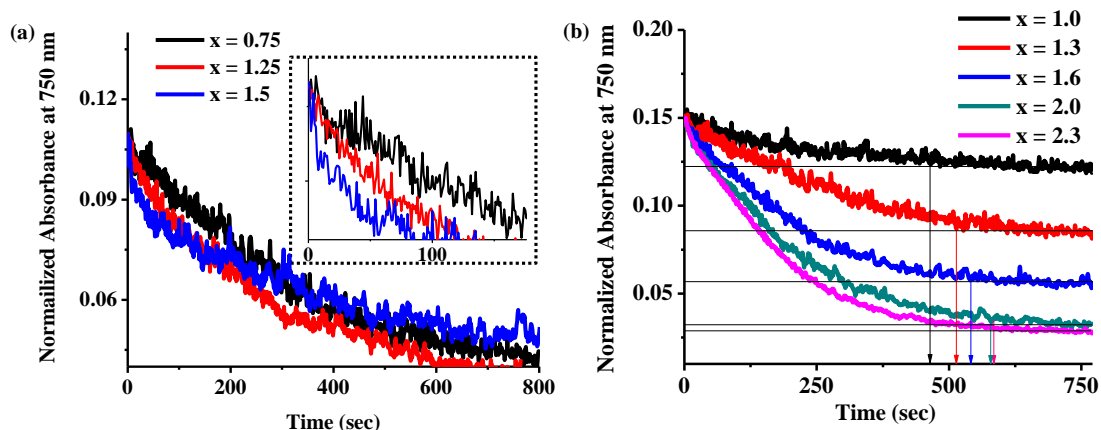


Figure 2.24. (a) and (b) UV-vis trend of *MVCHO.CS* with $x[n]+[m]$ and $[n]+x[m]$ experiments respectively followed at 750 nm, ($[MVCHO] = [CS] = 1 \text{ mM}$, $\text{pH} = 11.0$, H_2O). Inset (a) shows the growth region at lesser time points (b) arrow drop lines show the time of saturation.

We also went ahead and performed nuclei and monomer variation experiments with **12A**. Increasing the percentage of nuclei clearly increased the rate of scattering decay which relates to rate of growth. Moreover when nuclei concentration was kept constant and monomer concentration was varied, higher monomer percentages took longer time to saturate (Figure 2.24). Both of these experiments reiterate the previous hypothesis of living supramolecular polymerization.

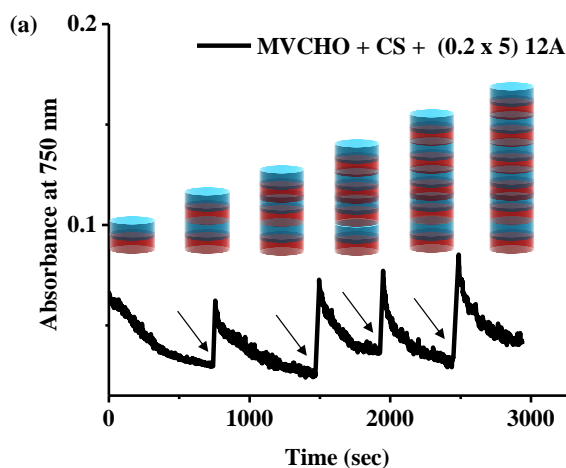


Figure 2.25. UV-vis trend of *MVCHO.CS* with 1.0 eq of *12A* in 5 batches followed at 750 nm, black arrow signifies addition of a new batch ($[MVCHO] = [CS] = 1 \text{ mM}$, $\text{pH} = 11.0$, H_2O). Schematic represents the sequential growth of stacks.

Furthermore we also demonstrated the sequential addition which in this case could be done up to 5 cycles (0.2x5). First cycle has a lag phase and the subsequent 4 cycles do not (Figure 2.25). This clearly suggests that these additions are indeed sequential.

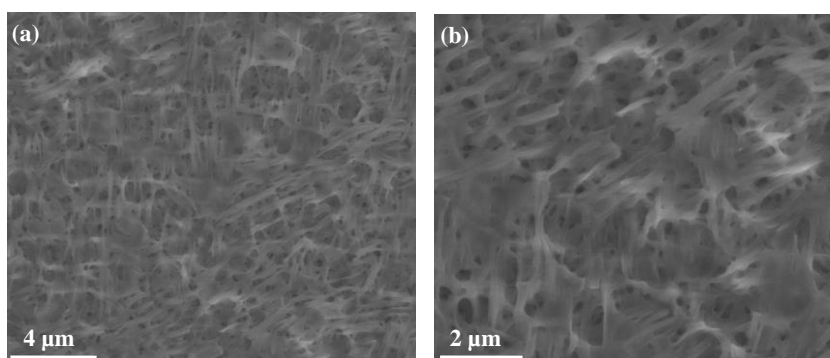


Figure 2.26. (a)-(b) FE-SEM images of *MVCHO.CS* with 1.0 eq of *12A* ($[MV.CHO] = [CS] = 1 \text{ mM}$, $\text{pH} = 11.0$, H_2O).

Another important analysis was the morphology of the aggregate. FE-SEM analysis of **MC-12** clearly suggests linear aggregates (Figure 2.26). This is in accordance with the previously proposed growth model.

2.2.2. Hetero-Nucleation

Generation of a supramolecular hetero structure is not a trivial task. As shown in Chapter 1 only a few such systems are known. In a follow up of the previous discussion on nucleation driven assembly of **MC-8A** and **MC-12A**, we hypothesized another batch addition experiment but in this case the amines in two different batches would be different. As seen before depending on the length of alkyl chain and its inherent extent of aggregation different alkyl chains aggregate at different rates with **5A**, **6A** forming imines but not good enough for aggregation. We think that introduction of a preformed nuclei of a higher alkyl amine may help in advancing this equilibrium. If it works out, this would also be a viable strategy to form a supramolecular hetero-structure.

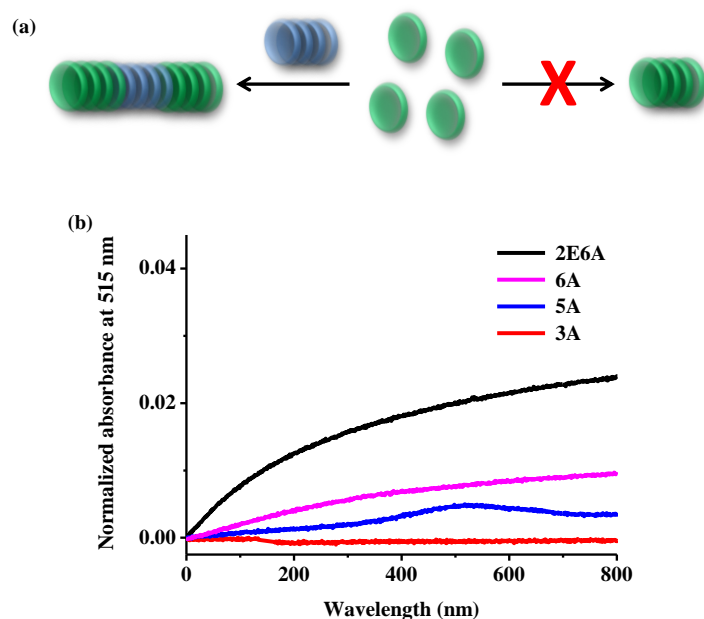


Figure 2.27. (a) Schematic showing nucleation assisted hetero structure formation for amines whose adducts cannot aggregate individually. (b) UV-vis trend of **MVCHO.CS** with 0.5 eq of various amines after seeding with 0.5 eq. of **8A**, followed at 515 nm ($[MVCHO] = [CS] = 1 \text{ mM}$, $\text{pH} = 11.0$, H_2O).

In an experiment, to a pre formed nuclei of 0.5 eq. **8A** we added 0.5 eq. of various less/non self-assembling alkyl amines. **3A** showed no aggregate formation, however **5A** and **6A** showed partial aggregate formations which was a considerable improvement. **2E6A** showed

aggregate formation without a sigmoidal lag phase representing the hetero nucleation (Figure 2.27).

To cement this fact further we compared these **8A** seeded aggregates with their un-seeded forms. A clear change in kinetics was seen in all except **3A** clearly suggesting that **MC-8A** nuclei was able to propagate assemblies of other amine adducts (Figure 2.28). This also proves our hypothesis that preformed nuclei, in this case **8A**, can enhance the equilibrium constant of other less performing amine adducts. This is perhaps due to the fact that nuclei formation is an energy intensive step. Lesser concentration of the adduct does not drive the product in aggregate direction. However as the seed is introduced the energy intensive step of nuclei formation is no longer required and hence a reaction push occurs towards higher aggregation.

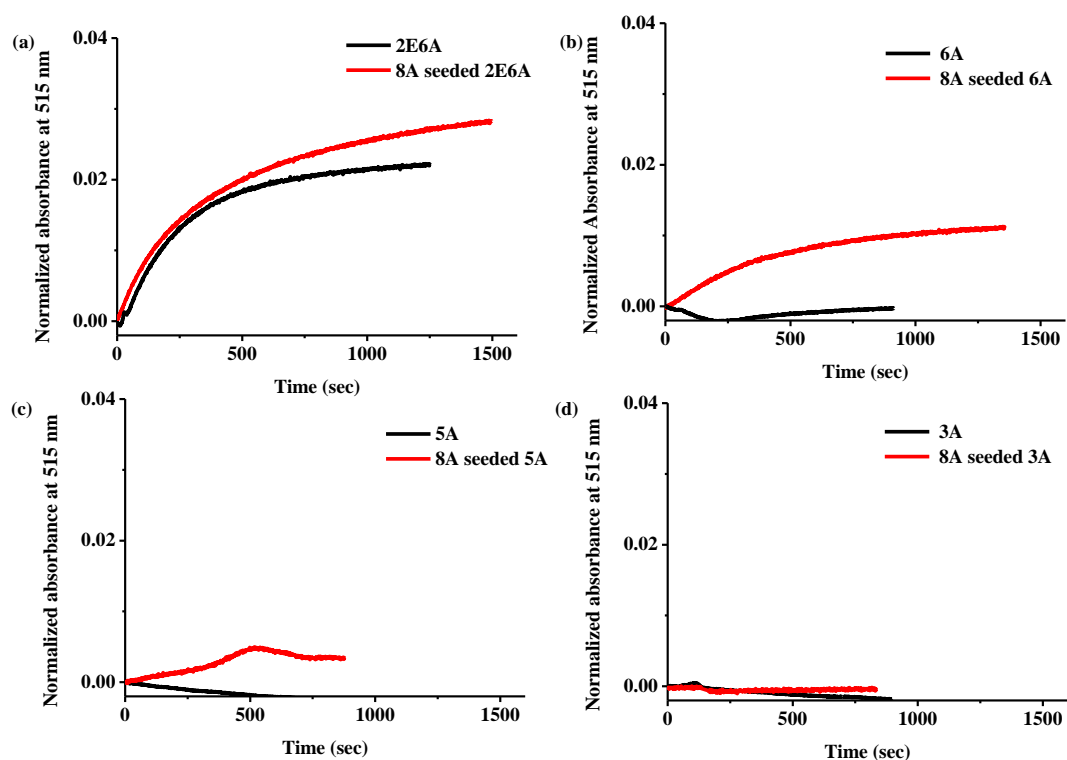


Figure 2.28. (a)-(d) UV-vis trend of *MVCHO.CS* with 0.5 eq of various amines after seeding and before seeding with 05. Eq. of **8A**, followed at 515 nm ($[MVCHO] = [CS] = 1 \text{ mM}$, $\text{pH} = 11.0$, H_2O). Scales of the four figures have been kept constant for comparison of relative acceleration of aggregation.

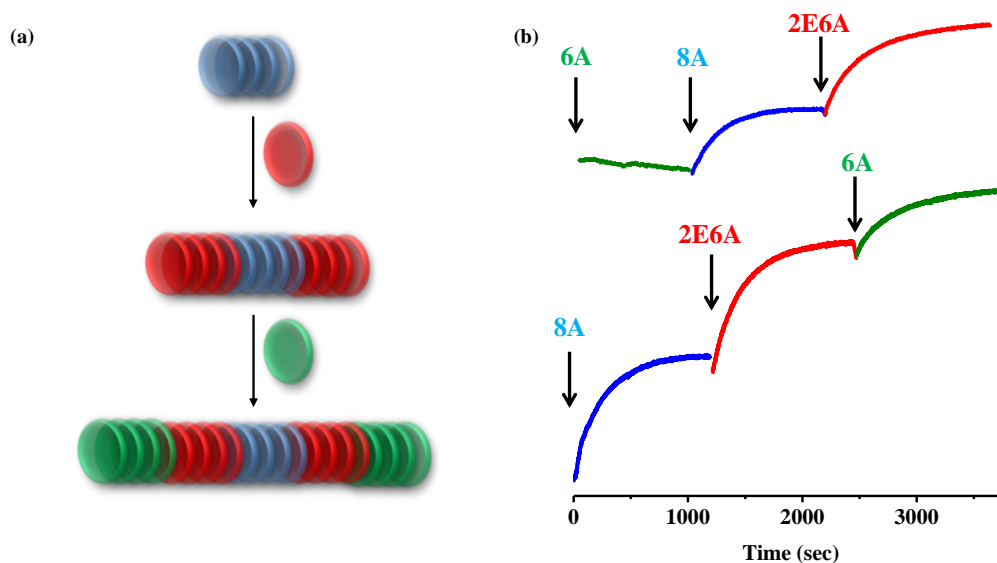


Figure 2.29. (a) Schematic showing the growth of multi-block assembly via consecutive nucleation. (b) UV-vis trend of *MVCHO.CS* for multi-block with 0.33 eq. of each amine, arrows signify their addition, trend followed at 515 nm ($[MVCHO] = [CS] = 1$ mM, pH = 11.0, H_2O).

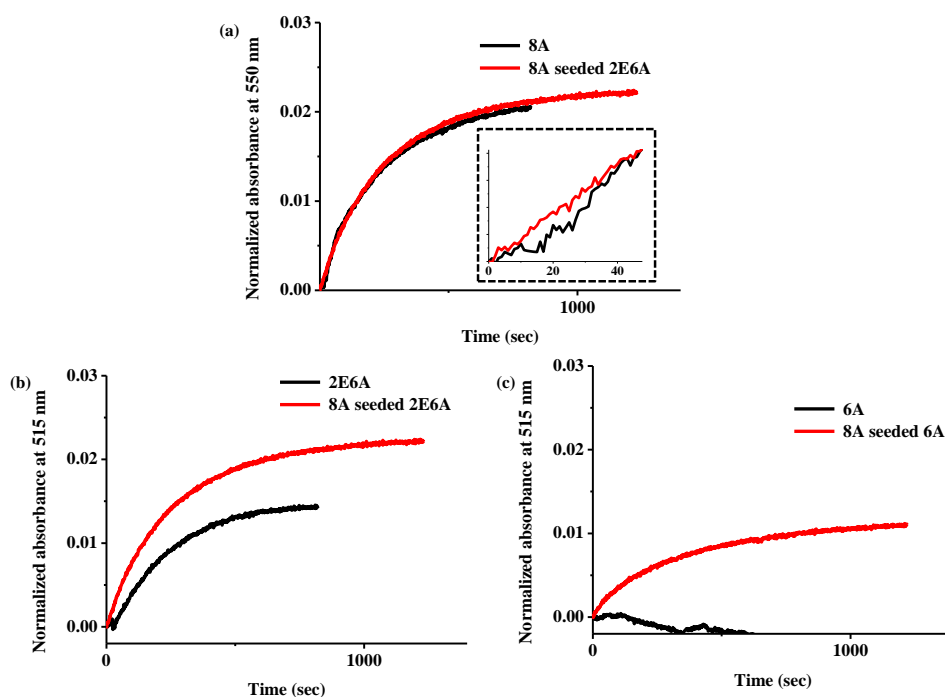


Figure 2.30. (a)-(d) UV-vis trend of *MVCHO.CS* with 0.5 eq of various amines after seeding and before seeding in the multi-block experiment, followed at 515 nm ($[MVCHO] = [CS] = 1$ mM, pH = 11.0, H_2O).

We further performed the hetero nucleation experiment with three batches, selecting **6A**, **2E6A** and **8A** as participating amines. In an experiment that started with **8A** as nuclei, **2E6A** was added as the second component and **6A** as the third component (Figure 2.29). The respective growth curves were compared to their un-seeded counterparts to demonstrate the increase in kinetics (Figure 2.30).

Both **2E6A** and **6A** showed considerable rate increase compared to their native trends. **2E6A** increased enough to compare with the growth rate of un-seeded **8A** barring the sigmoidal trend. In another multi block experiment we started with **6A** and then subsequent addition of **8A** and **2E6A**. **6A** showed no growth and this resulted in **2E6A** nucleated growth over **8A**. We understand that there can be re-equilibration of amines due to imine exchange over time. Though in an aggregate form this is expected to be slow, further studies are to be carried out to understand their dynamics in aggregate systems.

These preliminary experiments form the basis of investigation into multi-block structures in future and are an exciting possibility that can be easily achieved through this process.

2.3. Conclusion and Outlook

The basis for experiments in this Chapter started with a biological inspiration so that one could mimic the reaction driven assembly and temporal control of aggregates. We have employed CT interaction as a directional growth factor and imine bond as a dynamic reaction. During the course of this discussion we have proved that not only living supramolecular polymerization can be achieved in this process very easily but also hetero-structures with multiple blocks can be formed in a controlled manner.

Considering the fact that processes demonstrated in this chapter are quite rare in general systems, a demonstration of common system with a defined approach towards these problems signifies perhaps an opening of much greater avenues. The studies in this chapter though give answers to a general approach towards complex and controlled aggregate architecture; it also

opens possibilities for more novel questions. Some of these questions regarding block structure formation is under investigation in our lab for future possibilities and possible gateways to a highly controlled supramolecular environment.

2.4. Experimental Section

General Methods:

NMR Measurements: NMR spectra were obtained with a Bruker AVANCE 400 (400 MHz w.r.t. ^1H nuclei) Fourier transform NMR spectrometer with chemical shifts reported in parts per million (ppm).

Optical Measurements: Electronic absorption spectra were recorded on a Perkin Elmer Lambda 900 UV-Vis-NIR Spectrometer.

Dynamic light scattering (DLS) Experiments: The measurements were carried out using a NanoZS (Malvern UK) employing a 532 nm laser at a back scattering angle of 173° . The samples were measured in a 10 mm glass cuvette. A dead time (Time between sample loading and starting of measurement by the machine) of around 45 seconds is present in all measurements.

Field Emission Scanning Electron Microscopy (FE-SEM). FE-SEM measurements were performed on NOVA NANO SEM 600 (FEI) operated at 15 kV, by drop casting the solution on glass substrate. All samples were recorded in low vacuum mode (FE-SEM).

Transmission Electron Microscopy (TEM): TEM measurements were performed on a JEOL, JEM 3010 operated at 300 kV. Samples were prepared by placing a drop of the solution on carbon coated copper grids followed by drying at room temperature. The images were recorded with an operating voltage 300 kV.

Cryo TEM: To study the length of fibres at different time points, samples were prepared using FEI Vitrobot system by plunge freezing in liquid ethane to preserve the native structure. Following are the parameters that were used: Blot time (s) – 1.0, Blot force – 0, Wait time (s) –

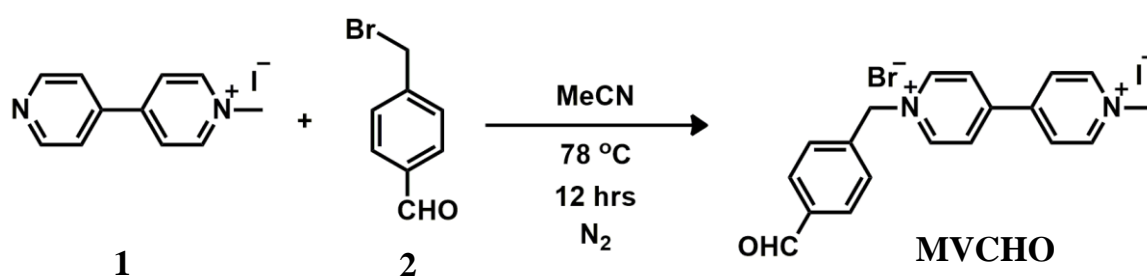
1.0, Blot total – 1, Drain time (s) – 0.5. The temp was maintained at 22 and humidity was >90. Holey carbon grids were used sample preparation bought from EMS. Imaging was done using Tecnai G2 Spirit Bio-TWIN Transmission Electron Microscope at 100kV.

Viscosity Measurements: Viscosity measurements were performed on Anton Paar MCR 302 rheometer (air bearing). The measuring system was CP50-1 and the measuring cell configuration was P-PTD 200/80/Air. The gap between the surface and cone plate was 0.101 mm. Viscosity was measured over time at a constant shear rate of 50 Hz. Temperature was kept constant at 25 °C. A dead time (Time between sample loading and starting of measurement by the machine) of around 180 seconds is present in all measurements.

Materials: *n*-Propyl amine, *n*-Pentyl amine and *n*-Octyl amine were procured from Spectrochem. *n*-Hexyl amine (99%) and *n*-Dodecyl amine (98%) were ordered from Sigma Aldrich. 2-Ethyl hexyl amine (99%) was procured from Acros organics. All the chemicals were not further purified and used as such. Phosphate buffer solutions of various pHs was made according to the reported protocol.²³

Synthesis:

MVCHO:



Scheme 2.1. Synthetic scheme for synthesis of MVCHO.

Procedure: **1** and **2** were dissolved in dry acetonitrile and allowed to react for 12 hours under nitrogen atmosphere. The resultant orange colour precipitate was filtered and subsequently washed with chloroform and acetonitrile. The precipitate was then dried and analysed (98%

yield). ^1H NMR (400 MHz, D_2O): δ 10.03 (s, 1H), 9.25 (d, 2H, $J = 6.88$ Hz), 9.10 (d, 2H, $J = 6.80$ Hz), 8.64 (d, 2H, $J = 6.84$ Hz), 8.58 (d, 2H, $J = 6.72$ Hz), 8.09 (d, 2H, $J = 8.20$ Hz), 7.45 (d, 2H, $J = 8.2$ Hz), 6.11 (s, 2H), 4.55 (s, 3H); ^{13}C NMR δ_c (100 MHz, D_2O): 195.6, 150.8, 149.6, 146.3, 145.8, 138.9, 136.6, 131.0, 129.7, 127.3, 126.8, 64.2, 48.4; ^{13}C DEPT 135 NMR δ_c (100 MHz, D_2O): 195.6 (+), 146.3 (+), 145.8 (+), 131.0 (+), 129.7 (+), 127.3 (+), 126.8 (+), 64.2 (-), 48.4 (+); HRMS (ESI): m/z : calcd for M i.e. $\text{C}_{19}\text{H}_{18}\text{BrIN}_2\text{O}$: 495.9647, for $[\text{M}-\text{Br}-\text{I}-\text{H}]^+$ i.e. $\text{C}_{19}\text{H}_{17}\text{N}_2\text{O}$: 289.1335, found $[\text{M}-\text{Br}-\text{I}-\text{H}]^+$: 289.2403.

1 and **2** were synthesized and adequately analysed according to reported procedures.^{24,25} **CS** and **MV** were synthesized according to the reported procedures and sufficiently characterized.^{26,27}

2.5. References and Notes

1. Belowich M. E.; Stoddart J. F. *Chem. Soc. Rev.* 2012, **41**, 2003.
2. Janeliunas D.; van Rijn P.; Boekhoven J.; Minkenberg C. B.; van Esch J. H.; Eelkema R. *Angew. Chem. Int. Ed.* 2013, **52**, 1998.
3. Wang G.; Wu G.; Wang Z.; Zhang X. *Langmuir* 2013, dx.doi.org/10.1021/la405000a.
4. Wang G.; Wang C.; Wang Z.; Zhang X. *Langmuir* 2011, **27**, 12375.
5. Wang G.; Wang C.; Wang Z.; Zhang X. *Langmuir* 2012, **28**, 14567.
6. Wang C.; Wang G.; Wang Z.; Zhang X. *Chem. Eur. J.* 2011, **17**, 3322.
7. Minkenberg C. B.; Homan B.; Boekhoven J.; Norder B.; Koper G. K.M.; Eelkema R.; van Esch J. H. *Langmuir* 2012, **28**, 13570.
8. Boekhoven J.; Poolman J. M.; Maity C.; Li F.; van der Mee L.; Minkenberg C. B.; Mendes E.; van Esch J. H.; Eelkema R. *Nat. Chem.* 2013, **5**, 433.
9. Nguyen R.; Allouche L.; Buhler E.; Giuseppone N. *Angew. Chem. Int. Ed.* 2009, **48**, 1093.
10. Ciesielski A.; El Garah M.; Haar S.; Kovaříček P.; Lehn J.-M.; Samorì P. *Nat. Chem.* 2014, **6**, 1017.
11. Zhang X.; Wang C. *Chem. Soc. Rev.* 2011, **40**, 94.
12. Wang C.; Yin S. C.; Xu H. P.; Wang Z. Q.; Zhang X. *Angew. Chem., Int. Ed.*, 2008, **47**, 9049.

13. Wang C.; Guo Y. S.; Wang Y. P.; Xu H. P.; Wang Z. Q.; Zhang X. *Angew. Chem., Int. Ed.* 2009, **48**, 8962.
14. Liu K.; Yao Y.; Liu Y.; Wang C.; Li Z.; Zhang X. *Langmuir* 2012, **28**, 10697.
15. Huang Z.; Yang L.; Liu Y.; Wang Z.; Scherman O. A.; Zhang, X. *Angew. Chem. Int. Ed.* 2014, **53**, 5351.
16. Jain A.; George S. J. *Mat. Today* 2015, **18**, 206.
17. Rao K. V.; Jayaramulu K.; Maji T. K.; George S. J. *Angew. Chem. Int. Ed.* 2010, **49**, 4218.
18. Rao K. V.; George S. J. *Chem. Eur. J.* 2012, **18**, 14286.
19. Kumar M.; Rao K. V.; George S. J. *Phys. Chem. Chem. Phys.* 2014, **16**, 1300.
20. (a) Sagade A.; Rao K. V.; George S. J.; Datta A.; Kulkarni G. U. *Chem. Commun.* 2013, **49**, 5847; (b) Sagade A. A.; Rao K. V.; Mogera U.; George S. J.; Datta A.; Kulkarni G. U. *Adv. Mater.* 2013, **25**, 559.
21. Mogera U.; Sagade A. A.; George S. J.; Kulkarni G. U. *Sci. Rep.* 2014, **4**, 4103.
22. Robinson M. E.; Lunn D. J.; Nazemi A.; Whittell G. R.; Cola L. D.; Manners I. *Chem. Commun.* 2015, **51**, 15921.
23. <http://delloyd.50megs.com/moreinfo/buffers2>.
24. Yamaguchi H.; Harada A. *Biomacromolecules* 2002, **3**, 1163.
25. Chatterjee S.; Ramakrishnan S. *Chem. Commun.* 2013, **49**, 11041.
26. Ghosh A.; Rao K. V.; George S. J.; Rao C. N. R.; *Chem. Eur. J.* 2010, **16**, 2700.
27. Rao K. V.; Jayaramulu K.; Maji T. K.; George S. J. *Angew. Chem. Int. Ed.* 2010, **49**, 4218.

Chapter-3

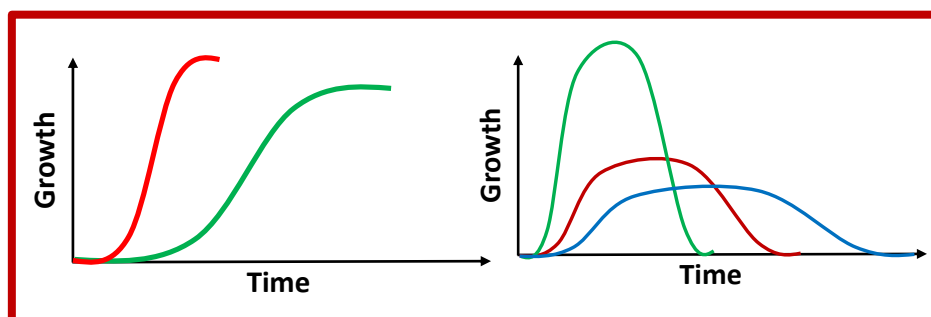
*Programmable Growth and Decay of Dynamic
Charge-Transfer Stacks*

Chapter-3

Programmable Growth and Decay of Dynamic Charge-Transfer Stacks

Abstract

Temporal control over materials in relation to their growth and decay is something in which biological systems are adept at. In such systems since most aggregates or complexes are linked via chemical reaction, any stimuli that changes their kinetics can bring about a change in growth or decay profiles of these aggregates. Comparing the biological prowess to the current status in devising strategies to synthetically achieve such a control warrants an urgent need of investigation. Development of these strategies can bring about a sea of change in applications targeted by self-assembled structures thus opening up a new dimension for academic interest. We in this chapter intend to develop common strategies for controlling the growth and decay of a chemical reaction governed self-assembly. Self-assembly controlled by imine bond formation that was detailed in previous chapter has been built upon to test the stimuli responsiveness of these aggregates. We have used strategies such as competitive inhibition, delayed pH activation and deactivation through various chemical stimuli. These impetuses assist us in achieve not only aggregates with control growth profile but also self-assembled structures with programmed temporal decay profiles essentially rendering the process dissipative.



3.1. Introduction

Temporal control over soft matter gets its inspiration from biological systems. As mentioned by Prof. Uri Alon in his book “*An Introduction to Systems Biology: Design Principles of Biological Circuits*”, timescale of the transcription factor binding to DNA site (~1 sec) to transcribe a gene (~ 1 min) to finally translation of a protein (~2 min), each layer of the process is chemical reaction controlled and time bound.¹ Such a time bound system not only requires a strict temporal control of its components but also equal accessories to modulate the time frames accordingly depending on the external stimuli.

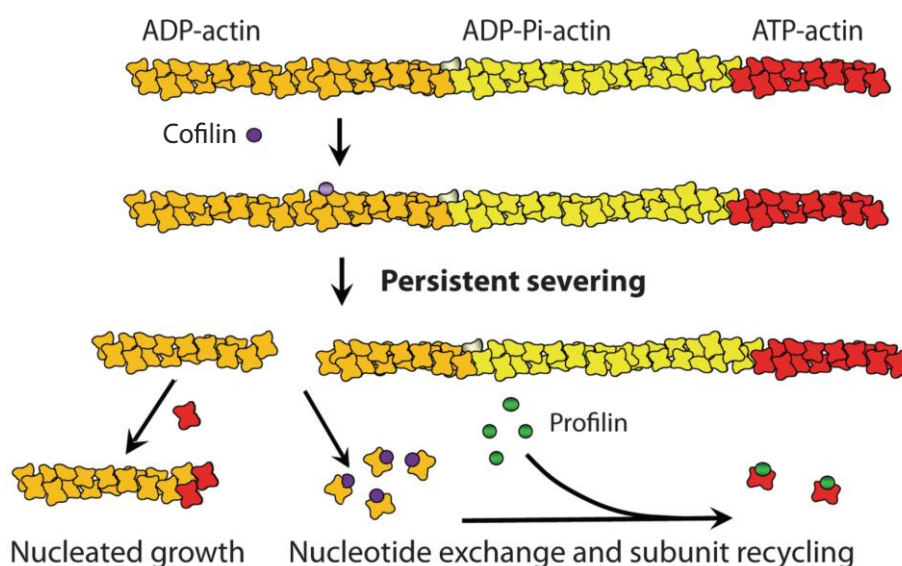


Figure 3.1. Schematic showing the perturbation in actin polymerization behaviour caused by profilin (green) and cofilin (purple). (Reproduced with permission from Ref. 2).

These temporal signals percolate through to the cytoskeletal assembly as well as there are well defined factors to program the growth and decay of these protein assemblies. Taking the example of actin assemblies again proteins such as “profilin” exist which bind to actin and inhibit nuclei formation, thus controlling the rate of growth (Figure 3.1). Also, from the same process

dynamic instability exists in actin due to ATPase nature of F-actin as well as due to presence of accessories such as “cofilin” which when bound to actin aggregates breaks them catastrophically.² Though just two accessories have been mentioned here, obviously there are a huge amount of other co-factors which bring about this temporal control.³

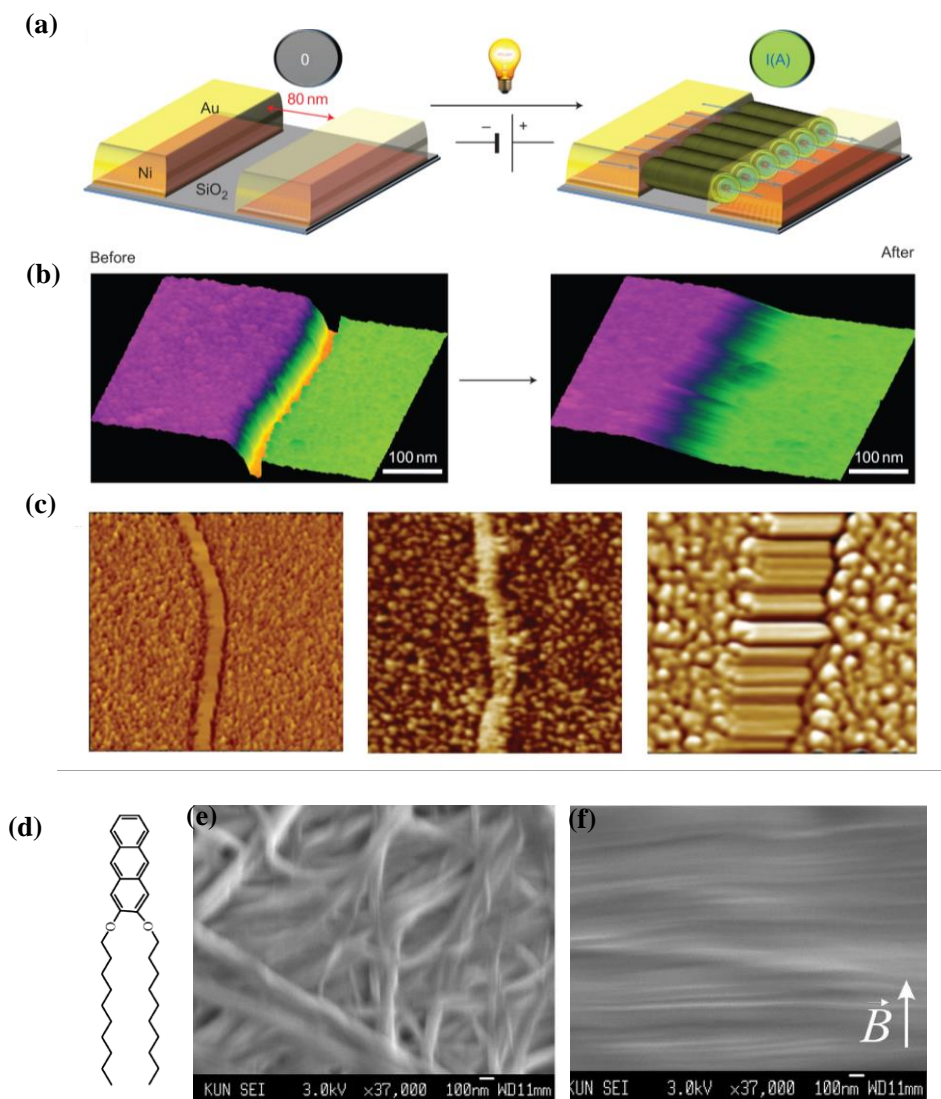


Figure 3.2. (a) Schematic representation of alignment across gold electrodes upon application of light and potential, (b) AFM image of the electrode gap before (left) and after (right) of light irradiation, (c) AFM phase images of electrode gap before [1500 x 1500 nm²](left), after [1500 x 1500 nm²](middle) and after [250 x 250 nm²](right) irradiation. (d)-(f) FE-SEM images of supramolecular fibers before and after magnetic field exposure respectively. (Figure 3.2a-c reproduced with permission from Ref. 8, Figure 3.2d-f reproduced with permission from Ref. 9).

On the question on temporally controlled growth there have been reports in inorganic minerals where few salts act as nucleation inhibiting agent thus slowing down the mineralization process.^{4,5,6} Even ice nucleation has been temporally inhibited by addition of polyvinyl alcohol and anti-freezing glycol proteins.⁷ However if one looks at soft-matter assembly or small molecule assembly along with having very few examples of temporally controlled assembly as it is, to the best of our knowledge there does not seem to be an approach where one can delay the lag phase further employing a rational strategy. Decreasing the lag phase obviously has been shown by seeding however the other way round process seems to be challenging and significant considering slower nuclei formation can be used theoretically to induce larger control structurally and functionally to the material. If one considers a simple example of aggregate alignment across an electrode (via an electric field or a magnetic field) (Figure 3.2),^{8,9} which is topic of significant importance in supramolecular electronics, it can be better exerted if the temporal growth of the aggregate is slower. This is because aligning stimuli such as electric and magnetic field would have a higher aligning response from the smaller aggregate and thus may result in aligned structures. Slow nucleation can also be helpful in hetero structure formation as nuclei would be kinetically stable for a longer time. Considering these arguments in the coming discussion we would try and achieve a delayed growth based on stimuli response of imine formation in our system.

Moving on to controlled decay of materials, one must in synthetics systems, as in biological systems, move to assemblies under non-equilibrium and dissipative assemblies. There has been a surge in research on this particular topic in recent years and new methodologies are being devised to attain such a material. Walther *et al.* have used ingenious systems where a charge based assembly is transiently formed due to dormant deactivator role played by **Urease** and lactones ((Figure 3.3a,b).^{10,11} These assemblies are charge based and do not operate on a reversible chemical reaction, therefore a nucleation elongation growth has not been identified in such systems. Ulijn *et al.* have taken the route of a bio-catalytic assembly where they clearly show the evolution of a kinetic assembly over a thermodynamic one and can be refuelled various times

as well (Figure 3.3c).¹² Considering transient nano structures work of Zhang *et al.* deserves a mention. They have coupled their polymer assembly with a well-known clock reaction $\text{IO}_3^- - \text{NH}_3\text{OH}^+ - \text{OH}^-$. The release and uptake of iodine in this system makes the polymers aggregate as iodine binds to the ethylene glycol chains rendering them hydrophobic (Figure 3.4).¹³

Considering these few examples of assembly under non-equilibrium conditions one can realise that more investigation is required into these systems. Moreover new stimuli-responsive assemblies need to be developed while expanding the horizon on chemical functionalities of these systems. The system that we have chosen is a charge transfer based aggregate as has been detailed in Chapter 2.

Apart from creating a new imine based system for transient assembly there lays a greater additional advantage. Excellent electronic properties of these charge transfer stacks have been shown by our group in past years.¹⁴ A temporally programmed decay of such as material therefore could be of excellent advantage in “Transient-electronics”.^{15,16,17} Transient electronics refers to an electronic circuit that can be destructed overtime via external stimuli (Figure 3.5). These materials find applications from military to medicinal areas. Most of these materials dissolve on thermal or a solvent induced dissolution but a material which is internally programmed with a destruction code is not known and therefore needs to be seriously analysed. It is in this respect our approach can be vital in developing a new material with great prospects. Moreover we possess an additional advantage that our assemblies can be refuelled and re-assembled with preservation of the transient nature up to a few cycle.

Considering the above discussion we would like to delve into the experiments, on our system, representing the same. We would first discuss controlled growth and then follow it up with controlled decay of supramolecular assemblies.

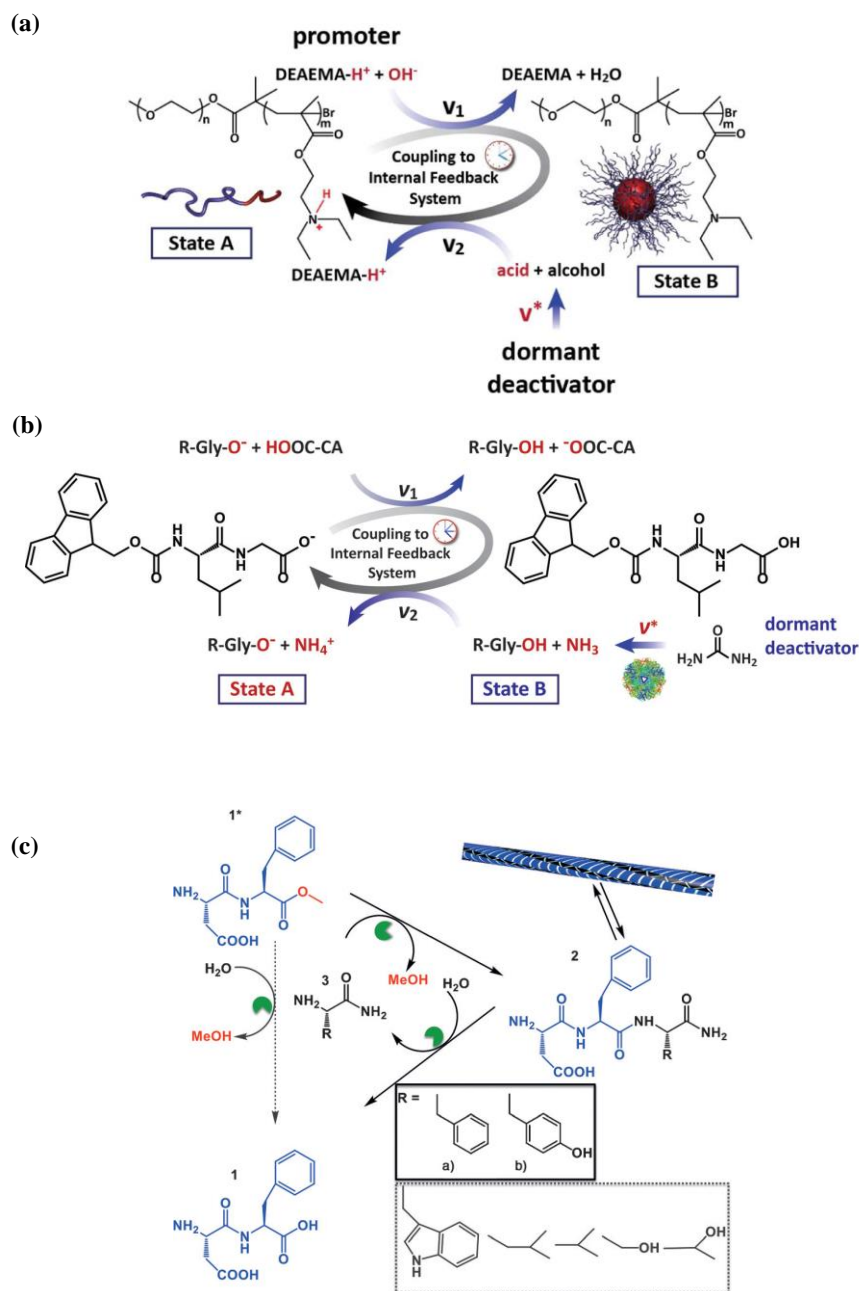


Figure 3.3. (a) Schematic representation ester hydrolysis being used as a dormant deactivator on polymer assemblies, (b) Schematic representation *Urease* being used as a dormant deactivator in small molecule assemblies and (c) Schematic representation of bio-catalytic transient assembly (Figure 3.3a-b reproduced with permission from Ref. 11,10 respectively, Figure 3.3c reproduced from with permission Ref. 12).

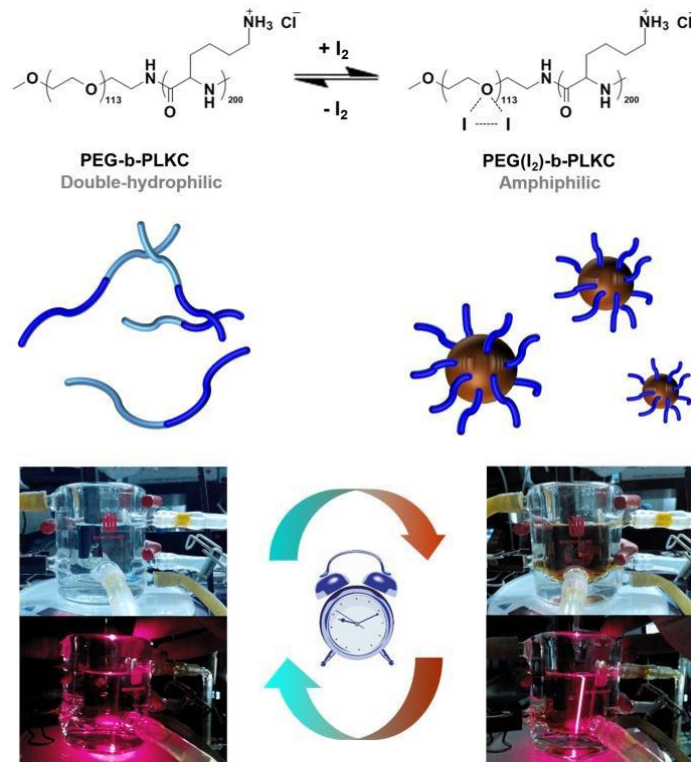


Figure 3.4. Schematic representation of dissipative polymer assemblies coupled to a clock reaction (Reproduced from with permission Ref. 13).

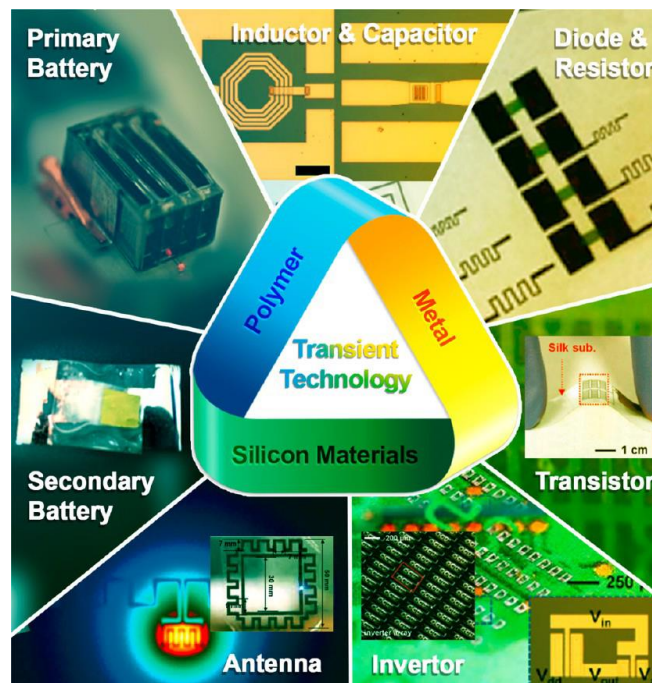


Figure 3.5. Schematic representation of areas where transient electronics finds application (Reproduced from with permission Ref. 16).

3.2. Results and Discussion

As shown in Chapter 2, imine formation is a stimuli responsive reaction (Figure 3.6a). Therefore we chose two strategies to delay growth. First being ligand dilution in which along with the self-assembling alkyl amine we add a non-assembling amine thus slowing down the nuclei formation (Figure 3.6b) (*vide infra*). Second strategy is using stimuli to gradually increase pH from neutral to basic. This in turn slows down the nuclei formation as a finite time is required to reach the activation pH (Figure 3.6c) (*vide infra*).

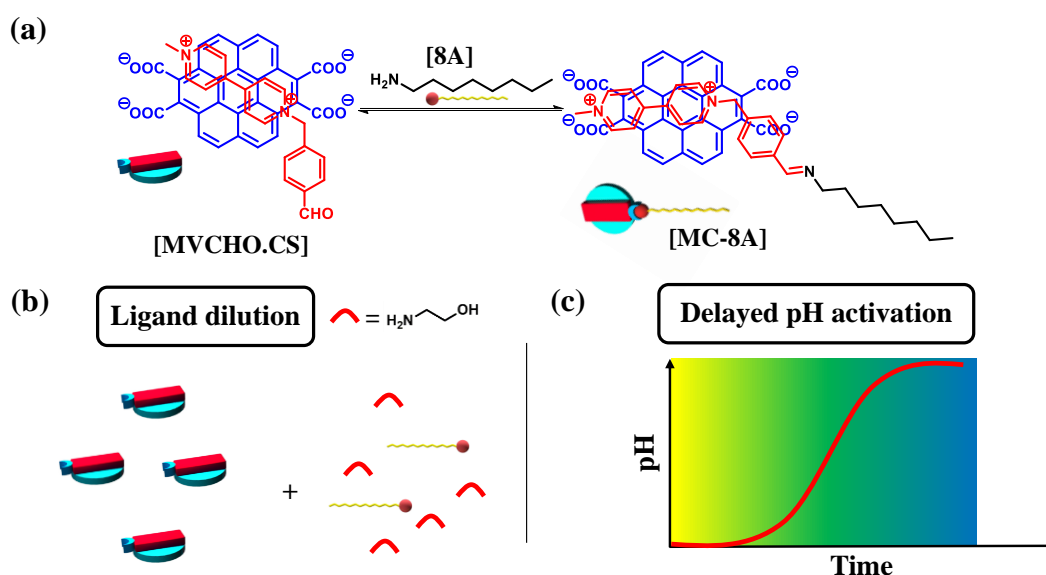


Figure 3.6. (a) Chemical equation representing the system under study, (b) schematic representation of delay in growth through ligand dilution. Small red arcs is representing ethanol amine which acts as a competitive inhibitor and (c) Schematic representation delayed pH change from neutral to basic (yellow to blue color represents neutral to basic pH changes) as a prospective tool for delayed growth.

3.2.1. Controlled Growth by Ligand Dilution

Imine bond formation has been used in through detail to explore dynamic libraries as illustrated in Chapter 2. The structural diversity of available amines allow use of various substrates in these libraries and are often put to compete in order to perturb the outcome of the ensemble.¹⁸ These outcome are mostly thermodynamic products and rarely kinetic.

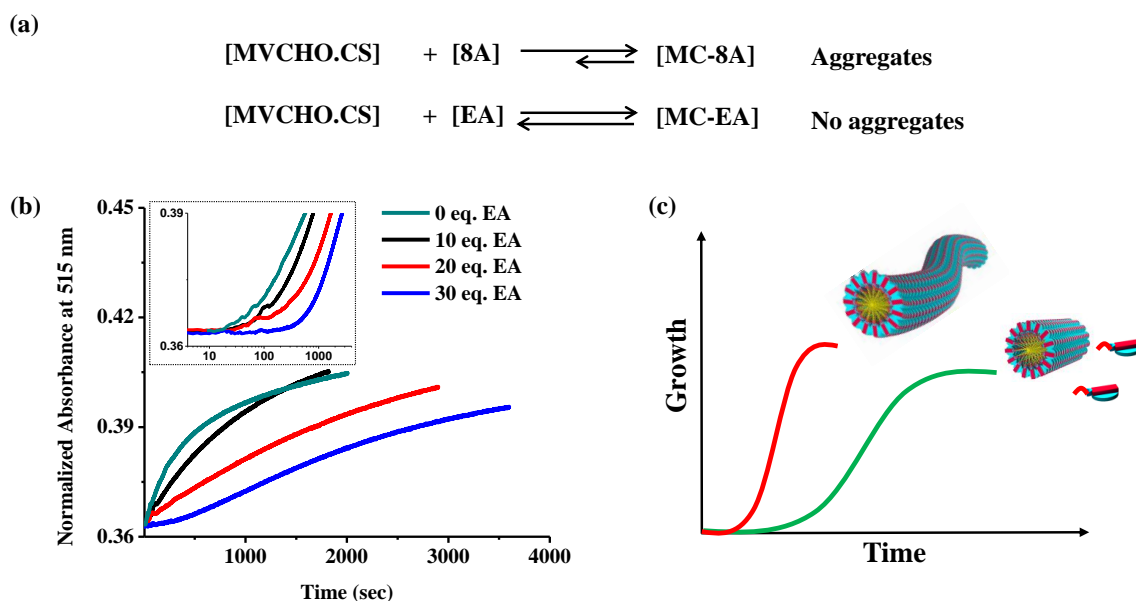


Figure 3.7. (a) Chemical equation representing the system equilibrium established due to addition of ethanol amine (EA), (b) Kinetic trace followed at 515 nm (inset: same graph on log scale to easily elucidate the change in lag phase). ($[\text{MVCHO.CS}] = 1 \text{ mM}$, $[\mathbf{8A}] = 0.5 \text{ mM}$, $\text{pH} = 11.0$, $[\text{Phosphate buffer}] = 50 \text{ mM}$) and (c) Schematic representing the ethanol amine induced scenario.

This competition of substrates is largely limited to libraries which do not form extended aggregates. Thus, considering the uniqueness of our system we hypothesized that such a competition between two amine substrates, one which is ethanol amine (EA) is traditionally higher in reactivity and is also present in ≥ 20 eq. excess compared to the second substrate and second is a *n*-octyl amine (**8A**) which self-assembles with a defined kinetics, would be an interesting experiment to follow (Figure 3.7a). In a blank sample with MVCHO.CS and 0.5 eq. of **8A** kinetics was very fast with a lag phase of 12 seconds and completion time of nearly 2000 seconds. Following this, in separate samples, we introduced various equivalents of EA ranging from 10 to 30 equivalents with respect to MVCHO.CS (20-60 equivalents with respect to **8A**) along with 0.5 equivalents of **8A**. As seen in Figure 3.7b there is a discernable slowing down in kinetics with increase of EA eqs. The lag phase changed from 12 seconds to nearly 150 seconds which corresponds to slowing down of nucleation by factor of nearly 13. We believe this slowing down is because of the fact that an additional equilibrium has been introduced in the solution with

addition of **EA** which is competing for **MVCHO.CS** population. **EA** being in excess and being more reactive consumes **MVCHO.CS** population to form **MC-EA**, however as **MC-8A** begins to form and starts to aggregate there is an attrition in **MC-EA** population which gives way to a lesser reactive product with **8A** but more energetically favourable due to aggregation which **MC-EA** cannot provide. This thus results in slower nuclei formation (Figure 3.7c). Such inhibitory completion is as mentioned earlier very common in dynamic libraries but has not been reported previously in terms of temporal control that it can exert on growth of extended aggregates thus exemplifying the simplicity and scope of development in our system.

3.2.2. Control of Growth by Delayed pH Activation

Urease is an enzyme that acts on **Urea** in presence of water to release two molecules of ammonia and one molecule of carbon dioxide. As ammonia is formed it increases the pH of the solution gradually. Apart from changing the pH the activity of **Urease** itself is pH dependent with less reactivity at pH = 4, peaking at pH = 7, and finally decaying again with further increase in pH. Therefore from acidic to neutral this change is autocatalytic as it increases the enzyme kinetics and beyond neutral it is inhibitory as the activity of the enzyme then decreases. This phenomena makes pH changes an integral part of **Urease** kinetics.

With respect to our system it is well documented and has also been shown in Chapter 2 that extent of imine formation depends largely on pH of the solution. Since in our case we use alkyl amines pKa of whom lay around at 8.3, this refers to the point that below this pH all amines are protonated and no longer available for imine formation. Above that however depending on the pH various ratios of protonated to pristine amine exist which thus decide the rate as well as the extent of reactivity. Therefore in our system an enzyme like **Urease** would be of extreme value as it would add an extra kinetics of pH change and this finite time of activation of amines would thus decide the retardation produced in the nucleation of **MC-8A** aggregates.

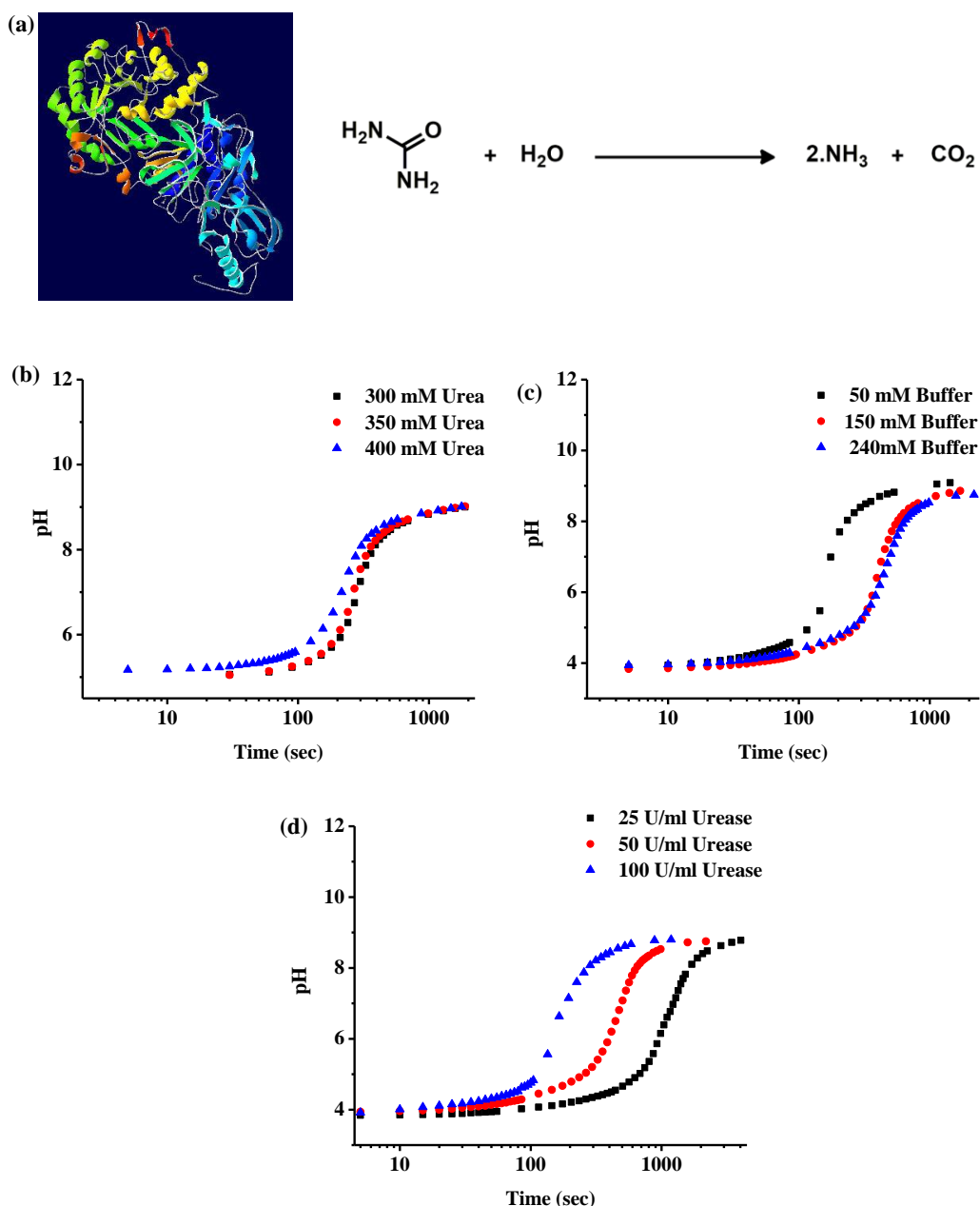


Figure 3.8. (a) Crystal structure of *Urease* accompanied by the chemical reaction representing the degradation of *Urea* by the same, (b)-(d) Kinetic pH traces (b: [*Urease*] = 50 U, 240 mM pH = 4 buffer, c: [*Urease*] = 50 U, [*Urea*] = 400 mM, pH = 4 buffer d: 240 mM pH = 4 buffer, [*Urea*] = 400 mM). (Figure 3.8a is copyrighted for free use, and has been taken from the following link <https://commons.wikimedia.org/w/index.php?curid=104129>).

However before we could start the nucleation experiments we needed to decide the solution parameters which include three main components that is concentration of **Urea**, concentration of buffer and concentration of the enzyme **Urease**. As shown in Figures 3.8b-d a systematic pH study was done with variation of these three components. Figure 3.8b shows the

variation of **Urea** concentration with buffer and **Urease** concentration kept as constant. We see that in the range that we have varied the **Urea** concentration there is neither a huge difference in kinetics nor in the final pH attained. Variation of buffer concentration (Figure 3.8c) however showed that below a critical concentration the kinetics of pH increase becomes fast (comparing 50 and 150 mM buffers).

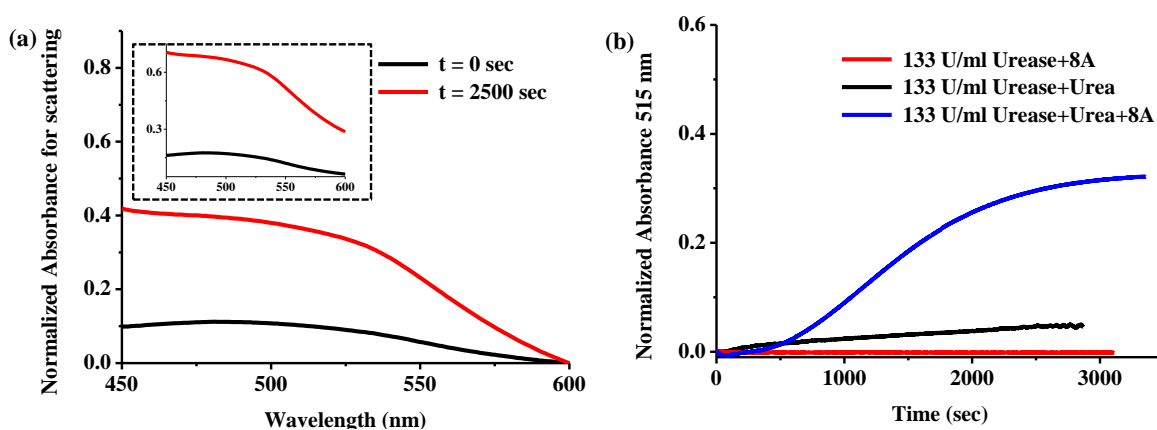


Figure 3.9. (a) UV-vis absorption spectra of [MC-8A] evolution ($[Urease] = 133\text{ U}$, $[Urea] = 400\text{ mM}$, $200\text{ mM pH} = 7$ buffer, $[MVCHO.CS] = 1\text{ mM}$, $[8A] = 5\text{ mM}$) inset shows the unnormalized UV-vis absorption spectra, (b) Kinetic traces followed at 515 nm ($[Urea] = 400\text{ mM}$, $[MVCHO.CS] = 1\text{ mM}$, $[8A] = 5\text{ mM}$, $200\text{ mM pH} = 7$ buffer).

This observation is perhaps due to the neutralization of buffer capacity by the dissolved gases such as ammonia and carbon dioxide. Since this neutralization process is basically a reaction between weak acid and a weak base such non-linear trend is manifested. The third and the final component is the variation of **Urease** (Figure 3.8d). With increasing amounts of the enzyme kinetics of pH increased consistently as expected. Moreover in the range of concentration selected there was very little difference in the final pH attained which is advantageous because of the fact that that kinetic changes that we observe would entirely be due to the enzyme activity and not due to different final pH. For our aggregation experiments **Urea** and buffer concentration was thus fixed to be 400 and 200 mM respectively. Enzyme concentration were varied from 30-133 U/ml. Starting pH was also changed from 4 to 7 as **CS** is susceptible to protonation and is not

stable in solution below that pH. Due to this fact we indeed loose a significant amount of delay time but this was necessary to ensure a comparatively homogenous starting solution.

We then proceeded to see the changes in UV absorption spectra that this **Urease** system brings about in **MVCHO.CS** solution. Figure 3.9a shows that as the pH of the solution increases a red shifted band evolves at around 520 nm which is the characteristic of aggregation. In this case we also see evolution of scattering as well which is indicated by the raised baseline of the solution. It should be noted that though is not visible in nascent final pH solution this scattering could be due a combined effect of H-bonding interaction of ammonia as well as generation of longer aggregates due to slower growth.

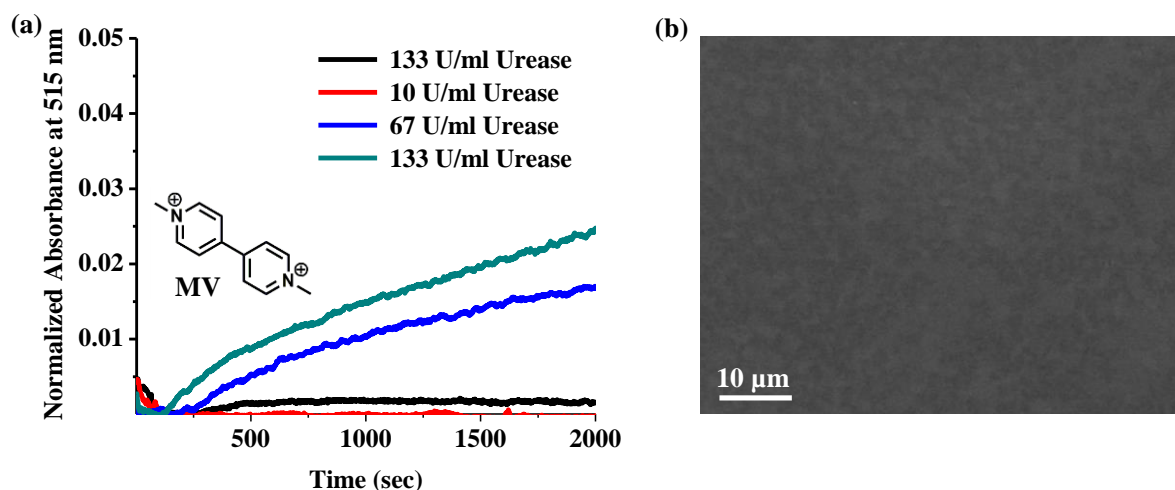


Figure 3.10. (a) Kinetic traces followed at 515 nm. Black trace represents **Urease** addition to a solution containing **MV**+**CS**+5 equivalents of **8A**. Other traces (red, green and blue) represent **Urease** addition to **MVCHO.CS**. Structure of **MV** is shown in the inset. ($[Urea] = 400 \text{ mM}$, $[MVCHO.CS] = 1 \text{ mM}$, $[8A] = 5 \text{ mM}$, $200 \text{ mM pH} = 7 \text{ buffer}$) and (b) FE-SEM image at the saturation point of the sample containing $[Urea] = 400 \text{ mM}$, $[MVCHO.CS] = 1 \text{ mM}$, $[Urease] = 133 \text{ U}$.

Though the aggregation due to imine formation is irrefutable (*vide infra*) the exact reason behind this evolution of scattering remains a hypothesis. To study the kinetics of growth of CT band we followed the 515 nm wavelength. We also carried out exclusion blanks to pinpoint the interaction of each component in the solution (Figure 3.9b). We saw no growth in the solution

devoid of **Urea**, stating that pH change is the primary reason behind this assembly and there are no secondary interaction between enzyme and **MVCHO.CS**. This also reiterated the fact that at pH = 7 there is no imine formation and hence no aggregate formation. To our surprise we saw less but not ignorable growth with a sample in which **Urea** and **Urease** were present but **8A** was absent. Significant growth was only seen in sample containing all the three components suggesting their importance in the system. Also to further elucidate the reason of growth in the sample containing **Urea** and **Urease** but devoid of **8A**, we did a systematic kinetic study (Figure 3.10). We suspected the reason behind these phenomena could be formation of small aggregates due to imine formation by a huge excess of ammonia. To strengthen this point we used **MV** (Viologen devoid of aldehyde group) instead of **MVCHO** in the solution and quite rightly did not see an aggregation clearly suggestive of the fact that aldehyde group is innately involved in this process. We varied the concentration of **Urease** in **MVCHO.CS** containing solution and saw an increasing kinetics with increase in **Urease** concentration. These experiments confirmed that these small aggregates are indeed due to imine formation between ammonia and **MVCHO.CS**. We also probed these aggregates under a field emission scanning electron microscope (FE-SEM) to see the possibility of ordered aggregates but all we could see were random depositions implying the lack of order in absence of the self-assembling agent i.e. **8A** (Figure 3.10b).

Having shown that in a multi-component system such as this there are minimal secondary interactions and side reactions. We went ahead to analyse the delayed pH activation role of **Urease** in assembly of **MC-8A**. In two different batches of study we varied the enzyme concentration as well as the equivalents of **8A** (Figure 3.11a,b). With variation of enzyme concentration we could delay the growth up to 1000 secs. This delay of course was dependent of **8A** concentration again reiterating the fact that this assembly is due to imine formation alone. Since the time course of this aggregation results in scattering so we could monitor the kinetics at a red shifted wavelength (650 nm) (Figure 3.11c). The growth kinetics obtained here also nearly matched the kinetics of CT band growth suggesting a clear dependence. We also analysed the morphology of the resulting final solution with FE-SEM. We saw arrays of long, bundled, fibers

spanning a few micro meters reiterating the linear growth model propagated in Chapter 2 (Figure 3.11d, 3.12). The arrays of fibers look dissimilar to one we got in chapter C. The reason behind is perhaps the same as the one which produces scattering and though only effects the tertiary structure is difficult to be completely understood.

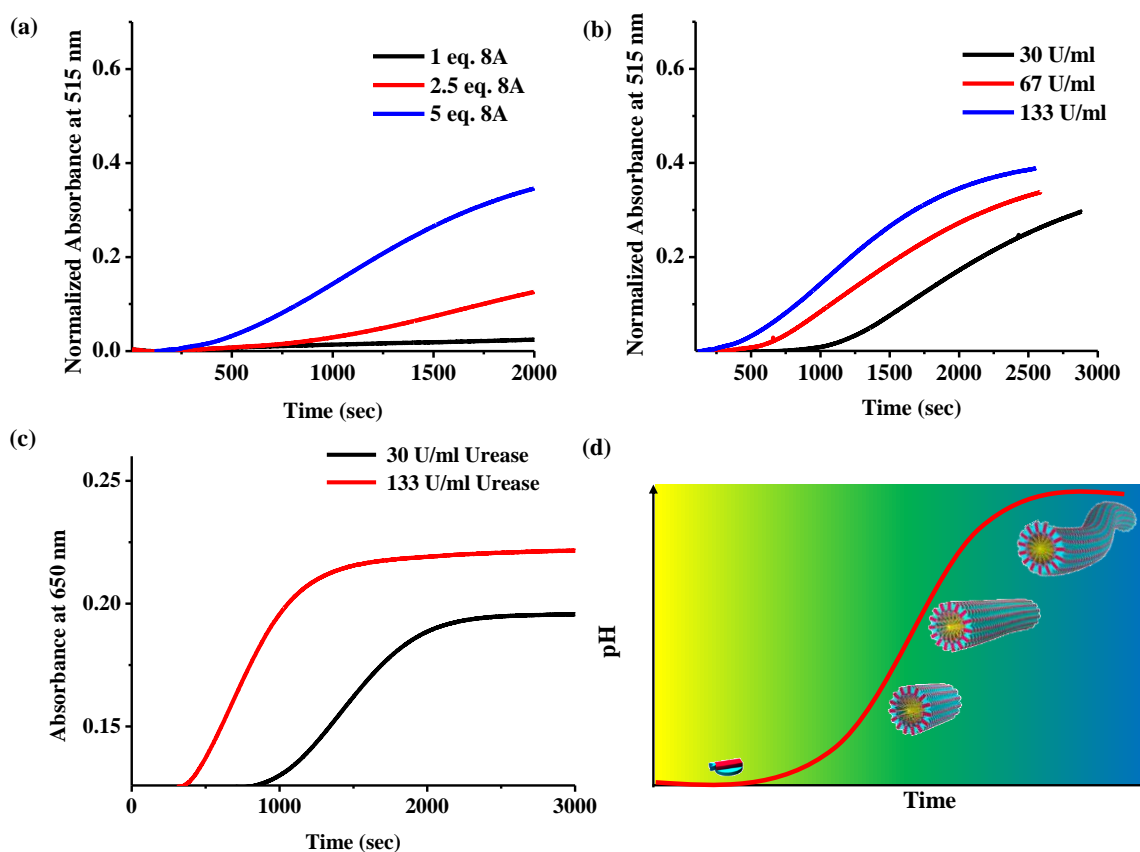


Figure 3.11. (a) and (b) Kinetic traces followed at 515 nm with variation of [8A] and [Urease] respectively. (c) Kinetic traces followed at 650 nm with variation of [Urease] (a: [Urea] = 400 mM, [MVCHO.CS] = 1 mM, [Urease] = 133 U, 200 mM pH = 7 buffer, b and c: [Urea] = 400 mM, [MVCHO.CS] = 1 mM, [8A] = 5 mM, 200 mM pH = 7 buffer) (d) Schematic representation of the scenario.

3.2.3. Controlled Decay of Supramolecular Fibers

To control the decay of our aggregates which are governed by imine formation we again took advantage of the fact that these bonds are highly pH sensitive. Thus, to disaggregate our system we need to go from basic to neutral pH. Therefore contrary to the previous section we need a

stimuli that can not only change pH gradually but also is kinetically delayed. This delay is necessary as fast immediate pH quencher would not allow any growth to occur as the time required to reach the neutral pH would be too less. Having understood the kinetics of **MC-8A** growth we therefore need a stimulus whose actions are delayed as much as to allow a finite time for growth.

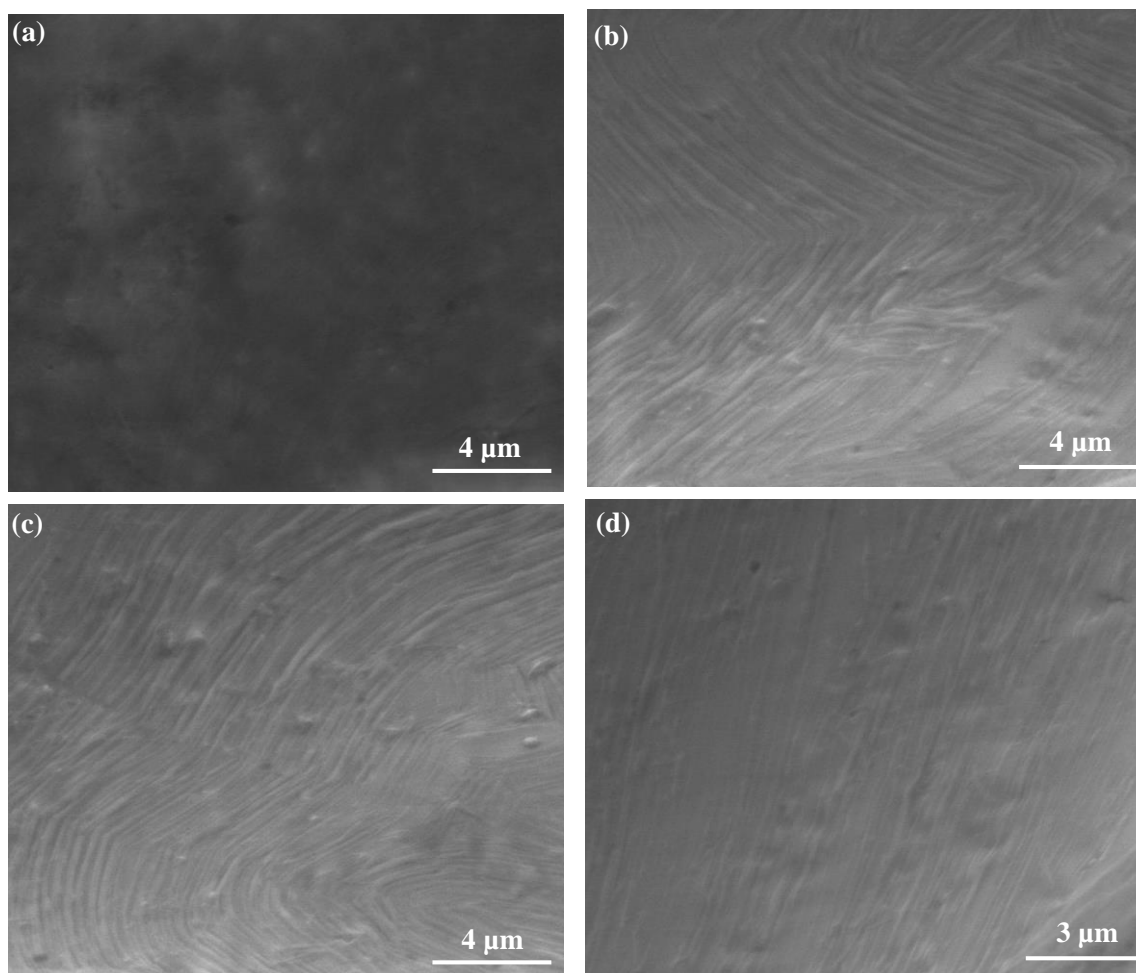


Figure 3.12. (a)-(d) FE-SEM images showing elongated linear fibers ($[Urea] = 400 \text{ mM}$, $[MVCHO.CS] = 1 \text{ mM}$, $[Urease] = 133 \text{ U}$, $[8A] = 5 \text{ mM}$, $200 \text{ mM pH} = 7 \text{ buffer}$).

To fulfil this scenario we employed use of saponification of esters as a potential stimulus (Figure 3.13a). Esters in presence of base consume hydroxyl ions to facilitate their hydrolysis into carboxylate (until the pK_a is reached) and alcohol. This consumption of hydroxyl ions thus starts decreasing the pH. Various esters hydrolyse at different rates depending on their structural and electronic constraints thus the abundance of structural diversity of esters allows us to choose from

a plethora of molecules such that the selected ester fits our kinetic requirement. Also the saponification reaction is known to be gradual which also makes it ideal for our use. In the final experiment to show the controlled decay we wish to use esters along with **8A** in a solution of **MVCHO.CS** at pH = 11.

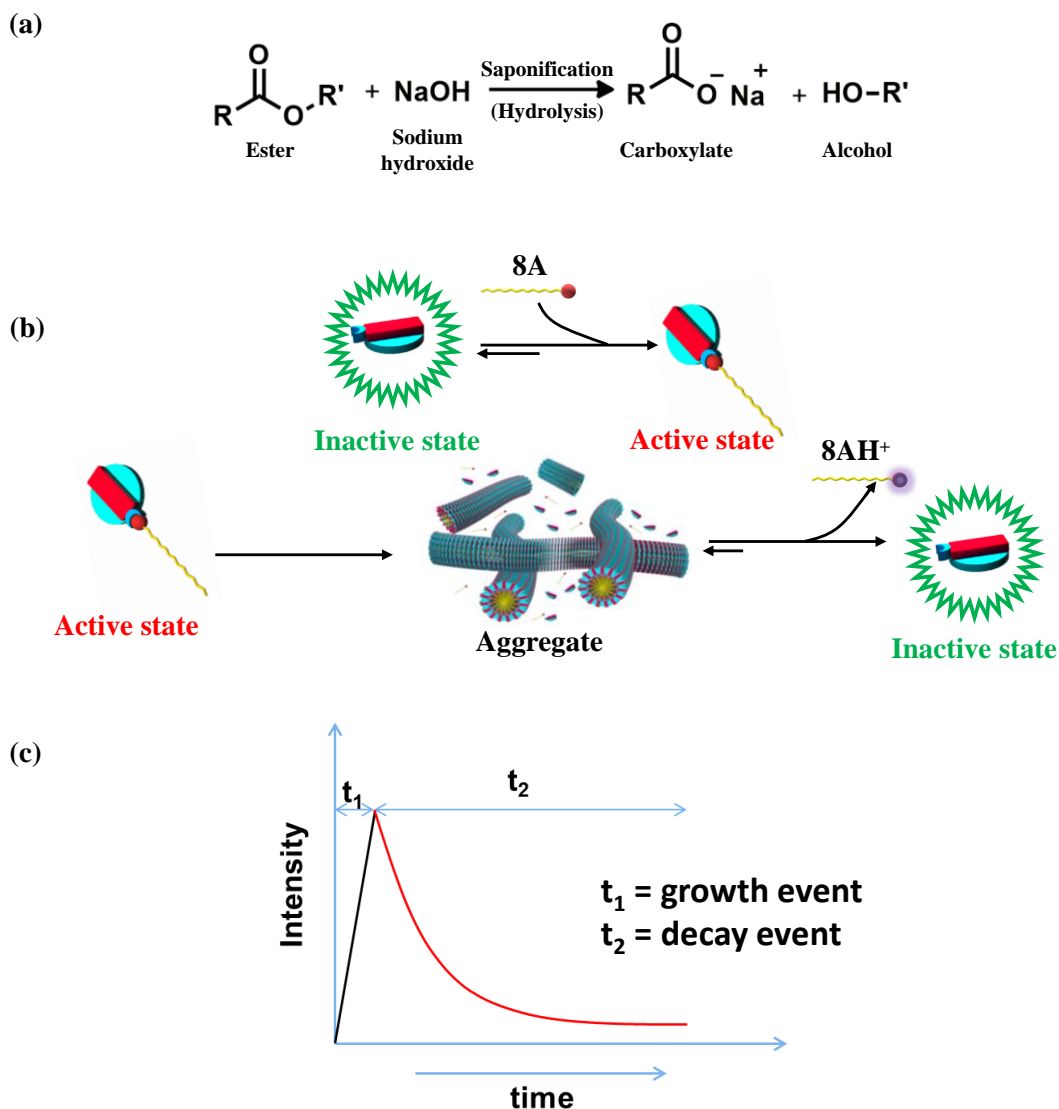


Figure 3.13. (a) Chemical reaction representing the saponification of ester, (b) Schematic representing the prospective transient aggregation and (c) schematic representing the transiency with two distinct kinetic events.

Considering the kinetic requirements are met we envisage that there would be a finite growth event before the continuously decreasing pH starts to take effect. This would thus result in a decay event producing a transiently aggregated state whose life time can thus be controlled by the

kind of ester as well as the concentration of ester (Figure 3.13 b,c). After looking at the literature we realised that among various ester that can fit our kinetic criteria,¹¹ the ones which were readily available, are gamma-Butyrolactone (γ -BL), epsilon-Caprolactone (ϵ -CL) and beta-Butyrolactone (β -BL). The pH kinetic trends of these lactones suggested that their decay was gradual and would allow us ample of time to play around with transient state lifetime (Figure 3.14).

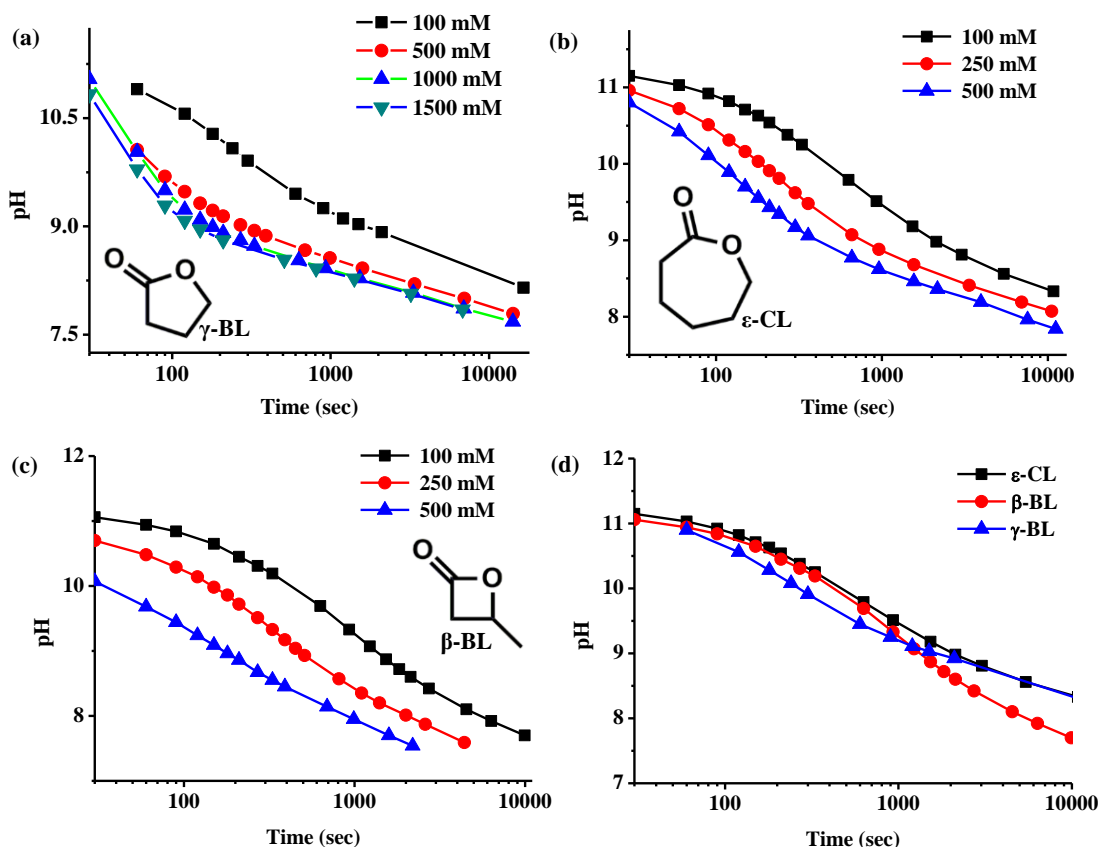


Figure 3.14. (a)-(c) Kinetic pH traces of various concentrations of different lactones (50 mM, pH = 11 buffer) and (d) Comparative pH traces of various lactones [lactone] = 100 mM.

To see the changes in the UV-vis absorption spectra we followed the kinetics and recorded individual spectra with time lapse. As a prototype the experiment was done with 500 mM of γ -BL with starting pH = 11. It can be clearly seen that the absorbance increases with the maxima shifting from 492 nm to 505 nm signifying the growth phase.

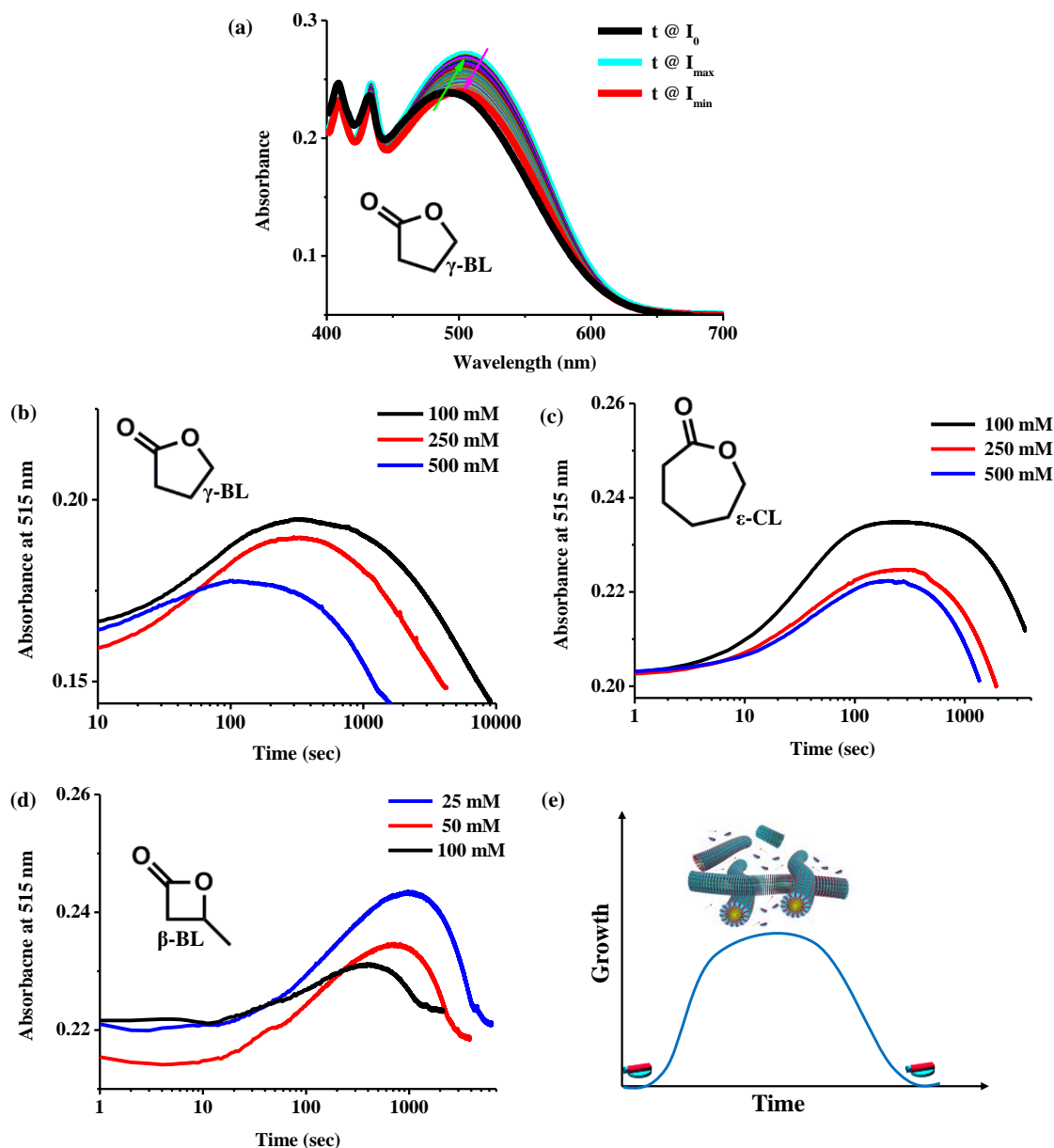


Figure 3.15. (a) UV-vis absorption spectra following the changes in CT band over time ($[\gamma\text{-BL}] = 250 \text{ mM}$), (b)-(d) Kinetic UV-vis traces followed at 515 nm of various concentrations of different lactones (50 mM, pH = 11 buffer, $[\text{MVCHO.CS}] = 1 \text{ mM}$, $[\text{8A}] = 5 \text{ mM}$) and (d) Schematic representation of the transient aggregation scenario.

Consequently it starts to decrease gradually and finally comes back to similar absorbance with maxima at 500 nm, signifying the disaggregation phase (Figure 3.15a). This process was then followed at 515 nm for all the three lactones (Figure 3.15b-e). Figure clearly suggests a growth phase and a decay phase. The life time of the decay phase varies not only with the concentration of lactones but also with the kind of lactone. For γ -BL on one hand the lifetime can

be modulated from less than 100 secs to roughly around 500 secs. However as the lactone is varied this life time can be increased to roughly 950 secs (β -BL, ϵ -CL).

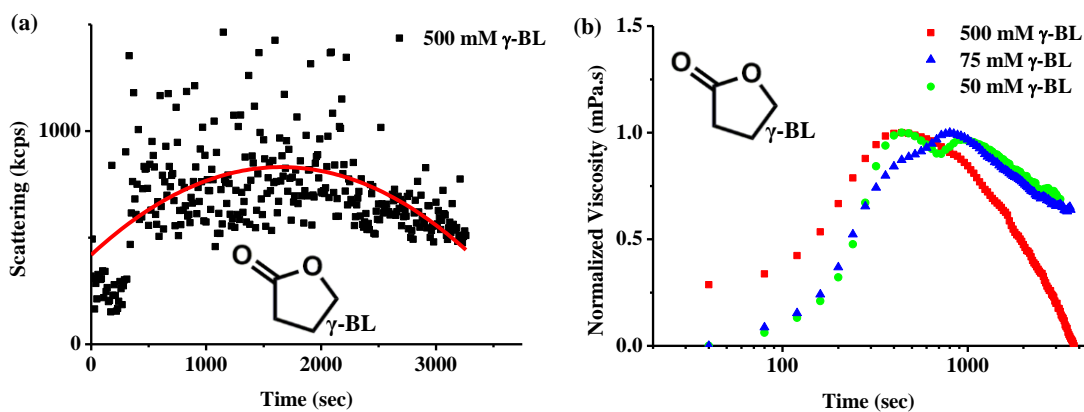


Figure 3.16. (a) Transient trace followed over time via DLS (red polynomial fit to follow the eye) ($[\gamma\text{-BL}] = 500 \text{ mM}$, 50 mM , $\text{pH} = 11$ buffer, $[\text{MVCHO.CS}] = 1 \text{ mM}$, $[\text{8A}] = 5 \text{ mM}$), and (b) Transiency followed via viscosity measurement various concentrations of $\gamma\text{-BL}$ (50 mM , $\text{pH} = 11$ buffer, $[\text{MVCHO.CS}] = 1 \text{ mM}$, $[\text{8A}] = 5 \text{ mM}$).

Having already mentioned that lifetime of lactone depends on both structural and electronic factors, one can see the correlation of pH traces with the transient lifetime achieved by various lactones. ϵ -CL for example is the slowest hydrolysing lactone and thus has highest transient life time. Within β -BL and γ -BL the pH kinetic is non-trivial as the former is faster before $\text{pH} = 9$ but falls down drastically after that as compared to γ -BL. These two opposing factors perhaps play a complex role in the growth kinetics as in β -BL even though the onset is late the lifetime is still comparable to γ -BL.

Having established that the transient growth can be achieved we followed the same process with dynamic light scattering (DLS) and viscosity measurements (Figure 3.16). The experiments were done on solutions containing γ -BL as a model lactone. Both scattering and viscosity measurements reiterated the trend of a transient behaviour with the lifetime of the transient sample being clearly varying with varying concentrations of the lactone.

Having established the transiency of the aggregates we went on ahead to see the possibility of refuelling assemblies. We envisaged that since the decay is due to protonation of the alkyl amine

and introduction of few microliters of Conc. NaOH solution might refuel the ensemble towards another cycle of transiency (until the lactone is exhausted) (Figure 3.17).

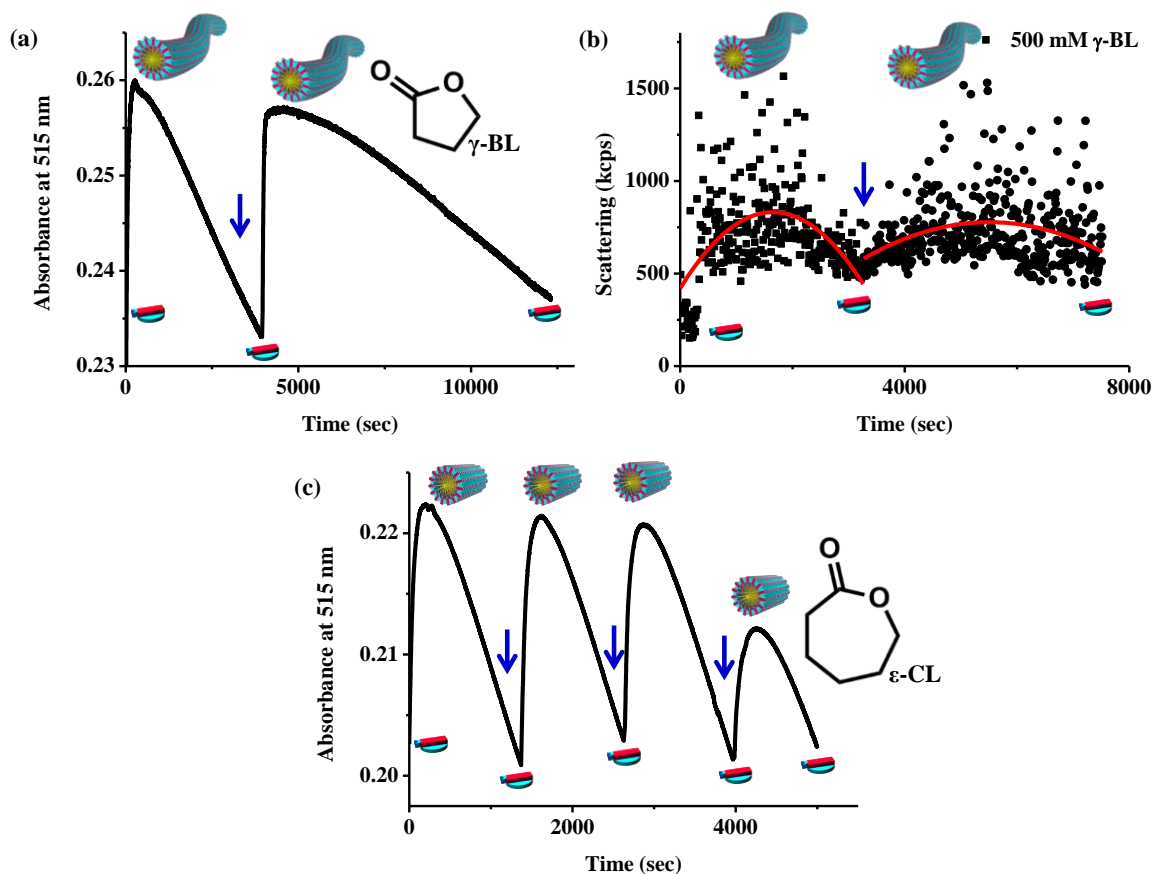


Figure 3.17. (a) and (b) Transient refueling traces followed over time via UV-vis (515 nm) and DLS (red polynomial fit to follow the eye, blue arrow indicates conc. NaOH addition) ($[\gamma\text{-BL}] = 100 \text{ mM}$, 50 mM $\text{pH} = 11$ buffer, $[\text{MVCHO.CS}] = 1 \text{ mM}$, $[\text{8A}] = 5 \text{ mM}$), and (c) Transient refueling traces followed over time via UV-vis (515 nm) (blue arrow indicates conc. NaOH addition) ($[\epsilon\text{-CL}] = 500 \text{ mM}$, 50 mM $\text{pH} = 11$ buffer, $[\text{MVCHO.CS}] = 1 \text{ mM}$, $[\text{8A}] = 5 \text{ mM}$).

We performed this experiment with 100 mM of γ -BL and 500 mM of ϵ -CL to signify the various lifetimes and cycles of transiency that can be achieved. In case of 100 mM of γ -BL 31.25 μl of 1.6M NaOH was introduced at the point signified by the blue arrow in the figure. The process was monitored by UV-vis (at 515 nm) as well as DLS. Both UV and DLS trends clearly show that indeed these assemblies can be refurbished and once revived again undergo controlled decay. The first cycle is clearly faster than the second one. We hypothesize this is due to the concentration of lactone has decreased from the initial point as we saw previously a decreased

concentration results in slower transient cycle. For 500 mM of ϵ -CL we used 5 μ l of 1.6 M NaOH as the refuelling agent and indeed due to the faster kinetics we could go up to four cycles of transient assemblies. The fourth cycle however has lesser amplitude and also is slightly slower as compared to previous cycles. This again could be due to consumption of lactone and an added fact that same amount of NaOH cannot revive the same amount of amines as the shear consumption of hydroxyl ions pile up.

3.3. Conclusion and Outlook

In this chapter the advantage of imine governed assemblies comes to the foray. The innate stimuli responsiveness of imine bonds can be innovatively utilized to attain a variety of novel properties that were previously either not explored or limited to only a few systems. We show for the first time that kinetics of aggregate formation can be inhibited by competition dynamics and also be controlled via a bio-catalytic route. Time span of the nuclei has been a major concern in temporal nucleation elongation assembly due to which most of the compounds are discarded for the purpose. A modulation of the lag phase and particularly slowing it down by more than a factor of 80 can therefore be considered quite optimistic for the development of future materials. Along with controlled growth we also showed that these aggregates can be made transient and thus a dissipative assembly of these molecules is also possible. As discussed earlier a handful of materials show such a property and brings us closer in mimicking nature on dynamically instable systems. We show that not only the lifetime of these aggregates under non-equilibrium can be completely programmed they can also be refuelled with restoration of the transient behaviour as well.

Thus we believe, considering the various available stimuli and dynamic bonds currently at ones disposal, that this chemistry of alkyl amine fuelled self-assembly opens various avenues for further research in quest of novel applicability as well as closer biological mimicry both of which are necessary for further advancements in capabilities of supramolecular chemistry.

3.4. Experimental Section

General Methods:

Optical Measurements: Electronic absorption spectra were recorded on a Perkin Elmer Lambda 900 UV-Vis-NIR Spectrometer.

Dynamic light scattering (DLS) Experiments: The measurements were carried out using a NanoZS (Malvern UK) employing a 532 nm laser at a back scattering angle of 173°. The samples were measured in a 10 mm glass cuvette. A dead time (Time between sample loading and starting of measurement by the machine) of around 45 seconds is present in all measurements.

Field Emission Scanning Electron Microscopy (FE-SEM). FE-SEM measurements were performed on NOVA NANO SEM 600 (FEI) operated at 15 kV, by drop casting the solution on glass substrate. All samples were recorded in low vacuum mode (FE-SEM).

Viscosity Measurements: Viscosity measurements were performed on Anton Paar MCR 302 rheometer (air bearing). The measuring system was CP50-1 and the measuring cell configuration was P-PTD 200/80/Air. The gap between the surface and cone plate was 0.101 mm. Viscosity was measured over time at a constant shear rate of 50 Hz. Temperature was kept constant at 25 °C. A dead time (Time between sample loading and starting of measurement by the machine) of around 180 seconds is present in all measurements.

pH Measurements: pH was measured by Malvern control dynamics pH meter. pH values were recorded manually at defined time periods and then plotted into trends.

Materials: Ethanol amine, gamma-Butyrolactone (99%), epsilon-Caprolactone (97%) and beta-Butyrolactone (98%) were procured from Sigma Aldrich. Urea and Urease (From kidney beans, 380 U/mg) was ordered from SRL. *n*-Octyl amine was procured from Spectrochem. All the chemicals were not further purified and used as such. Acetate and phosphate buffer solutions of various pHs was made according to the reported protocol.¹⁹

Synthesis: Synthesis of **MVCHO** has been reported in Chapter 2. **CS** and **MV** were synthesized according to the reported procedures and sufficiently characterized.^{20,21}

3.5. References and Notes

1. Alon U. *An Introduction to Systems Biology: Design Principles of Biological Circuits* 2006, Chapman and Hall publishers.
2. Bamberg J. R.; Bernstein B. W. *F1000 Biology reports* 2010, **2**, 62.
3. Hall A. L.; Warren V.; Dharmawardhane S.; Condeelis J. J. *Cell Biol.* 1989, **109**, 2207.
4. Thieme K.; Rüssel C. *J. Eur. Cer. Soc.* 2014, **34**, 3969.
5. Li L.; Buchet R.; Wu Y. *Anal. Biochem.* 2008, **381**, 123.
6. Benton W. J.; Collins I. R.; Grimsey I. M.; Parkinson G. M.; Rodger S. A. *Faraday Discuss.* 1993, **95**, 281.
7. Congdon T.; Dean B. T.; Kasperczak-Wright J.; Biggs C. I.; Notman R.; Gibson M. I. *Biomacromolecules* doi: 10.1021/acs.biomac.5b00774.
8. Faramarzi V.; Niess F.; Moulin E.; Maaloum M.; Dayen J.-F.; Beaufrand J.-B.; Zanettini S.; Doudin B.; Giuseppone N. *Nat. Chem.* 2012, **4**, 485.
9. Shklyarevskiy I. O.; Jonkheijm P.; Christianen P. C. M.; Schenning A. P. H. J.; Del Guerzo A.; Desvergne J.-P.; Meijer E. W.; Maan J. C. *Langmuir* 2005, **21**, 2108.
10. Heuser T.; Weyandt E.; Walther A. *Angew. Chem. Int. Ed.* 2015, **54**, 13258.
11. Heuser T.; Steppert A.-K.; Lopez C. M.; Zhu B.; Walther A. *Nano Lett.* 2015, **15**, 2213.
12. Pappas C. G.; Sasselli I. R.; Ulijn R. V. *Angew. Chem. Int. Ed.* 2015, **54**, 8119.
13. Wang G.; Tang B.; Liu Y.; Gao Q.; Wang Z.; Zhang X.; *Chem. Sci.* 2016, **7**, 1151.
14. Sagade A.; Rao K. V.; George S. J.; Datta A.; Kulkarni G. U. *Chem. Commun.* 2013, **49**, 5847.
15. Park C. W.; Kang S.-K.; Hernandez H. L.; Kaitz J. A.; Wie D. S.; Shin J.; Lee O. P.; Sottos N. R.; Moore J. S.; Rogers J. A.; White S. R. *Adv. Mater.* 2015, **27**, 3783.

16. Fu K. K.; Wang Z.; Dai J.; Carter M.; Hu L. *Chem. Mater.* 2016, doi:10.1021/acs.chemmater.5b04931.
17. <http://www.gizmag.com/transient-materials-dissolve-when-triggered/31540/>
18. Belowich M. E.; Stoddart J. F. *Chem. Soc. Rev.* 2012, **41**, 2003.
19. <http://delloyd.50megs.com/moreinfo/buffers2.html>
20. Ghosh A.; Rao K. V.; George S. J.; Rao C. N. R.; *Chem. Eur. J.* 2010, **16**, 2700.
21. Rao K. V.; Jayaramulu K.; Maji T. K.; George S. J. *Angew. Chem. Int. Ed.* 2010, **49**, 4218.

Chapter 4

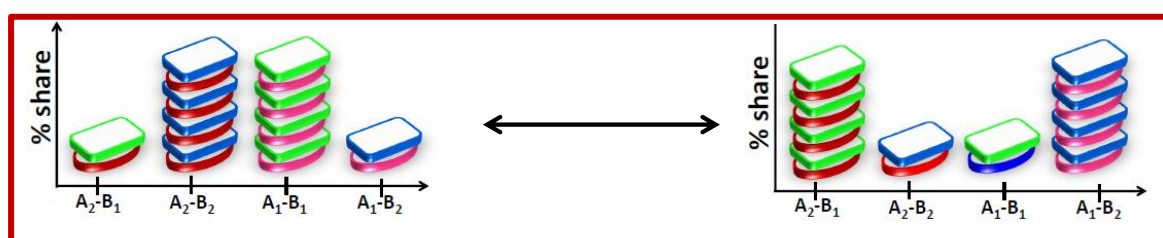
***Aggregation Controlled Rearrangement of an Ensemble
Containing Non-covalent Charge Transfer Stacks***

Chapter 4

Aggregation Controlled Rearrangement of an Ensemble Containing Non-covalent Charge Transfer Stacks

Abstract

Biological systems and nature in general works in ensembles with their components under constant rearrangement based on the external driving factors. Aggregation is another ubiquitous characteristic of such systems and is a requirement for fulfillment of various functions. We in this work show that in an ensemble of synthetic systems which are non-covalently bound, aggregation can be a deciding factor in tipping the equilibrium towards rearrangement and hence enrichment of the desired product. Using charge transfer interaction for non-covalent stacks and supramolecular amphiphile approach as an aggregating drive we show that in a prototype [2x2] such a reconfiguration of an ensemble is indeed possible.

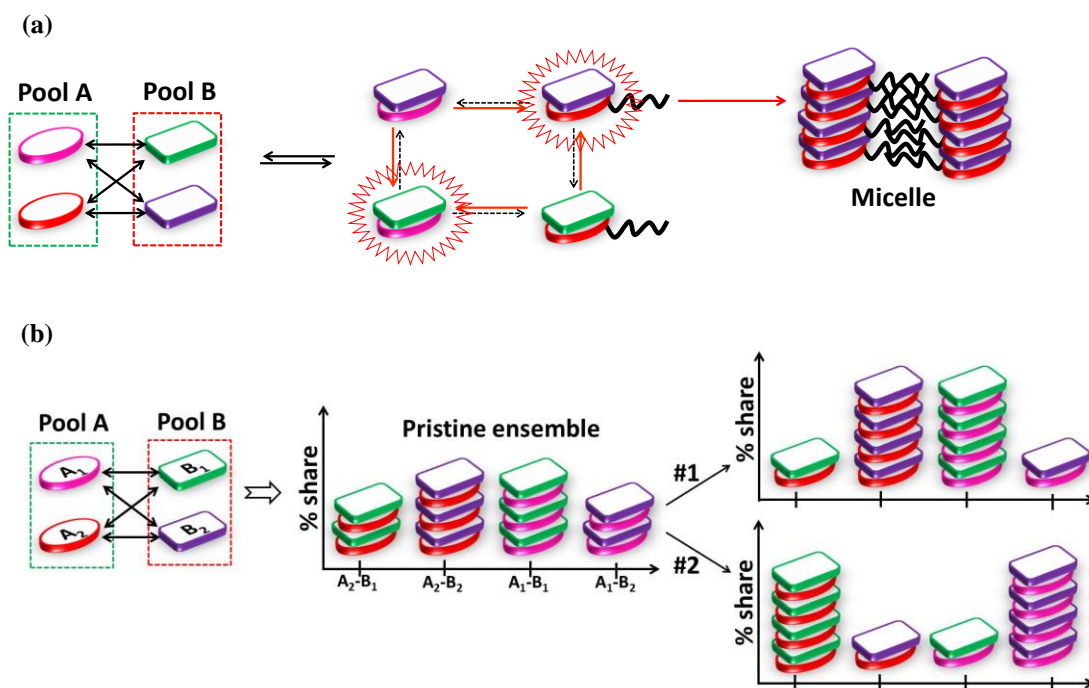


4.1. Introduction

Aggregation of molecular systems as a phenomenon has been under study for decades and its new facets are still being gradually uncovered.^{1,2,3} One of the many avenues that are being probed is the effect of aggregation on an ensemble. There have been inspiring breakthroughs resulting in understanding the role aggregation plays in stabilizing a particular product in an ensemble of rotaxane forming molecules, formation of a dynamic oligomer of conjugated molecules and even biasing the enzymes towards reversed hydrolysis.^{4,5,6} These works draw inspiration from adaptive biological ensembles, few examples of which are lipid rafts and bovine serum albumin aggregates.^{7,8} In both of the above mentioned biological processes aggregation serves as a functional tool that drives reaction equilibrium of supramolecular ensemble. However synthetic systems that have been able to study supramolecular ensembles are either controlled by their covalent connectivity or are discrete/dimeric host guest complexes and an extensive study of ensembles of extended supramolecular assemblies have not been possible.^{9,10} There have been various approaches to analyze an ensemble and the effort to resolve them becomes complex as the number of parameters increase.^{11,12} Another major factor responsible for this is the difficulty of analysis that extended supramolecular assemblies bring about, unlike the use of HPLC and NMR that covalent and discrete host guest driven ensembles respectively. In this work the difficulty of analysis has been circumvented by using various charge-transfer (CT) pairs such that their band gap tuning provides us with differential absorption signatures and hence a direct route for analysis.

On a more mechanistic point to control an ensemble one needs to come up with a strategy to decrease the free energy (ΔG) of one of the components and hence let the equilibrium enrich it.¹³ In this respect, aggregation has been used in dynamic systems earlier to converge to a thermodynamic minimum in an ensemble. In biological systems as well aggregation controlled equilibrium are fairly evident. In this context for synthetic systems, to the best of our knowledge, a rearrangement of a dynamic non-covalent aggregate ensemble has not been attempted.

4.2. Results and Discussion



Scheme 4.1. (a) Schematic presenting the enrichment of an ensemble component via supramolecular amphiphile approach and (b) schematic representation of ensemble reconfiguration.

In this work we investigate the possibility to have a control over a [2x2] ensemble of non-covalent aggregates. The term “control over an ensemble” here refers to the ability to control the major and minor products of the ensemble i.e. the ability to increase the share of the major products or on the other side of spectrum make the minor products the major one (Scheme 1a). The initial criterions should be however that the non-covalent interaction we choose must be dynamic and we should be able to stabilize a given component without changing its mode of binding. For this purpose the non-covalent dynamic interaction we chose is the charge transfer (CT) interaction. The prime reasons for this choice being the well documented dynamic nature of the CT molecules and their ability to serve as directed agents of one dimensional self-assembly. Also, molecules showing CT interaction can be made to aggregate without significantly changing their binding mode via a supramolecular amphiphile approach (Scheme 1b).¹⁴ Supramolecular amphiphiles are defined as amphiphiles generated through non-covalent bonding of two or more components. In

our case supramolecular amphiphiles are generated by non-covalent association of electron donor amphiphilic electron acceptor as a proof of concept we took a [2x2] ensemble comprising of two electron acceptors methyl viologen and dicationic naphthalene dimide (**MV**, **NDI-dc**) and two electron donors coronene salt and perylene salt(**CS**, **PS**) respectively (Figure 4.1a). Electron acceptors have their amphiphilic counterparts (**MV-12**, **MV-16** and **NDI-8**) (Figure 4.1a) which would be employed in the ensemble without the parent molecule to study the effect of aggregation on ensemble percentages. Moreover to solve an ensemble one needs to get a good approximation of individual components formed which had been rather difficult in non-covalent aggregates as neither NMR nor HPLC, which have proven indispensable in previously studied ensembles, can be used to good effect. Keeping the above point in mind we choose the CT pairs such that there is good exclusivity in their absorption spectra. Thus, at concentrations (10^{-3} M) where very less free molecules are present ($\leq 1.5\%$) i.e. almost all molecules participate in CT interactions; a simple absorption measurement at an exclusive wavelength will give an estimation of one of the components and hence solving the complete ensemble (Figure 4.1b,c). Another major criterion that needs to be adhered to is that the 4 combinations of CT pairs possible in this [2x2] matrix must be narcissistically self-sorted aggregates. Various studies suggesting this criterion have been performed and pointed out in the text as and when required (*vide infra*). All the molecules were synthesized according to previously reported procedures.

Before going into the [2x2] matrix we need to get estimation about the association and dynamic characteristics of individual pairs. Therefore first we performed titration experiments for each CT pair. To a given concentration of electronic donors (**CS**, **PS**), various equivalents of electronic acceptors (**MV**, **NDI-dc**) were added and the quenching in emission of **CS** and **PS** were monitored in individual case. This profile of emission was fit to a 1:1 binding model giving the association constants (Figure 4.2-4.6).¹⁵

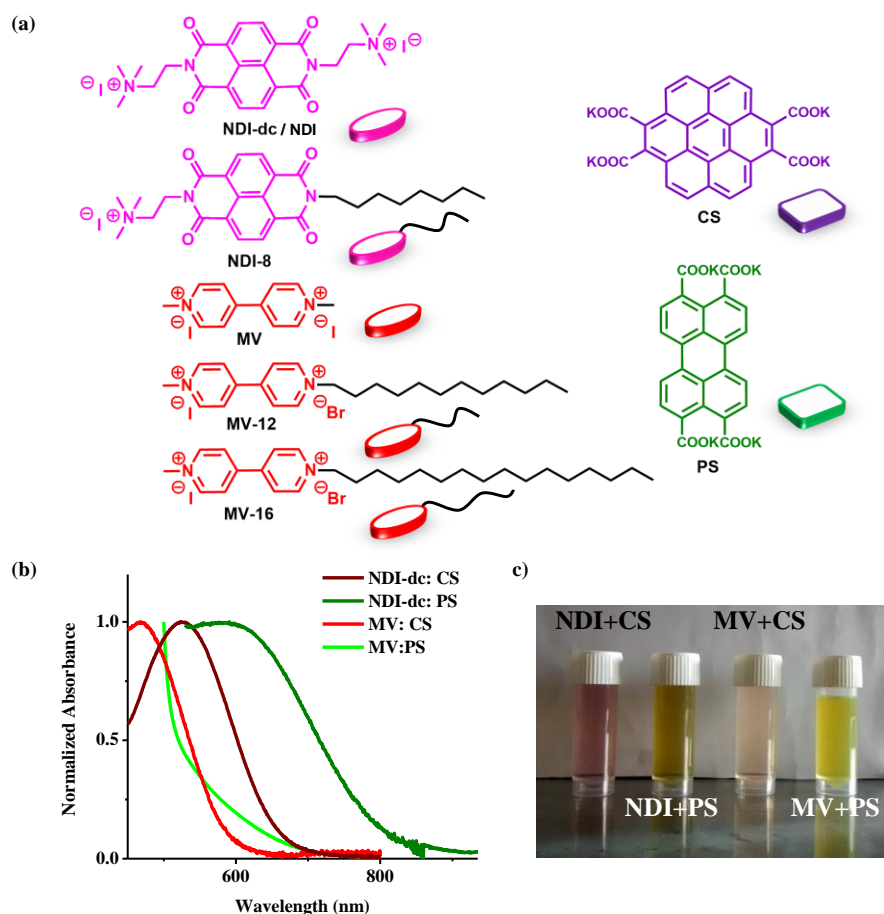


Figure 4.1. (a) Molecular structure of electron acceptors and donors under study (b) Normalized UV-vis absorption spectra of CT bands from the combination of CT pairs and (c) Photograph of various CT solutions.

The values of association constants suggests that among the nascent pool (no amphiphilic structures) **NDI-dc-CS** is the best CT pair ($3 \times 10^6 \text{ M}^{-1}$) followed by **MV-CS** ($1 \times 10^6 \text{ M}^{-1}$), **NDI-dc-PS** ($2.5 \times 10^5 \text{ M}^{-1}$) and lastly **MV-PS** ($5.9 \times 10^4 \text{ M}^{-1}$). The result also suggests that among the nascent pool of **NDI-dc** is the best acceptor and **CS** the best donor and alternatively **MV** and **PS** are worst acceptor and donors respectively.

Furthermore if one were to hypothesize a [2x2] mixture containing **NDI-dc**, **MV**, **CS** and **PS** based on the association capabilities and the fact that the pairs narcissistically self-sort (*vide infra*) one can predict that **NDI-dc-CS** would have the major share in that ensemble.

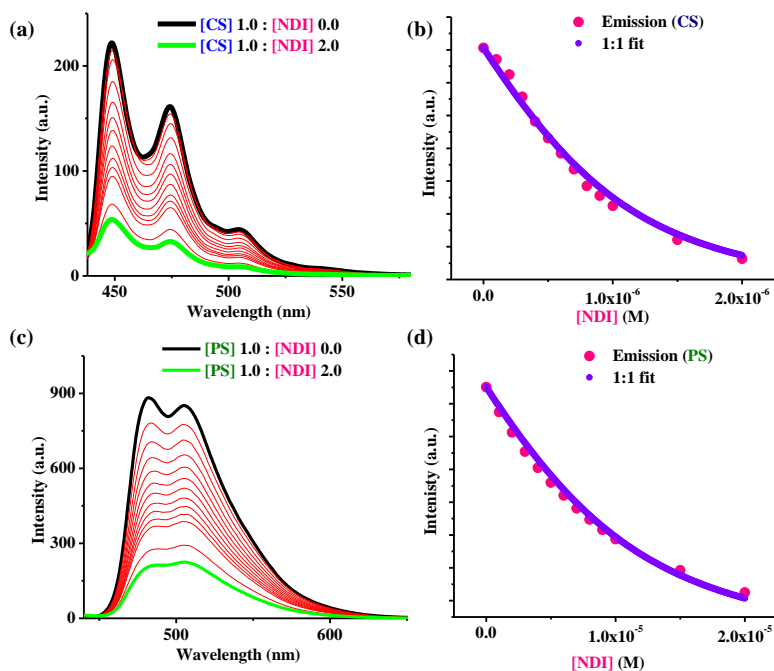


Figure 4.2. (a) and (c) are the emission spectra following the quenching curves, in a) $[CS] = 10^{-6}$ M with various equivalents of **NDI-dc** and in (c) $[PS] = 10^{-5}$ M, with various equivalents of **NDI-dc** ($l = 2$ nm). (b) and (d) follow the quenching trend for (a) and (c) respectively.

The other compositions of the ensemble are not trivial to predict based on association constants as in an ensemble they can be affected by agnostic and antagonistic relations.¹⁶ We also performed titration experiments between donors (**CS**, **PS**) and amphiphilic acceptors (**MV-12**, **MV-16**).

The association constants obtained for **MV-12-CS** and **MV-16-CS** ($3.8 \times 10^6 \text{ M}^{-1}$ and $4 \times 10^6 \text{ M}^{-1}$ respectively) suggested that indeed the amphiphilic nature had the capability to increase the binding affinity compared to nascent **MV-CS**. Moreover in [2x2] ensembles containing amphiphile counterparts of **MV** $\{(\text{MV-12,NDI-dc,CS,PS})$ and $(\text{MV-16,NDI-dc,CS,PS})\}$ the percentage binding of **CS** to the **MV** moiety can tip off its binding to the **NDI** as $K_a(\text{MV-16-CS})$ and $K_a(\text{MV-12-CS})$ is greater than $K_a(\text{NDI-dc-CS})$.

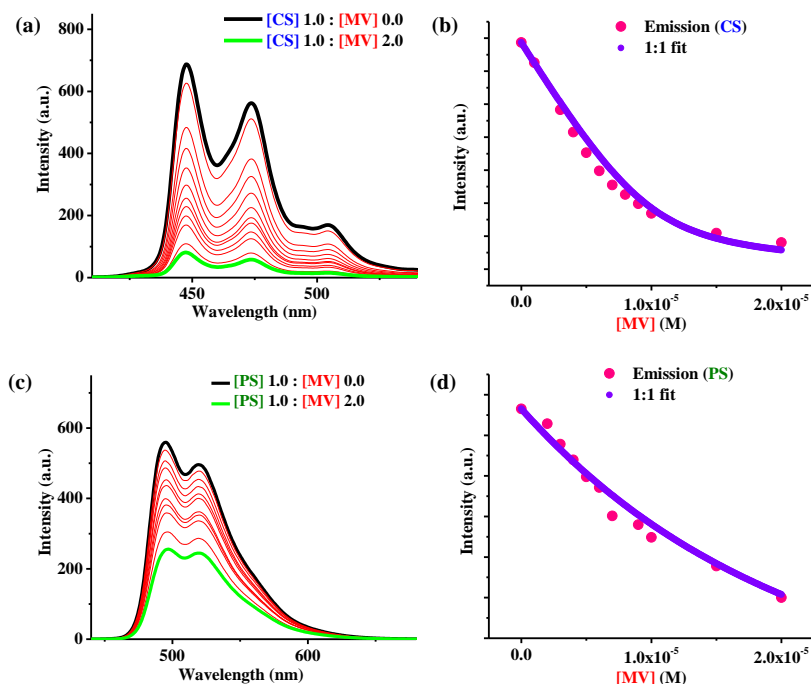


Figure 4.3. (a) and (c) are the emission spectra following the quenching curves, in a) $[CS] = 10^{-5} M$ with various equivalents of MV and in (c) $[PS] = 10^{-5} M$, with various equivalents of MV ($l = 2$ mm). (b) and (d) follow the quenching trend for (a) and (c) respectively.

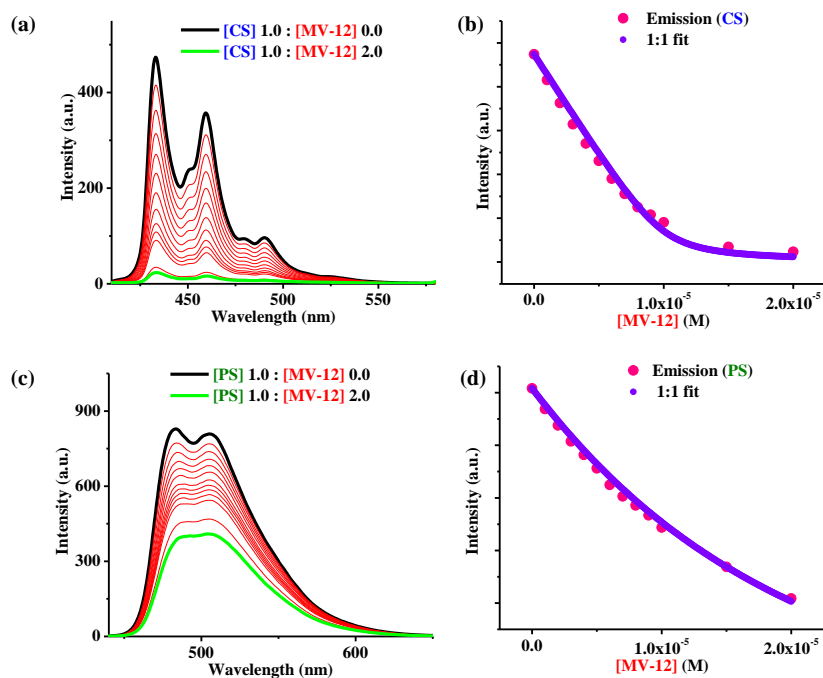


Figure 4.4. (a) and (c) are the emission spectra following the quenching curves, in a) $[CS] = 10^{-5} M$ with various equivalents of MV-12 and in (c) $[PS] = 10^{-5} M$, with various equivalents of MV-12 ($l = 2$ mm). (b) and (d) follow the quenching trend for (a) and (c) respectively.

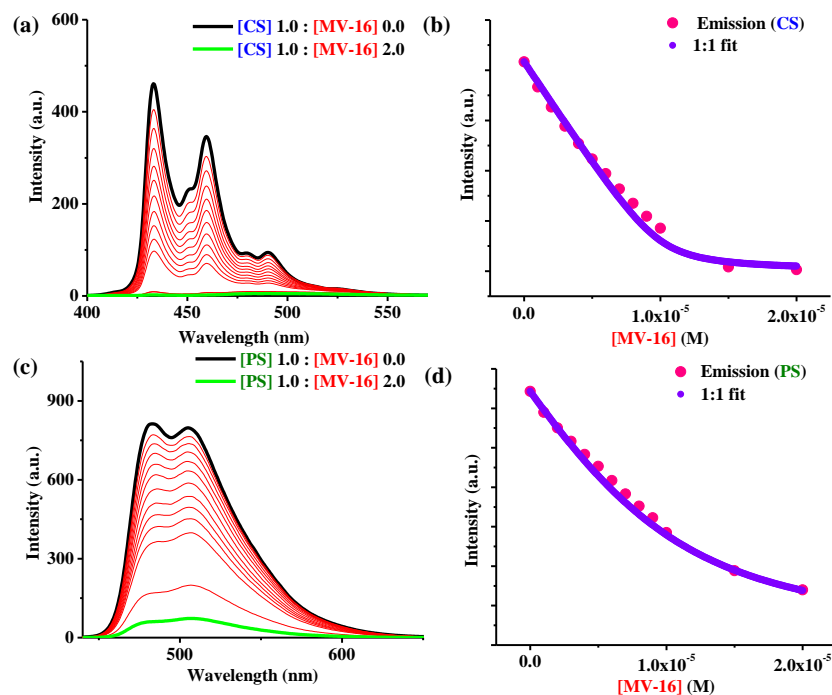


Figure 4.5. (a) and (c) are the emission spectra following the quenching curves, in a) $[CS] = 10^{-5} M$ with various equivalents of **MV-16** and in c) $[PS] = 10^{-5} M$, with various equivalents of **MV-16** ($l = 2 \text{ mm}$). (b) and (d) follow the quenching trend for (a) and (c) respectively.

CT pairs	$K_a (M^{-1})$	CT pairs	$K_a (M^{-1})$
NDI:CS	3×10^6	MV-12:CS	3.8×10^6
NDI:PS	2.5×10^5	MV-12:PS	6.7×10^4
MV:CS	1×10^6	MV-16:CS	4×10^6
MV:PS	5.9×10^4	MV-16:PS	3×10^5

Figure 4.6. Table showing the derived association constant values of various CT pairs

We also performed dynamic light scattering experiments with a 632 nm laser to get an estimate of their aggregating tendencies. **NDI-dc-CS**, **MV-CS** and **MV-PS** showed aggregates of sizes 123, 104, 92 nm respectively (Figure 4.7). Unfortunately size of **NDI-dc-PS** aggregates could not be reliably measured due to it having CT absorption in that region. DLS measurements on **MV-16-CS** and **MV-16-PS** showed average size distribution of 3040 and 1439 nm respectively (Figure 4.7). DLS measurements clearly suggest that not only nascent complexes are

oligomeric aggregates but the supramolecular amphiphile approach effectively increases the size of aggregates.

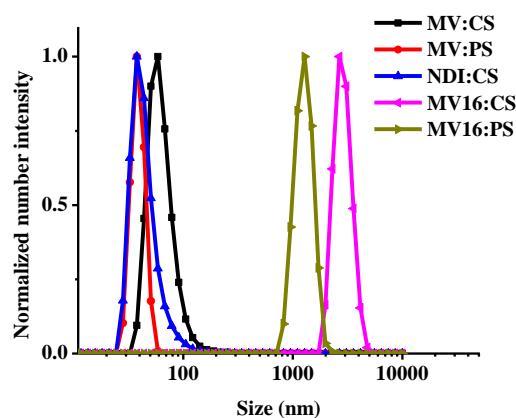


Figure 4.7. DLS Measurements of various samples concentration of each component is $10^{-3}M$ in 10% MeOH and H_2O

Having deciphered the association tendency of the CT pairs we went on to carry 1H -NMR exchange studies to delve into the exchange dynamics of the CT pairs and to study their self-sorting behaviour. For this purpose we performed experiments keeping the acceptor (**NDI-dc**, **MV**) equivalent constant and varying the percentages of **CS** and **PS** in each case, while keeping the net equivalent of (**CS+PS**) same as that of the acceptor (Figure 4.8-4.9). In cases (**NDI-dc**, [**CS+PS**]) and (**MV**, [**CS+PS**]) the variation of **NDI-dc** and **MV** peaks were a weighted average of their contribution in **CS** and **PS** containing stack. This suggests the stacks are highly dynamic at room temperature. More over when the ppm shift is plotted versus the net **CS** or **PS** concentration the trend came out to be linear for both **NDI-dc** and **MV**. This suggests a tendency of **MV-CS**, **MV-PS** and **NDI-dc-CS**, **NDI-dc-PS** stacks to narcissistically self-sort.

We further went on and analysed the behaviour of a [2x2] ensemble comprised of the CT pairs. However as mentioned before to analyse the matrix we need to take advantage of the exclusive absorption range greater than 700 nm where only **NDI-dc-PS** absorbs (Figure 4.1b). Therefore any absorbance in this region is a direct reflection of its concentration in the ensemble. We thus, performed a UV-vis absorption titration of depicting a standard curve for all possible

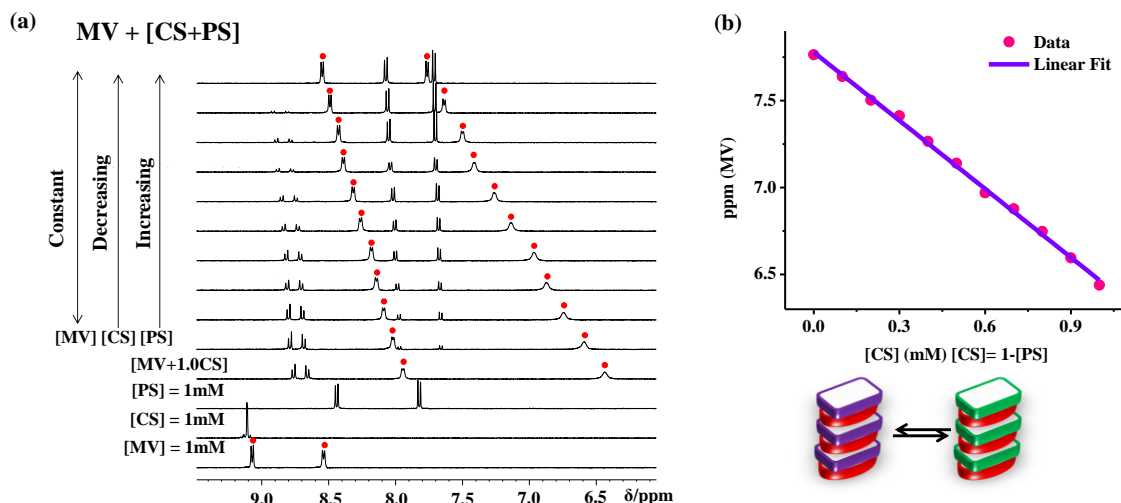


Figure 4.8. (a) $^1\text{H-NMR}$ titration in which $[\text{MV}] = 1 \text{ mM}$ and for various ratios of $[\text{CS}]$ and $[\text{PS}]$ such that $[\text{CS} + \text{PS}] = 1 \text{ mM}$. Solvent being 10% CD_3OD in H_2O and (b) Linear trend following the ppm shifts of MV protons in Figure 4.8a.

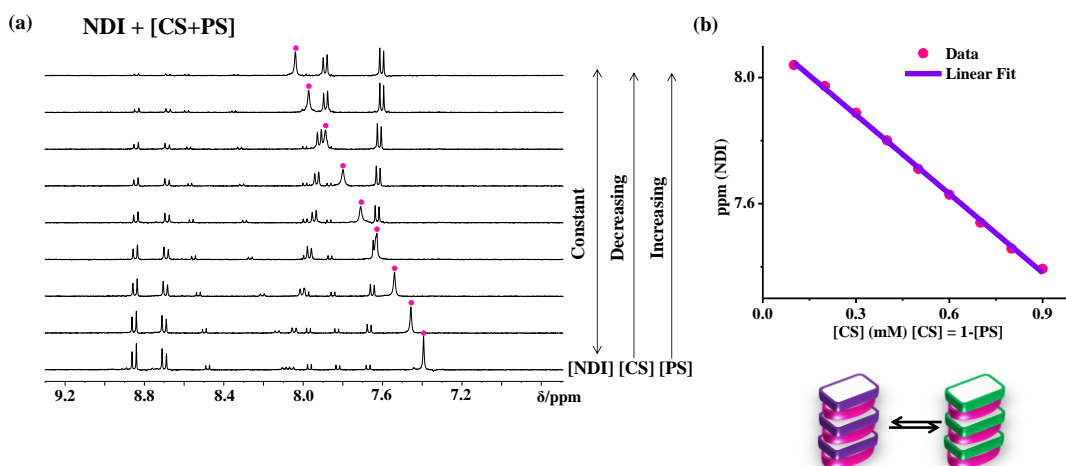


Figure 4.9. (a) $^1\text{H-NMR}$ titration in which $[\text{NDI-dc}] = 1 \text{ mM}$ and for various ratios of $[\text{CS}]$ and $[\text{PS}]$ such that $[\text{CS} + \text{PS}] = 1 \text{ mM}$. Solvent being 10% CD_3OD in H_2O and (b) Linear trend following the ppm shifts of NDI-dc protons in Figure 4.9a.

concentrations of **NDI-dc-PS** while in competition with **CS**. In other words we kept **NDI-dc** concentration constant and varied the ratios of **CS** and **PS** keeping the summation concentration same as that of **NDI-dc**. We then plotted the absorbance at 750 nm versus the net concentration of **NDI-dc-PS**. This linear fit gave us a calibration curve with which the ensemble can now be solved (Figure 4.10).

From the available molecules we constructed four ensembles and analysed their constituents. First ensemble consisted of **MV**, **NDI-dc**, **CS** and **PS** each was taken as 10^{-3} M in 10% MeOH in H_2O (Figure 4.11). The absorption of this mixture at 750 nm suggested that 38% of the **NDI-dc** is in **NDI-dc-PS** complex. Since the ensemble is completely bound, this points towards a 62% of **NDI-dc** in **NDI-dc-CS**. More over from the agnostic and antagonistic relations 38% of **MV** was calculated to be in **MV-CS** and 62% in **MV-PS**.

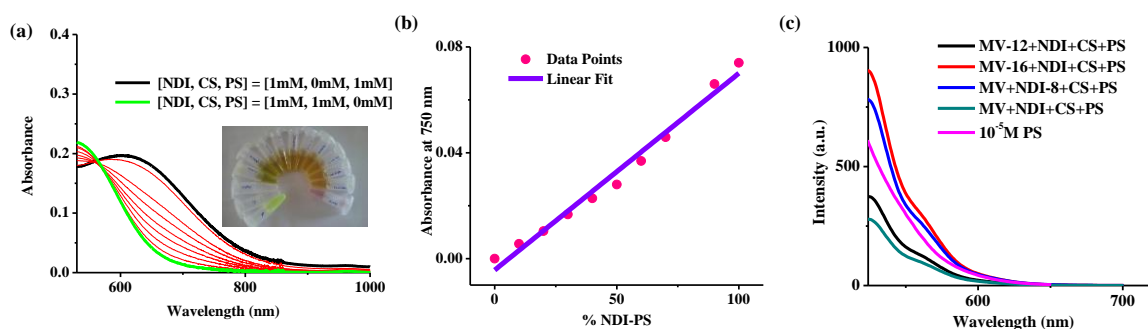


Figure 4.10. (a) and (b) Calibration curves plot with $[NDI-dc] = 1$ mM with various ratios of $[CS]$ and $[PS]$ such that $[CS+PS] = 1$ mM. (c) Emission spectra of ensembles compared with $[PS] = 10^{-5}$ M to get an idea of the free molecules present in the ensemble (with each component of 1 mM). The graph suggests that $[MV+NDI-dc+CS+PS]$ has 0.5% free **PS**, $[MV-12+NDI-dc+CS+PS]$ has 1.3% free **PS**, $[MV-16+NDI-dc+CS+PS]$ has 1.5% free **PS** and $[MV+NDI-8+CS+PS]$ has 0.64% free **PS**. All free **PS** percentages are quite low and hence for all practical purposes ensemble calculation is done by assuming all CT pairs are bound to each other.

From the thermodynamic data this seems possible as the maximum share is of the strongest pair and rest ensemble has equilibrated accordingly. We then looked into our second ensemble which consisted of **MV-12**, **NDI-dc**, **CS** and **PS** replacing the **MV** in nascent ensemble with **MV-12**. Analysing this ensemble in a similar manner gave 62% of the **NDI-dc** is in **NDI-dc-PS** complex and 38% of **NDI-dc** in **NDI-dc-CS**. Alternatively, 62% of **MV** was calculated to be in **MV-CS** and 38% in **MV-PS**. The share of **MV-CS** could be further enhanced by using **MV-16**. In the case of ensemble consisting of **MV-16**, **NDI-dc**, **CS** and **PS** the ensemble was comprised of 70% of the **NDI-dc** is in **NDI-dc-PS** complex and 30% of **NDI-dc** in **NDI-dc-CS**. Alternatively, 70% of **MV** was calculated to be in **MV-CS** and 30% in **MV-PS** (Figure 4.12). In other words the minor product in the nascent ensemble was enriched via an introduction of its amphiphilic

counterpart which increases its aggregating tendency and thereby purging the equilibrium towards it.

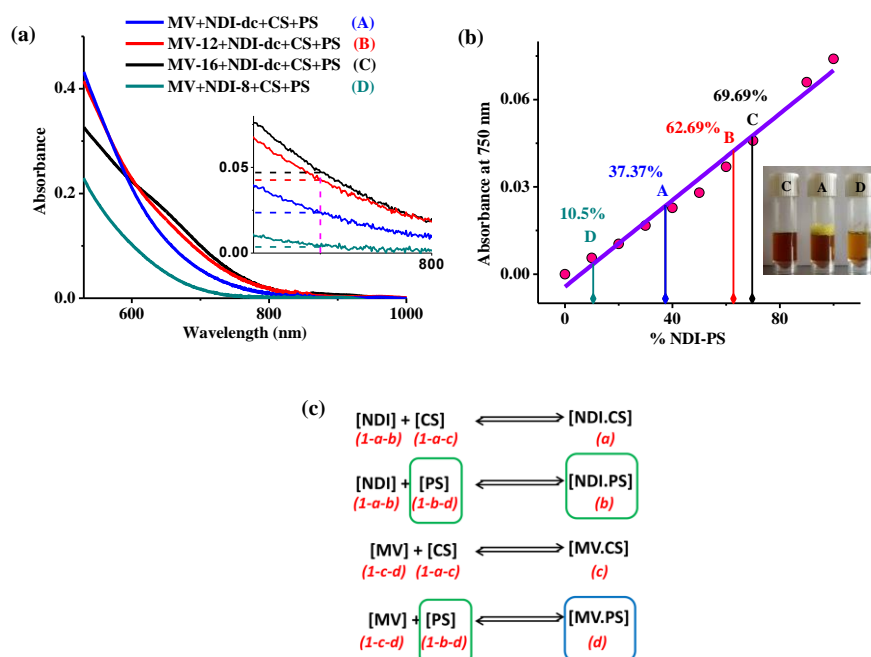


Figure 4.11. a) UV-vis absorption spectra of the $[2 \times 2]$ ensembles with inset showing the zoomed region near 750 nm. Each component has a concentration of 10^{-3} M, in 10% MeOH in H_2O ($l = 5$ mm), b) Percentage calculation of % NDI-dc-PS in the ensemble by the calibration curve with inset showing the ensemble photographs. c) Chemical equations depicting the equilibrium concentrations of the ensemble. With free PS assumed to be negligible. $1-b-d = 0$ and hence suggesting that $b+d=1$. Moreover CS being a stronger donor than PS has better chances of binding than PS and hence $1-a-c = 0$ suggesting $a+c=1$. From these calculations now ensemble can be solved.

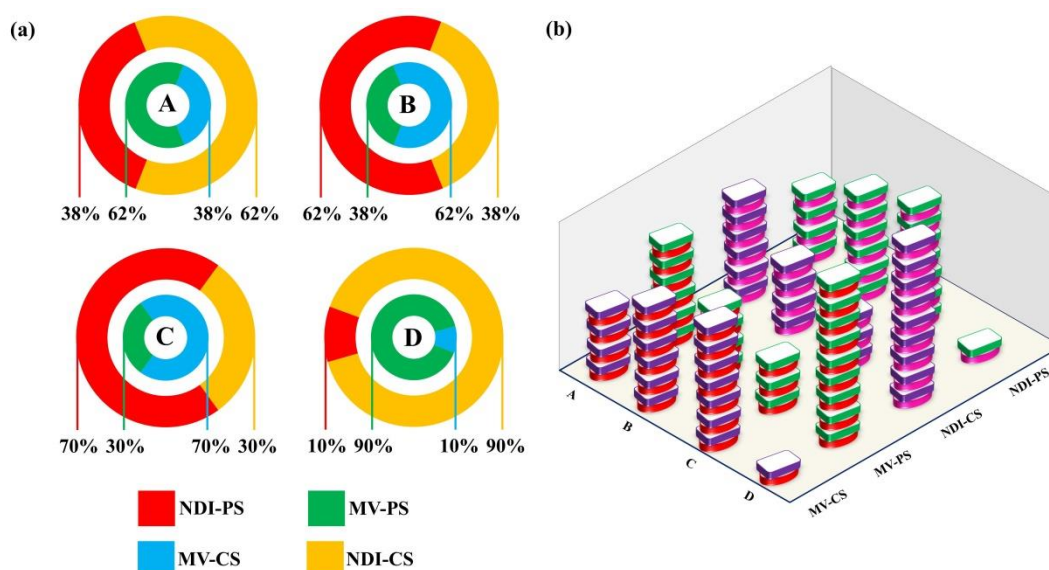


Figure 4.12. (a) and (b) Pie charts and bar graph showing the ensemble shares.

Furthermore with this approach we could not only increase the percentage of the minor product, we could increase the nascent percentage of the major product even further. In the fourth and final ensemble consisting of **MV**, **NDI-8**, **CS** and **PS** a precipitate formed as soon as the components were mixed. The mixture was centrifuged and the supernatant was analysed. This showed the presence of nearly 10% of the **NDI-dc** in **NDI-dc-PS** complex and 90% of **NDI-dc** in **NDI-dc-CS**. Alternatively, 10% of **MV** was calculated to be in **MV-CS** and 90% in **MV-PS**. A $^1\text{H-NMR}$ measurement of the supernatant also suggested differential consumption of **CS** by **NDI-8** with majority of **PS** and **MV** in solution (Figure 4.13).

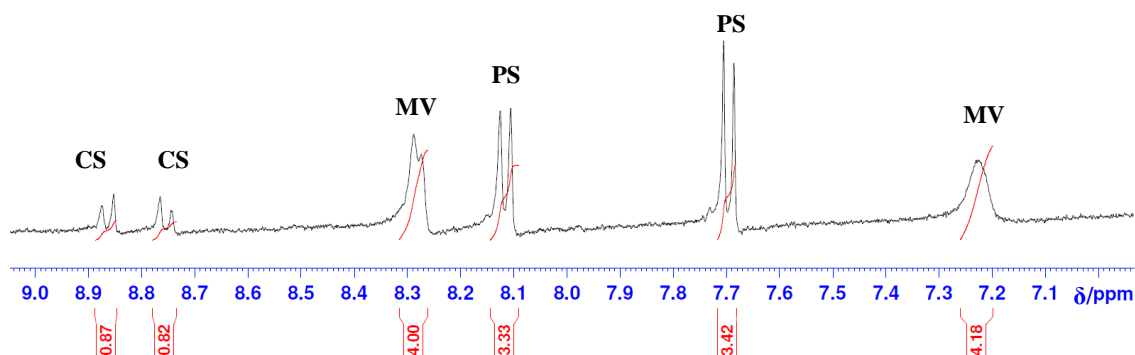


Figure 4.13. $^1\text{H-NMR}$ of the supernatant belonging to the ensemble **MV+NDI-8+CS+PS**.

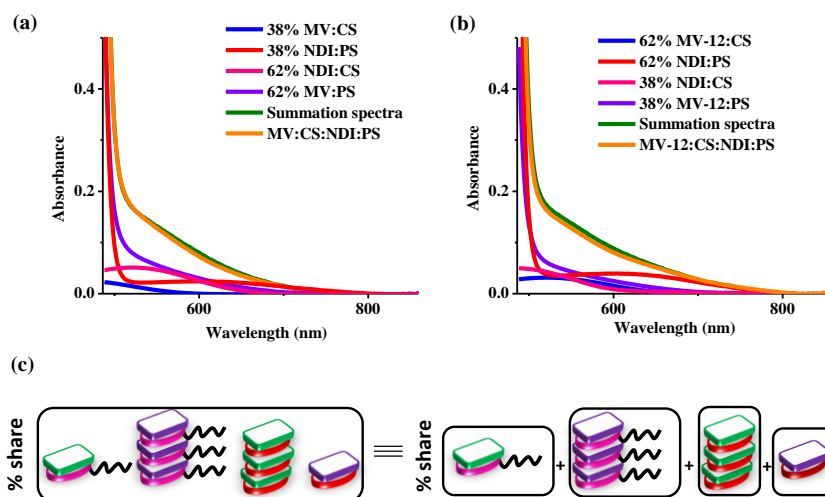


Figure 4.14. (a) and (b) Showing the summation spectra comparison along with the individual components. In the ensemble each component is 10^{-3} M in 10% MeOH in H_2O ($l = 2$ mm) and (c) schematic showing the gist of UV-vis absorption spectra suggesting summation of components is similar to an ensemble.

We were aware that our calculation is based on determination of just one specie and thus to rule out any local effects we hypothesize that the obtained ensemble spectra should match with a mathematical sum of individual pairs each multiplied with the share percentage obtained via ensemble calculation (Figure 4.12). To our delight the ensembles held to this test suggesting that not only our calculated percentages are a depiction a global ensemble also since that sum of each component was equal to the ensemble a narcissistic self-sorting was crucially established (Figure 4.14).

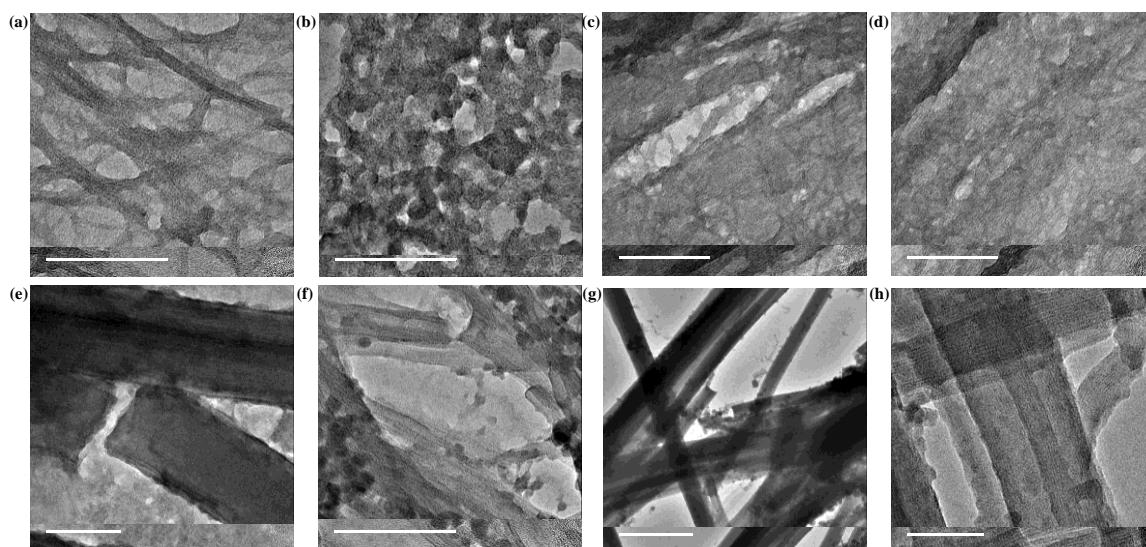


Figure 4.15. TEM images of (a) **MV-16+CS**, (b) **MV-16+PS**, (c) and (d) **MV-16+NDI-dc+CS+PS**, (e) **NDI-8+CS**, (f) **NDI-8+PS**, (g) and (h) **MV+NDI-8+CS+PS** concentration of each is 10^{-3} M drop casted from a 10% MeOH in H_2O solution.

To further strengthen our conclusions we analysed the ensembles as well as individual components by Transmission electron microscopy (TEM) (Figure 4.15). Looking for the fact that ensemble morphology should resemble the individual morphology of the major component. From the TEM analysis we observed that **MV-16-CS** was majorly bundles of long unilamellar cylindrical micelle and **MV-16-PS** were an agglomerate of ill formed nano-tapes (Figure 4.15 a,b). On the other hand, **NDI-8-CS** showed well-formed and arranged nano tapes with molecular striations depicting aggregating stacks clearly visible. **NDI-8-PS** showed ill formed tapes with the order seen in **NDI-8-CS** clearly missing (Figure 4.15 e,f) The ensemble **MV-16**, **NDI-dc**, **CS** and

PS predominantly showed long unilamellar cylindrical micelles further supporting our conclusions similar to **MV-16-CS** (Figure 4.15 c,d).

On the other side ensemble containing **MV**, **NDI-8**, **CS** and **PS** was very similar to morphology of **NDI-8-CS** (Figure 4.15 g,h). The morphological resemblance of the ensemble with the majority product clearly proves the point of ensemble reconfiguration and that it indeed occurs on a global level. Additionally it could be argued that over all UV response can also be achieved if CT stacks occur in supramolecular blocks as major portion would be comprised of individual CT fibres and only interfaces comprising of hetero CT stacks. This remote possibility can thus be overruled by the morphological signatures obtained.

4.3. Conclusion and Outlook

In conclusion we prove that an ensemble of non-covalent aggregates can be reconfigured based on the ubiquitous stimuli of aggregation. It is for the first time that such a reconfiguration has been attempted and completely analysed which has proved to be a challenging task in the past. We clearly showed the enrichment of minor products as well as enhancement of major products both based on the principle of aggregation controlled equilibrium. This study would prove a stepping stone for its dynamic extension which would warrant a transient introduction of aggregation. Moreover such a control of an ensemble based on aggregating cue can be a starting of a logical step towards functionality based selection in an ensemble, hence nearing to a scenario towards natural evolutionary selection.¹⁷

4.4. Experimental Section

General Methods:

NMR Measurements: NMR spectra were obtained with a Bruker AVANCE 400 (400 MHz w.r.t. ¹H nuclei) Fourier transform NMR spectrometer with chemical shifts reported in parts per million (ppm).

Optical Measurements: Electronic absorption spectra were recorded on a Perkin Elmer Lambda 900 UV-Vis-NIR Spectrometer and emission spectra were recorded on Perkin Elmer LS 55 Luminescence Spectrometer.

Transmission Electron Microscopy (TEM): TEM measurements were performed on a JEOL, JEM 3010 operated at 300 kV. Samples were prepared by placing a drop of the solution on carbon coated copper grids followed by drying at room temperature. The images were recorded with an operating voltage 300 kV.

Dynamic light scattering (DLS) Experiments: The measurements were carried out using a NanoZS (Malvern UK) employing a 532 nm laser at a back scattering angle of 173°. The samples were measured in a 10 mm glass cuvette. A dead time (Time between sample loading and starting of measurement by the machine) of around 45 seconds is present in all measurements.

Synthesis: CS,^{14b} PS,¹⁸ MV,^{14b} MV-12,^{14b} MV-16,^{14b} NDI-dc,¹⁹ NDI-8²⁰ were synthesized according to the reported procedures and sufficiently characterized.

4.5. References and Notes

1. (a) Brunsveld L.; Folmer B. J. B.; Meijer E. W.; Sijbesma R. P. *Chem. Rev.* 2001, **101**, 4071; (b) De Greef T. F. A.; Smulders M. M. J.; Wolffs M.; Schenning A. P. H. J.; Sijbesma R. P.; Meijer E. W. *Chem. Rev.* 2009, **109**, 5687; (c) Hoeben F. J. M.; Jonkheijm P.; Meijer E. W.; Schenning A. P. H. J. *Chem. Rev.* 2005, **105**, 1491.
2. (a) Aida T.; Meijer E.W.; Stupp S.I. *Science* 2012, **335**, 813; (b) Krieg E.; Bastings M. M. C.; Besenius P.; Rybtchinski B. *Chem. Rev.* 2016, **116**, 2414; (c) Babu S. S.; Praveen V. K.; Ajayaghosh A. *Chem. Rev.* 2014, **114**, 1973.
3. (a) Jain A.; George S. J. *Mat. Today* 2015, **18**, 206; (b) Appel E. A.; del Barrio J.; Loh X. J.; Scherman O. A. *Chem. Soc. Rev.* 2012, **41**, 6195.
4. (a) Corbett P. T.; Leclaire J.; Vial L.; West K. R.; Wietor J.-L.; Sanders J. K. M.; Otto S. *Chem. Rev.* 2006, **106**, 3652; (b) Au-Yeung H. Y.; Pantos G. D.; Sanders J. K. M. *J. Org. Chem.*

- 2011, **76**, 1257; (c) Otto S.; Kubik S. *J. Am. Chem. Soc.* 2003, **125**, 7804; (d) Au-Yeung H. Y.; Cougnon F. B. L.; Otto S.; Pantos G. D.; Sanders J. K. M. *Chem. Sci.* 2010, **1**, 567; (e) Cougnon F. B. L.; Au-Yeung H. Y.; Pantos G. D.; Sanders J. K. M. *J. Am. Chem. Soc.* 2011, **133**, 3198; (f) Li J.; Nowak P.; Otto S. *J. Am. Chem. Soc.* 2013, **135**, 9222.
5. Janeliunas D.; van Rijn P.; Boekhoven J.; Minkenberg C. B.; van Esch J. H.; Eelkema R. *Angew. Chem. Int. Ed.* 2013, **52**, 1998.
6. Toledano S.; Williams R. J.; Jayawarna V.; Ulijn R. V. *J. Am. Chem. Soc.* 2006, **128**, 1070.
7. Janes P. W.; Ley S. C.; Magee A. I. *J. Cell Biol.* 1999, **147**, 447.
8. Taubes G. *Science* 1996, **271**, 1493.
9. Mukhopadhyay P.; Zavalij P. Y.; Isaacs L. *J. Am. Chem. Soc.* 2006, **128**, 14093.
10. Chakrabarti S.; Mukhopadhyay P.; Lin S.; Isaacs L. *Org. Lett.* 2007, **9**, 2349.
11. (a) Huskens J.; Mulder A.; Auletta T.; Nijhuis C. A.; Ludden M. J. W.; Reinhoudt D. N. *J. Am. Chem. Soc.* 2004, **126**, 6784; (b) Zhang K.-D.; Sakai N.; Matile S. *Org. Biomol. Chem.* 2015, **13**, 8687; (c) Zhang K.-D.; Matile S. *Angew. Chem. Int. Ed.* 2015, **54**, 8980; (d) Iglesias M. G.; Peuntinger K.; Kahnt A.; Krausmann J.; Vázquez P.; Rodríguez D. G.; Guldi D. M.; Torres T. *J. Am. Chem. Soc.* 2013, **135**, 19311; (e) Huang Z.; Yang L.; Liu Y.; Wang Z.; Scherman O. A.; Zhang X. *Angew. Chem. Int. Ed.* 2014, **53**, 5351.
12. (a) Ghosh S.; Mukhopadhyay P.; Isaacs L. *J. Syst. Chem.* 2010, **1**, 1; (b) Garcia C. M.; Garcia J. C.; Perez A. M. L.; Mayoral M. J.; Bilbao N.; Rodriguez D. G. *Angew. Chem. Int. Ed.* 2016, **55**, 223; (c) Berdugo C.; Nalluri S. K. M.; Javid N.; Escuder B.; Miravet J. F.; Ulijn R. V. *ACS Appl. Mater. Interfaces* 2015, **7**, 25946; (d) Perl A.; Casado A. G.; Thompson D.; Dam H. H.; Jonkheijm P.; Reinhoudt D. N.; Huskens J. *Nat. Chem.* 2011, **3**, 317.
13. Ulijn R. V.; Janssen A. E. M.; Moore B. D.; Halling P. J. *Chem. Eur. J.* 2001, **7**, 2089.
14. (a) Zhang X.; Wang C. *Chem. Soc. Rev.* 2011, **40**, 94; (b) Rao K. V.; Jayaramulu K.; Maji T. K.; George S. J. *Angew. Chem. Int. Ed.* 2010, **49**, 4218; (c) Rao K. V.; George S. J. *Chem. Eur. J.* 2012, **18**, 14286; (d) Kumar M.; Rao K. V.; George S. J. *Phys. Chem. Chem. Phys.* 2014, **16**, 1300.

15. Thordarson P.; Coumans R. G. E.; Elemans J. A. A. W.; Thomassen P. J.; Visser J.; Rowan A. E.; Nolte R. J. M. *Angew. Chem.* 2004, **116**, 4859.
16. Giuseppone N.; Lehn J.-M. *Chem. Eur. J.* 2006, **12**, 1715.
17. (a) Zayed J. M.; Nouvel N.; Rauwald U.; Scherman O. A. *Chem. Soc. Rev.* 2010, **39**, 2806; (b) Giuseppone N. *Acc. Chem. Res.* 2012, **45**, 2178.
18. Rao K. V.; Datta K. K. R.; Eswaramoorthy M.; George S. J. *Angew. Chem. Int. Ed.* 2011, **50**, 1179.
19. Sissi C.; Lucatello L.; Krapcho A. P.; Maloney D. J.; Boxer M. B.; Camarasa M. V.; Pezzoni G.; Menta E.; Palumbo M. *Bioorg. Med. Chem.* 2007, **15**, 555.
20. Jalani K.; Kumar M.; George S. J. *Chem. Commun.* 2013, **49**, 5174.

Chapter-5

Strategies for Dissipative Conformational and Ensemble Control

Chapter-5

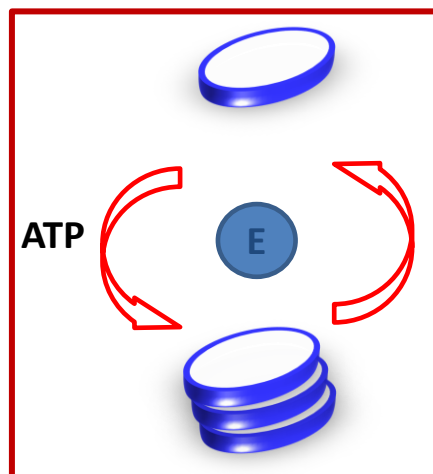
Strategies for Dissipative Conformational and Ensemble Control

Abstract

Biological systems operate under non-equilibrium or dissipative conditions. This refers to the point that for every task, energy is consumed in the system. At the molecular level, in most cases, molecules like Adenosine tri-phosphate (ATP) act as fuel in a dissipative cycle to bring about conformational and aggregate changes in the biological environment. These changes then result as physical functional and operations carried out by a biological system.

Though in the previous chapters we have discussed about aggregates out of equilibrium a special mention is warranted on ATP driven systems. Mastery over using ATP is perhaps rudimentary in not only understanding biological systems better but also to develop synthetic systems which are operationally closer to biological systems.

In this chapter we explore the possibilities of a dynamic conformational change under non-equilibrium fuelled by ATP. We also develop on the concepts explored in Chapter 4 and demonstrate the effect an aggregate under non-equilibrium can have on a multi-component ensemble.



5.1. Introduction

Adenosine Triphosphate (ATP) is the biological energy currency.¹ Though this is quite a ubiquitous statement, one needs to understand what it actually means with respect to biological assemblies and protein conformations. In a simplistic sense it refers to the fact that biomolecules conformational or structural changes when ATP binds to them, the energetic cost however is paid for by the hydrolysis of phospho-diester bonds. Since these transformations need to be reversible, every cycle dissipates energy in terms of degradation of ATP. This leads to conformations and aggregates under non-equilibrium.

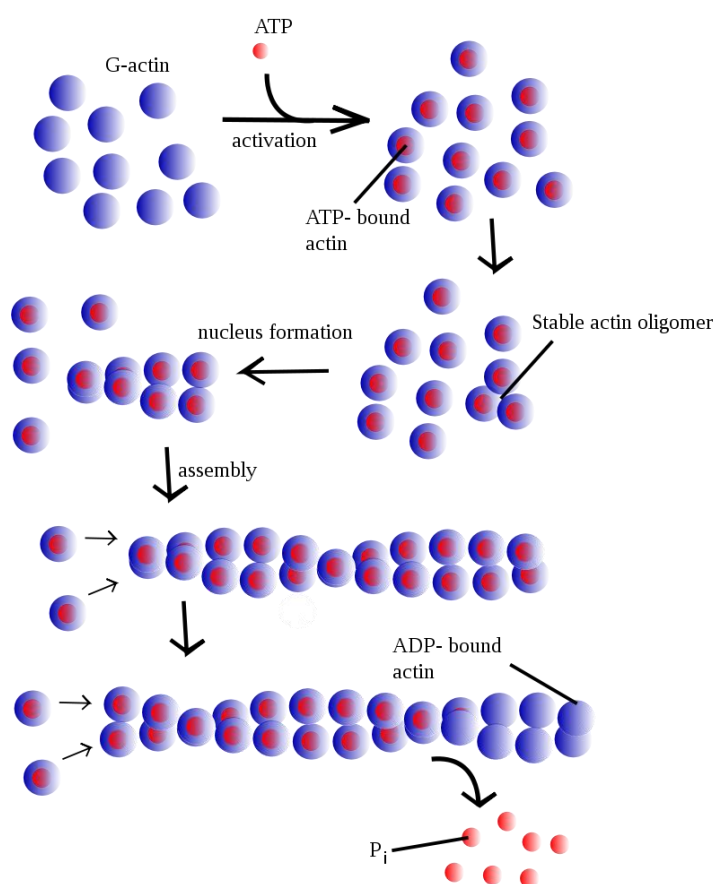


Figure 5.1. Schematic representation of ATP driven actin polymerization and ATPase action of F-actin that converts ATP to ADP and thus starts the depolymerisation process. The process is dissipative and ATP is the driving fuel (Reproduced with permission from Ref. 5).

Being under non-equilibrium allows these systems to be controlled with fuel demand and degradation kinetics. The two famous examples of this ATP driven energy economy are Actin fibers

which represent ATP driven Aggregation²⁻⁶ and ABC Proteins (ATP binding cassette protein) which signify ATP driven conformation change.⁷

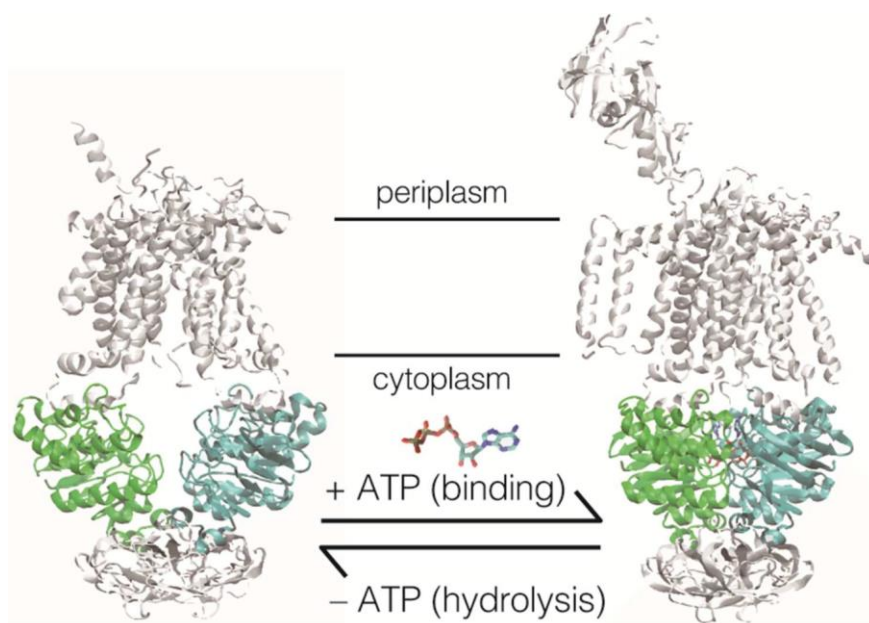


Figure 5.2. Schematic representation of ATP driven conformational changes in ABC protein (ATP binding cassette protein) (Reproduced with permission from Ref. 7).

Actin growth has been detailed in previous chapters, however a few minutiae warrant their mention. ATP binds to G-actin (Inactive form) to convert it to F-actin (Active form). These F-actin further aggregate to form nuclei and thus form elongated aggregates. F-actin however is also an ATPase which further hydrolyses bound ATP converting it to ADP and in turn converting F-actin back to G-actin. This produces aggregates under non-equilibrium which charge ATP molecules for this process to occur again, thus the dissipative growth (Figure 5.1).

On the other side there are several examples of ATP induced conformational changes in biological systems. One such prominent example is ABC proteins. These proteins fall under the class of conformation changing ion transporters. They switch their conformation on binding with ATP to open form and substrates can be transferred across the membrane. However the conformation reverses on ATP hydrolysis. This conformation switch thus requires ATP as a fuel (Figure 5.2). Considering the rarity of artificially self-assembled systems under non-equilibrium itself, ATP governed systems need to be extensively explored for enormous possibilities.

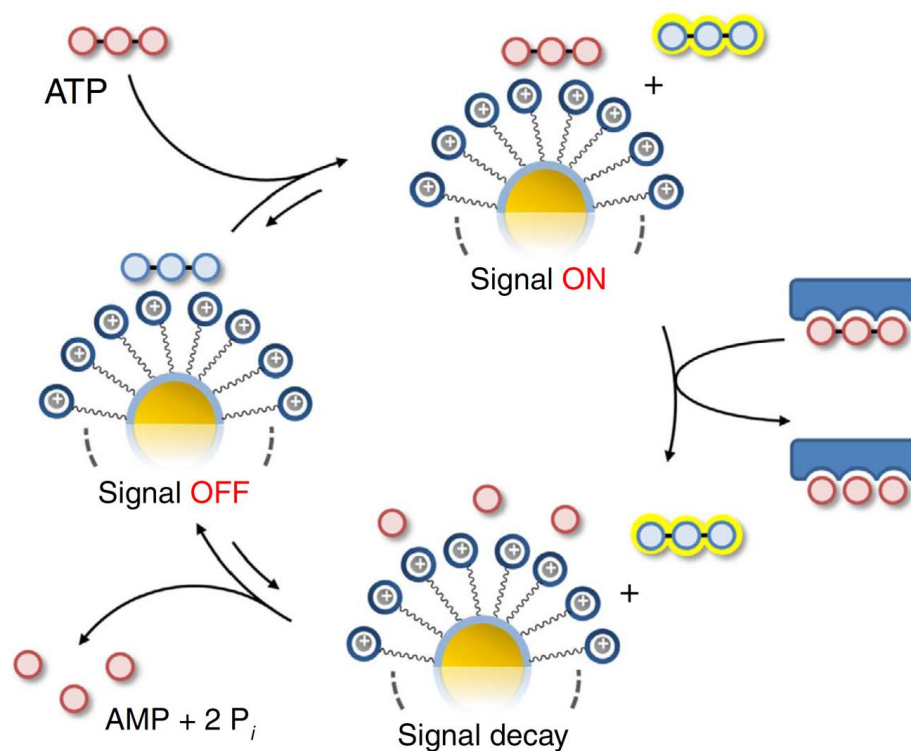


Figure 5.3. Schematic representation of ATP driven transient signal generation on a nanoparticle platform (Reproduced with permission from Ref. 8).

There have only been a few reports in which synthetic systems have used ATP as a dissipative fuel. *Prins et al.* have used ATP ion exchange to displace dyes into fluorescent state on a nanoparticle platform. This ATP however exists transiently as it is being subsequently hydrolysed by Potato apyrase (Degrades ATP to AMP). This process finally results in quenching of dye fluorescence, resulting in transient signal generation (Figure 5.3).⁸ Further the same group has advance the similar chemistry to transient lipid vesicles, the bilayer hydrophobic environment of which can host transient reactions as well (Figure 5.4).⁹

Considering these reports the dearth of current knowledge on ATP driven systems needs to be eradicated, hence the need on further research in this particular area. More over as mentioned in the introduction fuel driven conformational changes are highly relevant as well, however remain completely unexplored.

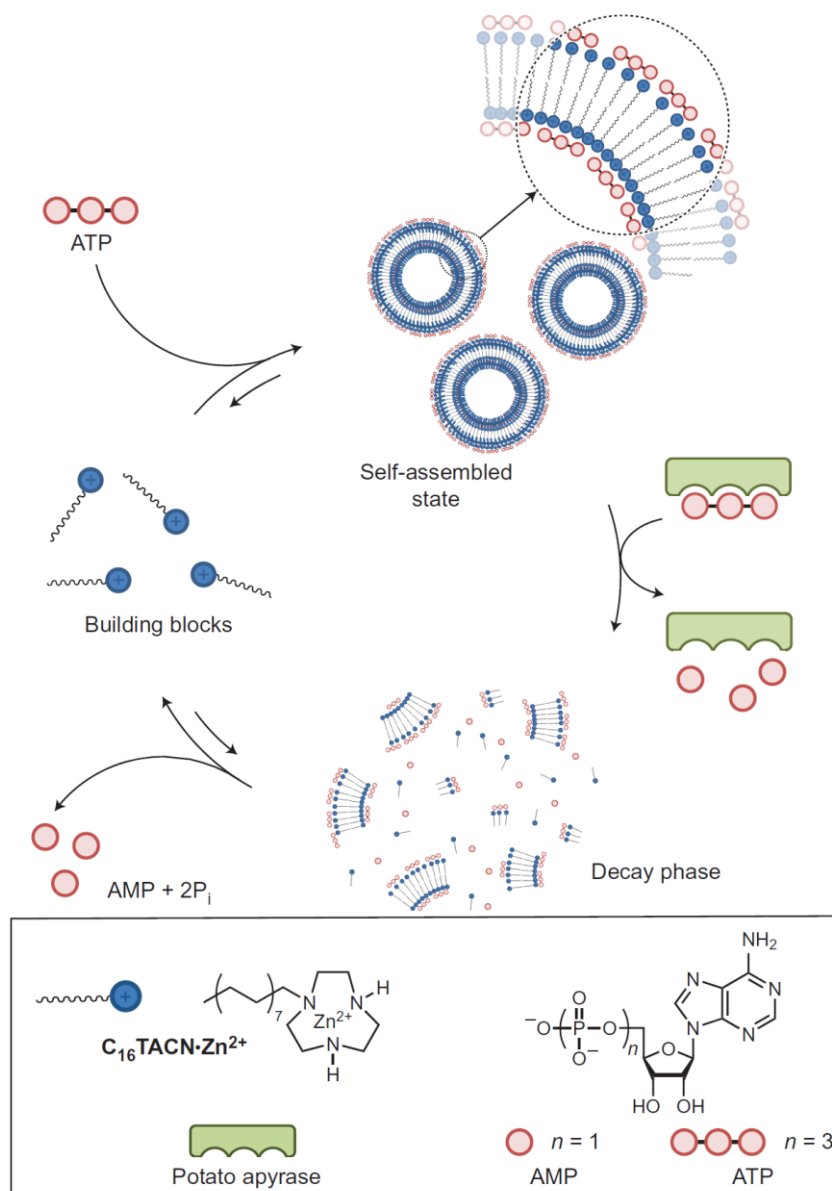


Figure 5.4. Schematic representation of ATP driven transient vesicle formation (Reproduced with permission from Ref. 9).

Recently, from our lab we reported a Zinc picolyl ethylene diamine appended Naphthalene diimide moiety (**ZnNDPA**). **ZnNDPA** binds with biological phosphates to give helical aggregates. These helical conformations are different on binding with ATP, ADP and AMP respectively. In this work we were able to decipher the hydrolysis rates of ATP to P_i as CIAP (Calf Intestinal Alkaline Phosphatase) acts on them (Figure 5.5).¹⁰⁻¹²

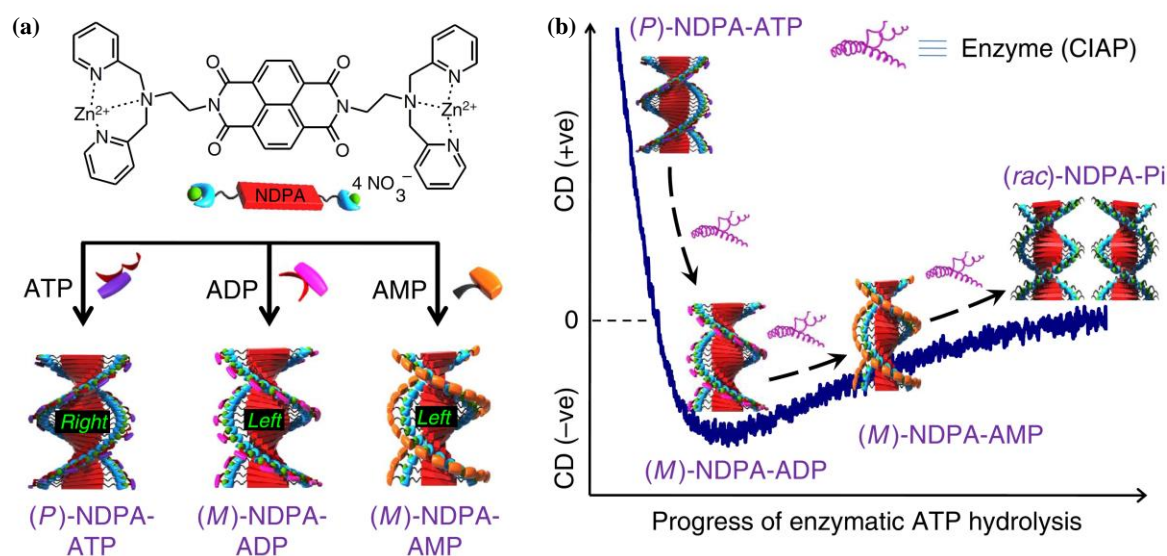


Figure 5.5. (a) Differential conformational response of NDPA assembly with ATP (right handed helix), ADP and AMP (left handed helix) and (b) Time trace of ATP hydrolysis as followed by circular dichroism (Reproduced with permission from Ref. 12).

5.2. Results and Discussion

In this Chapter we demonstrate both conformational and aggregate control fuelled by ATP. This was achieved by introducing ATP in a solution containing the chromophores, with the solution environment capable of hydrolysing ATP. This would generate a transient population of ATP and if the chromophores binding with ATP is fast enough the whole process would result in a dissipative cycle of signal generation. In the complete cycle (from initial stage to intermediate aggregates and back to initial stage) ATP molecules are being spent as a fuel and fresh equivalents of ATP are required to start the process all over again. Prime requisites for a molecule to show such a property are fast response on interacting with a stimuli and a linear response to stimuli concentration which would imply absence of any signal amplification and memory mechanisms.

For aggregate control however we have gone a step ahead and demonstrated ensemble control (Chapter 4) under non-equilibrium conditions. In this section we would first discuss about conformational control followed by ensemble control.

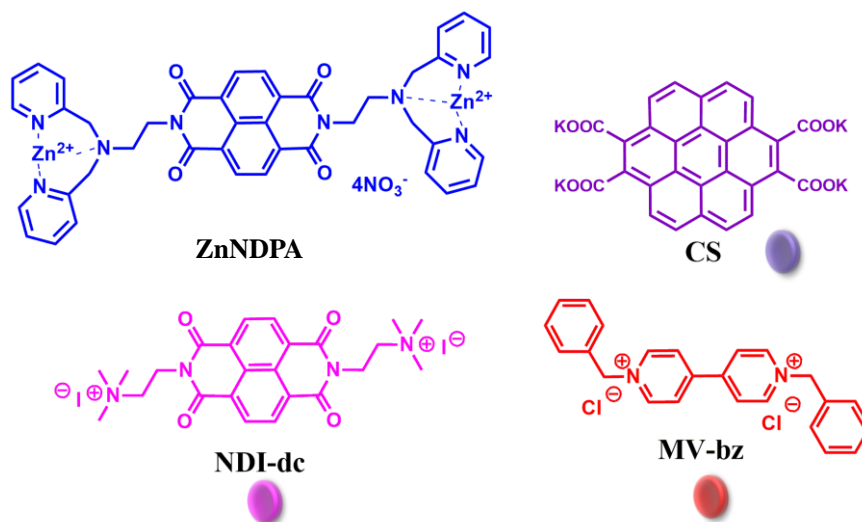


Figure 5.6. Molecular structures of compounds under investigation.

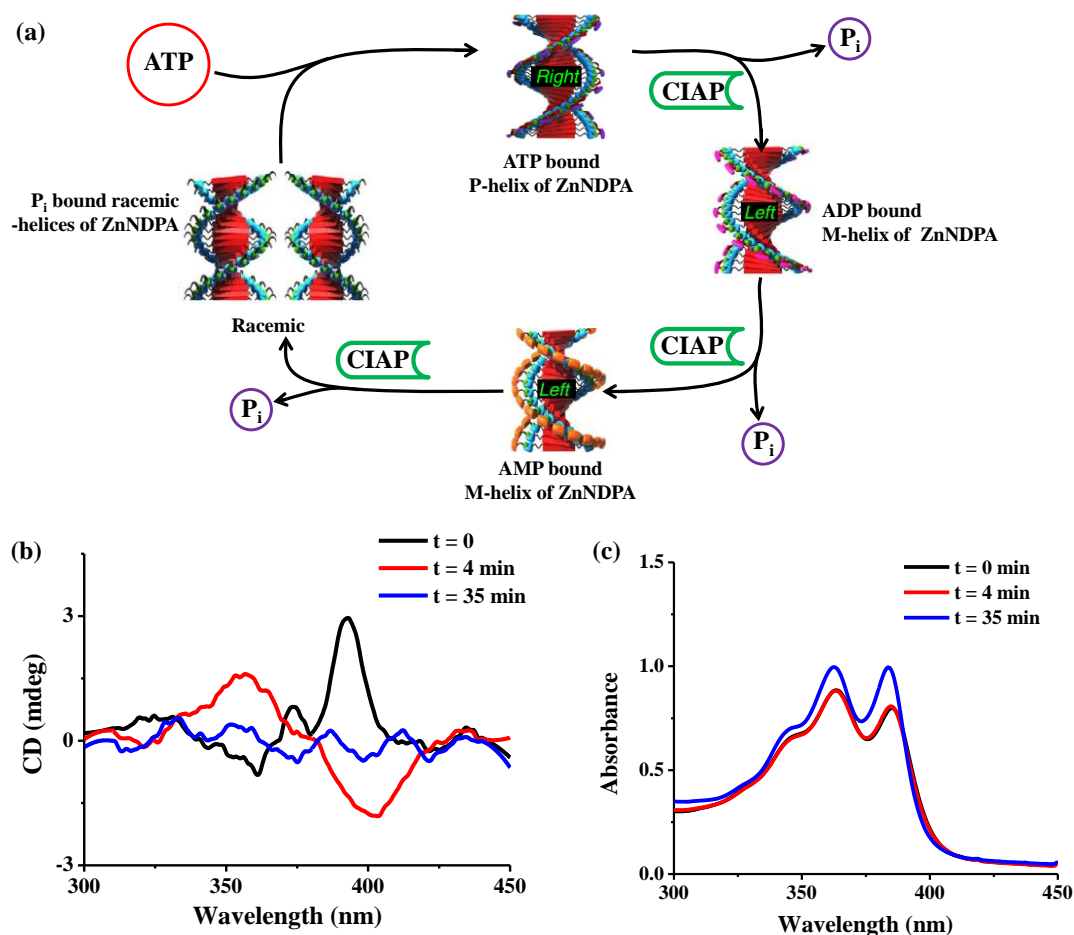


Figure 5.7. (a) Schematic representation of ATP driven conformational change in ZnNDPA, (b) and (c) Time lapse CD and UV spectra of $[ZnNDPA] = 5 \times 10^{-5} M$, $[ATP] = 1 eq.$, $[CIAP] = 1.12U$, $40^\circ C$. (CIAP = Calf intestinal alkaline phosphatase, P_i = Phosphate).

5.2.1. Conformational Control Under Non-Equilibrium

To explore the conformational control with ATP as a fuel we used **ZnNDPA** stacks as the model system. Initially it exists as racemic mixture of stacks and on addition of ATP converts into right handed stacks. In this case however CIAP is also present in the solution. Binding of ATP and conformational changes are much faster than enzyme hydrolysis. Therefore binding occurs first and then followed by subsequent conformational change, resulting in a right-handed helix under non-equilibrium. Moreover as ATP is hydrolysed it converts to ADP and subsequent AMP. ADP and AMP however form a left-handed helix changing the conformation completely. This in fact is not the end of the cycle as AMP also hydrolyses into achiral phosphates, demonstrating that not only right-handed conformation is under non-equilibrium but also the left-handed one (Figure 5.7). This is a unique system in which multiple conversions in conformation occur in one dissipative cycle. In an oscillating or dissipative system however a greater advantage exists if one can modulate the signal amplitude and frequency. The signal in this case is the CD response which translates into the chiral conformation of the aggregate. The amplitude would thus relate to length of the stack and the extent of chiral inscription and frequency would thus be the rate of change of chiral conformation of the stack. The importance of modulation of amplitude and frequency becomes evident if we revisit the example of ABC proteins in biological systems. As mentioned before these are ion transporters with the flux governed by ATP fuel kinetics. Change in amplitude and frequency of the conformation change would directly translate in change of ion flux and the hence the functionality. We in our system intend to prove that amplitude and frequency changes of a conformational response can be accommodated. A future direction of the work obviously would be the coupling of a function to this conformational change as in biological systems. Such a property signifies the hallmark of flexibility in a synthetic system. We envisaged that in our system this can be done by variation of enzyme concentrations. To our delight we were able to prove this fact by variation of both frequency (2.5×10^{-4} to 6.6×10^{-4} Hz) and amplitude (8-6 mdeg) with enzyme variation (0.56–1.68 U). Increase in frequency with increase in enzyme concentration is well expected, however the change in amplitude needs to be commented on. With increasing amount of enzyme since the enzyme takes lesser time to

degrade ATP, lesser residence time of ATP results in decreased aggregated length and hence the lesser amplitude (Figure 5.8). Noticeably the subsequent cycles are not depreciated in signal intensities signifying a good selectivity for ATP amid a huge amount of background phosphate.

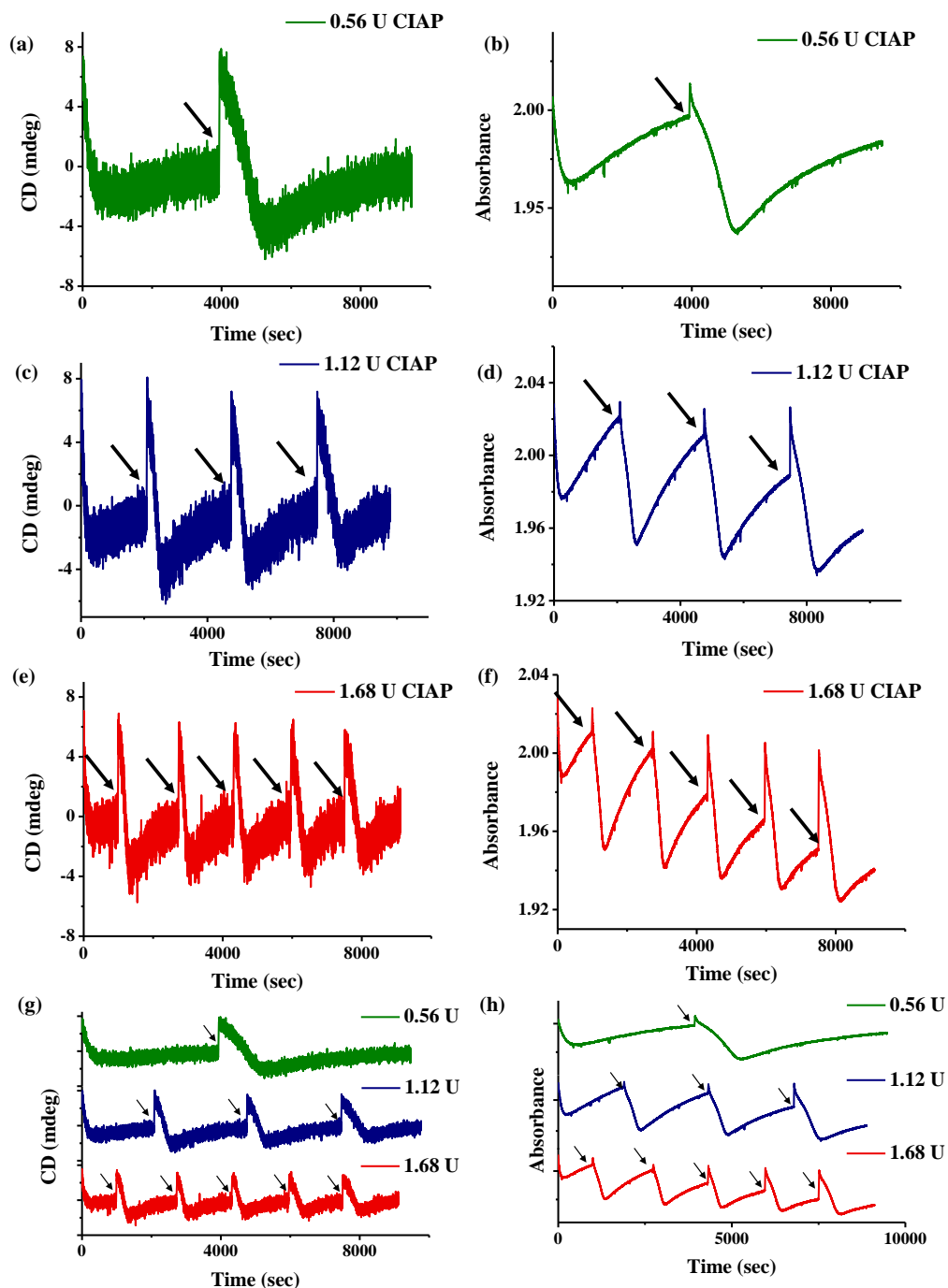


Figure 5.8. (a), (c), (e) CD spectra followed at 390 nm with variable enzyme concentrations and (b), (d), (f) its corresponding absorption trace. (g) and (h) are cumulative comparisons in CD and UV-vis spectra respectively. $[ZnNDPA] = 5 \times 10^{-5} M$, $[ATP] = 1 eq.$, $[CIAP] = variable$, black arrows suggest subsequent ATP addition.

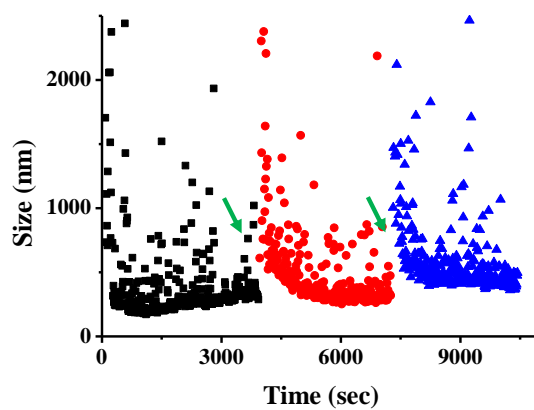


Figure 5.9. DLS size distributions with time of $[ZnNDPA] = 5 \times 10^{-5} M$, $[ATP] = 1 eq.$, $[CIAP] = 1.12 U$, green arrows suggest subsequent ATP addition.

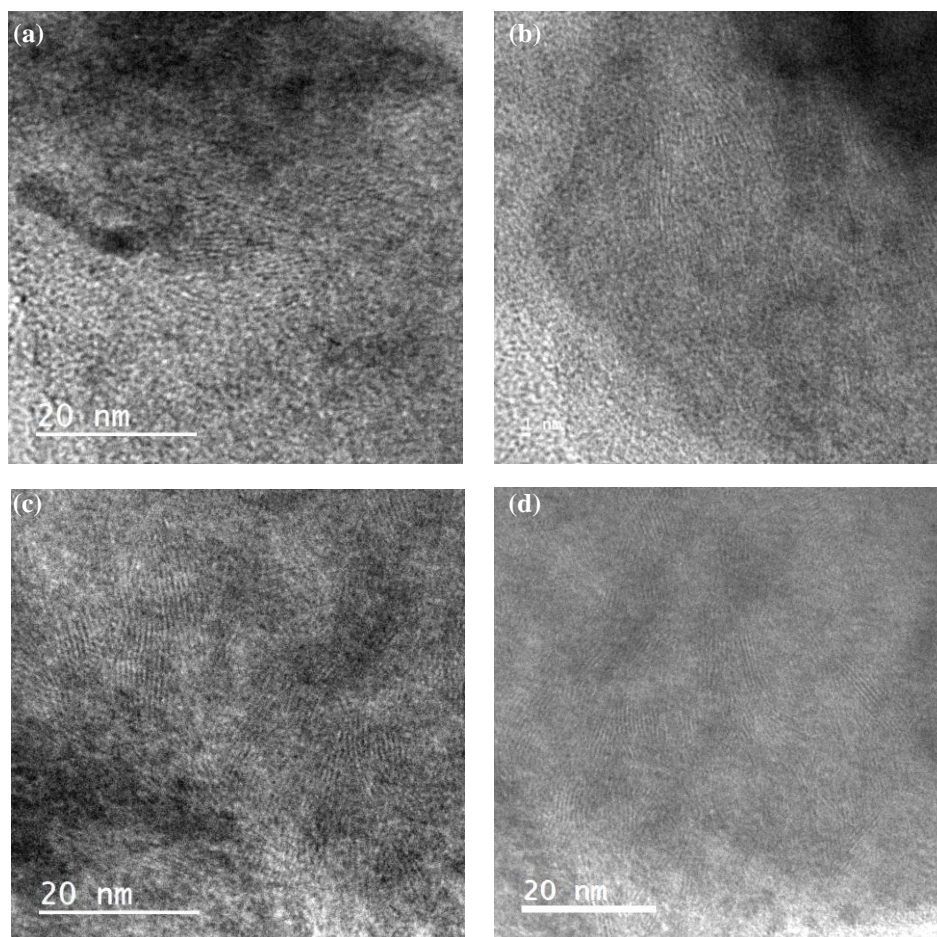


Figure 5.10. (a)-(d) TEM images of $[ZnNDPA] = 5 \times 10^{-5} M$ with $[ATP] = 1 eq.$, linear striations suggestive of aggregate morphology.

This conformation change also brings about change of length of stacks of **ZnNDPA**. This fact is supported by size measurements from Dynamic light scattering (DLS) over time periods of a cycle. As soon as ATP is added the aggregate size increases at first and then gradual decreases due to enzyme action (Figure 5.9). This cycle can be repeated multiple times. We also performed morphology experiments on these aggregates and from transmission electron microscopy (TEM) analysis we could see individual fibers as seen from the visible striations (Figure 5.10).

5.2.2. Ensemble Control Under Non-Equilibrium

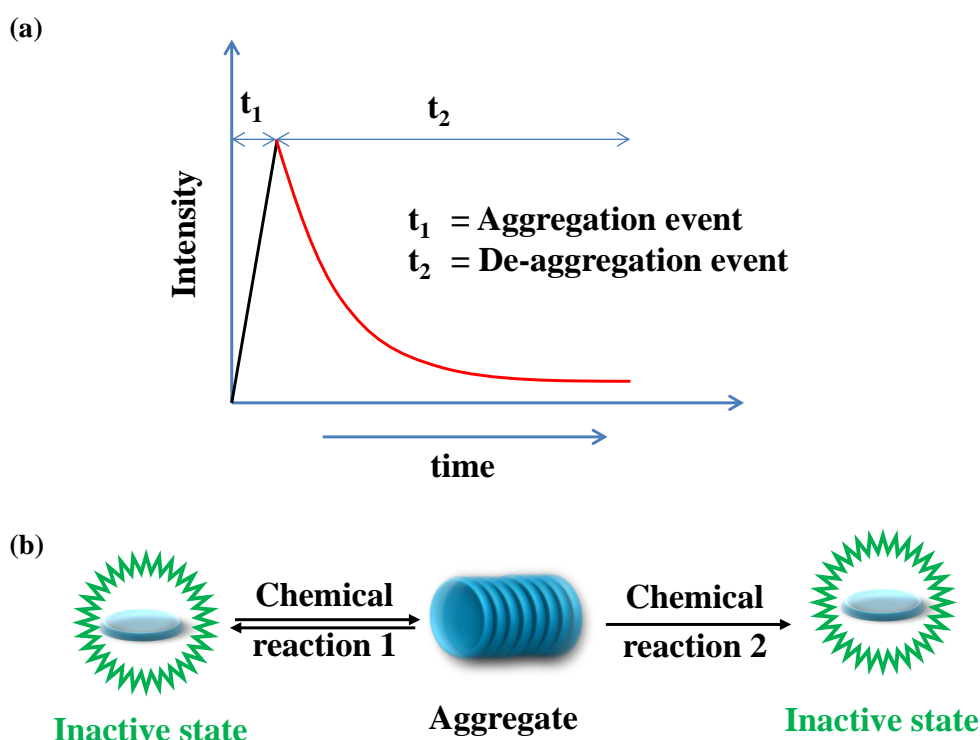


Figure 5.11. Schematic and chemical representation of aggregates under equilibrium.

Moving forward the concept of aggregation induced change in a supramolecular ensemble (Chapter 4) we envisaged to perform the same phenomena under non-equilibrium conditions. Since in this case we need to bring about an ensemble change via aggregation, our first priority should be achieving aggregation under non-equilibrium conditions. To get advantage towards ensemble re-configuration we chose a higher association constant binding moiety (Chapter 4) as the starting material i.e. **NDI-dc** (Figure 5.6). Similar to conformational control we envisage that ATP binding to **NDI-dc** would be kinetically much faster as compared to the disaggregation event by subsequent

hydrolysis by CIAP. The kinetic difference in these two reactions should bring about a finite time period in the whole cycle with peaking at transient aggregation of **NDI-dc** (Figure 5.11).

Unfortunately in this particular system ATP did not induce appreciable chirality to **NDI-dc** therefore we relied on emission changes on aggregation as a sensitive source to monitor aggregation. Upon addition of ATP emission quenched but started to build up gradually due to enzymatic hydrolysis. With subsequent addition of ATP the cycle could be repeated. The amplitude in this case varies with subsequent addition, perhaps due decreased selectivity of ATP in presence of residual phosphates (Figure 5.12).

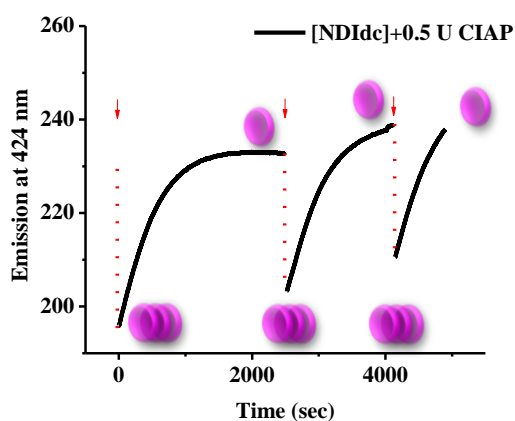


Figure 5.12. Emission intensity of **NDI-dc** followed at 424 nm (red arrows suggest ATP addition) $[\text{NDI-dc}] = 1 \times 10^{-4} \text{ M}$, $[\text{ATP}] = 10 \text{ eq.}$, $[\text{CIAP}] = 0.5 \text{ U}$, Buffer pH = 9.

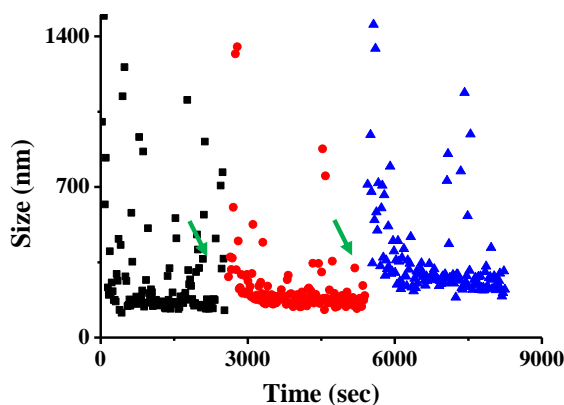


Figure 5.13. DLS size distributions with time of $[\text{NDI-dc}] = 1 \times 10^{-4} \text{ M}$, $[\text{ATP}] = 10 \text{ eq.}$, $[\text{CIAP}] = 0.5 \text{ U}$, green arrows suggest subsequent ATP addition, Buffer pH = 9.

We followed the similar cycle with DLS and saw dramatic changes in size of their aggregates in each cycle. Upon addition of ATP size increased but was subsequently decreased due to enzymatic action. These experiments prove conclusively that **NDI-dc** aggregates can be achieved under dissipative conditions with ATP being the fuel.

We then moved ahead to a two component system with **NDI-dc** and **CS** being electron acceptor and donor respectively. Upon mixing **CS** emission is quenched due to the ground state charge transfer (CT) but comes up on addition of ATP. ATP results in **NDI-dc** aggregation and thus releasing the **CS** to be free and emissive. Upon addition of CIAP however this emission decreases again due to reformation of the ground state CT. This transient response can be followed as dissipative cycles both in terms of **CS** emission and CT absorption. As soon as ATP is added **CS** emission comes up. But gradually decreases due to subsequent enzyme action and eventual CT reformation. This dissipative cycle can be followed with multiple cycles. Inverse trend is however seen in absorption spectra as CT absorption decreases on addition of ATP and builds up gradually signifying its reformation (Figure 5.14).

We went further ahead to study a three component system including **MV-bz +NDI-dc + CS**. In this system **NDI-dc** and **MV-bz** compete for **CS**. Initially when three components are mixed **NDI-dc** forms CT with **CS** preferentially and exists in major fraction compared to CT complex between **MV-bz** and **CS** (Chapter 4). As ATP is added **NDI-dc** and **CS** CT band decreases and results in subsequent formation of CT between **MV-bz** and **CS** as seen from the absorption spectra (Figure 5.15a). This transient cycle can again be followed by absorption spectra which results in subsequent regaining of **NDI-dc** and **CS** CT interaction (Figure 5.51b).

In summary in addition to Chapter 4 where we show that aggregation can control an ensemble, in this section we demonstrate that if aggregation is controlled under dissipative conditions and ensemble can in effect be also affected by it and can thus be controlled under non-equilibrium conditions.

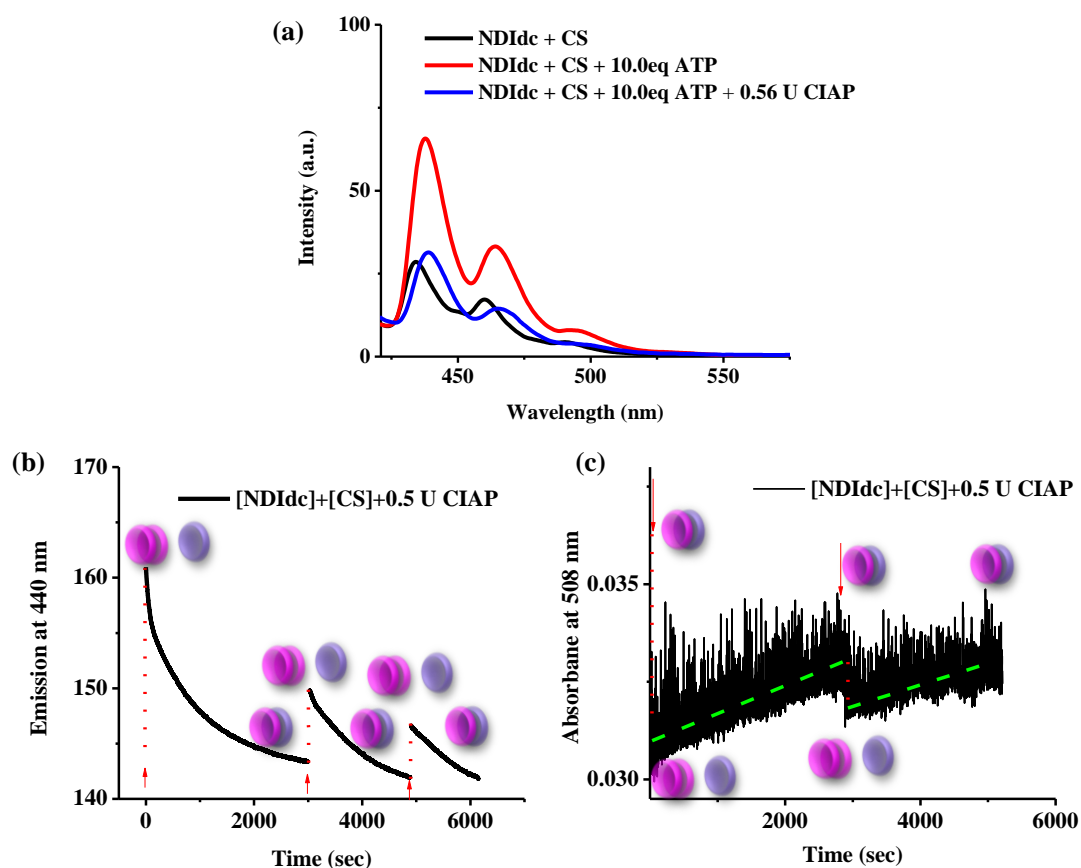


Figure 5.14. (a) Emission spectra of *NDI-dc* + *CS* responsive to ATP and CIAP. (b) and (c) Emission spectra of *CS* followed at 440 nm and Absorption spectra followed at 508 nm with time respectively. $[NDI-dc] = [CS] = 1 \times 10^{-4} M$, $[ATP] = 10 eq.$, $[CIAP] = 0.5 U$, red arrows suggest subsequent ATP addition, Buffer pH = 9

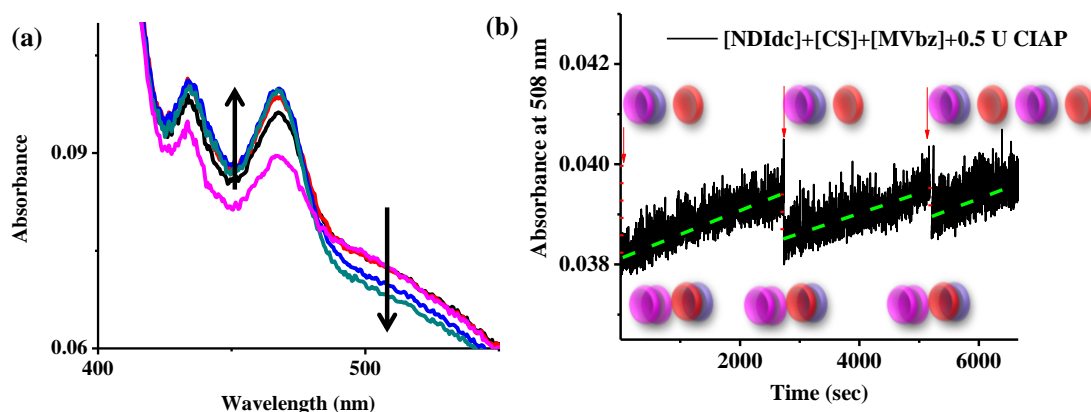


Figure 5.15. (a) Absorption spectra of *MV-bz* + *NDI-dc* + *CS* responsive to various eq. of ATP. (b) Absorption spectra followed at 508 nm with time respectively. $[NDI-dc] = [CS] = [MV-bz] = 1 \times 10^{-4} M$, $[ATP] = 10 eq.$, $[CIAP] = 0.5 U$, red arrows suggest subsequent ATP addition, Buffer pH = 9

5.3. Conclusion and Outlook

In this chapter we start with a premise of demonstrating that synthetic systems as well one can achieve conformational and aggregation control under dissipative cycles of ATP fuel. With assistance of ATP binding chromophores we show that ATP driven dissipative systems can be built and various operations can be carried out in a transient cycle. Using **ZnNDPA** we showed that conformation of an aggregate can be switched multiple times under a dissipative influence before reaching back the initial stage. We also showed that the amplitude as well as the frequency of such a transformation can be clearly controlled by enzyme concentrations. Using a different set of molecules we also build upon previously ventured concept of aggregation driven ensemble change. By controlling the aggregation by ATP transiently we could categorically show ensemble exchange for up to three components.

With the above two observations we show that this area of research is quite novel and is obviously filled with enormous possibilities, not just in effort to mimic nature but to be able to do logical commands driven by an external fuel, due impetus on its importance is warranted.

5.4. Experimental Section

General Methods:

Optical Measurements: Electronic absorption spectra were recorded on a Perkin Elmer Lambda 900 UV-Vis-NIR Spectrometer and emission spectra were recorded on Perkin Elmer LS 55 Luminescence Spectrometer. Circular Dichroism measurements were performed on a Jasco J-815 spectrometer where the sensitivity, time constant and scan rate were chosen appropriately. Corresponding temperature dependent measurements were performed with a CDF – 426S/15 Peltier-type temperature controller with a temperature range of 263-383 K.

Transmission Electron Microscopy (TEM): TEM measurements were performed on a JEOL, JEM 3010 operated at 300 kV. Samples were prepared by placing a drop of the solution on carbon coated copper grids followed by drying at room temperature. The images were recorded with an operating voltage 300 kV.

Dynamic light scattering (DLS) Experiments: The measurements were carried out using a NanoZS (Malvern UK) employing a 532 nm laser at a back scattering angle of 173°. The samples were measured in a 10 mm glass cuvette. A dead time (Time between sample loading and starting of measurement by the machine) of around 45 seconds is present in all measurements.

Materials: Calf intestinal alkaline phosphatase (CIAP) (2.8 U/mg) was ordered from SRL. Adenine tri-phosphate disodium hydrate (99%) was procured from Sigma Aldrich. Phosphate buffer solutions of various pHs was made according to the reported protocol.¹³

Synthesis: CS,¹⁴ MV-bz,¹⁵ ZnNDPA,¹² NDI-dc¹⁶ were synthesized according to the reported procedures and sufficiently characterized.

5.5. References and Notes

1. Westheimer, F. H. *Science*, 1987, **235**, 1173.
2. Shikinaka K.; Takaoka S.; Kakugo A; Osada Y.; Gong J. P. *J. App. Pol. Sci.* 2009, **114**, 2087.
3. Lowery L. A.; Vactor D. V. *Nat. Rev. Molecular cell Biology* 2009, **10**, 332.
4. Kasai M.; Asakura S.; Oosawa F. *Biochim. Biophys. Acta.* 1962, **57**, 22 .
5. Häggström, Mikael. "Medical gallery of Mikael Häggström 2014". Wikiversity Journal of Medicine 1 (2). doi:10.15347/wjm/2014.008. ISSN 20018762. - Walter F., PhD. Boron (2003) Medical Physiology: A Cellular And Molecular Approach, Elsevier/Saunders, pp. 1,300 ISBN: 1-4160-2328-3. Page 28, Public Domain, <https://commons.wikimedia.org/w/index.php?curid=3425975>.
6. Mitchison T.; Kirschner M. *Nature* 1984, **312**, 237.
7. Hayashi T.; Chiba S.; Kaneta Y.; Furuta T.; Sakurai M. *J. Phys. Chem. B* 2014, **118**, 12612.
8. Pezzato C.; Prins L. J. *Nat. Commun.* 2015, doi: 10.1038/ncomms8790.
9. Maiti S.; Fortunati I.; Ferrante C.; Scrimin P.; Prins L. J. *Nat. Chem.* 2016 doi: 10.1038/nchem.2511.
10. Kumar M.; George S. J. *Chem. Commun.* 2012, **48**, 10948.

11. Kumar M.; George S. J. *Chem. Sci.* 2014, **5**, 3025.
12. Kumar M.; Brocorens P.; Tonnelé C.; Beljonne D.; Surin M.; George S. J. *Nat. Commun.* 2014, doi: 10.1038/ncomms6793.
13. <http://delloyd.50megs.com/moreinfo/buffers2.html>
14. Ghosh A.; Rao K. V.; George S. J.; Rao C. N. R.; *Chem. Eur. J.* 2010, **16**, 2700.
15. Xu J.-F.; Huang Z.; Chen L.; Qin B.; Song Q.; Wang Z.; Zhang X. *ACS Macro Lett.* 2015, **4**, 1410.
16. Sissi C.; Lucatello L.; Krapcho A. P.; Maloney D. J.; Boxer M. B.; Camarasa M. V.; Pezzoni G.; Menta E.; Palumbo M. *Bioorg. Med. Chem.* 2007, **15**, 555.

Chapter-6

Photo-Chemistry on Clay-Chromophore Hybrids

Chapter-6a:

***Shining the Light on Clay-Chromophore Hybrids: Layered
Templates for Accelerated Ring Closure Photo-Oxidation***

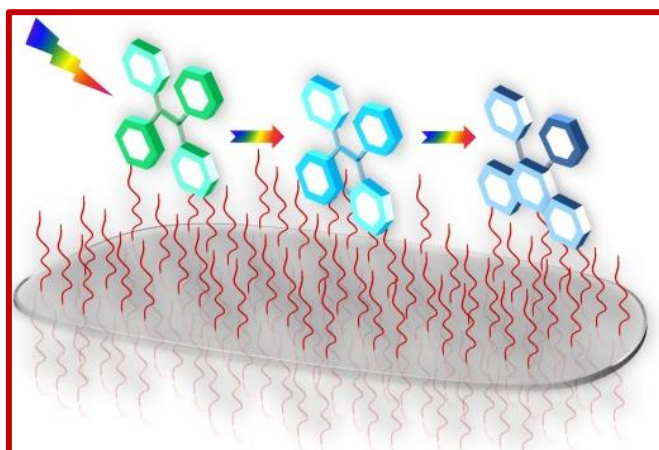
Chapter-6b:

***Light Induced in-situ Post-Modification of Clay-Chromophore
Hybrids for Multiple White Light Emissions***

Shining the Light on Clay-Chromophore Hybrids: Layered Templates for Accelerated Ring Closure Photo-Oxidation

Abstract

Templates with specific microenvironments have been long employed to facilitate specialized reactions. From enzymes to metal organic frameworks (MOFs), various systems have exerted their prowess to effect specific chemical reactions. We in this Chapter present, for the first time, acceleration of a ring closure photo-oxidation due to the specific structural constraints provided by layered materials. A stilbene derivative has been used as a prototype reactant and the dihydrophenanthrene intermediate has been isolated and characterized en route to complete photo-oxidation. Combining the gathered evidence, possible mechanism for the chemical transformation has been proposed. Kinetic analysis showed that layered materials help to manipulate the rate of electrocyclic ring closure and in turn accelerate the complete reaction sequence. The structural microenvironment induced by layered materials could be a unique platform to probe and stabilize plethora of photo-oxidative reactions and intermediates.



Publication based on this work: *Chem. Sci.* 2015, **6**, 6334.

6a.1. Introduction

Molecular templates have been long known to provide local environments for specific chemical reactions by virtue of its structural and functional prowess. Enzymes, DNA are some naturally occurring examples.¹ Interior environment of polymers, artificial cage like systems such as MOFs and their discrete versions have been well explored for probing interesting reactions and intermediates.^{2,3} Unique chemical reactions have also been demonstrated by exploiting inorganic layered compounds with functional interlayer galleries⁴ which can be considered as analogues of aforementioned inorganic templates and thus can be explored for reactions susceptible to confinement effects.⁵ Layered compounds such as clay have been a subject of interest in a wide variety of fields especially for studying the photo-physical properties of dye conjugates.⁶ Chemical reactions that are governed by light are most susceptible to pre-organization. However only handful of light mediated chemical transformations have been carried out on clay surfaces and ring closure photo-oxidation of stilbene systems have been one of the rarely investigated themes in clay microenvironments.⁵ Furthermore the sensitizers employed for these photo-oxidation reactions (external sensitizers or inherent ions in the clay) photo-resulted in either [2+2] dimers or fission products of the ethylene bond.⁷ Ring closure photo oxidation reactions in stilbene systems to phenanthrene derivatives are synthetically important as they are one of the important steps in synthesis of various poly-aromatic hydro-carbons.⁸ This reaction has also been studied in detail with special impetus on trapping the di-hydrophenanthrene intermediate. The di-hydrophenanthrene derivative has been isolated only in anaerobic conditions and has been a key step in control-ling the rate of the overall reaction.^{9,10} In the reaction sequence ring closure turns out to be the slower step and hence the rate determining step. As soon as di-hydrophenanthrene is formed it is oxidized to its phenanthrene analogue.^{9,10} Hence, increasing the rate of ring closure will enhance the rate of phenanthrene formation. Generally, these reactions are carried out in presence of an oxidizing agent such as 2,3-dichloro-5,6-dicyano-1,4-benzoquinone (DDQ)

or I₂, owing to the slow photo-chemical reaction rate.¹¹ It has therefore been a challenge to look for a strategy to enhance the rate of such reactions photo-chemically.

In this Chapter we, for the first time, observe that kinetic pathways of organic photo reactions can be modulated on layered inorganic templates. Photoreactions on stilbene derivatives have been a research venue for decades; however it has been shown for the first time in this chapter that its ring closure photo-oxidation kinetics can be biased while it is conjugated on an inorganic clay surface. In addition, during the photo-reaction process we have isolated a di-hydro phenanthrene derivative as an intermediate which has proved to be a challenging task in the past. These derivatives are generally very unstable and their complete characterization as described in this Chapter is very rare.

6a.2. Results and Discussion

6a.2.1. Design Strategy

The inorganic template we have used to construct the microenvironment for chemical modification is amino clay (**AC**).^{12a} It has a structure analogous to 2:1 trioctahedral smectite with an approximate composition of R₈Si₈Mg₆O₁₆(OH)₄, where R stands for covalently linked aminopropyl chains (Figure 6a.1a). These clays do not have sensitizing action because of the absence of metal ions such as Al³⁺ and Fe³⁺.¹²

Moreover, the optically transparent nature of the **AC** facilitates photochemical reactions and its high dispersity helps in maintaining the reaction mixture homogeneous. **AC** when mixed in water undergoes exfoliation, resulting in a clear solution, owing to the spontaneous protonation of the amine groups on the surface. Recently many possibilities that can arise from the use of amino clay (**AC**) as a soft hybrid for various photo-physical prospects have been explored.¹²

Tetraphenylethylene (**TPE**) and its derivatives are stilbene analogues having a rich history of photo-physical and photo-chemical phenomena.¹³ With regards to photo-physical properties they are known to show higher quantum yield of emission once their

rotating phenyl propellers are arrested in motion.¹⁴ Enhanced emission due to restricted rotation has been used extensively for applications in opto-electronics and as fluorescent probes.¹⁴ On the other hand TPEs, being derivatives of stilbenes, also undergo the unique photo-chemical modifications such as the photo-oxidation which yields the phenanthrene derivative after a [4+2] electrocyclic ring closure.⁹ We envisage that conjugating TPE moieties on clay can result in restricted rotation of the phenyl rings which can enhance the probability of ring closure. Considering the nature of our inorganic template (positively charged amino clay) a negatively charged TPE derivative was selected i.e. tetraphenylethylene tetra potassium salt (**TPTS**) (Figure 6a.1b).

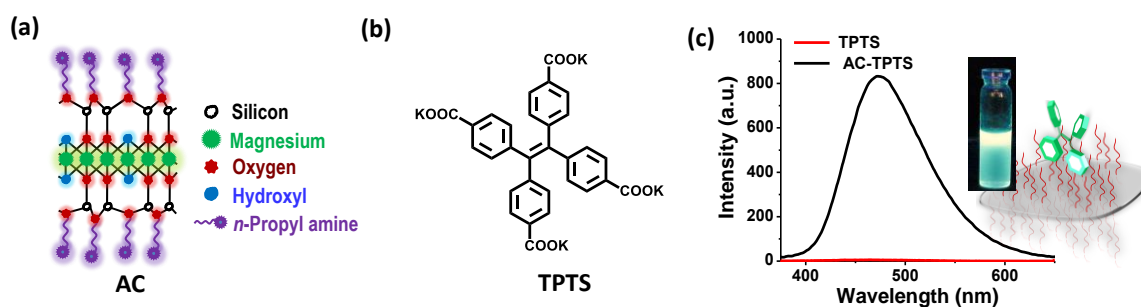


Figure 6a.1. (a) Schematic showing the structure of amino clay (AC), (b) Molecular structure of **TPTS** and (c) Emission spectra showing the enhanced emission from **TPTS** ($10^{-4}M$) on binding to AC (0.9 wt%), this dye conjugated state has been designated as **AC-TPTS**, ($l = 1$ cm, $\lambda_{exc} = 350$ nm, water) (inset shows the photograph of 365 nm illuminated solution of the clay-dye conjugate alongside the respective schematic).

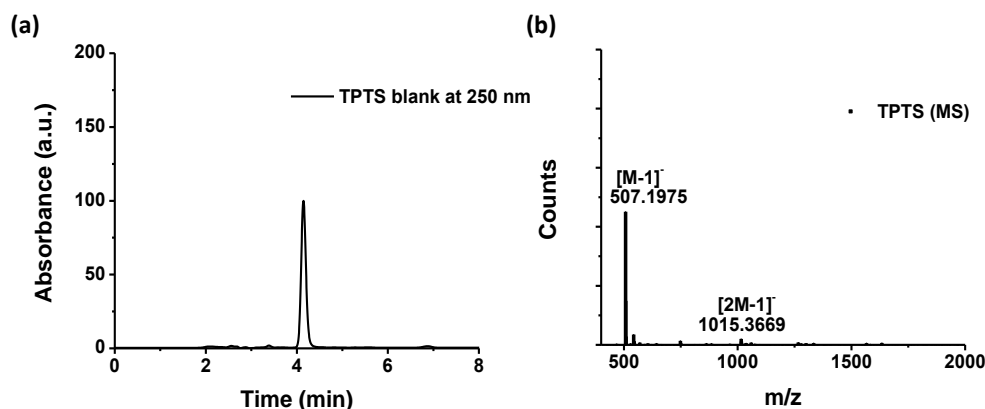


Figure 6a.2. (a) HPLC trace of **TPTS acid** obtained by monitoring the absorbance at 250 nm, (b) ESI-HRMS of **TPTS acid**.

TPTS was synthesized according to the known procedure¹⁵ and the molecule was characterized by NMR spectroscopy and mass spectrometry (MS) (Figure 6a.2 and 6a.3). **TPTS** has been studied in the past for its restricted rotation in MOFs by Dincă *et al.*¹⁶ Photochemistry on this molecule however has not been explored. Considering the classic model of electrocyclic ring closure, photo-oxidation of **TPTS** is expected to proceed to phenanthrene derivative (**PHES**) via a 4,4'-di-hydro phenanthrene intermediate (**DHPS**) (Figure 6a.4c).⁹

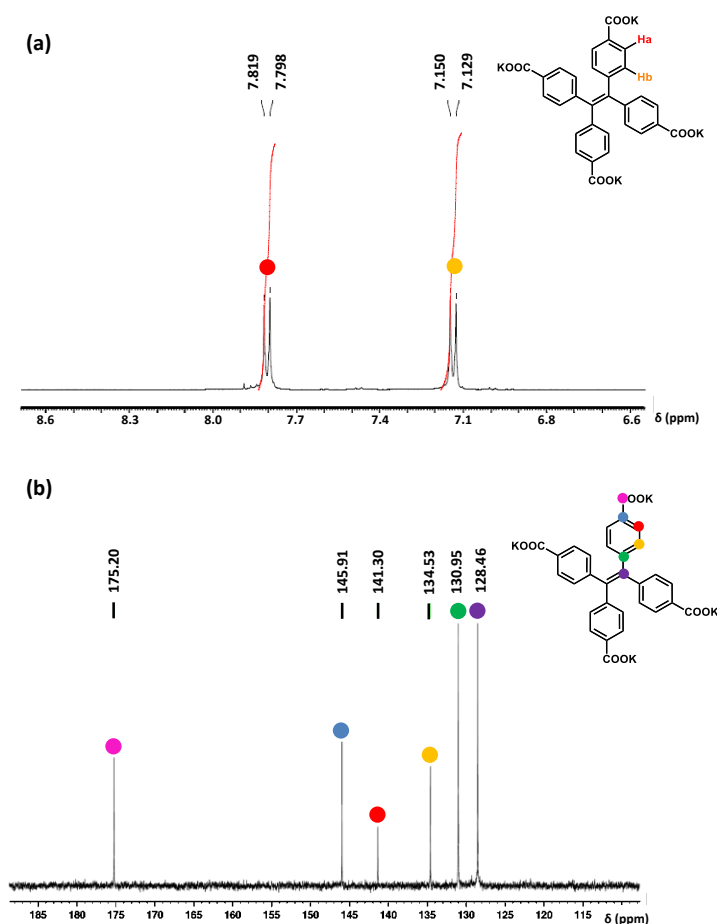


Figure 6a.3. (a) and (b) ¹H and ¹³C-NMR spectra of TPTS in D₂O respectively.

6a.2.2. Clay-Dye Conjugation

Preliminary experiments suggested that **TPTS** when conjugated with **AC** results in restriction of rotation of phenyl rings. The flattening of $^1\text{H-NMR}$ peaks and the emission enhancement in the clay-dye conjugate (**AC-TPTS**) (Figure 6a.1c) strongly support the restricted rotation of phenyl rings on clay surfaces (Figure 6a.5).

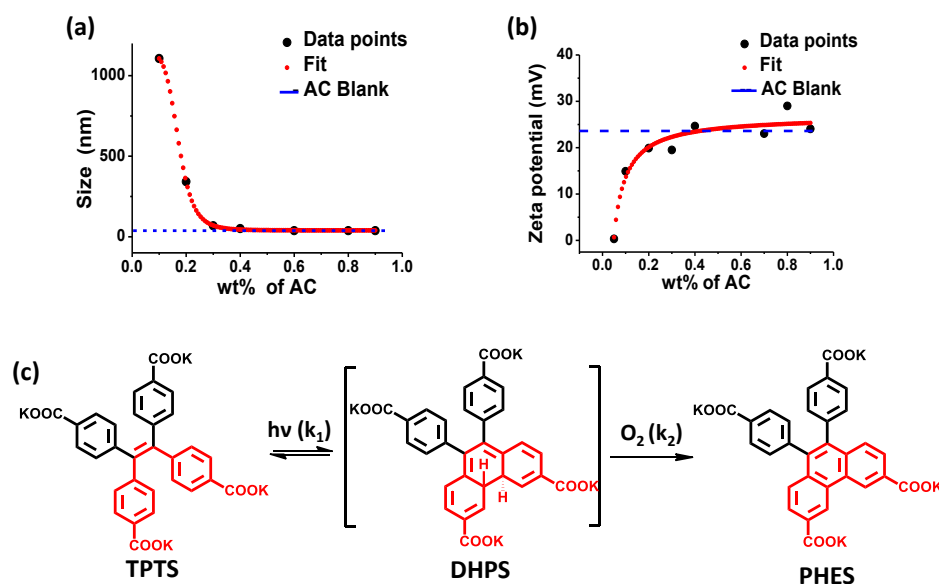


Figure 6a.4. (a), (b) DLS and Zeta potential trends of **TPTS** (10^{-4}M) with various weight percentages of **AC**. (c) Reaction sequence showing the expected photo-oxidation reaction undergone by **TPTS** (stilbene moieties marked in red). k_1 , and k_2 mentioned above the arrowheads are the forward rate constants.

To further understand the characteristics of the clay-dye conjugate, to a fixed concentration of aq. **TPTS** (10^{-4}M) various wt% of **AC** were added and their dynamic light scattering (DLS) and Zeta potential data were recorded (Figure 6a.4a-b). It can be evidently seen that beyond neutralization point in zeta potential (0 mV at 0.03 wt%), size and charge density of the conjugate approaches that of single **AC** sheets. Therefore to study the photochemistry of **TPTS** on clay surface, concentration of **AC** is fixed at 0.9 wt% as it ensures complete binding and a highly homogenous dispersion.

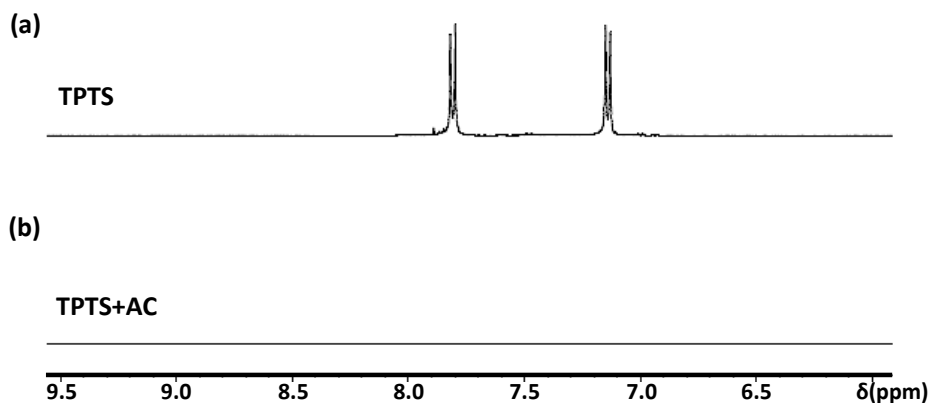


Figure 6a.5. (a) and (b) ^1H NMR spectra of **TPTS** in D_2O and **TPTS+AC** conjugate respectively. (a) and (b) show that as soon as **TPTS** is conjugated to 0.9 wt% **AC** the phenyl proton peaks disappear in the conjugate. We hypothesize this is due to the increase in T_2 relaxation time caused by the restricted rotation of phenyl rings on clay surfaces. This increase in T_2 is then responsible of broadening to the extent of flattening the proton peaks.

6a.2.3. Photo-Chemical Studies

Before analysing the photo-chemical characteristics of **AC-TPTS** we sought to understand the chemistry of aqueous **TPTS** solution under light (Figure 6a.6). A 10^{-4} M solution of **TPTS** was irradiated under a 254 nm lamp (Figure 6a.6a,b). Initially at $t = 0$ the emission is quenched due to non-radiative decay processes.⁸ With time the evolution of an emission with λ_{max} at 404 nm could be observed (Figure 6a.6b) signifying the formation of phenanthrene derivative. The intensity of the band at 400 nm was plotted against time which showed a monotonic increase in intensity (Figure 6a.6c). The reaction took around 750 mins to complete. Liquid chromatography-mass spectrometry (LC-MS) analysis of a 100 min aliquot showed two peaks (marked as 1 and 2 in Figure 6a.6d). The UV/vis absorption spectra and MS of fraction 1 corroborated with the starting material (**TPTS**) while fraction 2 pertained to **PHES**, as evident from the $[\text{M}-2]$ ion in MS signifying loss of two protons due to oxidative ring closure (Figure 6a.7).

Time dependent ^1H -NMR measurements were made of the irradiated sample and visual interpretation of the ^1H -NMR showed signs of C_2 -symmetric species being formed which also confirms the existence of the phenanthrene derivative (Figure 6a.8). Having known

that the chemistry involving in the photo-conversion of stilbene derivatives to phenanthrene is a two-step process (Figure 6a.4c), observation of a monotonic conversion into the final product points to the case of series reactions with $k_2 > k_1$. Considering the fact that di-hydrophenanthrene intermediate is highly susceptible to oxidation, the hypothesis seems reasonable.⁹ Therefore the evolution of phenanthrene can be fit into this specific limiting case of reaction in series and rate constant can be extracted (Figure 6a.10). However from the steady state data only the slower reaction step (k_1) i.e. the rate constant involved in electrocyclic ring closure, can be extracted (Figure 6a.9). After fitting to an appropriate function k_1 was found to be $3.7 \times 10^{-3} \text{ s}^{-1}$.

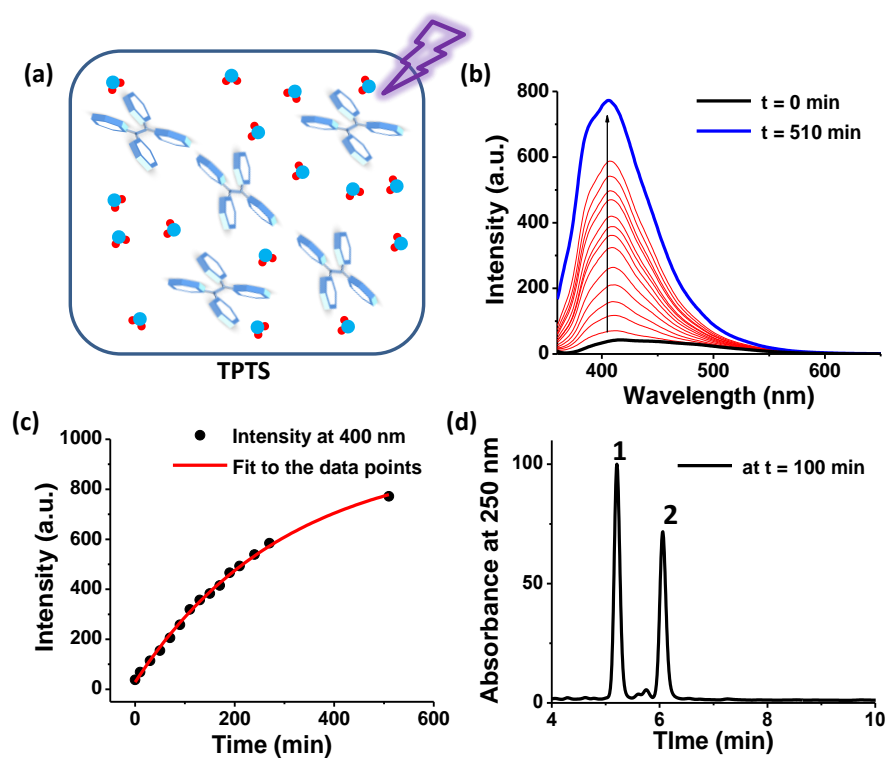


Figure 6a.6. (a)-(d) (top panels) Represent the photo-oxidation of nascent *TPTS* while (e)-(h) (bottom panels) represent photo-oxidation of the *TPTS* and *AC* conjugate in aqueous solution ($[TPTS] = 10^{-4}M$, $l = 1 \text{ cm}$, $\lambda_{exc} = 350 \text{ nm}$, water). (a) Schematic representation of irradiation of nascent *TPTS* molecules in water, b) Time dependent emission spectra of photo-oxidation of aqueous *TPTS* solution under 254 nm irradiation, (c) Fluorescence intensity trace at 400 nm of the photo-oxidation profile of *TPTS*, d) HPLC chromatogram after 100 mins of irradiation probed at 250 nm absorption.

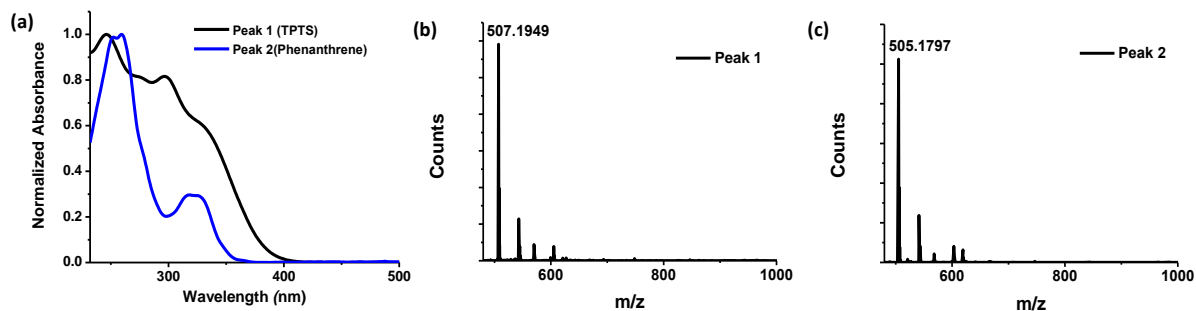


Figure 6a.7. (a) UV absorption spectra and (c), (d) ESI-MS of respective HPLC peaks in Figure 6a.6d.

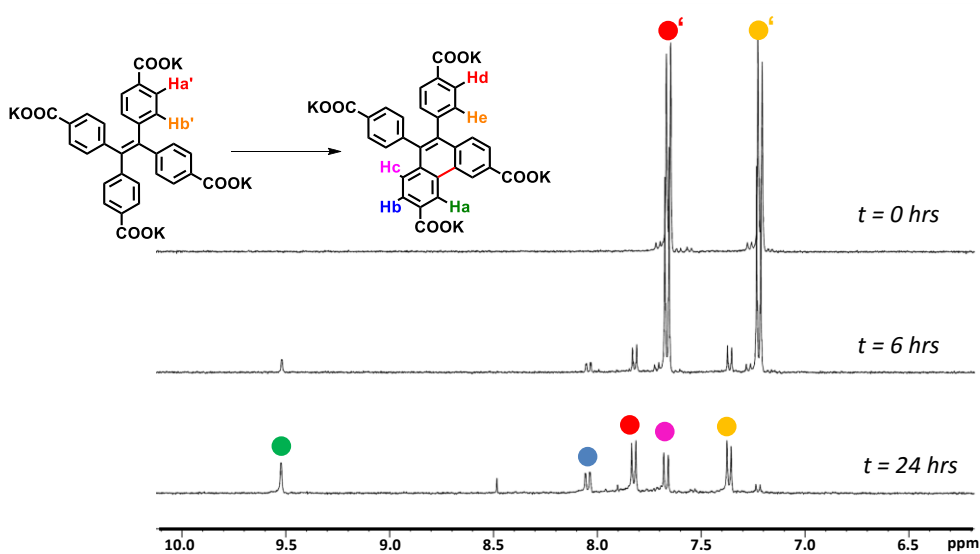


Figure 6a.8. ^1H -NMR spectra of TPTS in D_2O under various times of 254 nm illumination, inset shows the molecular structure of the transformation.

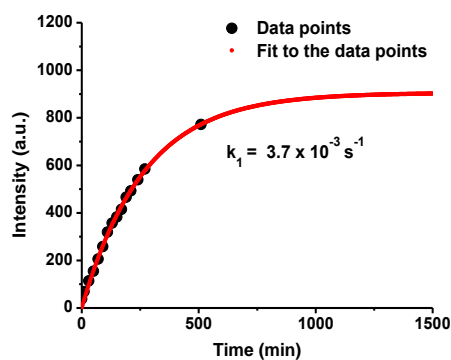


Figure 6a.9. Emission intensity trace at 400 nm of the photo-oxidation profile of TPTS (10^{-4}M , $l = 1\text{ cm}$, $\lambda_{\text{exc}} = 350\text{ nm}$, water) under 254 nm irradiation with a fit to equation 7 shown in Figure 6a.10.

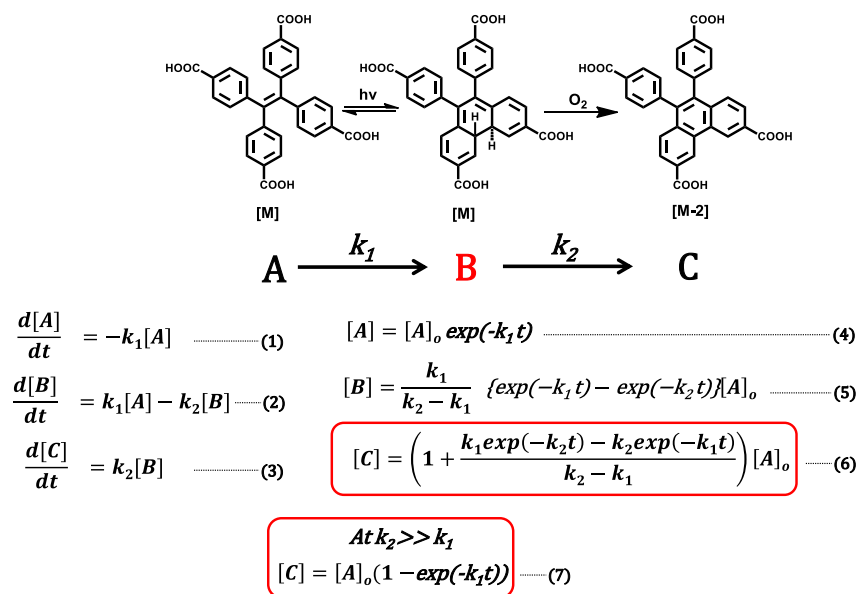


Figure 6a.10. (a) Kinetic equations showing the expression for a series reaction approximated for conditions of $k_2 \gg k_1$.

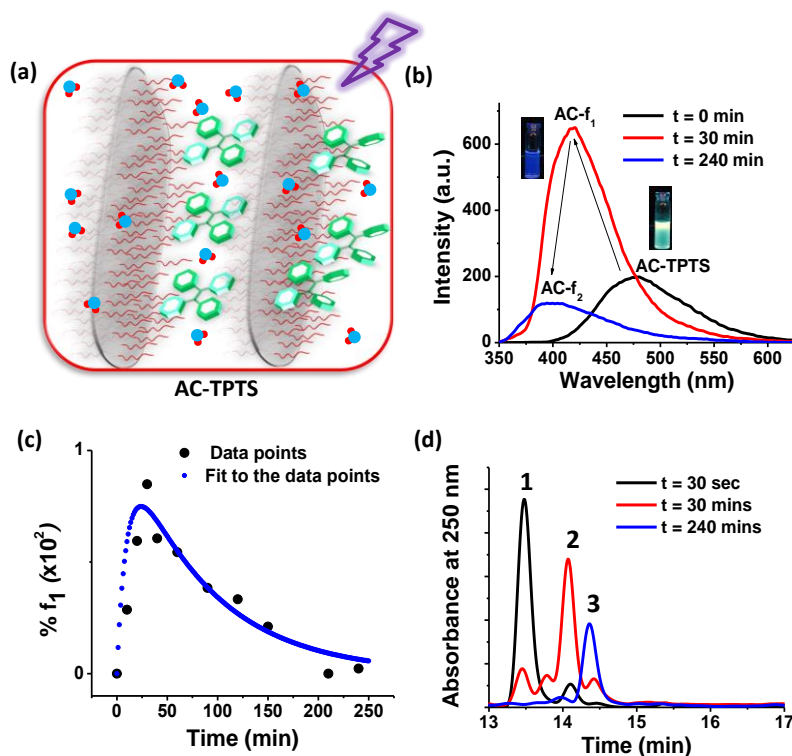


Figure 6a.11. (a) Schematic representation of irradiation of TPTS and AC conjugate, (b) Time dependent emission spectra of photo-oxidation of TPTS ($10^{-4}M$) and AC (0.9 wt%) conjugate under 254 nm irradiation (inset shows the photographs of 365 nm illuminated solutions of AC-TPTS and AC-f₁), (c) Fluorescence intensity trace at 400 nm of the photo-oxidation profile of TPTS and AC conjugate and (d) HPLC chromatograph at various times of irradiation probed at 250 nm absorption.

Interestingly, on the other hand clay-dye conjugate (**AC-TPTS**) (Figure 6a.11a) when irradiated with 254 nm light showed the progression to the final photoproduct via a two-step process as evident from the corresponding fluorescence changes (Figure 6a.11b-c). Initial state **AC-TPTS** ($\lambda_{\text{max}} = 475$ nm) after 30 mins went to a state **AC-f₁** ($\lambda_{\text{max}} = 420$ nm) and then finally after 240 mins to **AC-f₂** ($\lambda_{\text{max}} = 400$ nm). **AC-TPTS** to **AC-f₁** transition was rapid and reached a maximum at around 30 mins. Transformation of **AC-f₁** to **AC-f₂** was rather slow and took another 210 mins to complete (Figure 6a.11b). Remarkably the photo oxidation was complete in 240 mins which was one third of the time taken without **AC**. The compositions **f₁** and **f₂** were extracted from the clay conjugates (**AC-f₁** and **AC-f₂** respectively) and were analysed by LC-MS (Figure 6a.11d, 6a.12, 6a.13). LC-MS of **f₂** showed the formation of phenanthrene (**PHES**, marked with 3 in Figure 6a.11d).

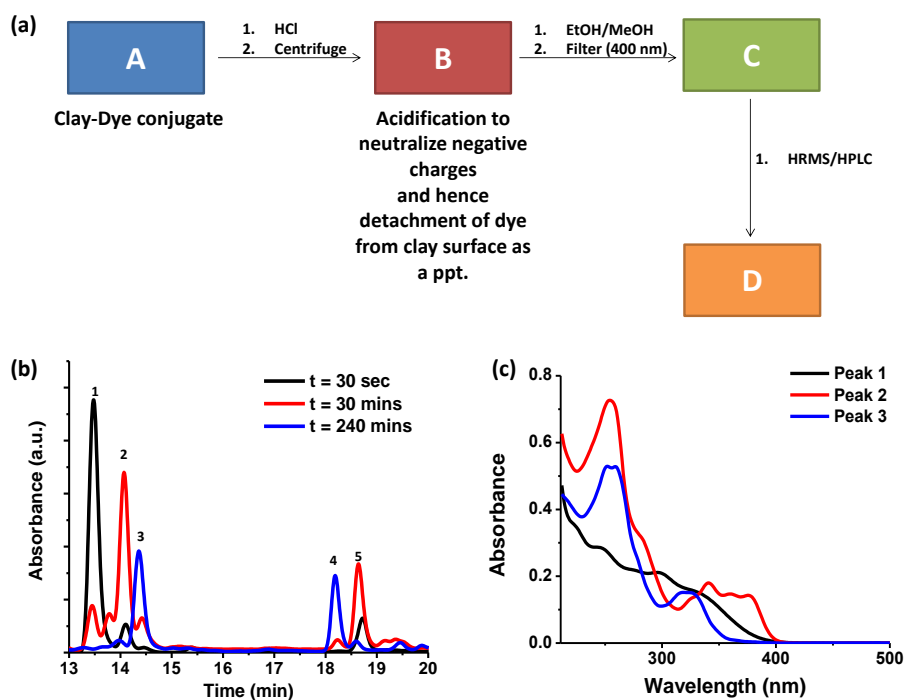


Figure 6a.12. (a) Extraction procedure of TPTS from clay. HRMS/HPLC carried out on the acidified product i.e. the carboxylic acid and not the carboxylate. (b) Complete HPLC profile of Figure 6a.11d. Peaks 4 and 5 are the by-products during the photo-irradiation. They are primarily decarboxylated versions of 2 and 3 (vide infra). (c) UV absorption spectra of respective HPLC peaks in Figure 6a.11d.

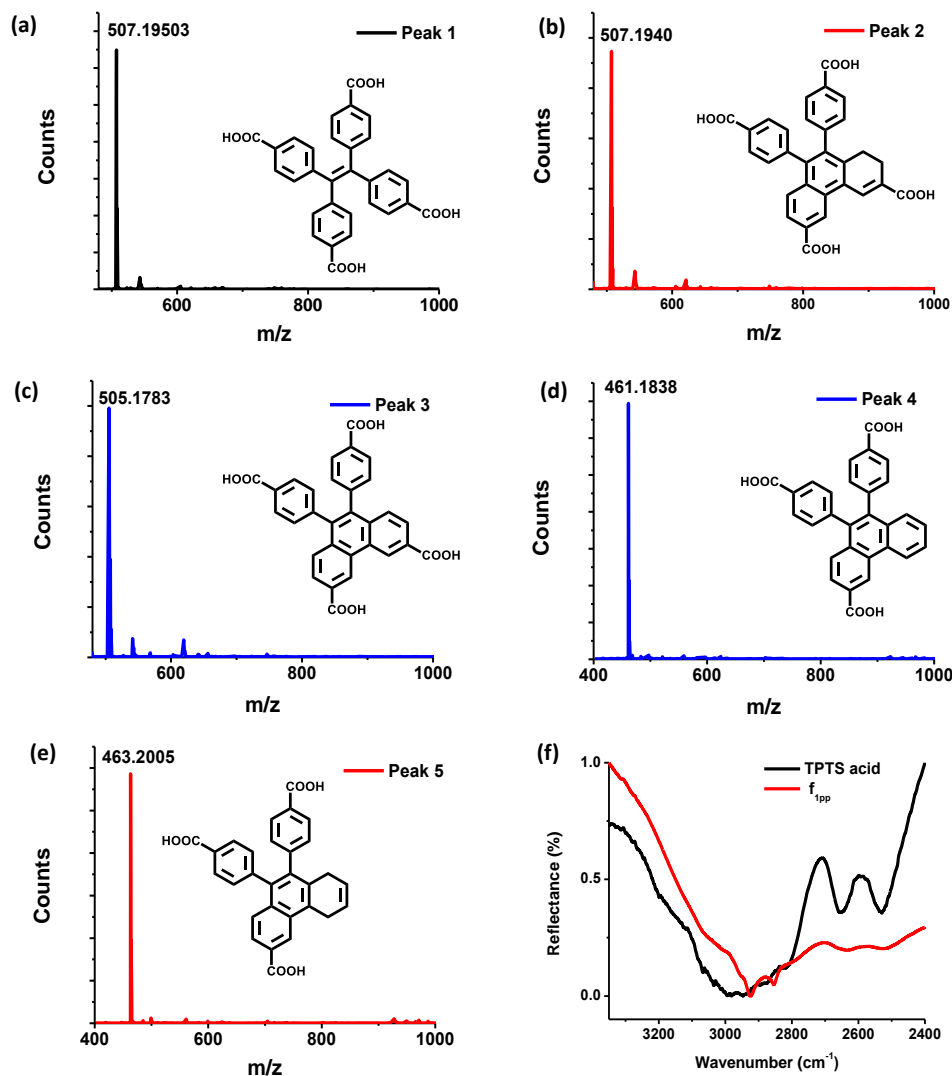


Figure 6a.13. (a)-(e) ESI-HRMS of respective HPLC peaks in Figure 6a.11d and Figure 6a.12b. (f) ATR-IR spectra of **TPTS acid** and extracted f_{1pp} .

UV/vis absorption and Electrospray ionization-Mass spectrometry (ESI-MS) performed on these fraction also corroborated with the conclusion that the f_2 is predominantly a phenanthrene derivative (**PHES**) (Figure 6a.13). LC-MS of **AC-TPTS** extract after 30 seconds of irradiation was majorly comprised of the starting material (**TPTS**, marked as 1 in Figures 6a.11d, 6a.13). It did however show traces of an intermediate peak (retention time (r.t.) = 14 mins) which eventually became the major peak in fraction f_1 after 30 mins (marked with 2 in Figure 6a.11d). Interestingly, UV/vis absorption of this fraction showed a red shifted band (366, 377 nm) as compared to the starting material (330 nm)(Figure 6a.12c). ESI-MS analysis however showed that

the mass of this intermediate was same as the starting material (Figure 6a.13). This evidence hints towards **f₁** to be comprised of a di-hydrophenanthrene derivative. Attenuated total reflectance-Infra red (ATR-IR) analysis done on the intermediate showed the shifting of C-H stretch to a lower wavenumber (2962 to 2924 cm⁻¹) as compared to the **TPTS acid** which also signifies the introduction of a sp³ hybridized C-H bond (Figure 6a.13f).

Since di-hydro phenanthrene derivatives have been rarely isolated and characterized we decided to do extensive characterization of these species.¹⁰ Visual interpretation of ¹H and ¹³C-NMR showed that the spectra deviates from C₂-symmetric spectra obtained for phenanthrene (See appendix Figure A1-A6). Moreover in ¹H-NMR two triplets could be clearly seen in the low field region of 2.6-2.8 ppm. From heteronuclear correlation spectra (HETCOR) (See appendix Figure A8-A9) these ¹H-peaks at around 2.6-2.8 ppm could be correlated with the -CH₂ peaks as determined by DEPT (Figure 6a.14). The remainder of the -CH correlations were also made once the 2D spectra was analysed (See appendix Figure A7). Having understood the carbon skeleton of the molecule we went ahead to decipher the proton correlation existing in **f_{1pp}**.

¹H-correlation spectroscopy (COSY) helped in understanding the through bond proton connections of the molecule (**f_{1pp}**, Figure 6a.15, See appendix Figure A10-A12). Protons H_i and H_g correlated with H_j and H_h respectively confirming the nascent aromatic structure of part of the molecule which did not taken part in the photo-reaction (Figure 6a.4c, See appendix Figure A10). Proton H_c correlated with H_d confirming the presence of an aromatic system in the modified part of the molecule (Figure 6a.15, See appendix Figure A10). Proton designated as H_a correlated with another aromatic proton H_c which signified a four proton meta coupling (Figure 6a.15, See appendix Figure A11). Moreover, proton H_b correlated with the low field -CH₂ proton signifying a four bond allylic coupling (Figure 6a.15, See appendix Figure A12). These two observations stated above strongly confirm that one part of the ring is aromatic and the other is not, thus explaining the loss of C₂-symmetry of the ¹H-NMR spectra. Furthermore these H_a and H_b proton were found to correlate in the nuclear overhauser effect (NOE) spectra, thus confirming the

relation between the aromatic and the non-aromatic parts (Figure 6a.15, See appendix Figure A13). Also H_f correlated to H_g via NOE, proving the connection between the photo-modified and nascent parts of the molecule (Figure 6a.15, See appendix Figure A13). Thus, the results derived from NMR spectra confirmed that the di-hydrophenanthrene (Peak 2 in Figure 6a.11d) that we obtained is the 1,2-di-hydro derivative (f_{1pp}). In addition to above discussed photoproducts the fraction f_1 and f_2 also contained decarboxylated products of di-hydrophenanthrene intermediate (f_{1dc}) and phenanthrene respectively, as a minor product, as elucidated from the chromatogram peaks at higher retention times, which has also been characterized with various techniques (Figure 6a.12b, See appendix Figure A14-A18). We hypothesize that the parent structure of f_{1pp} and f_{1dc} is indeed **DHPS** and f_{1pp} is perhaps formed by a sequence of [1,3]-sigmatropic shifts from **DHPS** (See appendix Figure A19). We also hypothesize that the origin of the decarboxylated derivative is an offshoot of the main reaction step. Thus the net composition of **DHPS** formed could be approximately translated to the summation of f_{1pp} and f_{1dc} (See appendix Figure A19).

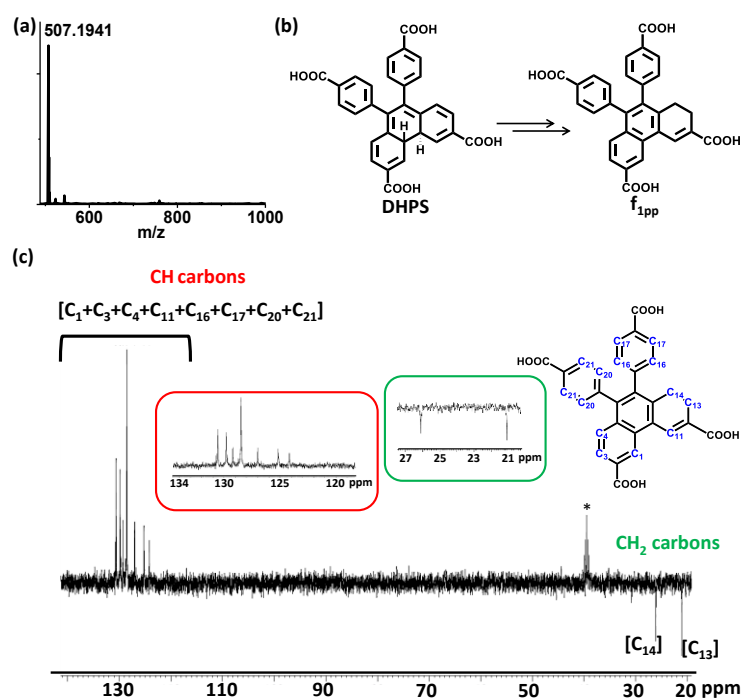


Figure 6a.14. (a) Shows the ESI-HRMS of f_{1pp} in negative ion mode, (b) Chemical transformation of **DHPS** to f_{1pp} and (c) shows DEPT spectra of f_{1pp} in CD_3OD (inset showing the zoomed ppm regions (120-134 and 21-27) and f_{1pp} structure with designated $-CH$ and $-CH_2$ carbons, * signifies $DMSO-d_6$ peak).

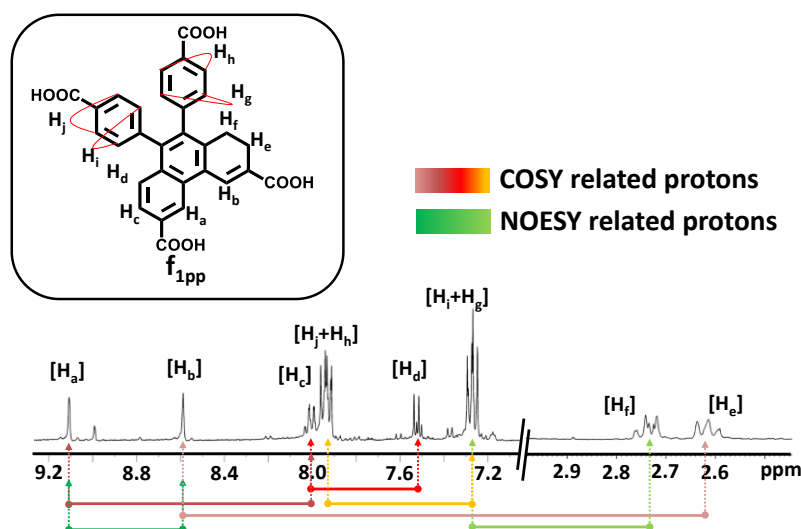


Figure 6a.15. ¹H-NMR spectra of **f**_{1pp} in CD₃OD (inset shows the molecular structure of **f**_{1pp} with designated protons). Lines and arrows below the ¹H-spectra show the summary of ¹H correlations observed in **f**_{1pp}

Coming back to the reaction in series scheme the time evolution shown in Figure 6a.11c resembles the one in which $k_1 > k_2$ (See appendix Figure A20). Hence fitting the kinetics to the appropriate function we derived the rate constants as $k_1 = 0.1 \text{ s}^{-1}$ and $k_2 = 1.2 \times 10^{-2} \text{ s}^{-1}$ (See appendix Figure A20). This particular photo-activity also suggests that in clay conjugates, k_1 was enhanced 100 fold compared to the nascent **TPTS** solution. The enhancement was to the extent that k_1 eventually became larger than k_2 hence suggesting that rate of formation of **DHPS** became higher than the rate of its subsequent oxidation. **DHPS** however is not photo-stable and owing to its photo-reactivity, is converted to **f**_{1pp} which is eventually oxidized to form **PHES** (See appendix Figure A19). To the best of our knowledge observations made above make this the only system in which the di-hydro phenanthrene derivative has been observed in aerobic conditions with a complete elucidation of the structure.

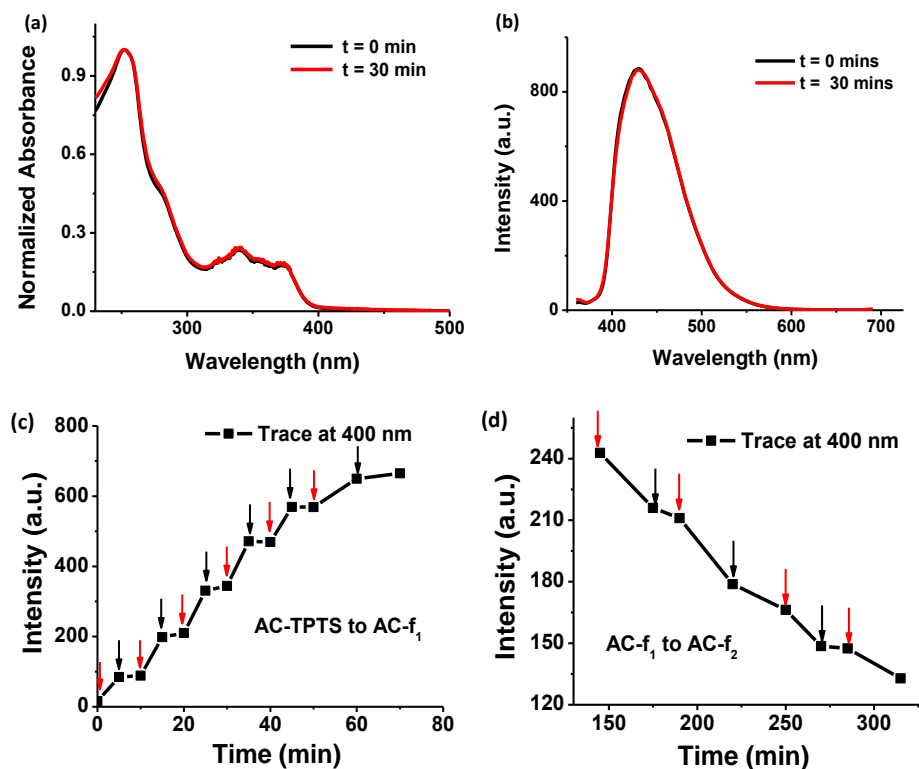


Figure 6a.16. (a) and (b) UV absorption and emission spectra respectively of f_{1pp} under varying exposure times of oxygen gas. (c) and (d) showing the emission intensity of AC (0.9 wt%) conjugated TPTS ($10^{-4}M$) ($l = 1$ cm, $\lambda_{exc} = 350$ nm, water) followed at 400 nm under light (red arrows, 254 nm irradiation) and dark conditions (Black arrows) for various times (a: AC-TPTS to AC- f_1 , b: AC- f_1 to AC- f_2)

Di-hydro phenanthrene derivatives are known to be highly susceptible to oxidation and most times atmospheric oxygen is capable of converting them to their oxidized counterpart.⁹ Therefore to a methanol solution of f_{1pp} we purged oxygen gas for over 30 mins. To our surprise absolutely no change was observed in UV/vis absorption and fluorescence measurements (Figure 6a.16a,b). This was quite anomalous as it hinted towards the fact that oxidation of f_{1pp} to phenanthrene is not driven by oxygen alone which is contrary to conventional wisdom. Figure 6a.16 c-d show that as the 254 nm irradiation over the clay-dye conjugates (AC-TPTS) is switched off, rates of both processes (AC-TPTS to AC- f_1 and AC- f_1 to AC- f_2) are significantly retarded. This points to the fact that not only TPTS to f_{1pp} is governed by light; f_{1pp} to PHES is also critically photo-controlled. Since the final oxidation cannot be done by light alone this hints that in this case f_{1pp} to

PHES is a rare situation of “true” photo-oxidation which refers to interaction of the excited state of the molecule with oxygen to give the oxidation product.¹⁷

Furthermore, we investigated the possibility of propyl amine chains (which are a component of **AC**) acting as a base in the photo reaction.¹⁸ Hence, we carried out the irradiation of **TPTS** in presence of varying amounts of *n*-propyl amine (Figure 6a.17). Kinetics of these transformations was far too slow, to be compared with **AC**, to have any significant impact on the reaction outcome (Figure 6a.18). These results clearly rule out the contribution of amino propyl groups as a base in clay for influencing the reaction rates and thus further reiterate that the conformation restriction perhaps plays a major role in the transformation.^{19,20}

6a.3. Conclusion and Outlook

In conclusion we have successfully shown that interlayer galleries can be used as a template to explore the increased rate of photo-oxidations in stilbene like systems. We show that there is a marked change in rate constants of photo-oxidation once **TPTS** is conjugated in galleries of amino clay (Figure 6a.19). This change points towards the use of restricted rotation of phenyl rings of **TPTS** on the **AC** sheet being an important factor in tipping the scales of rate constants. On clay the ring closure, which was initially a slow step, becomes 100 times faster hence overtaking the oxidation step. This presents a unique case in which electrocyclic ring closure was modulated on clay surfaces. This system also presents a unique study where, the usually unstable, di-hydrophenanthrene derivative was isolated in the form of 1,2-di-hydro phenanthrene and structurally analysed giving a major insight into the reaction process. The study thus opens the door to investigations of reactions involving variety of chromophores on layered materials as well as other variety of organic-inorganic hybrids and not just for their rate of reactions but also for stabilization of unusual intermediate states which can be achieved by this strategy.²¹

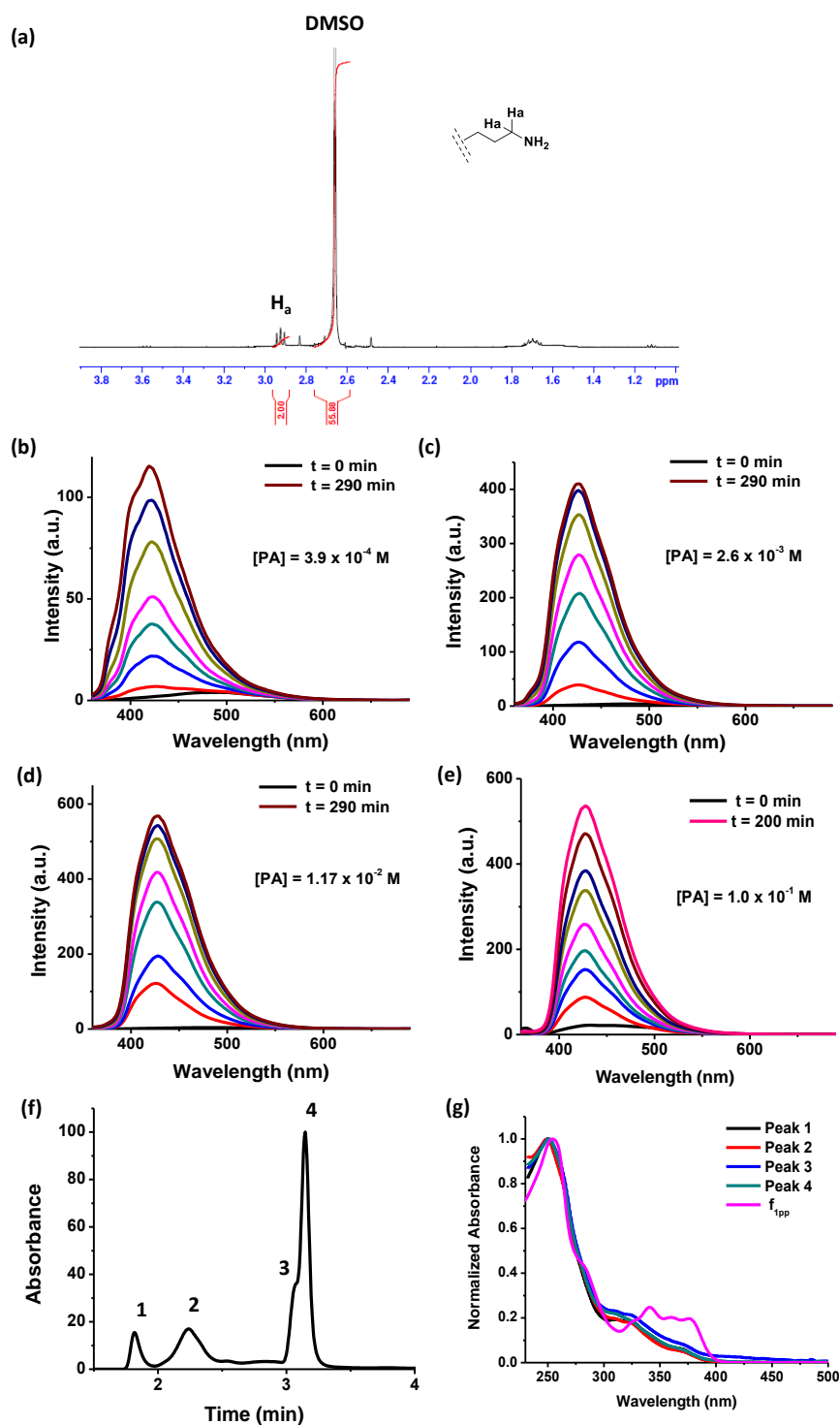


Figure 6a.17. (a) $^1\text{H-NMR}$ spectra of AC in D_2O with DMSO as an internal standard. Calculated amount of propyl amine chains is 0.0129 M per 1 ml of 1 wt% AC solution, (b) to (e) Time dependent emission spectra showing photo-irradiation of TPTS in various concentrations of propyl amine [PA], inset showing the concentrations and (f) HPLC trace of the saturated fraction after irradiation. (g) UV absorption spectra of various HPLC peaks in Figure 6a.17f as compared to the absorption of f_{1pp} (pink).

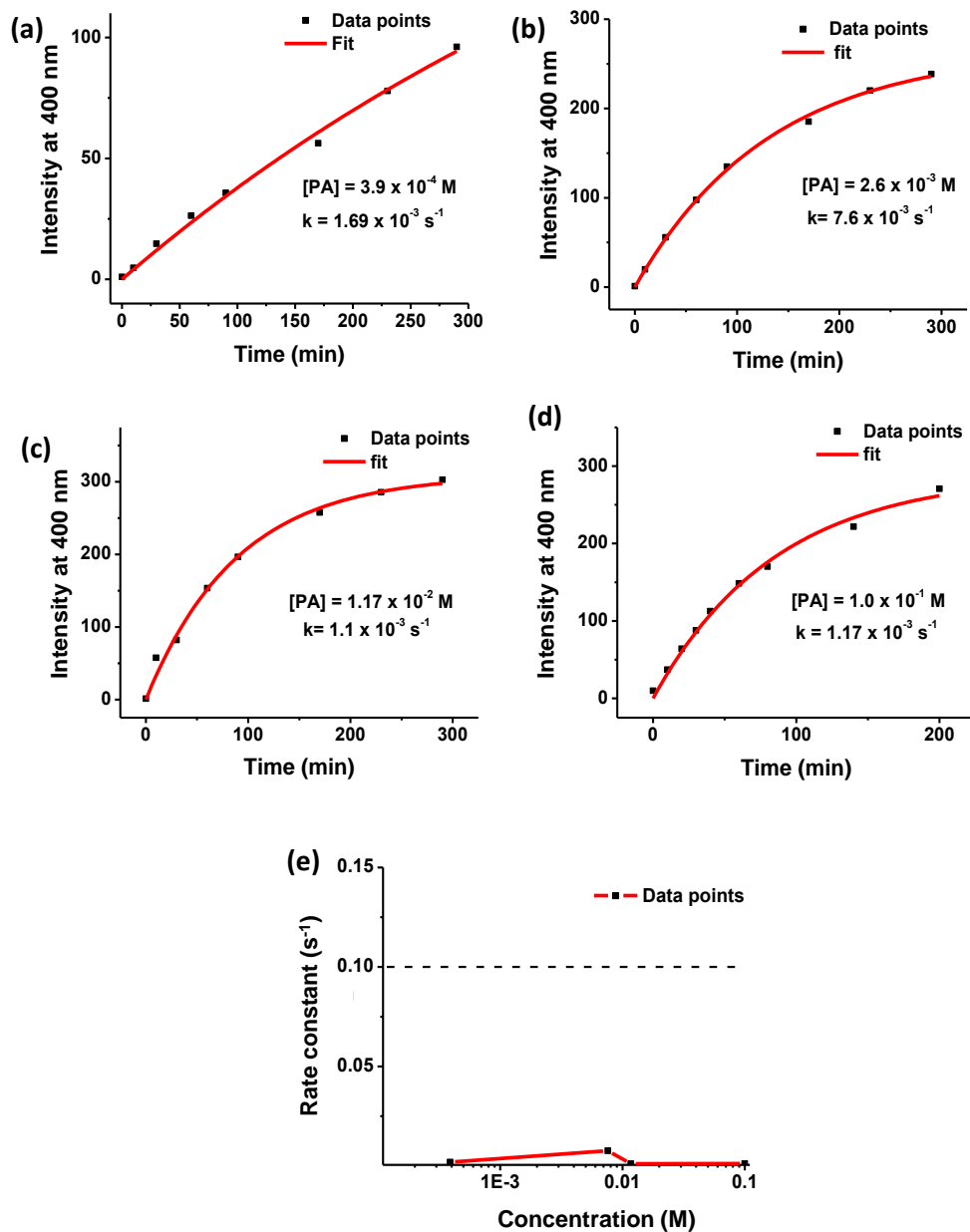


Figure 6a.18. (a) to (d) Time dependent trace at 400 nm showing photo-irradiation of TPTS in various concentrations of propyl amine [PA], inset showing the concentrations and the calculated rate constants. (e) Plot of rate constants with varying propyl amine [PA] concentrations. The dotted line represents the value of k_1 in TPTS and AC solution.

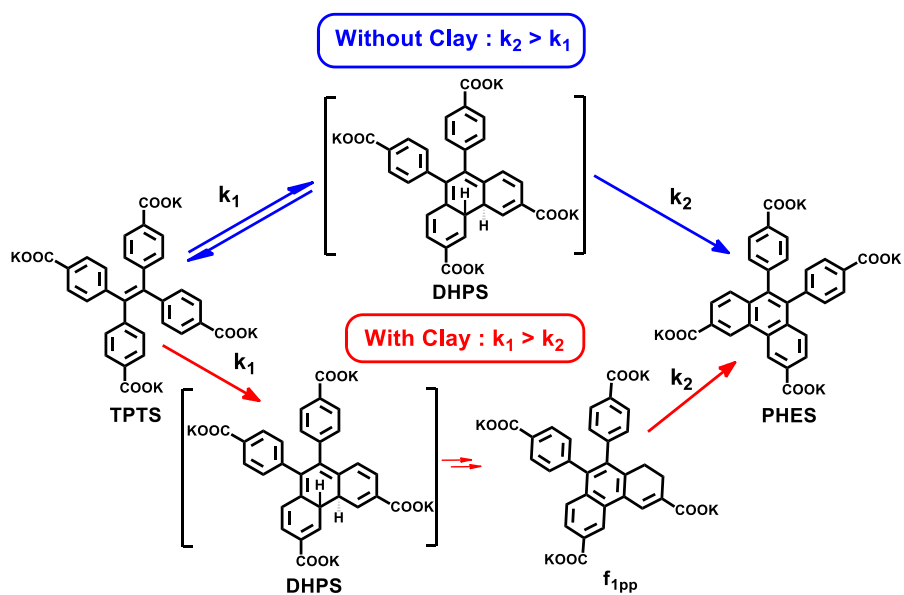


Figure 6a.19. Reaction sequence for nascent *TPTS* (Blue arrows) and *TPTS* inside AC (Red arrows).

6a.4. Experimental Section

General Methods: Unless otherwise noted, all reagents were used as received and all reactions were carried out under an argon atmosphere. All NMR experiments were recorded on Bruker AVANCE-400 MHz spectrometer at room temperature.

Optical spectroscopy: UV/Vis absorption and fluorescence spectra were recorded on a Perkin-Elmer Lambda 750 and Perkin-Elmer LS 55 spectrometer respectively. ATR-IR was measured on Perkin Elmer frontier machine with Pike gladiatr and diamond crystal. Range of measurement was from 400 to 4000 cm^{-1} , data interval was 0.2 cm^{-1} , resolution was 4 cm^{-1} and 16 scans were collected.

Irradiation: Irradiation was done in a 10 mm quartz cuvette (for small scale) and in a 100 ml glass beaker (for large scale). Lamp used was OSRAM puritec germicidal lamp HNS, 8W, G5 (G8T5/OF). In a general procedure the solution was placed inside the lamp chamber directly under the lamp.

ESI-HRMS: High Resolution Mass Spectra (HRMS) were recorded on a Agilent 6538 Ultra High Definition (UHD) Accurate-Mass Q-TOF-LC/MS system using electrospray ionization (ESI) (negative mode). Liquid chromatography (LC) is coupled with the instrument. Column used is Agilent ZORBAX eclipse plus C18 rapid resolution. Injection volume is 10ul methanol solution, eluent gradient is 40% MeCN to 90% MeCN over 40 mins. The other part of the solvent composition was 1% Ammonium formate in water. Flow rate is 0.4 ml/min.

Preparative HPLC: Shimadzu LC-8A with phenomenex luna 10u C18 (2), 250 X 10 mm, 10 micron was employed. Injection volume was 1 ml methanol solution, eluent gradient was 40% MeCN to 60% MeCN over 30 mins. The other part of the solvent composition was water. 0.1% Trifluoro acetic acid was used in all eluents. Flow rate was 8 ml/min.

Note: Chromatograms from Figures 6a.6d and 6a.11d probe the same species but the retention times are evidently different this is because for Figures 6a.6d HPLC column mentioned in ESI-HRMS was used and for 2h the one mentioned in preparative HPLC was employed. The reason behind this choice is that after clay extraction the methanol solution could still be not used in the ESI-HRMS as even very low concentration of residual clay saturated the MS chromatogram. Therefore in case of clay extracts a preparative HPLC was done (chromatograms of which are in Figure 6a.11d) and after purification of each fraction MS was performed individually. MS and the UV absorption spectra corroborated with the fact that we are monitoring the same species in Figure 6a.6d and 6a.11d.

Dynamic Light scattering and Zeta potential measurement: Measurements were carried out using a NanoZS (Malvern, UK) employing a 532 nm laser at a back scattering angle of 173°.

Synthesis

TPTS was prepared according to the reported procedure^[15]. ¹H-NMR, ¹³C-NMR, HPLC and HRMS have been shown in Figures 6a.2 and 6a.3. **TPTS acid:** ¹H-NMR (400 MHz, D₂O): δ = 7.80 (d, J = 8.4 Hz, 8H), 7.13 (d, J = 8.4 Hz, 8H)

¹³C-NMR (100 MHz, D₂O): δ = 175.20, 145.91, 141.30, 134.53, 130.95, 128.46

HRMS (ESI, negative mode) *m/z* (%): 507.1975 [M-1]⁻, calculated for C₃₀H₂₀O₈, 508.1158 gmol⁻¹

6a.5. Appendix

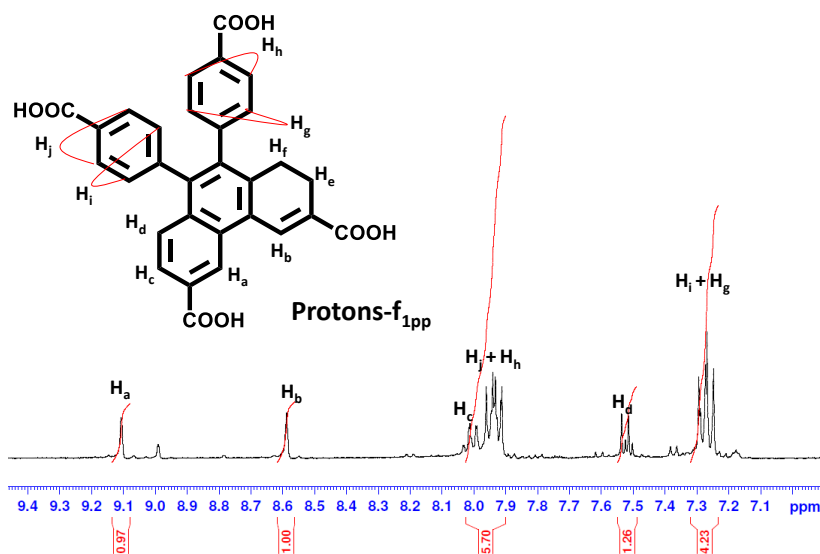


Figure A1. 1H -NMR of f_{1pp} in CD_3OD as shown in Figure 6a.15 with corresponding integrals (From region 7-9.5 ppm).

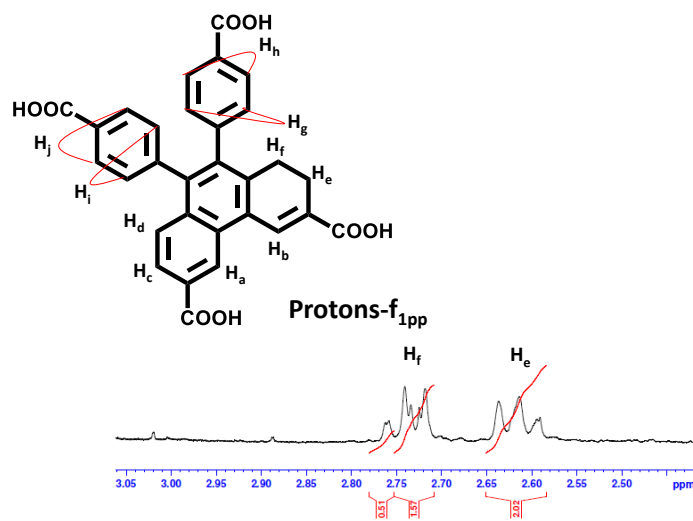


Figure A2. 1H -NMR of f_{1pp} in CD_3OD as shown in Figure 6a.15 with corresponding integrals (From region 2.5-3.0 ppm).

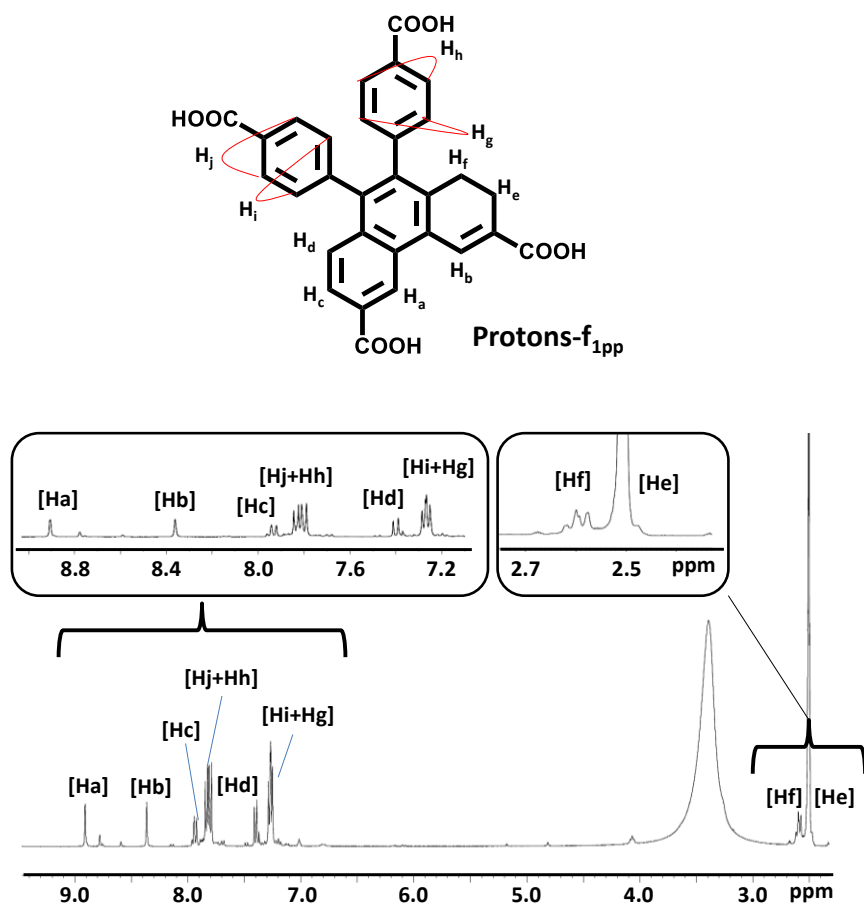


Figure A3. $^1\text{H-NMR}$ spectra of f_{1pp} in $\text{DMSO-}d_6$. f_{1pp} is not soluble enough in CD_3OD to carry out correlation experiments hence $\text{DMSO-}d_6$ was used as a solvent even though DMSO peak overlaps with proton peak of H_e . Correlations pertaining to H_e can be clearly seen despite the solvent overlap (vide infra, correlations are not due to DMSO solvent but entirely due to H_e as evident from HETCOR spectra Figure A6).

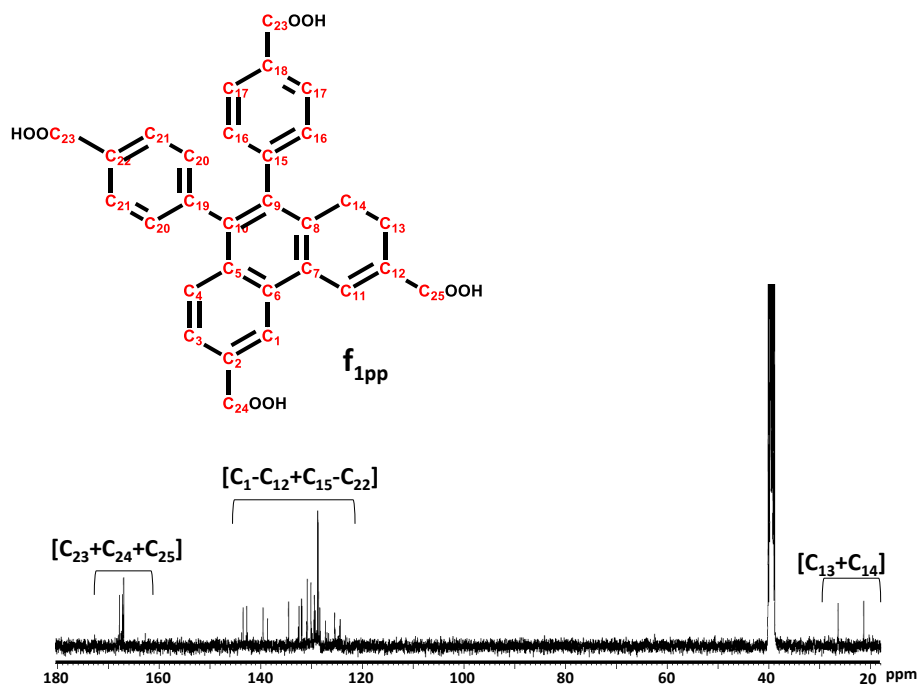


Figure A4. ^{13}C -NMR spectra of f_{1pp} in $\text{DMSO-}d_6$.

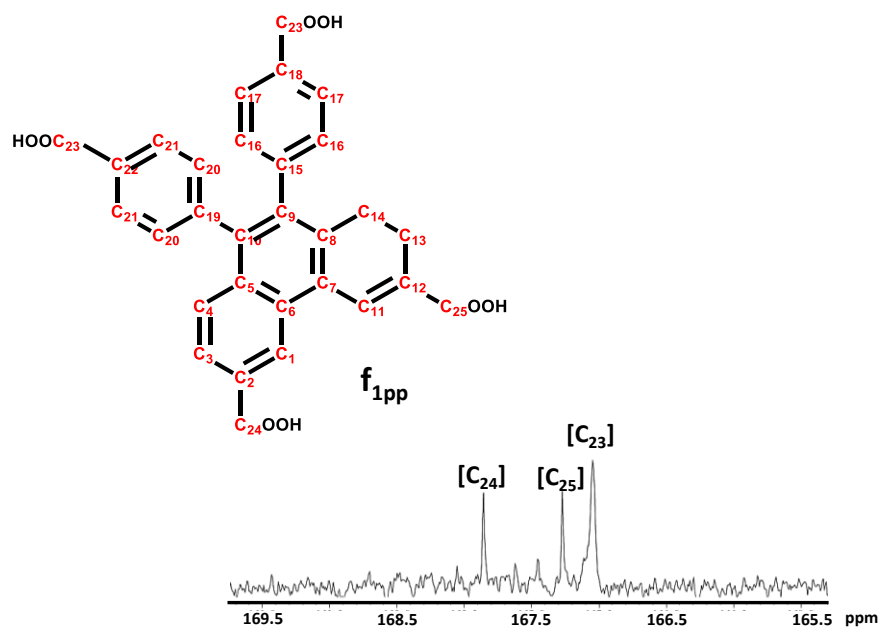


Figure A5. ^{13}C -NMR spectra of f_{1pp} in $\text{DMSO-}d_6$ zoomed in region between 165-170 ppm, 3 kinds of COOH carbons are visible which can be analyzed as: $2 \times C_{23}$, C_{24} and C_{25} , total 4 carbons.

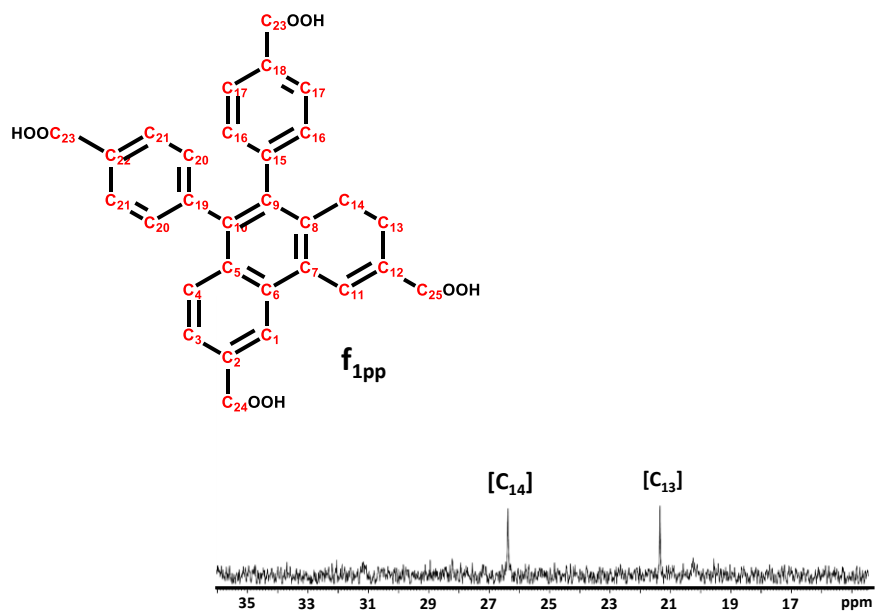


Figure A6. ^{13}C -NMR spectra of f_{1pp} in $\text{DMSO-}d_6$ zoomed in region between 15-35 ppm, 2 carbons in lower field suggesting two methylene carbons.

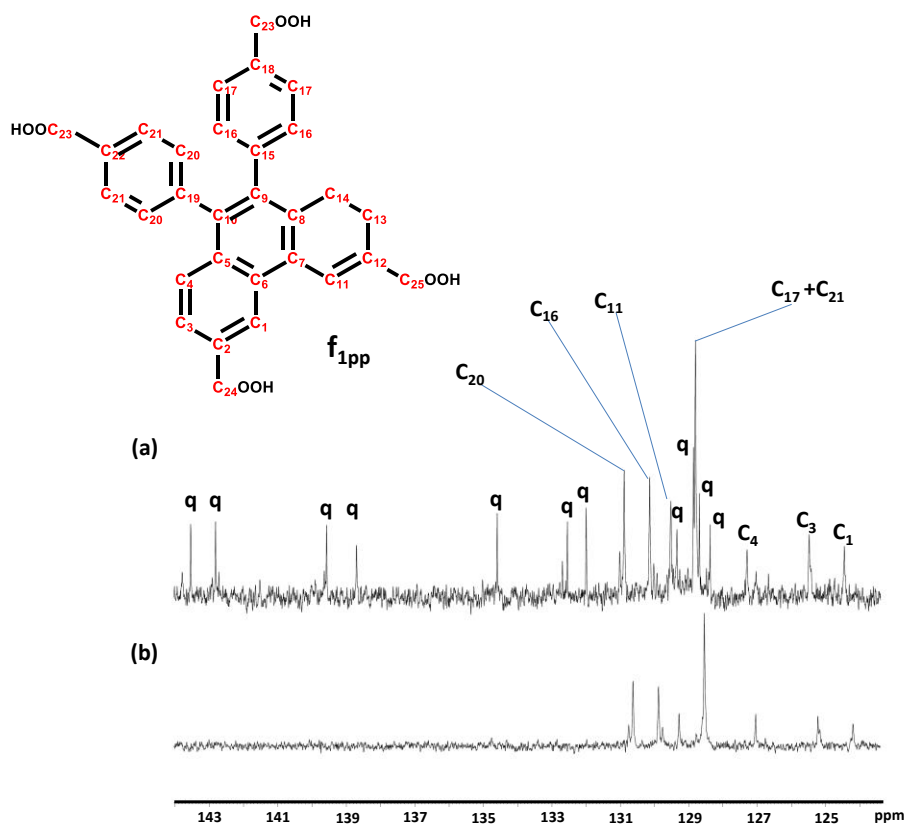


Figure A7. a) and b) ^{13}C and ^{13}C -DEPT NMR spectra respectively of f_{1pp} in $\text{DMSO-}d_6$ (peaks marked as “q” are quaternary carbons, CH carbons have been designated). Hence total **16 quaternary Carbons** (12+4); $C_{18} = C_{23}$ (from Figure A5 and A7). Total **12 C-H Carbons** $\{2x(C_{16}+C_{17}+C_{20}+C_{21}) + C_{11} + C_1 + C_3 + C_4\}$ (from Figure A7). Total **2 CH₂ Carbons** (from Figure A6), total **30 Carbons**

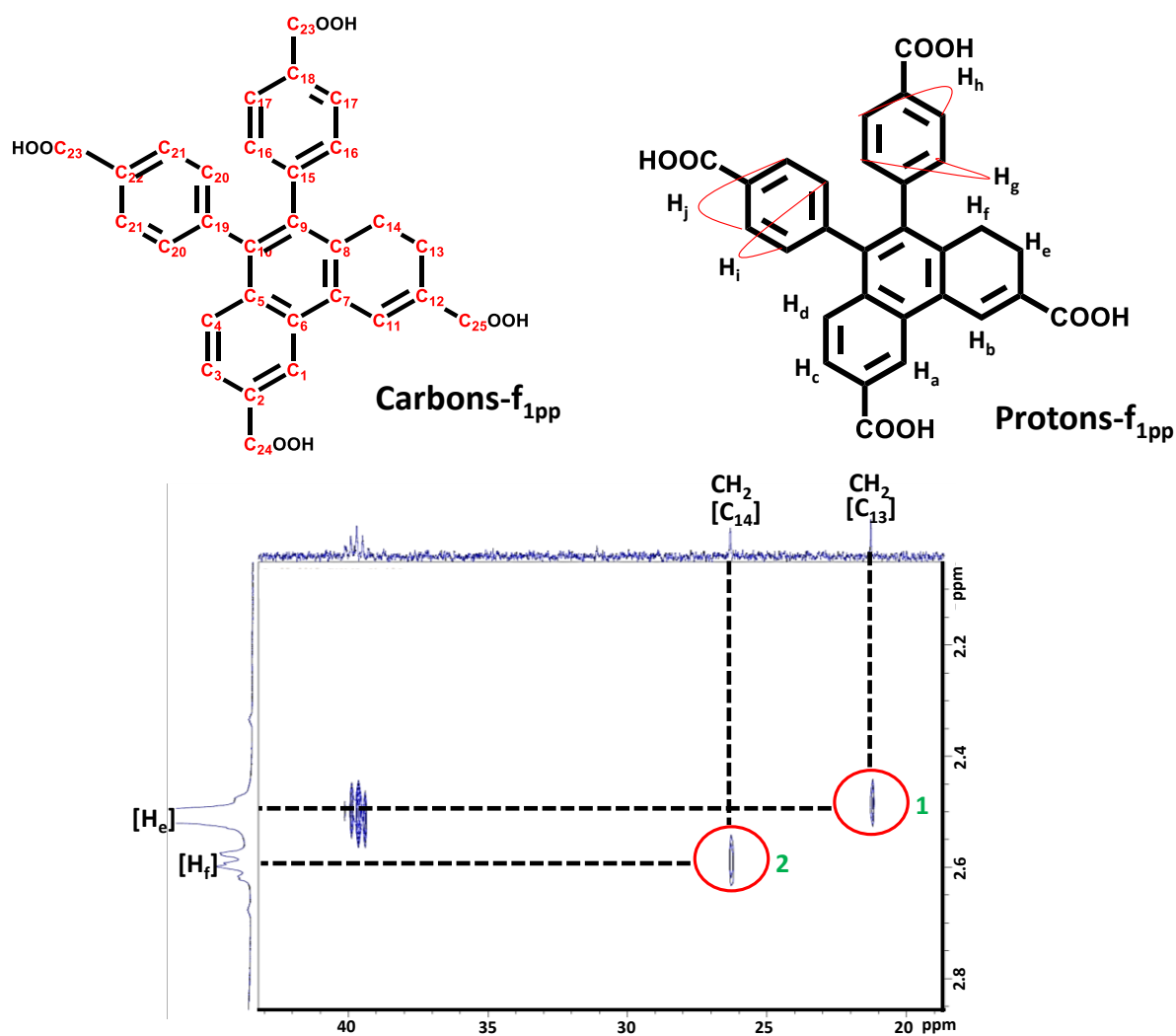


Figure A8. HETCOR 2D-NMR spectra (upfield region) showing correlation between ^{13}C and ^1H -nuclei of f_{1pp} in $\text{DMSO-}d_6$ (contours have been circled in red with correlation in black dashed lines). CH_2 carbons coupled to H_e and H_f

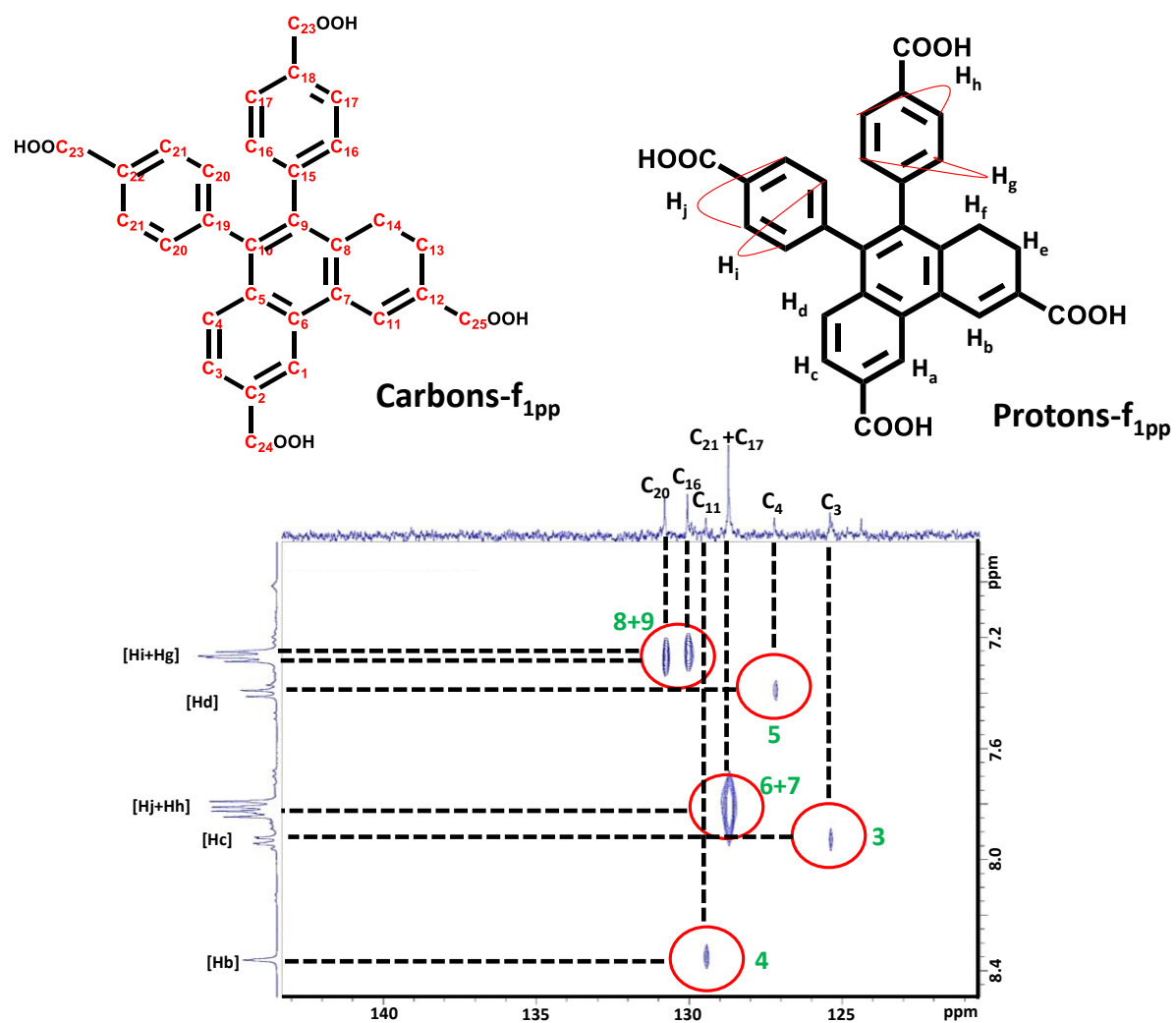


Figure A9. HETCOR 2D-NMR spectra (downfield region) showing correlation between ¹³C and ¹H-nuclei of *f*_{1pp} in DMSO-*d*₆ (contours have been circled in red with correlation in black dashed lines).

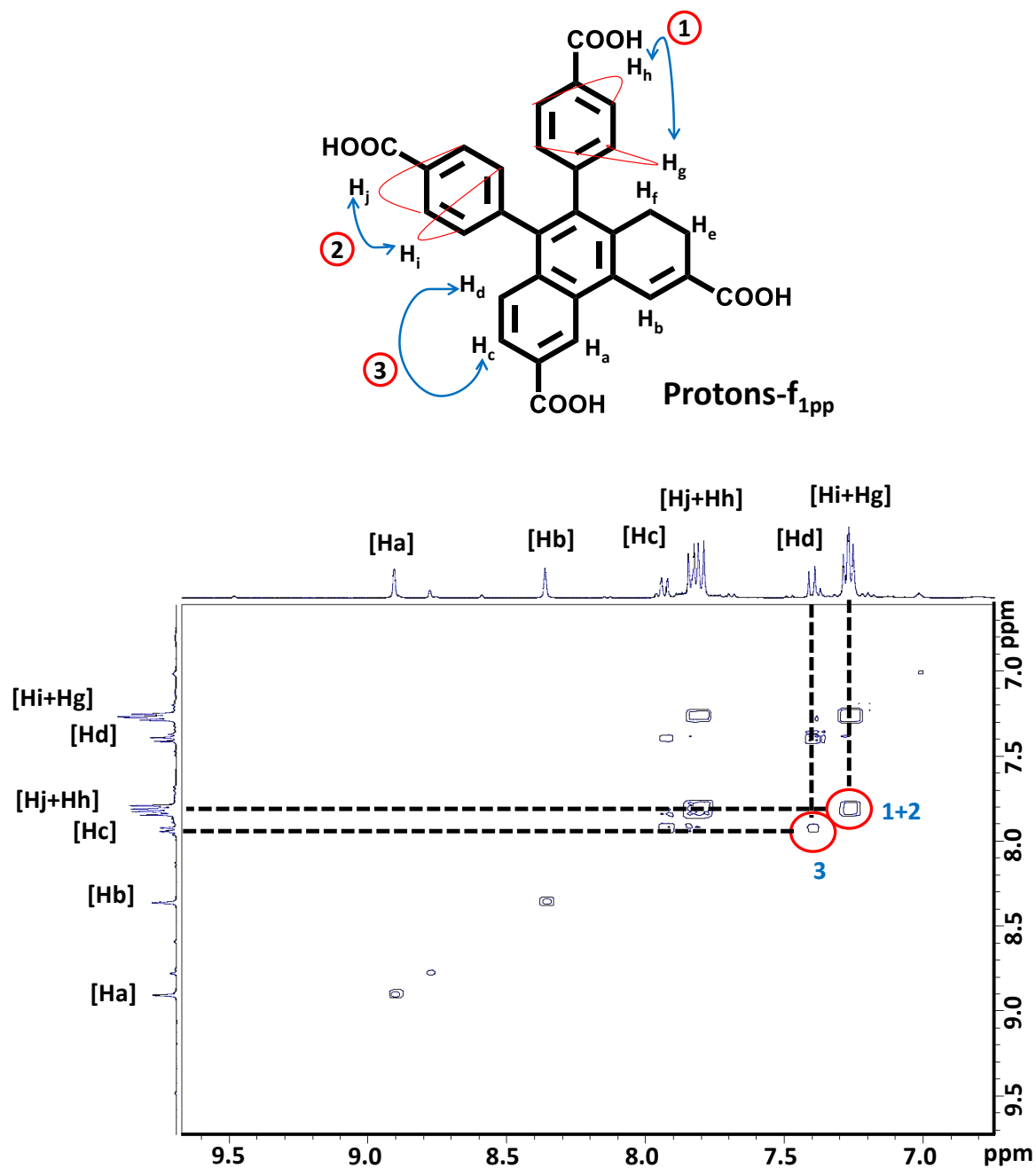


Figure A10. COSY 2D-NMR spectra showing correlation between 1H -nuclei of f_{1pp} in $DMSO-d_6$ (contours have been circled in red with correlation in black dashed lines) (3 bond couplings in downfield region)

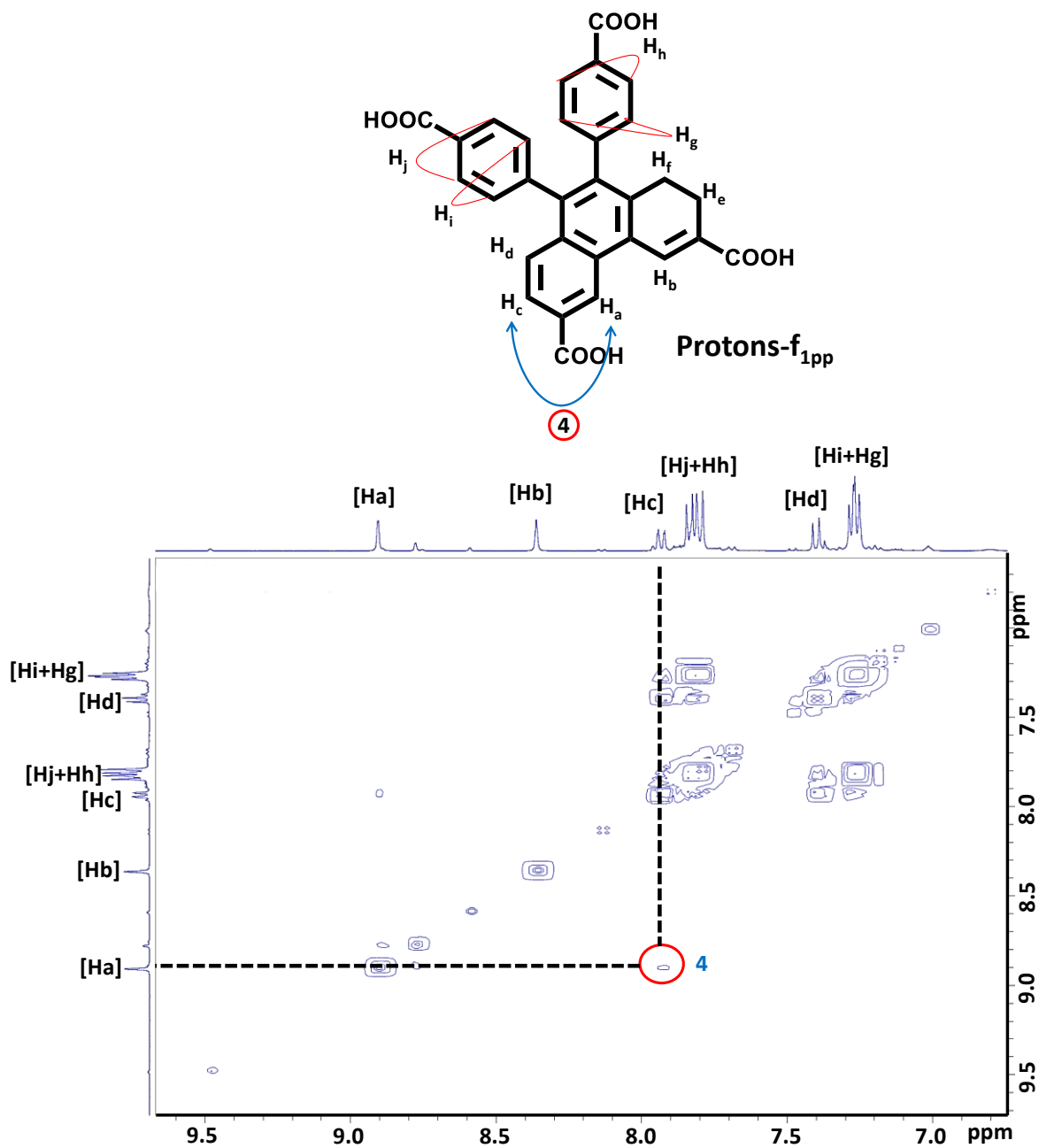


Figure A11. COSY 2D-NMR spectra showing correlation between ^1H -nuclei of f_{1pp} in $\text{DMSO-}d_6$ (contours have been circled in red with correlation in black dashed lines). Weak meta coupling between H_c and H_a . 4 bond coupling in downfield region also signifies aromaticity in one part of ring.

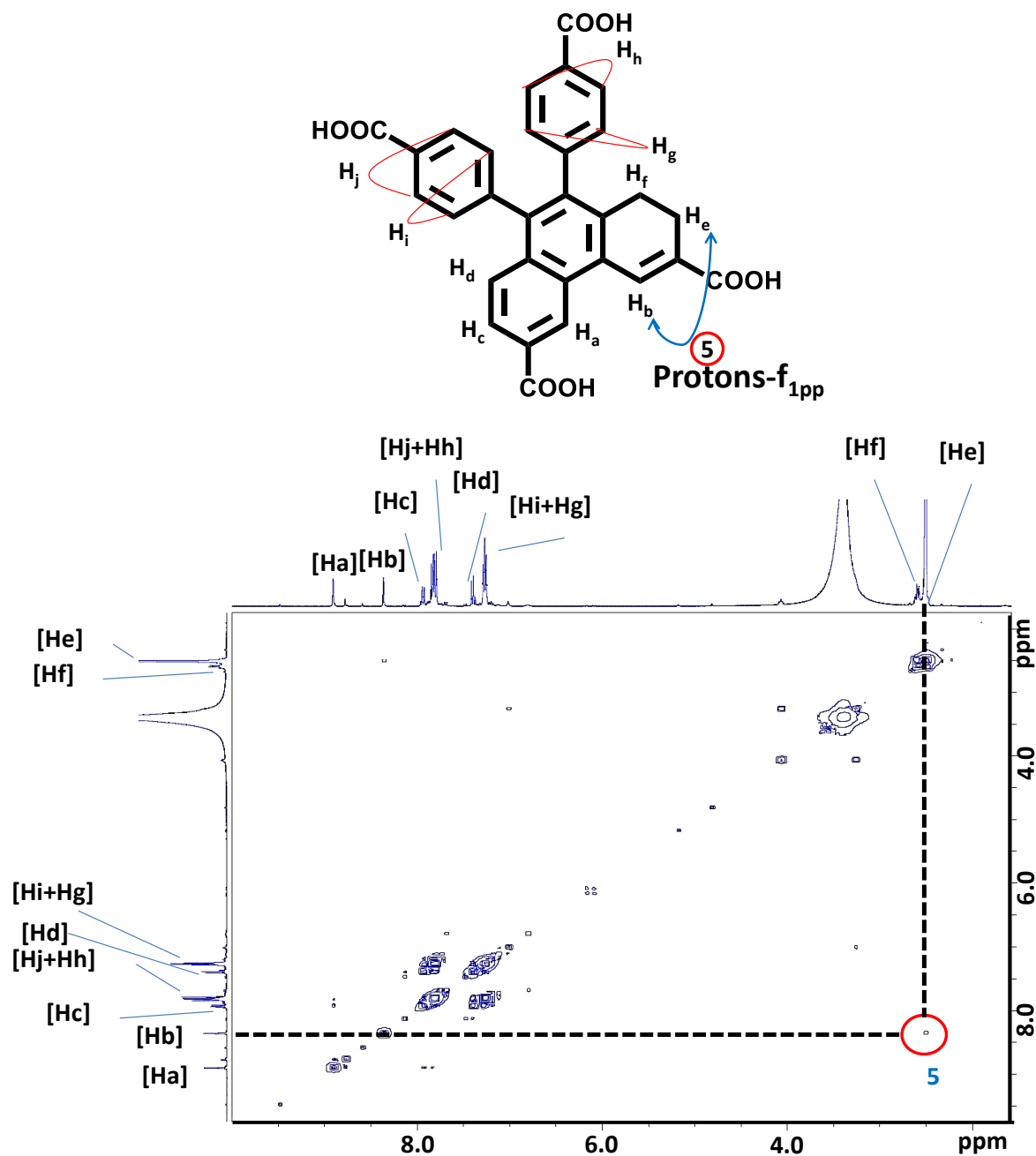


Figure A12. COSY 2D-NMR spectra showing correlation between ^1H -nuclei of f_{1pp} in $\text{DMSO-}d_6$ (contours have been circled in red with correlation in black dashed lines). Weak allylic coupling between H_e and H_b . 4 bond coupling in upfield region, also signifies lack of aromaticity in another part of ring. H_e and H_f coupling is not visible perhaps being very close to the diagonal peaks.

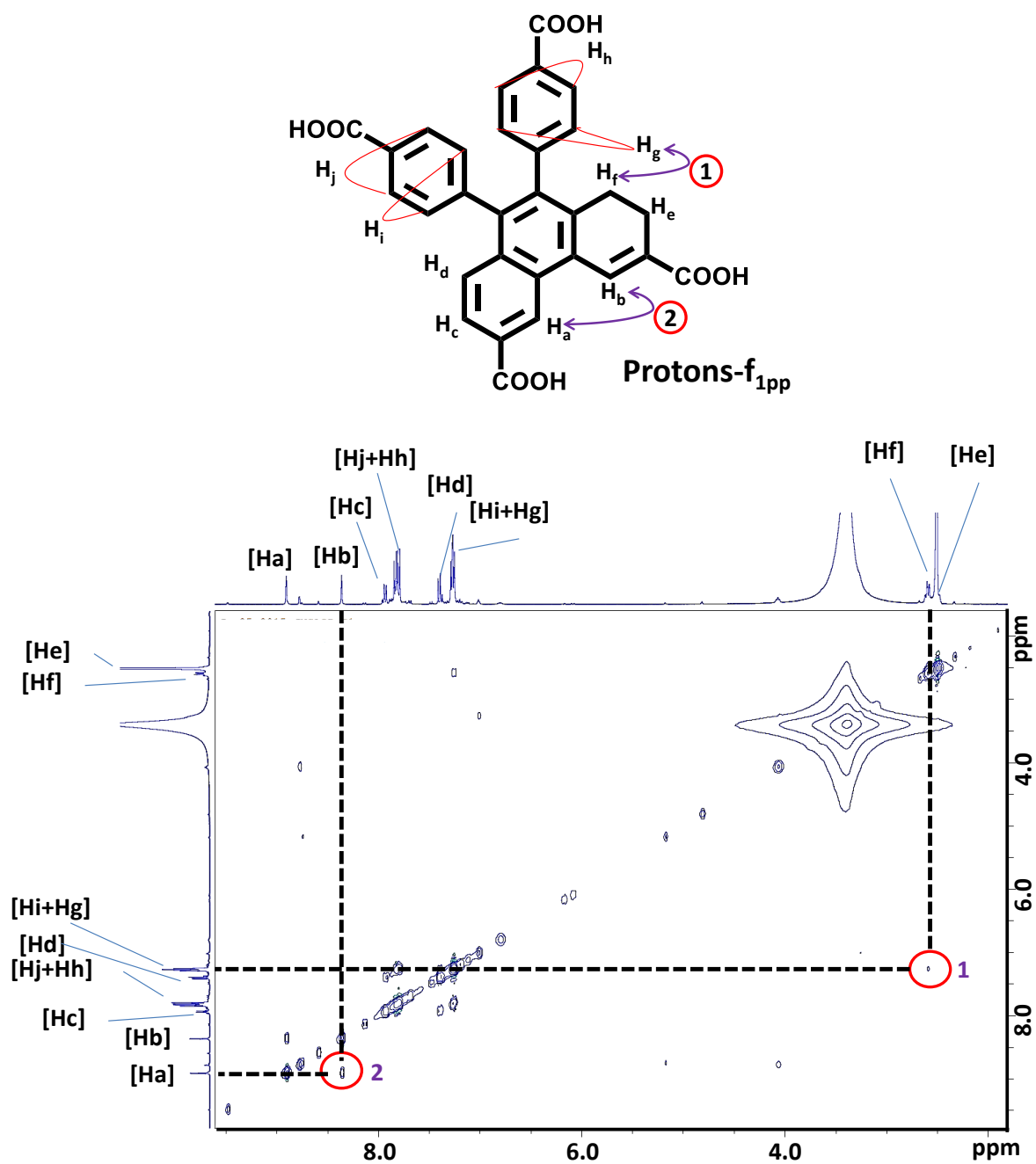


Figure A13. NOESY 2D-NMR spectra showing correlation between ^1H -nuclei of f_{1pp} in $\text{DMSO-}d_6$ (contours have been circled in red with correlation in black dashed lines). H_i - H_d coupling too close to diagonal peaks, hence perhaps not observed. Clear (H_a , H_b) and (H_f , H_g) NOE couplings confirm the proposed structure.

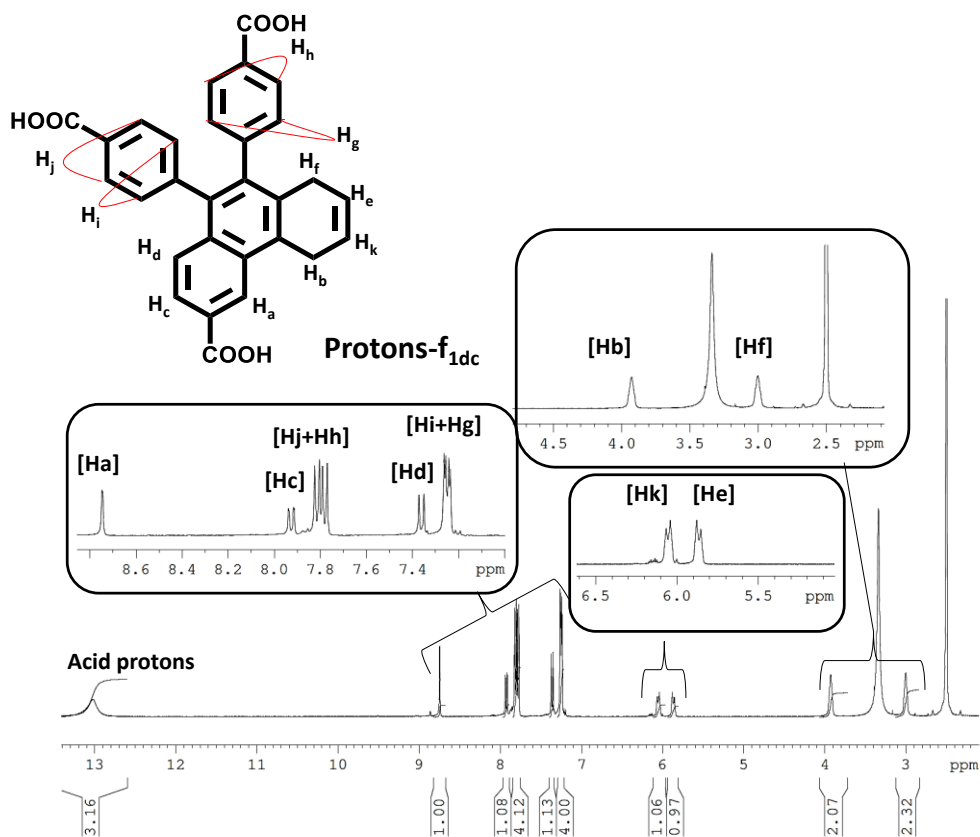


Figure A14. $^1\text{H-NMR}$ of f_{1dc} in $\text{DMSO-}d_6$.

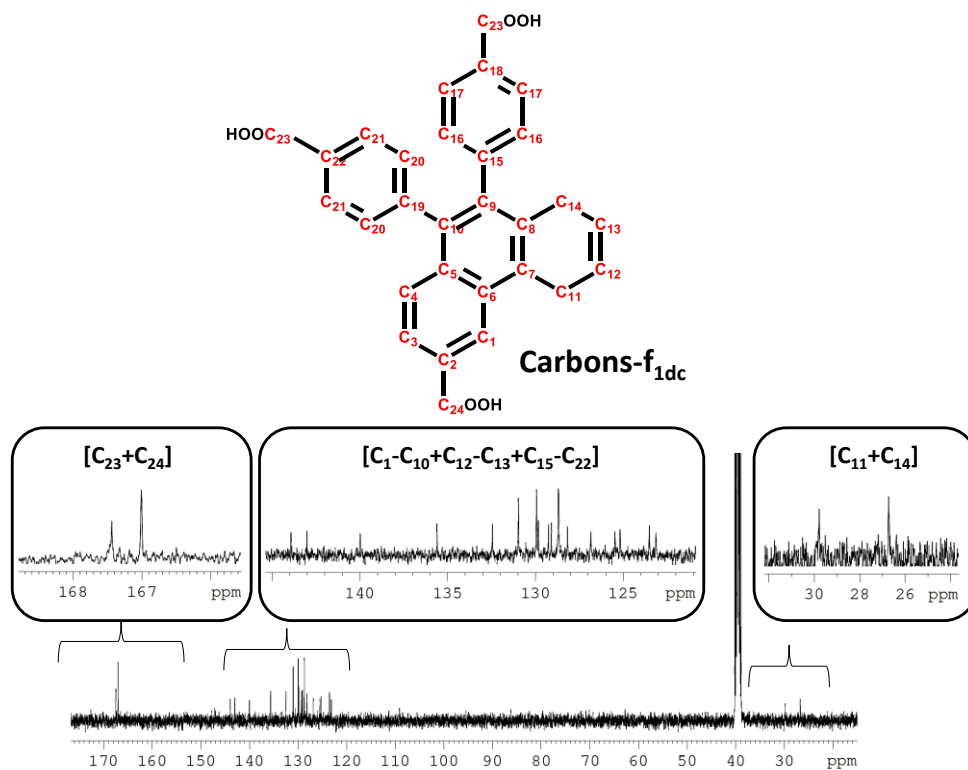


Figure A15. $^{13}\text{C-NMR}$ of f_{1dc} in $\text{DMSO-}d_6$.

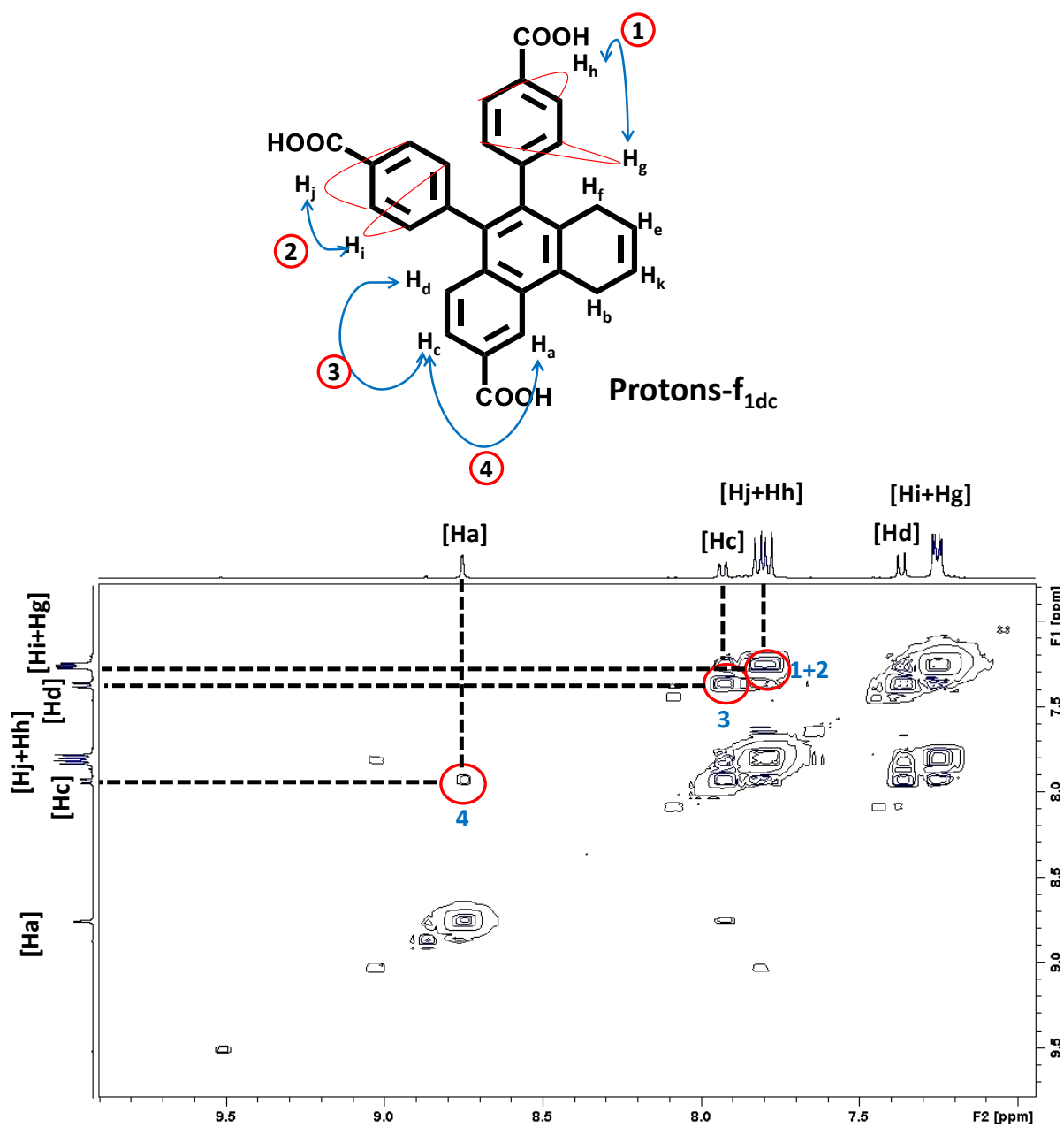


Figure A16. ^1H -COSY of f_{1dc} in $\text{DMSO-}d_6$ (contours have been circled in red with correlation in black dashed lines). 1, 2 and 3 are three bond couplings in down field region. 4 is the weak four bond meta-coupling between H_a - H_c signifying aromaticity in one part of the molecule.

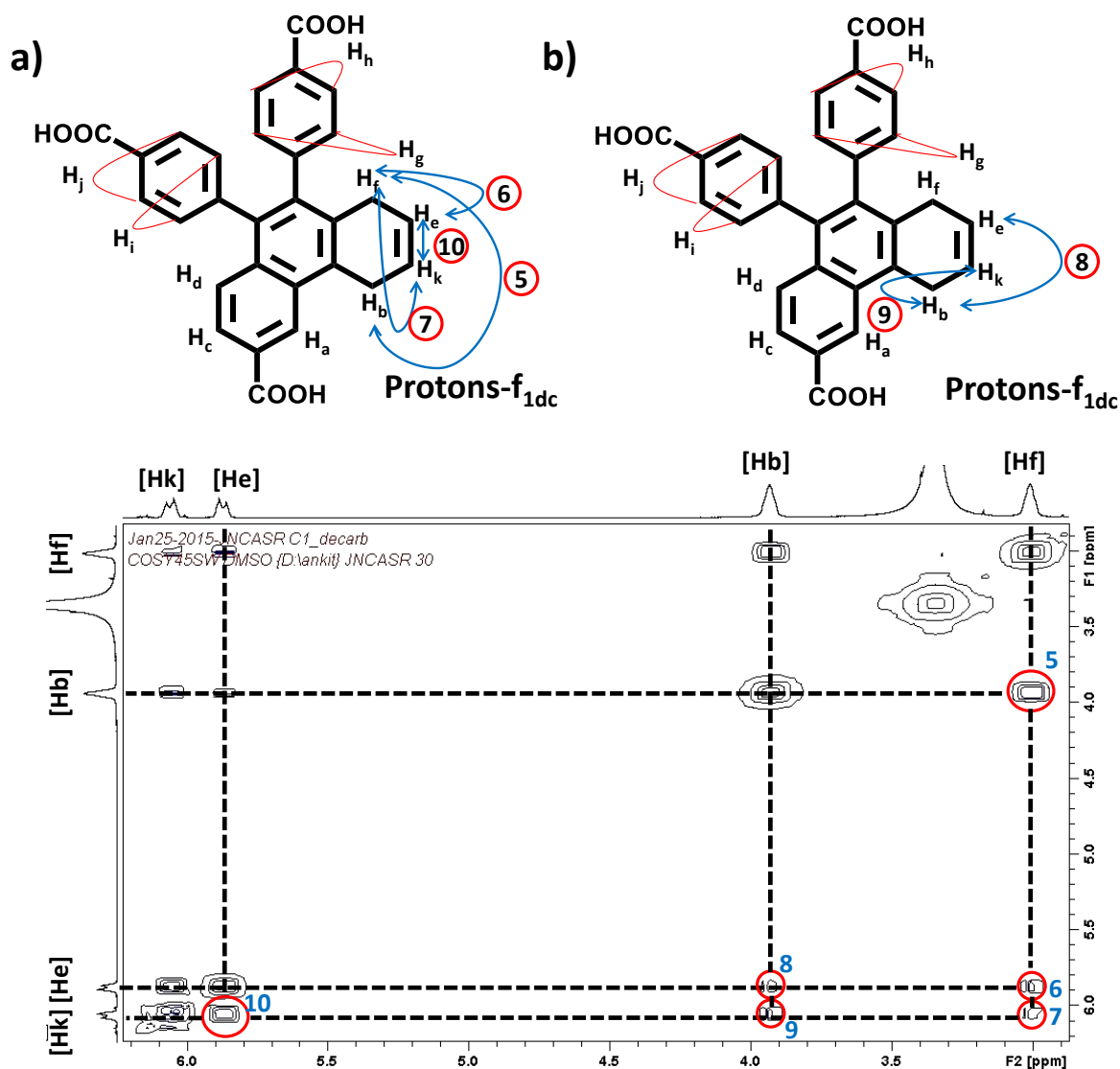


Figure A17. ^1H -COSY of f_{1dc} in $\text{DMSO-}d_6$ (contours have been circled in red with correlation in black dashed lines). Strong coupling between H_f and H_b (5) is a result of strong homo-allylic coupling which is characteristic of 1,4 cyclohexene systems. 6 and 9 are respective three bond couplings in sets (H_f , H_e) and (H_b , H_k). Similarly, 10 is a three bond coupling between H_k and H_e . 7 and 8 are allylic couplings in sets (H_f , H_k) and (H_b , H_e). downfield signifies lack of aromaticity in another part of ring.

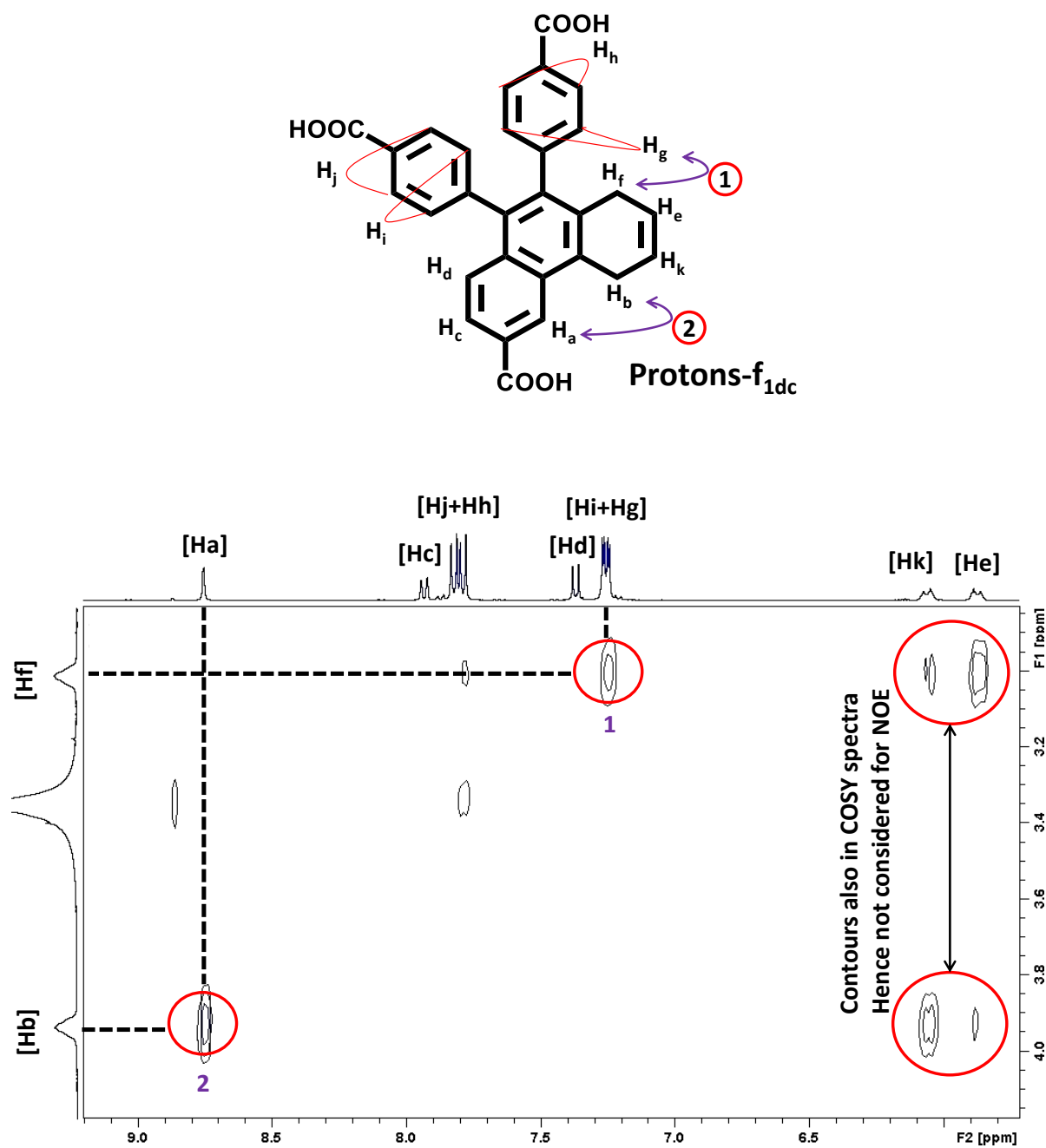


Figure A18. ^1H -NOE of f_{1dc} in $\text{DMSO-}d_6$ (contours have been circled in red with correlation in black dashed lines). H_i - H_d coupling too close to diagonal peaks, hence perhaps not observed. Clear (H_a , H_b) and (H_f , H_g) NOE couplings confirm the proposed structure.

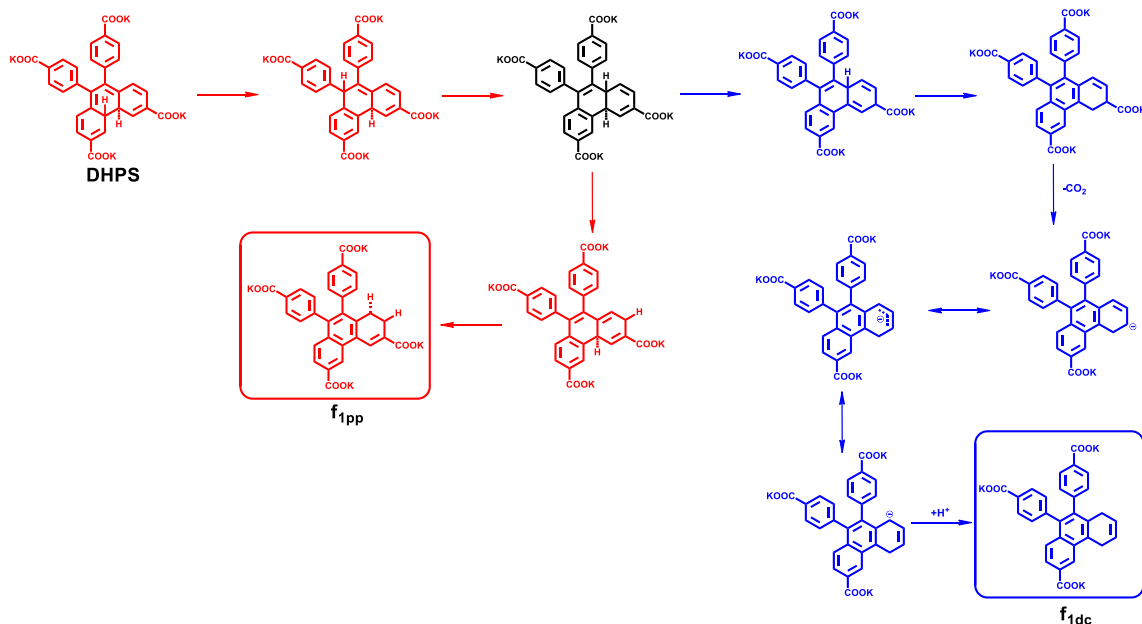


Figure A19. Proposed reaction pathway for f_{1pp} and f_{1dc} from **DHPS**. Hence $[DHPS] = [f_{1pp}] + [f_{1dc}]$.

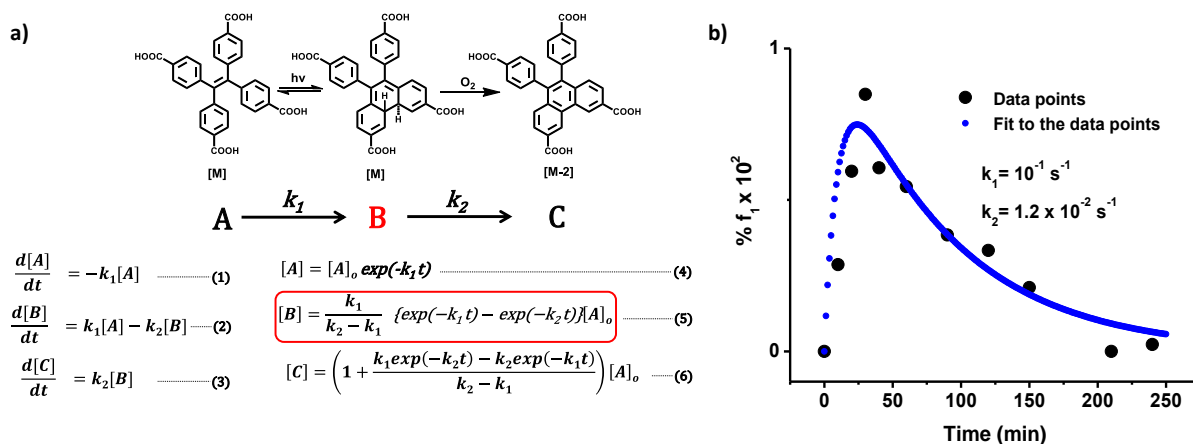


Figure A20. (a) Kinetic equations showing the expression for a series reaction, boxed reaction is the concentration profile of the intermediate. (b) Intensity trace at 400 nm of the photo-oxidation profile of **TPTS** and **AC** ($10^{-4}M + 0.9 \text{ wt\%}$, $l = 1 \text{ cm}$, $\lambda_{exc} = 350 \text{ nm}$, water) under 254 nm irradiation with a graphical fit to equation 5 shown in Figure A20a. Figure A20b shows the profile of intermediate f_1 with varying time. This has been plotted from the emission trace followed at 400 nm of the **TPTS** and **AC** conjugate as it was being irradiated (Figure 6a.11b). Trace at 400 nm in Figure 6a.11b actually follows the formation of f_{1pp} and f_{1dc} which are derivatives formed from **DHPS**. Calculating the net percentage of f_{1pp} and f_{1dc} formed from HPLC chromatograms at various stages of the irradiation the emission trace was normalized and hence fitted to equation 5 (Figure A20a).

6a.6. References and Notes

- 1 (a) Hanoian, P.; Liu, C. T.; Hammes-Schiffer, S.; Benkovic, S. *Acc. Chem. Res.* 2015, **48**, 482. (b) He, Y.-M.; Feng, Y.; Fan, Q.-H. *Acc. Chem. Res.* 2014, **47**, 2894. (c) Shibata, A.; Abe, H.; Ito, Y. *Molecules* 2012, **17**, 2446.
- 2 (a) Kawamichi, T.; Haneda, T.; Kawano, M.; Fujita, M. *Nature* 2009, **461**, 633. (b) Sato, H.; Matsuda, R.; Sugimoto, K.; Takata, M.; Kitagawa, S. *Nat. Mater.* 2010, **9**, 661. (c) Yoshizawa, M.; Klosterman, J. K.; Fujita, M. *Angew. Chem. Int. Ed.* 2009, **48**, 3418. (d) Distefano, G.; Suzuki, H.; Tsujimoto, M.; Isoda, S.; Bracco, S.; Comotti, A.; Sozzani, P.; Uemura, T.; Kitagawa, S. *Nat. Chem.* 2013, **5**, 335. (e) Yanai, N.; Uemura, T.; Ohba, M.; Kadowaki, Y.; Maesato, M.; Takenaka, M.; Nishitsuji, S.; Hasegawa, H.; Kitagawa, S. *Angew. Chem. Int. Ed.* 2007, **47**, 9883. (f) Kitao, T.; Bracco, S.; Comotti, A.; Sozzani, P.; Naito, M.; Seki, S.; Uemura, T.; Kitagawa, S. *J. Am. Chem. Soc.* 2015, **137**, 5231. (g) Park, In-H.; Medishetty, R.; Lee, H.-H.; Mulijanto, C. E.; Quah, H. S.; Lee, S. S.; Vittal, J. *Angew. Chem. Int. Ed.* 2015, **54**, doi: 10.1002/anie.201502179. (h) Stumpel, J. E.; Liu, D.; Broer, D. J.; Schenning, A. P. H. *J. Chem. Eur. J.* 2013, **19**, 10922. (i) Stumpel, J. E.; Ziółkowski, B.; Florea, L.; Diamond, D.; Broer, D. J.; Schenning, A. P. H. *J. ACS Appl. Mater. Interfaces* 2014, **6**, 7268. (j) Britt, D.; Lee, C.; Uribe-Romo, F. J.; Furukawa, H.; Yaghi, O. M. *Inorg. Chem.* 2010, **49**, 6387. (k) Nerbonne, J. M.; Weiss, R. G. *J. Am. Chem. Soc.* 1978, **100**, 2571. (l) Nerbonne, J. M.; Weiss, R. G. *J. Am. Chem. Soc.* 1979, **101**, 402. (m) Moorthy, J. N.; Venkatesan, K.; Weiss, R. G. *J. Org. Chem.* 1992, **57**, 3292. (n) Xu, H.-X.; Cheng, S.-F.; Yang, X.-J.; Chen, B.; Chen, Y.; Zhang, L.-P.; Wu, L.-Z.; Fang, W.; Tung, C.-H.; Weiss, R. G. *J. Org. Chem.* 2012, **77**, 1685.
- 3 Kang, J.; Rebek Jr, J. *Nature* 1997, **385**, 50.
- 4 (a) Thomas, J. K. *Acc. Chem. Res.* 1988, **21**, 275. (b) Ramakrishnan, V.; Yamamoto, D.; Sasamoto, S.; Shimada, T.; Nabetani, Y.; Tachibana, H.; Inoue, H. *Phys. Chem. Chem. Phys.* 2014, **16**, 23663. (c) Kole, G.K.; Vittal, J.J. *Chem. Soc. Rev.* 2013, **42**, 1755.
- 5 (a) Takagi, K.; Shichi, T.; Usami, H.; Sawaki, Y. *J. Am. Chem. Soc.* 1993, **115**, 4339. (b) van Damme, H.; Nijs, H.; Fripiat, J. J. *J. Mol. Catal.* 1984, **27**, 123. (c) Madhavan, D.; Pitchumani, K. *Photochem. Photobiol. Sci.* 2003, **2**, 95. (d) Ramamurthy, V.; Jockusch, S.; Porel, M. *Langmuir* 2015, doi.org/10.1021/la504130f.
- 6 Wang, Q.; Mynar, J. L.; Yoshida, M.; Lee, E.; Lee, M.; Okuro, K.; Kinbara, K.; Aida, T. *Nature* 2010, **463**, 339
- 7 (a) Ohkubo, K.; Nanjo, T.; Fukuzumi, S. *Org. Lett.* 2005, **7**, 4265. (b) Foote, C. F. *Tetrahedron* 1985, **41**, 2221.
- 8 (a) Amaya, T.; Ito, T.; Hirao, T. *Angew. Chem. Int. Ed.* 2015, **54**, 1. (b) Tran, M. N.; Chenoweth, D. M. *Angew. Chem. Int. Ed.* 2015, **54**, doi: 10.1002/anie.201502403.

- 9 (a) Rodier, J.-M.; Myers, A. B. *J. Am. Chem. Soc.* 1993, **115**, 10791. (b) Huang, G.; Ma, B.; Chen, J.; Peng, Q.; Zhang, G.; Fan, Q.; Zhang, D. *Chem. Eur. J.* 2012, **18**, 3886. (c) Bao, J.; Weber, P. M. *J. Am. Chem. Soc.* 2011, **133**, 4164. (d) Bromberg, A.; Muszkat, K. A. *J. Am. Chem. Soc.* 1969, **91**, 2860. (e) Bao, J.; Minitti, M. P.; Weber, P. M. *J. Phys. Chem. A* 2011, **115**, 1508. (f) Hu, R.; Lam, J. W. Y.; Deng, H.; Song, Z.; Zheng, C.; Tang, B. Z. *J. Mater. Chem. C* 2014, **2**, 6326.
- 10 (a) Lewis, F. D.; Kurth, T. L.; Kalgutkar, R. S. *Chem. Commun.* 2001, 1372. (b) op bet Veld, P. H. G.; Laarhoven, W. H. *J. Am. Chem. Soc.* 1977, **99**, 7221. (c) Doyle, T. D.; Benson, W. R.; Filipescu, N. *J. Am. Chem. Soc.* 1976, **98**, 3262.
- 11 Jørgensen, K. B. *Molecules* 2010, **15**, 4334.
- 12 (a) Patil, A.; Eswaramoorthy, M.; Mann, S. *Angew. Chem. Int. Ed.* 2004, **43**, 4928. (b) Rao, K. V.; Datta, K. K. R.; Eswaramoorthy, M.; George, S. J. *Adv. Mater.* 2013, **25**, 1713. (c) Datta, K. K. R.; Achari, A.; Eswaramoorthy, M. *J. Mater. Chem. A* 2013, **1**, 6707. (d) Rao, K. V.; Datta, K. K. R.; Eswaramoorthy, M.; George, S. J. *Angew. Chem. Int. Ed.* 2011, **50**, 1179. (e) Ishida, Y.; Kulasekharan, R.; Shimada, T.; Takagi, S.; Ramamurthy, V. *Langmuir* 2013, **29**, 1748. (f) Rao, K. V.; Datta, K. K. R.; Eswaramoorthy, M.; George, S. J. *Chem. Eur. J.* 2012, **18**, 2184. (g) Rao, K. V.; Jain, A.; George, S. J. *J. Mater. Chem. C* 2014, **2**, 3055. (h) Liu, M.; Ishida, Y.; Ebina, Y.; Sasaki, T.; Hikima, T.; Takata, M.; Aida, T. *Nature* 2015, **517**, 68.
- 13 (a) Barbara, P. F.; Rand, S. D.; Rentzepis, P. M. *J. Am. Chem. Soc.* 1981, **103**, 2157. (b) Hong, Y.; Lam, J. W. Y.; Tang, B. Z. *Chem. Soc. Rev.* 2011, **40**, 5361. (c) Shultz, D. A.; Fox, M. A. *J. Am. Chem. Soc.* 1989, **111**, 6311. (d) Zhao, Z.; Lamb, J. W. Y.; Tang, B. Z. *J. Mater. Chem.* 2012, **22**, 23726. (e) Szymanski, W.; Beierle, J. M.; Kistemaker, H. A.; Velema, W. A.; Feringa, B. L. *Chem. Rev.* 2013, **113**, 6114.
- 14 (a) Hong, Y.; Lama, J. W. Y.; Tang, B. Z. *Chem. Commun.* 2009, 4332. (b) Hong, Y.; Lam, J. W. Y.; Tang, B. Z. *Chem. Soc. Rev.* 2011, **40**, 5361. (c) Seo, J.; Chung, J. W.; Kwon, J. E.; Park, S. Y. *Chem. Sci.* 2014, **5**, 4845. (d) Shin, S.; Gihm, S. H.; Park, C. R.; Kim, S.; Park, S. Y. *Chem. Mater.* 2013, **25**, 3288.
- 15 Shustova, N. B.; McCarthy, B. D.; Dincă, M. *J. Am. Chem. Soc.* 2011, **133**, 20126.
- 16 Shustova, N. B.; Ong, Ta-C.; Cozzolino, A. F.; Michaelis, V. K.; Griffin, R. G.; Dincă, M. *J. Am. Chem. Soc.* 2012, **134**, 15061.
- 17 Knittel-Wismonsky, T.; Fischer, G.; Fischer, E. *Tetrahedron Lett.* 1972, **28**, 2853.
- 18 (a) Somers, J. B. M.; Couture, A.; Lablache-Combier, A.; Laarhoven, W. H. *J. Am. Chem. Soc.* 1985, **107**, 1387. (b) Almeida, J. F.; Castedo, L.; Fernandez, D.; Neo, A. G.; Romero, V.; Tojo, G. *Org. Lett.* 2003, **5**, 4939.
- 19 Although irradiation of TPE derivatives have been attempted in the aggregated state (ref.9 b,f), it does not yield the intermediate but rather just the phenanthrene derivative. The

molecule used is substituted with electron rich moieties and thus its oxidation rates would be significantly higher compared to ones with deactivating substituents such as in the present case.

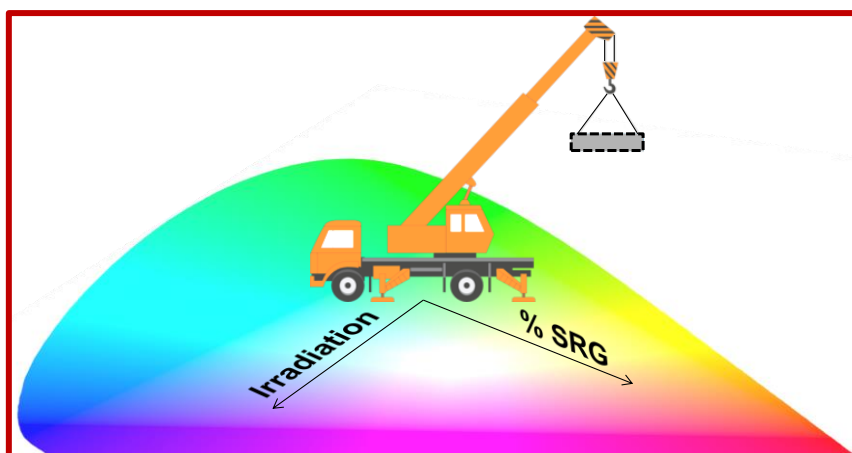
- 20 An interesting result was published as manuscript related to this work was being prepared; He, Z.; Shan, L.; Mei, J.; Wang, H.; Lam, J. W. Y.; Sung, H. H-Y.; Williams, I. D.; Gu, X.; Miao, Q.; Tang, B. Z. *Chem. Sci.* 2015, **6**, 3538). This paper describes the formation of di-hydrophenanthrene derivative upon aggregation and the stabilization has been pointed towards the molecular design with more π rings. Thus the stabilization of intermediate and subsequent oxidation perhaps has some bearing on the electronic effects as a result of functional groups present in the molecule as well.
- 21 (a) Liu, M.; Ishida, Y.; Ebina, Y.; Sasaki, T.; Aida, T. *Nat. Commun.* 2013, **4**, 2029. (b) Mizoshita, N.; Tani, T.; Inagaki S. *Chem. Soc. Rev.* 2011, **40**, 789. (c) Zhang, X.; Ballem, M. A.; Hu, Z.-J.; Bergman, P.; Uvdal, K. *Angew. Chem. Int. Ed.* 2011, **50**, 5729. (d) Zhang, X.; Ballem, M. A.; Ahrén, M.; Suska, A.; Bergman P.; Uvdal K. *J. Am. Chem. Soc.*, 2010, **132**, 10391. (e) Doris, S. E.; Lynch, J. J.; Li, C.; Wills, A. W.; Urban, J. J.; Helms, B. A. *J. Am. Chem. Soc.* 2014, **136**, 15702.

Chapter-6b

Light Induced in-situ Post-Modification of Clay-Chromophore Hybrids for Multiple White Light Emissions

Abstract

This Chapter uses soft clay chromophore hybrids to demonstrate a photo-modification strategy in which a white light standard can be converted into another via in situ generation of blue emitting chromophore. This strategy has been used to obtain various white light standards, post formulation, via simple irradiation.



Publication based on this work: *J. Mater. Chem. C*, 2016, **4**, 2748

6b.1. Introduction

Supramolecular design of white light emitting materials has been one of the major research frontiers in organic opto-electronics.^{1,2} Various supramolecular designs have been explored such as organogels and organic inorganic hybrids for light harvesting and white light emission.³⁻⁸ However, most of these materials have shown single white light emission and require re-mixing of ingredients for multiple color lights. Getting colors closer to multiple white light standards is therefore a challenging and tedious task in these materials. The general concept of white light emission revolves around creating a broad emission spectrum in the visible range which has been achieved either by mixing dyes with different colour emissions in appropriate amounts or as in case of single molecule white light emitters, carefully adjusting the molecular parameters. In either case for achieving a particular colour, mixture proportions are to be standardized individually. The advantageous strategy therefore could be to modulate the mixture such that various colours can be achieved from a single mixture. This strategy will be particularly useful if one were to apply it and achieve multiple white light standards from a single concoction.⁹ Herein we show the first report of a light induced post-modification of clay chromophore hybrids where same mixture of chromophores with color pertaining to a white light standard can be converted into another.

In recent years we have been working on amino-clay based soft hybrids for light harvesting.¹⁰⁻¹² In addition we have also shown that on amino-clay (**AC**) hybrids a tetraphenylethylene derivative (**TPTS**) which shows aggregation induced emission (**AIE**)¹³ can be converted into di-hydro phenanthrene derivative **PhP** photo-chemically (Figure 6b.1).¹⁴ Spectroscopically speaking during photo conversion the maxima of the emission spectra changes from 475 nm to 410 nm, and thus creates a blue emitting component (Figure 6b.2b). In this current report we wish to take advantage of this photo generation of the blue component and modify, post formulation, the clay hybrid containing green and red component (**TPTS** and **SRG** respectively) (Figure 6b.2a). Therefore by controlling the

irradiation time we would have a control on the concentration of blue chromophore and hence the effective colour of the hybrid. The complete synthesis and characterization of TPTS has been reported in our previous work.¹⁴

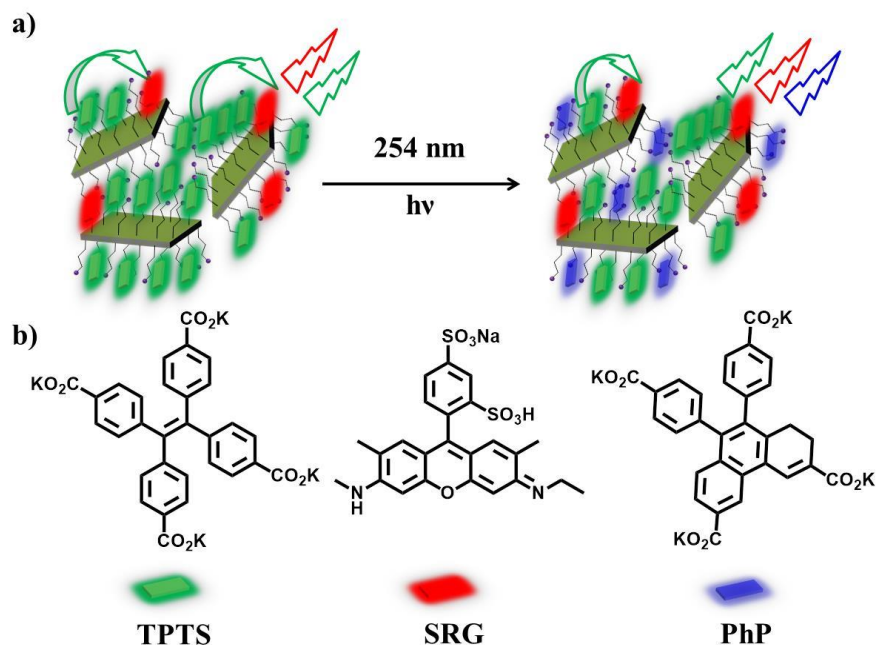


Figure 6b.1. (a) Schematic showing the strategy for photo-modulation of the clay hybrids, (b) Molecular structures of the TPTS, SRG and TPTS photoproduct (PhP).

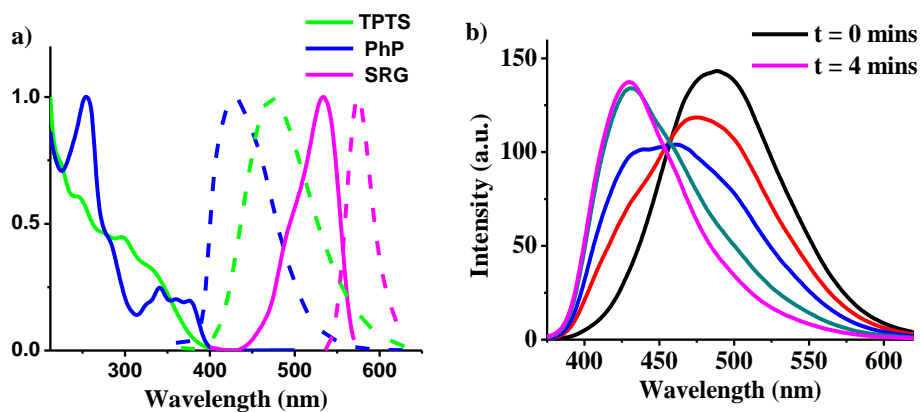


Figure 6b.2. (a) Absorption (bold) and emission (dash) spectra of TPTS, PhP and SRG. (b) Emission Spectra of $10^{-4}M$ TPTS with 0.4 wt% AC with varying times of 254 nm irradiation ($\lambda_{exc} = 330$ nm, $l = 2$ mm).

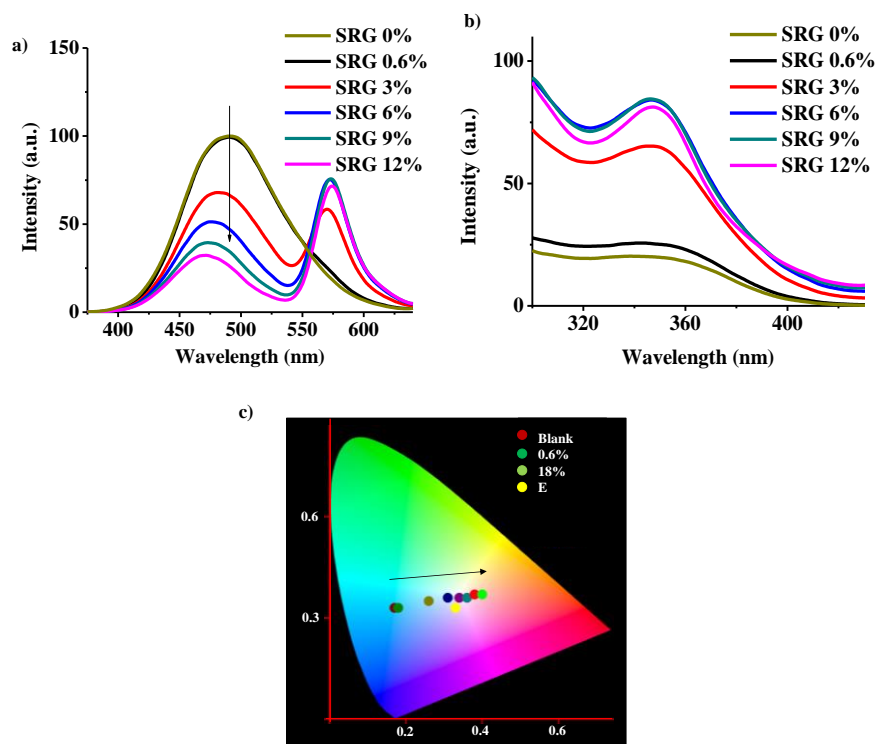


Figure 6b.3. (a) Emission spectra of *TPTS*+*AC* hybrid (10^{-4} M *TPTS*, 0.4 wt% *AC*, H_2O) with varying percentages of *SRG* (0% to 12%) excited at 330 nm, 2 mm cuvette, (b) Excitation Spectra of 10^{-4} M *TPTS* with 0.4 wt% *AC* with varying amounts of *SRG* ($\lambda_{mon} = 570$ nm, $l = 2$ mm) (c) 1931 CIE coordinates for respective hybrids with varying *SRG* percentage (0% to 18%) with equal energy white light (*E*, (0.33,0.33)) noted for reference.

6b.2. Results and Discussion

We first investigated the amino-clay (*AC*) hybrid assembly with *TPTS* and *SRG* chromophores. To an aqueous dispersion containing 0.4 wt% *AC* and 10^{-4} M *TPTS* we varied the percentage of *SRG* from 0% to 12%. With a concomitant increase in *SRG*% we saw a decrease in *TPTS* emission at 475 nm (Figure 6b.3a). This observation could be attributed to the partial Förster resonance energy transfer (FRET) from *TPTS* to *SRG*. To further strengthen this conclusion we performed excitation spectra at 570 nm which is attributed to the *SRG* emission region and monitored it between 300 to 410 nm which corresponds to the *TPTS* absorption region (Figure 6b.3b). As expected in cases with FRET the increase in acceptor percentage increased the intensity of excitation spectra in *TPTS* region suggesting the *SRG* emission increase is majorly contributed to energy

transfer from **TPTS**. We also performed Time correlated single photon counting (TCSPC) experiments on the hybrids to further investigate the FRET process. With 6% SRG we could clearly see a decrease in lifetime of the donor **TPTS** ($\lambda_{\text{mon}} = 474 \text{ nm}$, $\lambda_{\text{exc}} = 380 \text{ nm}$) and an increase in acceptor **SRG** lifetime ($\lambda_{\text{mon}} = 560 \text{ nm}$, $\lambda_{\text{exc}} = 380 \text{ nm}$) (Figure 6b.4).

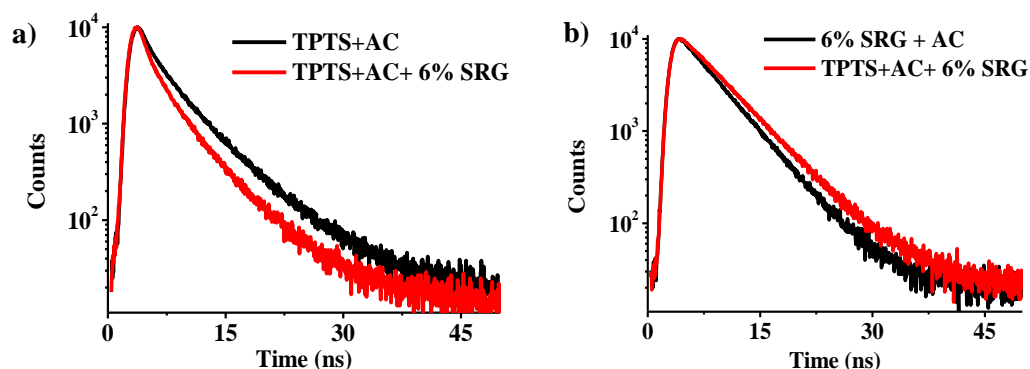


Figure 6b.4. TCSPC decay profiles of (a) 10^{-4} M **TPTS** with 0.4 wt% **AC** compared with 10^{-4} M **TPTS** with 0.4 wt% **AC** and 6% **SRG** and (b) 6% **SRG** with 0.4 wt% **AC** compared with 10^{-4} M **TPTS** with 0.4 wt% **AC** and 6% **SRG** ($\lambda_{\text{mon}} = 474$ and 570 nm respectively, $\lambda_{\text{exc}} = 380 \text{ nm}$). Energy transfer efficiency calculated from lifetime is 12.24%.

It is worth noting that extent of energy transfer decreases after 9% of **SRG** as seen in Figure 6b.3a,b. To investigate this we did control experiments containing **AC** with varying amounts of **SRG**. The excitation spectra at 570 nm suggested that **SRG** has a tendency to aggregate at higher percentages hence explaining the decrease in energy transfer efficiency. Moreover, as one investigates the emission colour of these hybrids it is clear that the 1931 CIE co-ordinates of the mixture lie just above the perfect white region and need a blue component to bring it to those co-ordinates (Figure 6b.3c, 8, 10).

However it is worth noting that even though the emission of hybrids is not in the pure white region they still lie close to other white standards. The above point is evident from the fact that **AC** hybrid with 10^{-4} M **TPTS** and 9% **SRG** has the CIE co-ordinates (0.34,0.36) close to D50 standard, and 15% (0.38,0.37) and 18% **SRG** (0.40,0.37) have it closer to F11 and F3 standard respectively (Figure 6b.8).

Having established the optical properties of two component hybrid assemblies we irradiated these dispersions with 254 nm to generate the blue component into the hybrids (Figure 6b.5). The samples were irradiated for total 4 mins in time periods of 30 secs. As hypothesized with prolonged irradiation the peak at 475 nm changed to 410 nm signifying the formation of **PhP** *in situ* (Figure 6b.6). Concomitant with the **PhP** generation is the decrease in **SRG** emission at 570 nm. TCSPC study of 6% **SRG** with 10^{-4} M **TPTS** in 0.4% **AC** after 4 mins of irradiation under 254 nm light showed that it is due to decrease in FRET as a result of the depleting concentration of **TPTS**.

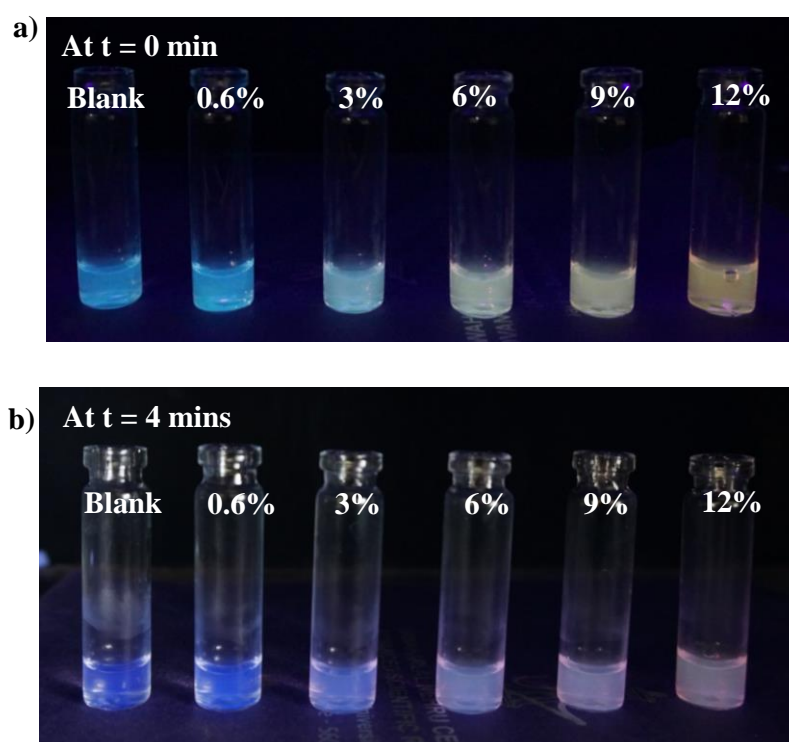


Figure 6b.5. (a) and (b) Photographs under 365 nm illumination of 254 nm irradiation progression over 4 mins of **TPTS+AC** hybrid.

Moreover, **PhP** does not undergo FRET with **SRG**. For a sample containing 6% **SRG** we monitored the fluorescence lifetime at 410 nm (**PhP** region) and 560 nm (**SRG** region) and observed almost no change in the lifetimes compared to the individual control samples, hence confirming this hypothesis (Figure 6b.7a-b). As a result of these photo-

modifications the emission colour of the dispersions moved towards lesser CIE co-ordinates due to the addition of the blue component (Figure 6b.5, 6b.8-6b.10). The drop casted films of these dispersions also followed this trend (Figure 6b.7c). We further calculated the 1931 CIE co-ordinates from the emission spectra of these dispersions and as we expected the generation of blue chromophore inside the mixture photo-tuned into various other white standards. The D50 standard of 9% **SRG** at $t = 0$ could be converted to nearly D55 (0.33, 0.34) after 30 secs of irradiation. Moreover, the 12% **SRG** dispersion which had (0.36, 0.36) as CIE co-ordinates at $t = 0$, changed to (0.35, 0.35) after 30 secs of exposure which is closer to F10, F8 and B white standards. Further irradiation converted it to (0.34, 0.33) and (0.33, 0.32) after 1 and 1.5 mins of irradiation, respectively.

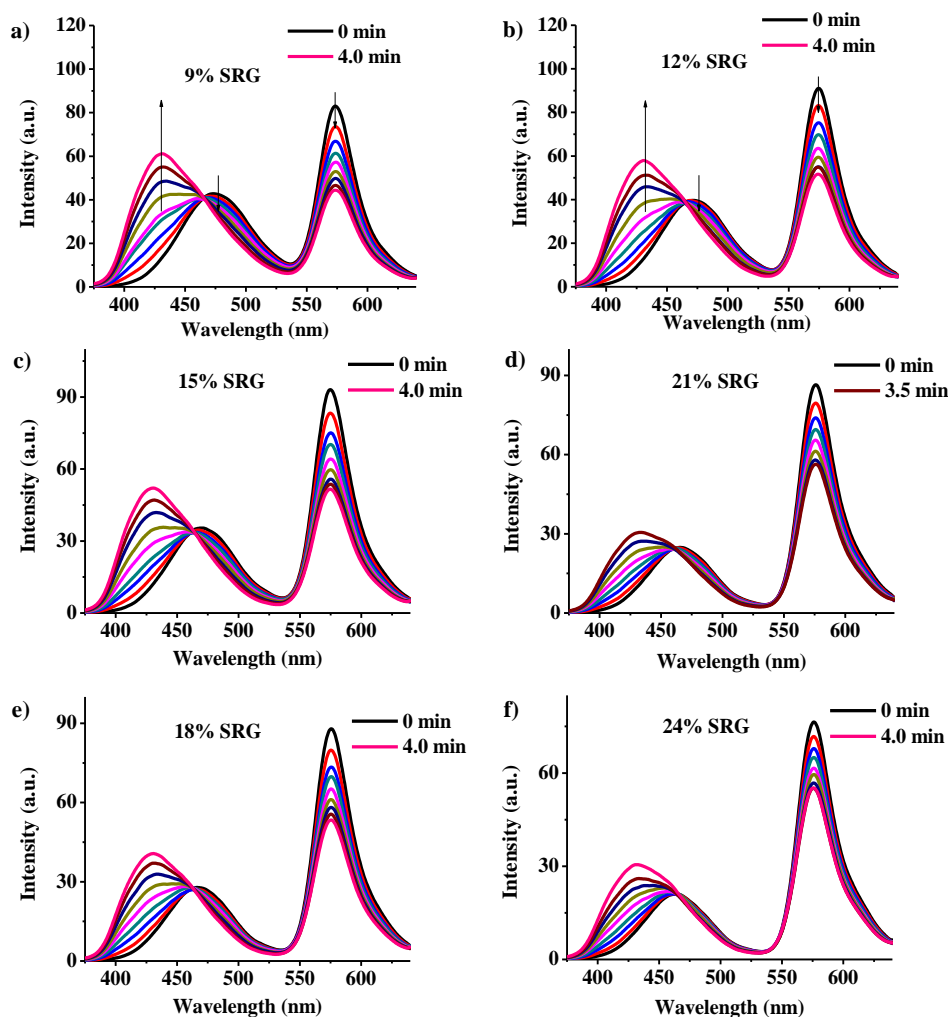


Figure 6b.6. (a)-(f) Emission Spectra of $10^{-4}M$ TPTS + 0.4 wt% AC with varying amounts of SRG under varying times of 254 nm irradiation ($\lambda_{exc} = 330$ nm, $l = 2$ mm).

These co-ordinates are very close to the equal energy white light standard E (Figure 6b.9, 6b.10). To the best of our knowledge this is the first report showing light mediated modification of materials to achieve excellent control over white light emission. These results thus show the photo-modulation of clay hybrids, post formulation, gives an added advantage that for various white lights we need not make different formulations due to inter conversion of colors via this approach.

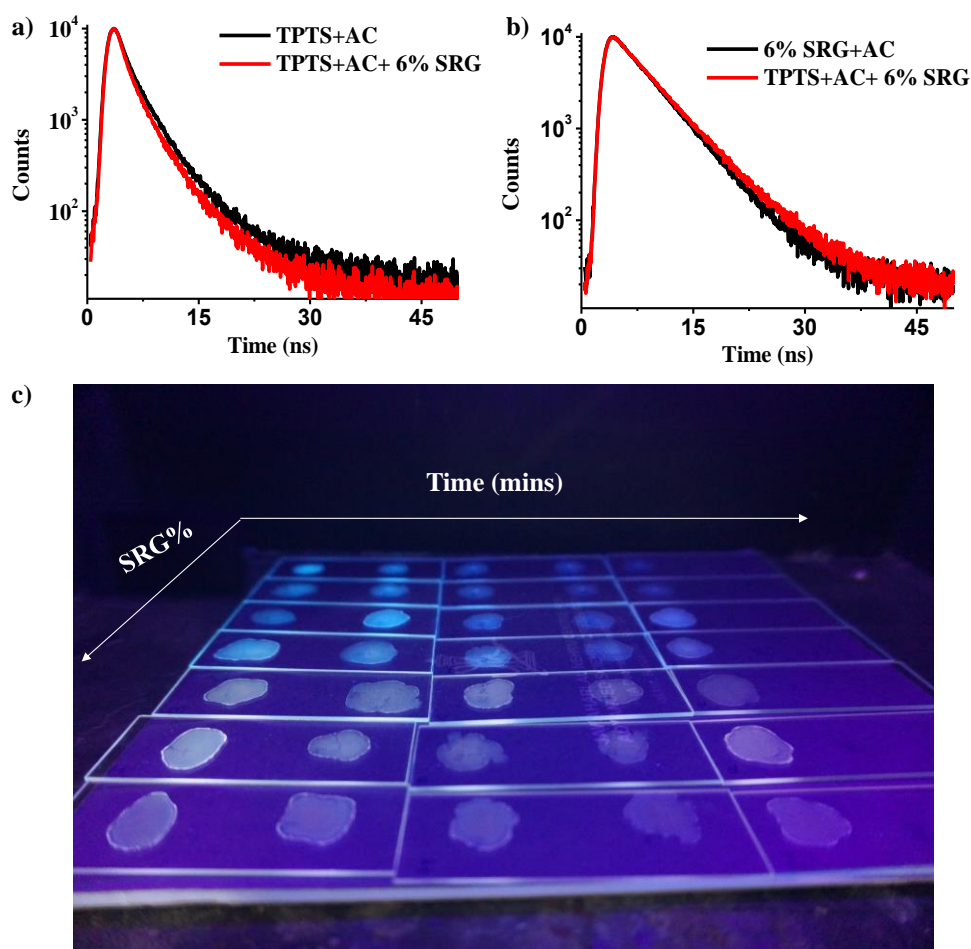


Figure 6b.7. TCSPC decay profiles of (a) $10^{-4}M$ TPTS with 0.4 wt% AC (after 4 min of 254 irradiation) compared with $10^{-4}M$ TPTS with 0.4 wt% AC and 6% SRG (after 4 min of 254 irradiation). (b) 6% SRG with 0.4 wt% AC compared with $10^{-4}M$ TPTS with 0.4 wt% AC and 6% SRG (after 4 min of 254 irradiation) ($\lambda_{mon} = 410$ and 570 nm respectively, $\lambda_{exc} = 380$ nm) and (c) Photographs under 365 nm illuminations of drop casted films of $10^{-4}M$ TPTS + 0.4 wt% AC with varying amounts of SRG under varying 254 nm irradiation.

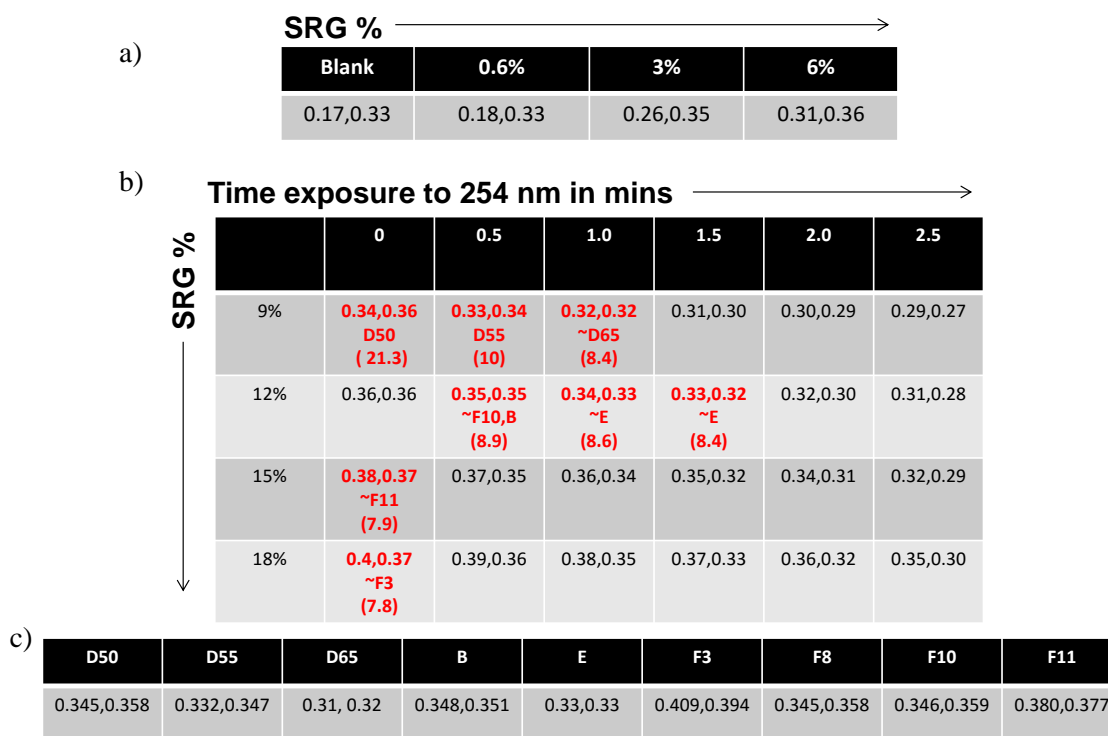


Figure 6b.8. (a) and (b) 1931 CIE coordinates of 10^{-4} M TPTS + 0.4 wt% AC with varying amounts of SRG under varying 254 nm irradiation (c) Actual 1931 CIE co-ordinates of white light standards. The numbers in parentheses represent fluorescence quantum yield in percentage.

We further tried and evaluated the stability of these hybrids in visible light. On a 9% SRG hybrid with 10^{-4} M TPTS in 0.4% AC we alternatively irradiated with 254 nm and visible light for 30 secs each and the emission spectra trend was followed at 400 nm. The trend clearly showed that the change occurred only during 254 nm illuminations and not during visible light illumination hence showing that these hybrids are stable to visible light and only photo-convert on 254 nm illuminations (Figure 6b.12). We also exposed the dispersion to diffused daylight and the hybrid showed sparing changes hence proving their stability (Figure 6b.12).

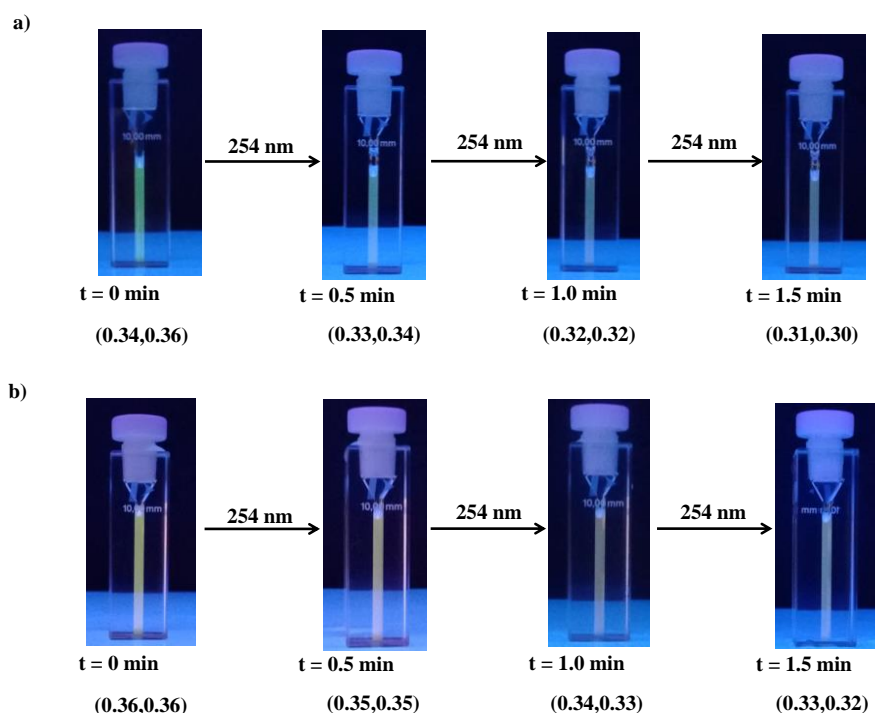


Figure 6b.9. (a) and (b) Photographs under 365 nm illumination of 254 nm irradiation progression over time of *TPTS*+*AC* hybrid containing 9% and 12% *SRG* respectively. The 1931 CIE coordinates of the hybrids are mentioned in parentheses.

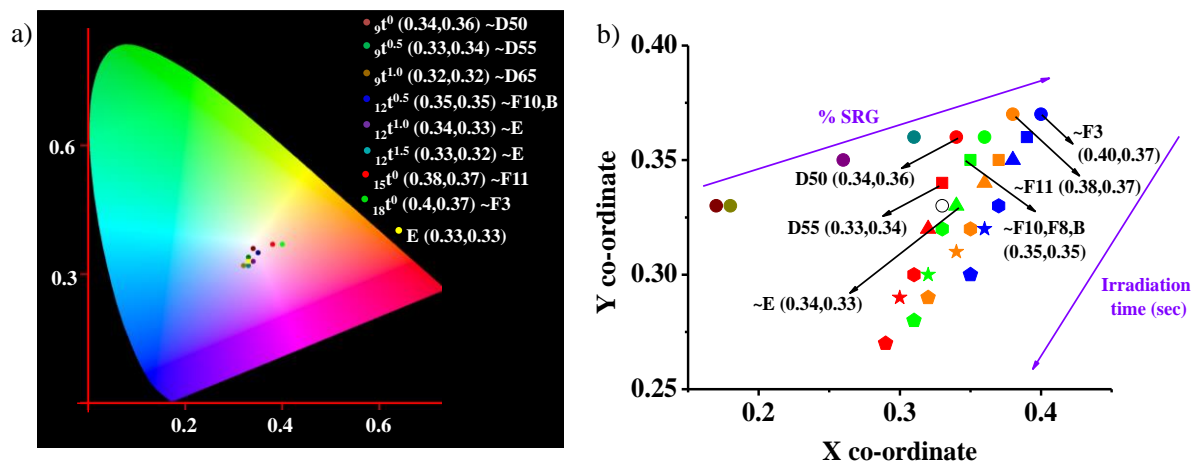


Figure 6b.10. (a) 1931 CIE co-ordinates of the various white lights obtained (notation of the legend ${}_x t^y$, x denotes the % of *SRG* and y denotes the time of 254 nm irradiation in minutes. The quantities in parentheses are the CIE co-ordinates and the notations next to it denote the white light standard they resemble and (b) 1931 CIE coordinates of $10^{-4}M$ *TPTS* + 0.4 wt% *AC* with varying amounts of *SRG* under varying 254 nm irradiation (0, 0.5, 1.0, 1.5, 2.0 and 2.5 minutes respectively) (same shape of represents same time of irradiation and same color represents same % of *SRG*).

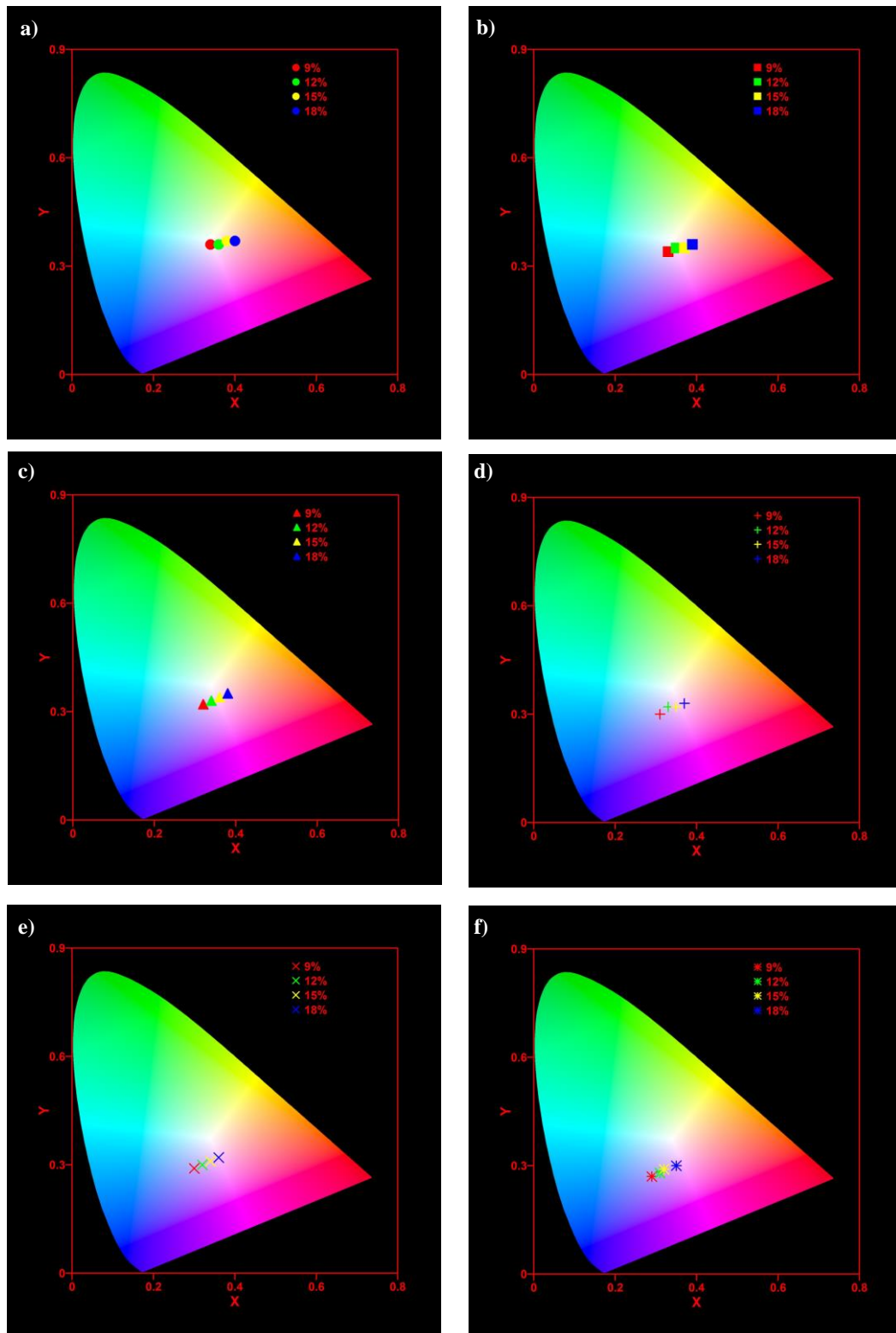


Figure 6b.II. (a) - (f) 1931 CIE coordinates of $10^{-4}M$ TPTS + 0.4 wt% AC with varying amounts of SRG under varying 254 nm irradiation (0, 0.5, 1.0, 1.5, 2.0 and 2.5 minutes respectively).

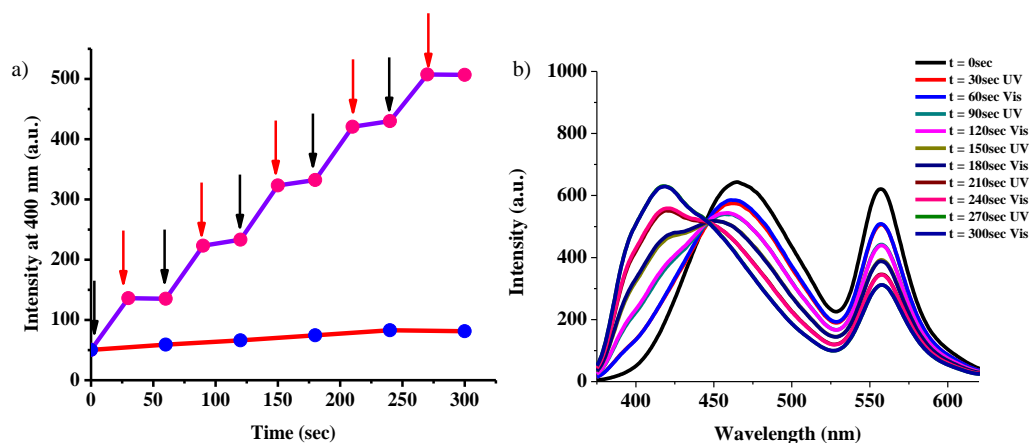


Figure 6b.12. (a) Emission spectra of 9% SRG with $10^{-4}M$ TPTS and 0.4 wt% AC monitored at 400 nm. For pink dots: (Black arrow suggests 254 nm illumination “ON” and visible light illumination “OFF”. Red arrow suggests visible light illumination “ON” and 254 nm illumination “OFF”). For blue dots: illumination under diffused sunlight over time. (b) Emission spectra of 9% SRG with $10^{-4}M$ TPTS and 0.4 wt% AC with alternate short UV and visible illumination for 30 secs each.

6b.3. Conclusion and Outlook

In conclusion we show an unprecedented control over the white light region via photo-modification of clay based hybrids. We take advantage of the *in situ* generation of blue emitting photoproduct and modify the colour of these hybrids via subsequent irradiations. This approach leads to interconversion of various white light emissions as various white lights standards can be achieved via mere irradiation which could have otherwise taken a painful route of mixture optimization. Moreover, we also prove that these hybrids are stable to visible light. We believe that this work is a proof of concept showing the strength of photo modification as a route to achieve subtle changes in optical properties of hybrids.

6b.4. Experimental Section

General Methods

Optical spectroscopy: UV/Vis absorption and fluorescence spectra were recorded on a Perkin-Elmer Lambda 750 and Perkin-Elmer LS 55 spectrometer respectively.

Irradiation: Irradiation was done in a 2x10 mm quartz cuvette. Lamp used was OSRAM puritec germicidal lamp HNS, 8W, G5 (G8T5/OF). In a general procedure the solution was placed inside the lamp chamber directly under the lamp.

TCSPC: Steady state PL spectra were collected using the 450 W xenon lamp as the source on the FLSP920 spectrometer, Edinburgh Instruments, while the lifetime measurements were carried out on an EPLED-380 ($\lambda_{\text{ex}} = 380$ nm) pico second pulsed Light emitting diode.

6b.5. References and Notes

- 1 (a) Kido J.; Kimura M.; Nagai K. *Science* 1995, **267**, 1332; (b) Furuta P. T.; Deng L.; Garon S.; Thompson M. E.; Fréchet J. M. J. *J. Am. Chem. Soc.* 2004, **126**, 15388.
- 2 (a) Praveen V. K.; Ranjith C.; Armaroli N. *Angew. Chem. Int. Ed.* 2014, **53**, 365; (b) Mukherjee S.; Thilagar P. *Dyes & Pigments* 2014, **110**, 2.
- 3 (a) Ajayaghosh A.; Praveen V. K.; Vijayakumar C.; George S. J. *Angew. Chem. Int. Ed.* 2007, **46**, 6260; (b) Molla M. R.; Ghosh S. *Chem. Eur. J.* 2012, **18**, 1290; (c) Varghese R.; Wagenknecht H.-A. *Chem. Eur. J.* 2009, **15**, 9307; (d) Maiti D. K.; Bhattacharjee R.; Datta A.; Banerjee A. *J. Phys. Chem. C* 2013, **117**, 23178.
- 4 (a) Abbel R.; van der Weegen R.; Pisula W.; Surin M.; Leclère P.; Lazzaroni R.; Meijer E. W.; Schenning A. P. H. J. *Chem. Eur. J.* 2009, **15**, 9737; (b) Vijayakumar C.; Praveen V. K.; Ajayaghosh A. *Adv. Mater.* 2009, **21**, 2059.
- 5 (a) Giansante C.; Raffy G.; Schäfer C.; Rahma H.; Kao M.-T.; Olive A. G. L.; Del Guerzo A. *J. Am. Chem. Soc.* 2011, **133**, 316; (b) Yang X.; Lu R.; Xue P.; Li B.; Xu D.; Xu T.;

- Zhao Y. *Langmuir* 2008, **24**, 13730; (c) Giansante C.; Schäfer C.; Raffy G.; Del Guerzo A. *J. Phys. Chem. C*, 2012, **116**, 21706.
- 6 (a) Vijayakumar C.; Sugiyasu K.; Takeuchi M. *Chem. Sci.* 2011, **2**, 291; (b) Tseng K.-P.; Fang F.-C.; Shyue J.-J.; Wong K.-T.; Raffy G.; Guerzo A. D.; Bassani D. M. *Angew. Chem. Int. Ed.* 2011, **50**, 7032; (c) Abbel R.; van der Weegen R.; Meijer E. W.; Schenning A. P. H. J. *Chem. Commun.* 2009, 1697; (d) Zhang X.; Rehm S.; Safont-Sempere M. M.; Wurthner F. *Nat. Chem.* 2009, **1**, 623.
- 7 Lei Y.-Y.; Jin Y.; Zhou D.-Y.; Gu W.; Shi X.-B.; Liao L.-S.; Lee S.-T. *Adv. Mater.* 2012, **24**, 5345.
- 8 (a) Li D.; Zhang Y.; Fan Z.; Chen J.; Yu J. *Chem. Sci.* 2015, doi: 10.1039/C5SC02044A; (b) Qin W.; Yang Z.; Jiang Y.; Lam J. W. Y.; Liang G.; Kwok H. S.; Tang B. Z. *Chem. Mater.* 2015, **27**, 3892; (c) Park S.; Kwon J. E.; Kim S. H.; Seo J.; Chung K.; Park S.-Y.; Jang D.-J.; Medina B. M.; Gierschner J.; Park S. Y. *J. Am. Chem. Soc.* 2009, **131**, 14043; (d) Mizoshita N.; Goto Y.; Tani T.; Inagaki S. *Adv. Mater.* 2009, **21**, 4798; (e) Mizoshita N.; Goto Y.; Maegawa Y.; Tani T.; Inagaki S. *Chem. Mater.* 2010, **22**, 2548; (f) Kumar C. V.; Chaudhari A. *J. Am. Chem. Soc.* 1994, **116**, 403; (g) Takagi S.; Tryk D. A.; Inoue H.; *J. Phys. Chem. B* 2002, **106**, 5455; (h) Ishida Y.; Shimada T.; Masui D.; Tachibana H.; Inoue H.; Takagi S. *J. Am. Chem. Soc.* 2011, **133**, 14280.
- 9 https://en.wikipedia.org/wiki/Standard_illuminant#White_points_of_standard_illuminants
- 10 (a) Rao K. V.; Jain A.; George S. J. *J. Mater. Chem. C* 2014, **2**, 3055; (b) Rao K. V.; Datta K. K. R.; Eswaramoorthy M.; George S. J. *Chem. Eur. J.* 2012, **18**, 2184.
- 11 Rao K. V.; Datta K. K. R.; Eswaramoorthy M.; George S. J. *Adv. Mater.* 2013, **12**, 1713.
- 12 Rao K. V.; Datta K. K. R.; Eswaramoorthy M.; George S. J. *Angew. Chem. Int. Ed.* 2011, **50**, 1179.
- 13 (a) Barbara P. F.; Rand S. D.; Rentzepis P. M. *J. Am. Chem. Soc.* 1981, **103**, 2157; (b) Hong Y.; Lam J. W. Y.; Tang B. Z. *Chem. Soc. Rev.* 2011, **40**, 5361; (c) Shultz D. A.; Fox M. A. *J. Am. Chem. Soc.* 1989, **111**, 6311; (d) Zhao Z.; Lamb Z, J. W. Y.; Tang B. Z. *J. Mater. Chem.* 2012, **22**, 23726; (e) Hong Y.; Lama J. W. Y.; Tang B. Z. *Chem. Commun.*

2009, 4332; (f) Hu R.; Lam J. W. Y.; Deng H.; Song Z.; Zheng C.; Tang B. Z. *J. Mater. Chem. C* 2014, **2**, 6326.

14 Jain A.; Achari A.; Mothi N.; Eswaramoorthy M.; George S. J. *Chem. Sci.* 2015, **6**, 6334.

Curriculum Vitae



Ankit Jain was born on February 1, 1985 in Jhansi, Uttar Pradesh (India). He finished his B.Tech in Bio-technology from SASTRA University, Thanjavur in 2009. After finishing his degree he joined Jawaharlal Nehru Centre for Advanced Scientific Research (JNCASR) as a research associate under Prof. Subi J. George. In 2011, He joined JNCASR as a Ph.D. student under Prof. Subi J. George. His research work at Supramolecular Chemistry Laboratory focused on dynamic charge transfer aggregates and self-assembly under non-equilibrium conditions. He has also worked on clay-chromophore conjugates and their pertinent photo-chemistry.

List of Publications

From Thesis

1. **A. Jain**, A. Achari, M. Eswaramoorthy and S. J. George, **Light induced in situ post-modification of clay-chromophore hybrids for multiple white light emissions**, *J. Mater. Chem. C*, 4, 2748-2751 (2016).
2. **A. Jain**, A. Achari, N. Mothi, M. Eswaramoorthy and S. J. George, **Shining the Light on Clay-Chromophore Hybrids: Layered Templates for Accelerated Ring Closure Photo-Oxidation**, *Chemical Science*, 6, 6334-6340 (2015).
3. **A. Jain**, A. Dhyani, P. Vemula and S. J. George, **Fuel driven temporal control over growth of dynamic charge-transfer stacks**, manuscript under submission.
4. **A. Jain** and S. J. George, **Aggregation Controlled Rearrangement of an Ensemble Containing Non-covalent Charge Transfer Stacks**, manuscript under submission.
5. **A. Jain**, S. Dhawan and S. J. George, **ATP driven dissipative control over conformation and length of aggregates**, manuscript under submission.

Other Publications

6. **A. Jain** and S. J. George, **New Directions in Supramolecular Electronics**, *Materials Today*, 18, 206-214 (2015).
7. S. J. George, **A. Jain** and K. V. Rao, **Supramolecular Materials for Opto-electronics** (Book Chapter), *RSC Smart Material Series*, (2014).
8. K. V. Rao, **A. Jain** and S. J. George, **Organic-Inorganic Light-Harvesting Scaffolds for Luminescent Hybrids**, *J. Mater. Chem. C*, 2, 3055-3064 (2014).
9. B. Narayan, S. P. Senanayak, **A. Jain**, K. S. Narayan and S. J. George, **Self-Assembly of π -Conjugated Amphiphiles: Free Standing, Ordered Sheets with Enhanced Mobility**, *Adv. Funct. Mater*, 23, 3053-3060 (2013).
10. H.S.S.R.Matte, **A. Jain** and S. J. George, **A covalently linked graphene-oligo(phenylenevinylene) adduct: self-organization and photo-physical properties**, *RSC Advances*, 2, 6290-6294 (2012).
11. **A. Jain**, K. V. Rao, C. Kulkarni, A. George and S. J. George, **Fluorescent Coronene Monoimide Gels via H-bonding Induced Frustrated Dipolar Assembly**, *Chem. Commun.*, 48, 1467-1469 (2012).

12. **A. Jain**, K. V. Rao, U. Mogera, A. A. Sagade and S. J. George, **Dynamic Self-Assembly of Charge-Transfer Nanofibers of Tetrathiafulvalene Derivatives with F4TCNQ**, *Chem. Eur. J.*, 17, 12355-12361 (2011).
13. **A. Jain**, K. V. Rao, A. Goswami and S. J. George, **Metal Selective Coordinative Self-Assembly of pi- Donors**, *J. Chem. Sci.*, 123, 773-781 (2011).
14. U. Maitra, **A. Jain**, S. J. George and C. N. R. Rao, **Tunable Fluorescence in Chromophore-Functionalized Nanodiamonds Induced by Energy Transfer**, *Nanoscale*, 3, 3192-3197 (2011).